Site U1426[1]

R. Tada, R.W. Murray, C.A. Alvarez Zarikian, W.T. Anderson Jr., M.-A. Bassetti, B.J. Brace, S.C. Clemens, M.H. da Costa Gurgel, G.R. Dickens, A.G. Dunlea, S.J. Gallagher, L. Giosan, A.C.G. Henderson, A.E. Holbourn, K. Ikehara, T. Irino, T. Itaki, A. Karasuda, C.W. Kinsley, Y. Kubota, G.S. Lee, K.E. Lee, J. Lofi, C.I.C.D. Lopes, L.C. Peterson, M. Saavedra-Pellitero, T. Sagawa, R.K. Singh, S. Sugisaki, S. Toucanne, S. Wan, C. Xuan, H. Zheng, and M. Ziegler[2]

Chapter contents

[1]Tada, R., Murray, R.W., Alvarez Zarikian, C.A., Anderson, W.T., Jr., Bassetti, M.-A., Brace, B.J., Clemens, S.C., da Costa Gurgel, M.H., Dickens, G.R., Dunlea, A.G., Gallagher, S.J., Giosan, L., Henderson, A.C.G., Holbourn, A.E., Ikehara, K., Irino, T., Itaki, T., Karasuda, A., Kinsley, C.W., Kubota, Y., Lee, G.S., Lee, K.E., Lofi, J., Lopes, C.I.C.D., Peterson, L.C., Saavedra-Pellitero, M., Sagawa, T., Singh, R.K., Sugisaki, S., Toucanne, S., Wan, S., Xuan, C., Zheng, H., and Ziegler, M., 2015. Site U1426. *In* Tada, R., Murray, R.W., Alvarez Zarikian, C.A., and the Expedition 346 Scientists, *Proc. IODP,* 346: College Station, TX (Integrated Ocean Drilling Program). doi:10.2204/iodp.proc.346.107.2015
[2]Expedition 346 Scientists' addresses.

Background and objectives

Integrated Ocean Drilling Program (IODP) Site U1426 is in the south central part of the marginal basin at 37°2.00′N, 134°48.00′E and 903 meters below sea level. The site is situated near the top of the Oki Ridge, which extends southwest–northeast and bounds the southern margin of the Yamato Basin. Site U1426 is at the same location as Ocean Drilling Program (ODP) Site 798 ~150 km to the north of Honshu Island (Fig. **F1**). The bathymetric setting of Site U1426 was chosen to minimize the influence of turbidites.

Site U1426 is under the influence of the second branch of the Tsushima Warm Current (TWC), which is a highly meandering current characterized by eddies (Hase et al., 1999). Previous results from Site 798 as well as from a piston core retrieved from almost the same location as Site U1426 during the site survey cruise suggest an average sedimentation rate of ~80 m/m.y. (Ingle, Suyehiro, von Breymann, et al., 1990). These rates are slightly higher than those found at previous IODP Sites U1423–U1425, but they are still low enough to detect the contribution of eolian dust from the Asian continent, considering the relatively large contribution of biogenic material at this site. Based on a moderate geothermal gradient of ~110°C/km (observed at Site 798), the opal-A/opal-CT boundary at Site U1426 was predicted to be at ~400 m core depth below seafloor (CSF-A) (see the **"Methods"** chapter [Tada et al., 2015b]) (Ingle, Suyehiro, von Breymann et al., 1990). We expected this to allow recovery of unconsolidated sediment back to at least 4 Ma, permitting reconstruction of eolian dust flux and provenance over this period in the southern part of the marginal basin. The relatively shallow depth of Site U1426 was also expected to provide better preservation of calcareous microfossils.

Located in the middle of the southern half of the IODP Expedition 346 latitudinal transect, Site U1426 lies at a relatively shallow depth in the expedition depth transect. Together with results from Sites U1423–U1425, Site U1426 will enable us to reconstruct changes in the position of the atmospheric Westerly Jet axis during the last ~5 m.y. and sea-surface temperature changes associated with the north–south movement of the Subpolar Front, as it is related to the strength of the TWC (Isoda, 2011). Finally, we will reconstruct changes in deepwater oxygenation and calcium carbonate compensation depth (CCD) during the last ~5 m.y. by combining results from the Expedition 346 depth transect sites.

doi:10.2204/iodp.proc.346.107.2015

Operations

Four holes were cored at Site U1426 (proposed Site YB-2) using the full and half advanced piston corer (APC) and the extended core barrel (XCB) (Table T1; see also Fig. F2 in the "Expedition 346 summary" chapter [Tada et al., 2015a]). Holes U1426A, U1426B, U1426C, and U1426D were cored to 396.7, 34.7, 204.0, and 99.4 m CSF-A (see the "Methods" chapter [Tada et al., 2015b]) and recovered 418.78, 35.82, 211.89, 103.71 m of core, respectively. A total of 95 APC and 2 XCB cores obtained 770.2 m of sediment (104.8% recovery). The advanced piston corer temperature tool (APCT-3) was deployed four times.

Transit from Site U1425

The 148 nmi transit to Site U1426 was covered in 13.4 h at an average speed of 11 kt. Sea passage ended at 0636 h on 3 September 2013. The vessel was maneuvered over the location coordinates, thrusters were lowered into position, and the vessel was turned over to dynamic positioning control. By 0715 h, the vessel was stabilized for rig floor operations to begin. A Falmouth Scientific positioning beacon (model BAP-547; SN1028W, 16 KHz, 206 dB) was deployed at 0822 h.

Hole U1426A

A three-stand APC/XCB bottom-hole assembly was assembled, and the drill string was run to the seafloor. After picking up the top drive and spacing out the drill string to 907.4 meters below rig floor (mbrf), which was 6.0 m deeper than the depth provided by the precision depth recorder, an APC core barrel was deployed. The first core barrel recovered 2.47 m of core, establishing a seafloor depth of 914.4 mbrf. Oriented APC coring continued using full-length nonmagnetic core barrels through Core 346-U1426A-28H at 256.2 m CSF-A. At this depth, the APC was switched to the half APC (4.7 m) system, and coring continued through Core 37H (297.0 m CSF-A), where a solid dolomite layer was encountered. The XCB was picked up and used to cut a 1.0 m core (38X) until breaking through the layer of resistance. Half APC coring resumed from that point and continued through Core 59H (396.7 m CSF-A). The hole was displaced with 160 bbl of 10.5 ppg mud. The top drive was set back, and the drill string was pulled clear of the seafloor at 2330 h on 4 September 2013, ending Hole U1426A. Total recovery for this hole was 418.78 m (105.6%). A total of 29 half APC cores were recovered. Four successful temperature measurements were taken using the APCT-3 temperature shoe at 31.0, 59.5, 88.0, and 116.5 m CSF-A, respectively.

Hole U1426B

The ship was offset 15 m north of Hole U1426A, and the bit was positioned 3 m lower at 910.4 mbrf. Hole U1426B was spudded at 0045 h on 5 September 2013. Recovery from the first core established a seafloor depth of 913.7 mbrf. APC coring continued with four cores recovered for intensive geochemistry sampling to 34.7 m CSF-A. By 0215 h, the last core barrel had been laid out and the rig floor prepared for tripping pipe. Because the hole was shallow, the pipe was tripped out of the hole with the top drive in place. The bit cleared the seafloor at 0230 h, officially ending Hole U1426B. Recovered core totaled 35.82 m (103%).

Hole U1426C

The ship was offset 15 m south of Hole U1426A. The top drive was picked up, the bit was positioned at 911.4 mbrf, and Hole U1426C was spudded at 0250 h on 5 September 2013. The mudline core established a seafloor depth of 914.4 mbrf. APC coring continued through Core 346-U1426C-15H to 128.3 m CSF-A. XCB Core 16X cut through a hard dolomite layer, allowing the continuation of APC coring. Full-length core barrels were used through Core 24H to 206 m CSF-A. The hole was plugged and abandoned with 80 bbl of 10.5 ppg mud. The drill string was pulled with the top drive to 895 mbrf, clearing the seafloor at 1425 h. This ended Hole U1426C. Total recovery for this hole was 211.9 m (103.9%). There were no half APC cores from this hole.

Hole U1426D

The ship was offset 15 m west of Hole U1426A. The top drive was picked up, and the bit was positioned at 909.4 mbrf. Hole U1426D was spudded at 1500 h on 5 September 2013. The sediment/water interface was recovered in Core 1H, establishing a seafloor depth of 914.4 mbrf. APC coring continued with 11 full-length cores recovered to 99.4 m CSF-A. The hole was plugged and abandoned with 40 bbl of 10.5 ppg mud. The top drive was set back, and the drill string was pulled clear of the seafloor at 2030 h. The bit subsequently cleared the rotary table at 2235 h. The rig floor was secured for transit, thrusters were raised, and sea passage to IODP Site U1427 began at 2342 h. Total recovery for this hole was 103.71 m (104.3%). There were no half APC cores taken from this hole.

Lithostratigraphy

Drilling at Site U1426 penetrated to a maximum subbottom depth of 396.7 m CSF-A in Hole U1426A, re-

covering a total of 418.78 m of sediment for a recovery rate of 106%. The detailed visual assessment of sediment composition, color, sedimentary structures, bioturbation intensity, and drilling disturbance was supplemented by petrographic analysis of smear slides (175 from Hole U1426A, 7 from Hole U1426B, 87 from Hole U1426C, and 29 from Hole U1426D) and bulk mineralogic analysis by X-ray diffraction (XRD) (43 samples; Table T2). Results from these analytical methods provide the basis for identification of sedimentary facies and facies associations and for the division of the stratigraphy into major lithologic units (Figs. F2, F3, F4, F5).

The sedimentary succession recovered at Site U1426 consists of a wide variety of lithologies: clay and silty clay with varying contents of biosilica, foraminifers, and calcareous nannofossils, as well as diatom, biosiliceous, and nannofossil ooze. Major lithologies are interbedded with tephra (volcanic ash) layers. Carbonate-rich sections are restricted to the upper 185 m CSF-A and to the interval between 296 and 341 m CSF-A of the succession. Intervals of laminated sediment are observed to 125 m CSF-A. At 54.8 and 297.6 m CSF-A in Hole U1426A, two diagenetic carbonate layers, each several centimeters thick, were recovered.

The stratigraphy is divided into two lithologic units (I and II) based on sedimentary structures and sediment composition. Unit I is further divided into two subunits (IA and IB). These lithologic units are not equivalent to the lithologic division of nearby Site 798 (Shipboard Scientific Party, 1990). Instead the division of Site U1426 follows in principle the classification of Tada (1994) and is consistent with the division of Units I and II at Sites U1424 and U1425. In the case of Site U1426, the boundaries mark distinct changes in the frequency of change of major lithologies within the unit, rather than changes of major lithology from one unit to the next. As at Sites IODP U1422–U1425, Unit I shows alternations of clay and diatom-rich clay to diatom ooze. Subunit IA shows characteristic, albeit somewhat less pronounced than at Site U1425, centimeter- to decimeter-scale alternations of diatom-rich clay and clay with a distinct dark–light color banding. In contrast, Subunit IB is characterized by intermediate-frequency alternations (3–5 m scale) of clay with diatom and nannofossil oozes, with subtle color changes between major lithologies. Unit II is characterized by thick intervals of diatom ooze and clay and shows a lower frequency of variability in general. Physical properties measurements, including natural gamma radiation (NGR), magnetic susceptibility, color reflectance, and dry bulk density profiles, reflect the various lithologies and unit boundaries (see **"Physical properties"**).

Figures F2, F3, F4, and F5 summarize the major characteristics and physical property profiles of the sedimentary sequence. Hole-to-hole correlation based on the distribution of lithologic units is shown in Figure F6.

Site U1426 appears to provide a complete pelagic to hemipelagic sedimentary sequence without major disturbances. At nearby Site 798, slumped sediment was described in interval 128-798C-7H-4, 86–120 cm (Shipboard Scientific Party, 1990). In Hole U1426A, the same interval was recovered in Sections 346-U1426A-7H-5 and 7H-6 (Fig. F7), and the description of Leg 128 was revisited. Clear indications for slumping processes are not present in the succession of Site U1426. However, several coarse-grained layers (including tephra layers and foraminifer-sand layers; Fig. F8) in Core 7H might indicate resedimentation and grain-size sorting by bottom currents. In interval 346-U1426D-9H-5, 138–147 cm, a layer with normal grading and foraminifer sand at its base is observed (Fig. F9).

Unit I

Intervals: 346-U1426A-1H-1, 0 cm, to 34H-3, 108 cm; 346-U1426B-1H-1, 0 cm, to 4H-CC, 38 cm; 346-U1426C-1H-1, 0 cm, to 24H-CC, 38 cm; 346-U1426D-1H-1, 0 cm, to 11H-CC, 20 cm

Depths: Hole U1426A = 0–283.78 CSF-A; Hole U1426B = 0–35.16 m CSF-A; Hole U1426C = 0–206.53 m CSF-A; Hole U1426D = 0–99.60 m CSF-A

Age: Holocene to late Pliocene (2.9 Ma)

Unit I consists of a wide range of major lithologies that alternate on different scales (from centimeter to meter). Dominant major lithologies are clay, silty clay, nannofossil-rich clay, and diatom ooze. The alternations show a distinct change in frequency. Based on this frequency change, Unit I is divided into Subunits IA and IB (Tada, 1994).

Subunit IA

Intervals: 346-U1426A-1H-1, 0 cm, to 14H-7, 121 cm; 346-U1426B-1H-1, 0 cm, to 4H-CC, 38 cm; 346-U1426C-1H-1, 0 cm, to 15H-2, 142 cm; 346-U1426D-1H-1, 0 cm, to 11H-CC, 20 cm

Depths: Hole U1426A = 0–125.63 m CSF-A; Hole U1426B = 0–35.16 m CSF-A; Hole U1426C = 0–125.42 m CSF-A; Hole U1426D = 0–99.60 m CSF-A

Age: Holocene to early Pleistocene (1.3 Ma)

Lithologies and structures

Subunit IA consists of clay, silty clay, and nannofossil-rich clay with interbedded foraminifer- and dia-

tom-rich layers (Figs. F2, F3, F4, F5). The major lithologies are interbedded with several centimeter-thick tephra layers (vitric and scoriaceous). Subunit IA in Hole U1426A contains a total of 38 tephra beds >0.5 cm thick (Fig. F10; Table T3).

The most characteristic sedimentary structure of Subunit IA is the decimeter-scale color banding with alternations of dark brownish, organic-rich intervals interspersed with lighter colored, bioturbated organic-poor intervals (Fig. F11). These alternations are reflected in the L*, a*, and b* records (see "Physical properties"). In detail, the light intervals are mainly composed of light greenish gray and pale yellowish gray diatom-rich clay. These light intervals are moderately to heavily bioturbated. The organic-rich dark intervals are composed of clay and in general have a sharp base. The characteristics of these layers have been described in detail for Sites U1424 and U1425. Compared to these other sites, the dark layers at Site U1426 are more enriched in foraminifers and nannofossils, which is consistent with its shallower water depth. The transition from dark to light is generally gradational but also very often disturbed by bioturbational mixing. Bioturbation is more intense in the lower part of Subunit IA (deeper than 50 m CSF-A), where color contrast between the bands is also reduced. In this portion of the sequence, bioturbation often impacts heavily on the preservation of the thin, darker banding and its contact with the light colored bands (Fig. F12). Many dark to light transitions show evidence of *Chondrites* burrows. In general, the upper part of Subunit IA is dominated by brownish colors, whereas the lower part of the unit is dominated by light greenish colors, indicating a decrease of organic carbon content toward the base of the unit. Some intervals of Subunit IA are laminated. These intervals are typically dark gray in color and consist of biosiliceous silty clay with increased occurrence of pyrite (e.g., Section 346-U1426B-3H-1). This type of lamination occurs only in the uppermost 45 m of Subunit IA. In contrast to the dark gray laminated sections, a second type of laminated sediment is composed of nannofossil ooze and has a pale yellowish gray color and no particularly high pyrite content. This especially noticeable pale yellow nannofossil ooze occurs only at ~42 m CSF-A. The Subunit IA/IB boundary is well defined by the occurrence of a third type of laminated sediment. This interval consists of diatom ooze and occurs in Section 346-U1426A-14H-7.

Composition

The principal components of lithologies in Subunit IA are of terrigenous and biogenic origin (see Site U1426 smear slides in "Core descriptions"). Terrigenous components are dominated by clay and fine silt size fractions. Volcanic glass is always present in the sediment as a minor dispersed composition (usually 5%–10% by visual estimate); however, volcanic glass and pumice account for nearly 100% of the tephra layers. Nannofossils dominate the biogenic fraction, with minor components of foraminifers and biogenic silica (mostly diatoms and sponge spicules). Preservation of nannofossils and foraminifers is very good throughout. The persistently high nannofossil content (Fig. F13) throughout Subunit IA is the most prominent feature at Site U1426, which is distinctly different from Sites U1422–U1425. Pyrite can be found in almost all sediment with concentrations from 1% to 20% and is especially rich in darker colored sediment. It usually occurs as framboids and/or in irregular masses and can even be found with well-developed crystal shapes (polyhedrons). Although dolomite is difficult to identify in smear slides, XRD analysis suggests that it is present in almost all intervals, although its concentration is very low (<1%–3%) throughout. However, it is enriched (20%–30%) in some layers (e.g., Section 346-U1426A-3H-2A) (Fig. F14).

Subunit IB

Intervals: 346-U1426A-14H-7, 121 cm, to 34H-3, 108 cm; 346-U1426C-15H-2, 142 cm, to 24H-CC, 38 cm

Depths: Hole U1426A = 125.63–283.78 m CSF-A; Hole U1426C = 125.42–206.53 m CSF-A

Age: early Pleistocene (1.3 Ma) to late Pliocene (2.9 Ma)

Lithology and structures

Subunit IB consists of intermediate-frequency alternations (3–5 m scale) of brown and olive-gray clay, brownish and olive-green and greenish gray biosiliceous-rich nannofossil ooze, biosiliceous-rich clay, and diatom ooze (Figs. F2, F4, F15). Subunit IB is distinguished from Subunit IA on the basis of sediment color and the frequency of color and clay content changes.

Subunit IB sediment is moderately bioturbated, which leads to an overall decrease in the preservation of original sedimentary structures. Tephra layers are a minor but common component of Subunit IB, and several tephra layers are >5 cm thick. They vary in color and type (vitric and scoria). Subunit IB lacks the characteristic centimeter- to decimeter-scale color banding of Subunit IA but instead shows clear color and lithologic cycles at a 3–5 m scale. These cycles mainly reflect alternations in clay content. Intervals with low clay content are diatom or nannofossil ooze.

Composition

The major lithologies in Subunit IB are dominated by fine-grained terrigenous and biosiliceous materials, the latter mostly diatoms. Calcareous nannoplankton and foraminifers are common in the upper part of Subunit IB. The lower part of the unit (172–283 m CSF-A in Hole U1426A) lacks biogenic carbonate. Biosilica rapidly becomes more abundant (>50%) from Section 346-U1426A-24H-5A downhole. Diatoms and siliceous sponge spicules are dominant in the biosilica fraction, whereas radiolarians and silicoflagellates are found only in rare or trace amounts (1%–5%). The above-mentioned siliceous fossil assemblages are observed in both the brownish and greenish color sediment in the "diatom ooze" category. Pyrite and volcaniclastic materials represent a minor component of sediment throughout Subunit IB.

Unit II

Intervals: 346-U1426A-34H-3, 108 cm, to 59H-CC, 17 cm

Depth: Hole U1426A = 283.78–396.87 m CSF-A

Age: Pliocene (>2.9 Ma)

Lithology and structures

Unit II shows lower frequency alternations of uniform dark green to gray clay with gray biosiliceous-rich clay and gray diatom ooze (Fig. **F16**). Sediment is generally slightly to heavily bioturbated throughout and has a fairly homogeneous, structureless appearance. Some intervals have high abundances of biogenic carbonate. Sediment deeper than 380 m CSF-A shows a distinct decrease in biogenic silica. Deeper than this depth, the major lithology is moderately indurated clay but with no clear evidence of opal-CT.

Composition

The major lithologies in Unit II are dominated by fine-grained terrigenous materials and biosiliceous components that are mostly diatoms. However, with the transition from Subunit IB to Unit II, the abundance of nannofossils rapidly increases again, ranging from common, abundant, and even dominant between Sections 346-U1426A-37H-2A and 48H-1A (296–341 m CSF-A). This phenomenon is not observed in Unit II of Sites U1422–U1425. The biosiliceous components rapidly decrease from >50% to <10% at around Section 54H-4A (Fig. **F17**). The preservation of diatoms decreases dramatically at this depth. These features may be related to diatom dissolution during diagenesis.

Bulk mineralogy

The results of XRD analysis of samples from Site U1426 are listed in Table **T2.** In general, the Pleistocene–Pliocene sediment at Site U1426 is composed mainly of quartz, calcite, plagioclase, and clay minerals (including smectite, illite, and kaolinite and/or chlorite), as well as biogenic opal-A and minor amounts of halite and pyrite. Calcite is a major mineral component in the upper part of the sedimentary succession but disappears deeper than ~200 m CSF-A.

Figure **F18** shows the downcore variations in peak intensity of the identified minerals at Site U1426. In general, the contents of quartz, plagioclase, smectite, illite, kaolinite and/or chlorite, K-feldspar, calcite, and opal-A show high variability throughout the sedimentary succession and especially between 50 and 300 m CSF-A. This large variability was not observed in Units I and II at Sites U1422–U1425. As expected, Site U1426 samples with a high opal-A or calcite content show a consistently lower abundance of silicate minerals. In summary, the average bulk mineralogy does not significantly change across unit boundaries. Subunit IB appears to show a larger amplitude of variability than Subunit IA and Unit II. However, the sampling resolution for the XRD analyses is not sufficient to resolve potential differences in the frequency of alternations in mineralogy within the units.

Tephra

Numerous (>200) visible tephra beds were observed in cores from Hole U1426A. Tephra beds with a thickness >0.5 cm are listed in Table **T3.** Several thick tephra layers (>20 cm) occur in the lower part of Unit I (intervals 346-U1426A-11H-3, 63–86.5 cm [91.11–91.345 m CSF-A], and 18H-6, 13–48 cm [162.13–162.48 m CSF-A]) and in Unit II (intervals 26H-4, 1.5–23 cm [230.645–230.86 m CSF-A], and 44H-2, 5–47 cm [322.18–322.60 m CSF-A]), whereas most of the beds have a thickness <1 cm. The total thickness of tephra beds and the number of discrete tephra layers with a thickness >0.5 cm in each core reach a maximum in Cores 7H to 9H. The number of tephra layers decreases deeper than Core 10H near the Brunhes/Matuyama paleomagnetic boundary. Some peaks in tephra thickness below this horizon indicate that rare but thick tephra deposition occurred during the period.

Several tephras were correlated to well-dated on-land and/or marine tephras such as U-Oki (~10.7 ka: intervals 346-U1426A-1H-2, 20–25 cm [1.70–1.75 m CSF-A], and 346-U1426D-1H-2, 19–20.5 cm [1.69–1.705 m CSF-A]), AT (~29.3 ka: intervals 346-U1426A-2H-1, 60–72 cm [3.10–3.22 m CSF-A], and 346-

U1426D-1H-3, 64–75.5 cm [3.64–3.755 m CSF-A]), U-Ym (~35 ka: interval 346-U1426A-2H-2, 29–32 cm [4.29–4.32 m CSF-A]), and Aso-4 (~88 ka: interval 346-U1426D-2H-4, 66.5–81 cm [9.565–9.71 m CSF-A]) tephras based on their characteristics and stratigraphic occurrence.

Tephras at intervals 346-U1426A-5H-3, 125–134 cm (34.75–34.84 m CSF-A), 346-U1426D-4H-3, 0–2.5 cm (26.29–26.315 m CSF-A), and 346-U1426D-6H-3, 17–20.5 cm (45.28–45.315 m CSF-A), are probably correlative to Ata-Th (240 ka), Aso-1 (250–270 ka), and Kb-Ks (520–530 ka) tephras, respectively, based on volcanic glass shard characteristics and heavy mineral compositions. Tephra beds at intervals 346-U1426A-11H-3, 63–86.5 cm (91.11–91.345 m CSF-A), and 18H-3, 1–7 cm (157.51–157.57 m CSF-A), are potentially correlated to the Ss-Pnk tephra (~1.6 Ma; Tamura et al., 2008; Satoguchi and Nagahashi, 2012) and the Eb-Fkd tephra (~1.7 Ma; Tamura et al., 2008; Satoguchi and Nagahashi, 2012), respectively, from the glass morphology. These initial correlations will be tested by shore-based petrographic and geochemical analyses.

Discussion

The sedimentary succession at Site U1426 documents the paleoceanographic history of the Yamato Basin from the Pliocene to the Holocene. Like the other sites drilled during Expedition 346, the lithostratigraphic characteristics appear to vary in a manner that is highly sensitive to global climate variability. The relatively rapid sedimentation at Site U1426 will allow for paleoclimate and paleoceanographic reconstructions at high resolution.

For division of the lithostratigraphic units, particular attention was paid to the frequency of lithologic changes. For nearby Site 798, a unit boundary was placed at ~220 meters below seafloor (mbsf), marking the downhole transition from the upper carbonate-rich part to the lower carbonate-poor sediment. Although such a division seems sensible from a lithologic point of view, it would be inconsistent with the lithostratigraphic framework for this marginal basin previously introduced by Tada (1994). Tada's (1994) classification of the marginal basin's lithologic units is based on sediment records from deeper water depths (>2500 m), well below the CCD. Site U1426 is substantially shallower (941 m) and therefore shifts in the depth of the CCD will have a greater impact on the local lithology, namely on carbonate preservation and content. Oceanographic as well as potential tectonic processes, such as uplift of the Oki Ridge, lifted the location of Site U1426 above the CCD during the early Pleistocene (~220 m CSF-A). However, this boundary is not correlatable across the basin because it strongly depends on local conditions, in particular the water depth of Site U1426 relative to other sites. Although Subunits IA and IB and Unit II at Site U1426 show some different lithologic characteristics compared to Site U1425 in the Kita-Yamato Trough or Site U1424 in the southeastern Japan Basin, certain features are persistent throughout. Therefore, the same lithostratigraphic concept has been applied to Site U1426 to emphasize correlatable features in the lithology that are not only basin wide (Japan Basin as well as Yamato Basin) but also across a wide range of water depths. The most striking basin-wide feature is variations in the frequency of change of the major lithology. This frequency decreases stepwise downhole. At Site U1426, the major steps occur at ~125 and 285 m CSF-A. At the same time, the amplitude of the lithologic changes decreases as well. These features reflect the changes in global climate variability across the Pliocene–Pleistocene.

The characteristic centimeter- to decimeter-scale color banding of Subunit IA is a recognizable lithostratigraphic feature that occurs basin wide during the Quaternary (Tada, 2004). Tada (1994) suggested that the deposition of organic-poor gray clay in the basin occurred under oxic conditions, whereas organic-rich dark brown layers were deposited during suboxic conditions, reflecting changes in ventilation of the marginal sea. Deposition of gray colored, laminated, and pyrite-rich intervals occurred potentially under euxinic conditions during the glacial maxima. The alternations between dark and light layers can be linked to global millennial-scale climate variability (Tada, 2004).

At Site U1426, dark–light cycles of Subunit IA are well developed in the upper 45 m. In contrast, the lower part of Subunit IA is strongly affected by bioturbation and the color cycles become less evident. At ~42.5 m CSF-A, a remarkable interval of partially laminated nannofossil ooze occurs that can be linked to a carbonate-rich layer in nearby Core MD01-2407 (Kido et al., 2007). This layer coincides with marine isotope Stage (MIS) 13. Because this interval of nannofossil ooze looks different from any other interval within Site U1426, one can conclude that oceanographic conditions in the marginal basin during MIS 13 were distinctly different. Unusual climatic and oceanographic conditions of unknown origin during MIS 13 have also been reported based on Chinese Loess Plateau records (e.g., Guo et al., 2000).

MIS 13 marks the onset of large-amplitude glacial–interglacial cycles after the mid-Pleistocene transition. Therefore, the intensified dark–light color banding in the upper 45 m appears to be linked to the recent period of more extreme glaciations. Gray

pyrite-rich laminated intervals are also restricted to the upper 45 m CSF-A, indicating the extreme sea level lowstands of the last 450,000 y have a particularly strong impact on the oxygenation of the marginal basin.

In contrast to Subunit IA, Subunit IB lacks centimeter- to decimeter-scale color banding. This is similar to what is observed at Sites U1422–U1425. Instead, Subunit IB is characterized by distinct 3–5 m alternations in the abundance of siliciclastic components, mainly the clay fraction. These alternations are particularly well depicted in the NGR profile (see **"Physical properties"**), with high NGR values indicating higher clay content in the sediment. With a sedimentation rate of ~10 cm/k.y. (see **"Stratigraphic correlation and sedimentation rates"**), these cycles seem likely to be linked to orbital cyclicity (41 k.y., obliquity), which dominated global climate and sea level fluctuations during the early Pleistocene. Orbital forcing has also been suggested as a possible explanation for the lithostratigraphic cycles at Site 798 (deMenocal et al., 1992).

Pliocene sedimentation at Site U1426 corresponds to the deposition of Unit II. Unit II is mainly composed of moderately to heavily bioturbated clay and diatom ooze with intervals of abundant nannofossils. Well-ventilated deep waters with high oxygen levels are indicated by the intensity of bioturbation, whereas the low frequency of lithologic changes reflects lower amplitude and lower frequency changes in Pliocene global climate. The decreased abundance and preservation of diatoms deeper than 380 m CSF-A represents the diagenetic dissolution of biogenic silica.

Biostratigraphy

At Site U1426, a ~397 m thick succession of Pliocene–Holocene sediment was recovered. Nannofossils are present shallower than 182.3 m CSF-A but are absent or rare deeper. Nannofossil Zones CN15/NN21 through CN13b/NN19 are recognized. Planktonic foraminifers are mainly confined to the upper part of the succession (shallower than ~172 m CSF-A), exhibiting moderate to poor preservation from ~172 to ~170 m CSF-A and good preservation shallower than ~99 m CSF-A. Planktonic foraminiferal assemblages shallower than ~172 m CSF-A generally indicate temperate to subarctic environments with intermittent incursions of subtropical species. The planktonic foraminiferal biostratigraphy spans Zones PF6 (Pliocene) through PF9 (Late Pleistocene). Benthic foraminifers occur intermittently throughout the Pliocene to Pleistocene succession, showing marked variations in abundance and preservation. The overall assemblage composition indicates bathyal paleodepths. The highly variable composition of the assemblages suggests fluctuating organic fluxes to the seafloor with episodic oxygen depletion and intense carbonate dissolution, particularly during the Pliocene. Radiolarians are generally common to abundant in the sequence, although they are rare or absent deeper than ~289 m CSF-A. The radiolarian biostratigraphy spans the *Larcopyle pylomaticus* Zone (Pliocene) through the *Botryostrobus aquilonaris* Zone (Late Pleistocene). Diatom preservation is good throughout the succession. Nevertheless, extreme diatom dissolution occurs deeper than 392.1 m CSF-A. Overall, diatom abundances are high through the succession and contain few/rare warm-water diatom species (*Azpeitia nodulifera, Fragilariopsis doliolus*, and *Thalassiosira leptopus*). High abundances of *Chaetoceros* spores and *Paralia sulcata* throughout the succession indicate a productive coastal environment. The diatom biostratigraphy spans the interval from Zones NPD 7B (Pliocene) to NPD 12 (Late Pleistocene). Twenty six datums, including 6 from calcareous nannofossils, 4 from planktonic foraminifers, 10 from radiolarians, and 6 from diatoms, are documented at this site. The nannofossil, planktonic foraminifer, radiolarian, and diatom datums generally agree with only some minor inconsistencies. The integrated calcareous and siliceous microfossil biozonation is shown in Figure **F19,** and microfossil datums are listed in Table **T4.** A biostratigraphic age-depth plot is provided in Figure **F20.** See **"Stratigraphic correlation and sedimentation rates"** for a discussion of sedimentation rates at Site U1426.

Calcareous nannofossils

Calcareous nannofossil biostratigraphy is based on the analysis of core catcher and split-core section samples from Holes U1426A and U1426B. Sixty of the 103 samples studied contain nannofossils (Table **T5**).

Nannofossils are present in Pleistocene sediment shallower than 182.3 m CSF-A in Hole U1426A with sporadic barren intervals throughout (Table **T5;** Fig. **F21**). Samples are generally barren deeper than 182.3 m CSF-A, with the exception of sporadic occurrences in core catcher samples from Cores 346-U1426A-37H, 40H, 41H, and 42H (between 298.4 and 317.3 m CSF-A). Preservation is generally moderate to good in Hole U1426A, with the best preservation occurring within the Pleistocene (Table **T5**). Only the uppermost four core catcher samples (i.e., shallower than 35.2 m CSF-A) from Hole U1426B were studied. Nannofossil preservation is moderate to good, and the assemblages are comparable to those documented in the upper portion of Hole U1426A.

Marked variations in nannofossil abundances occur through the uppermost ~182 m of the succession.

Nannofossil diversity at Site U1426 is higher than at previous Sites U1422–U1425. The nannofossil assemblage consists of 23 taxa, including *Braarudosphaera bigelowii, Calcidiscus leptoporus, Calcidiscus macintyrei, Coccolithus pelagicus, Dictyococcites* spp., *Emiliania huxleyi, Florisphaera profunda, Gephyrocapsa caribbeanica, Gephyrocapsa margerelii/muellerae, Gephyrocapsa oceanica, Gephyrocapsa* spp. (>4 µm), *Gephyrocapsa* spp. large (>5.5 µm), *Gephyrocapsa* spp. (<4 µm), *Helicosphaera carteri, Helicosphaera sellii, Pontosphaera japonica, Pontosphaera* spp., *Pseudoemiliania lacunosa, Reticulofenestra asanoi, Reticulofenestra minuta, Reticulofenestra minutula, Reticulofenestra* spp., and *Umbilicosphaera sibogae*.

Nannofossil Zones CN15/NN21 through CN13b/NN19 are recognized (Fig. **F19**) based on the first occurrence (FO) of *E. huxleyi*, the last occurrence (LO) of *P. lacunosa*, and the FOs of *G. oceanica* and *G. caribbeanica*. Additionally, the LOs of *R. asanoi* at 78.8 m CSF-A (Sample 346-U1426A-9H-CC), *H. sellii* at 117.7 m CSF-A (Sample 13H-CC), and *C. macintyrei* at 173.7 m CSF-A (Sample 20H-2W, 75 cm) with the presence of *G. oceanica* spp. large (>5.5 µm) from 117.3 to 117.7 m CSF-A (Samples 13H-CC to 14H-1W, 75 cm) provide good age control for the Pleistocene sequence. The pervasiveness of barren or sparse samples deeper than 182.3 m CSF-A (Sample 20H-CC) prevents further zonal assignments.

Radiolarians

A total of 46 core catcher samples from Hole U1426A were prepared for radiolarian analysis. Radiolarians are generally common to abundant shallower than 289.2 m CSF-A (Sample 346-U1426A-35H-CC), although they decrease deeper than this depth (Table **T6;** Fig. **F21**).

Ten biostratigraphic markers were found in Hole U1426A (Table **T4**). These span the *L. pylomaticus* Zone (Pliocene) through the *B. aquilonaris* Zone (Late Pleistocene) (Fig. **F19**). Based on the dominance of *Stylochlamydium venustum*, Sample 346-U1426A-1H-CC (2.4 m CSF-A) belongs to the *S. venustum* Interval Biozone (0.012–0.015 Ma) of Itaki and Ikehara (2003), equivalent to the last deglaciation. Pleistocene datums include the LOs of *Amphimelissa setosa* (0.08 Ma) and *Spongodiscus* sp. (0.29 Ma) at 12.1 m CSF-A (Sample 346-U1426A-2H-CC) and 31.6 m CSF-A (Sample 4H-CC), respectively. *Eucyrtidium matuyamai* is present at 117.7 m CSF-A (Sample 13H-CC), corresponding to the *E. matuyamai* Zone (1.03–1.98 Ma). The LO of *Axoprunum acquilonium* (1.2–1.7 Ma) is at 182.3 m CSF-A (Sample 20H-CC). Sample 22H-CC (201.2 m CSF-A) contains a single specimen of *Lamprocyrtis heteroporos* that suggests that it is older than 1.98 Ma. The Pleistocene/Pliocene boundary is close to the FO of *Cycladophora davisiana* (2.7 Ma) at 261.2 m CSF-A (Sample 29H-CC) and the LO of *Hexacontium parviakitaensis* (2.7 Ma) at 265.8 m CSF-A (Sample 30H-CC). The FO of *H. parviakitaensis* (3.9–4.3 Ma) occurs at 378.1 m CSF-A (Sample 55H-CC). The *Siphocampe arachnea* group is abundant from 382.7 (Sample 56H-CC) to 387.4 m CSF-A (Sample 56H-CC), suggesting that their acme zone is between 4.46 and 4.71 Ma.

Warm-water assemblages, including common *Dictyocoryne profunda, Dictyocoryne truncatum, Didymocyrtis tetrathalamus, Euchitonia furcata*, and the *Octopyle/Tetrapyle* group, are intermittent shallower than 172.4 m CSF-A (Sample 346-U1426A-19H-CC), suggesting interglacial inflow of the TWC during the early to Late Pleistocene. Sporadic occurrences of these species between 182.3 (Sample 20H-CC) and 349.8 m CSF-A (Sample 49H-CC) suggest reduced influence of the TWC during the late Pliocene to early Pleistocene.

Diatoms

Diatom biostratigraphy was based on smear slides from core catcher samples. Fifty seven core catcher samples were examined, and six datums were identified (Tables **T4, T7**). The LO of *Neodenticula koizumii* (2.0 Ma) at 127.17 m CSF-A (Sample 346-U1426A-14H-CC) marks the boundary between the base of Zone NPD 10 and the top of Zone NPD 9 (Yanagisawa and Akiba, 1998). The FO of *Neodenticula seminae* (2.4 Ma) in Sample 29H-CC (261.18 m CSF-A) and the LO of *Neodenticula kamtschatica* (2.6–2.7 Ma) in Sample 33H-CC (279.912 m CSF-A) mark the boundary between the base of Zone NPD 9 and the top of Zone NPD 8 (Yanagisawa and Akiba, 1998). The FO of *N. koizumii* (3.4–3.9 Ma) at 312.53 m CSF-A (Sample 41H-CC) defines the boundary between Zones NPD 8 and NPD 7Bb (Yanagisawa and Akiba, 1998). The LO of *Thalassiosira temperei* (5.44 Ma) in Sample 48H-CC and the FO of *Shionodiscus oestrupii* (5.56 Ma) at 359.3 m CSF-A (Sample 51H-CC) mark the boundary between Zones NPD 7Bb and NPD 7Ba (Yanagisawa and Akiba, 1998).

Diatom preservation is good throughout the succession. Nevertheless, extreme diatom dissolution occurs deeper than 392.1 m CSF-A. This dissolution most likely reflects the opal-A/opal-CT boundary.

Overall, diatom abundances are high (20%–60% and >60%) through the succession (Fig. **F21;** Table **T7**). At this site, rare (<2%) to few (2%–5%) abundances of warmer water diatom species (*A. nodulifera, F. doliolus*, and *T. leptopus*) are also present (Table **T7**). The high abundances (from 20% to 60%) of *Chaetoceros*

spores and *P. sulcata* indicate a productive coastal environment. Diatoms are also present in the foraminifer residue >63 and >150 µm (see **"Benthic foraminifers"** for more details).

Planktonic foraminifers

Planktonic foraminifers were examined in core catcher samples from Hole U1426A (57 samples). Relative abundance of taxa and visual estimates of assemblage preservation are presented in Table **T8.** Planktonic foraminifers are mainly confined to the upper part of the succession (Sample 346-U1426A-19H-CC; 172.4 m CSF-A and shallower) (Fig. **F21**). They are generally abundant, except for one barren horizon (Sample 3H-CC; 22.1 m CSF-A) and rare occurrences in Samples 10H-CC (88.8 m CSF-A) and 16H-CC (145.3 m CSF-A). Sample 20H-CC (182.3 m CSF-A) and deeper is mainly barren (Table **T8;** Fig. **F21**), except for Samples 37H-CC (298.4 m CSF-A) and 40H-CC (307.8 m CSF-A), which contain relatively abundant assemblages. Preservation is good shallower than 98.72 m CSF-A (Sample 11H-CC), becoming moderate to poor deeper than 107.3 m CSF-A (Sample 12H-CC) because of frequent fragmentation and pyritization. Partial dissolution and recrystallization of foraminiferal tests are most prominent in Sample 58H-CC (392.1 m CSF-A).

Planktonic foraminiferal assemblages shallower than Sample 346-U1426A-19H-CC (172.4 m CSF-A) are characteristic of temperate to subarctic environments with intermittent incursions of subtropical species. They mainly consist of *Globigerina bulloides, Neogloboquadrina pachyderma* (sinistral and dextral), and the *Neogloboquadrina kagaensis* group (*N. kagaensis* and *N. inglei*) with rare occurrences of *Globigerina umbilicata, Globigerina quinqueloba, Globigerinita glutinata, Globigerinoides ruber, Globigerinoides sacculifer, Globorotalia inflata, Globorotalia praeinflata, Globorotalia menardii, Globoturborotalita woodi, Neogloboquadrina dutertrei* (= *Neogloboquadrina himiensis*), *Neogloboquadrina incompta, Orbulina bilobata, Orbulina universa*, and *Pulleniatina obliquiloculata*. The subtropical species *G. ruber* and *G. sacculifer* occur in Sample 4H-CC (31.6 m CSF-A) but are rare deeper than this sample. The species *G. ruber* (pink), which ranges from 0.12 to 0.4 Ma in the Pacific and Indian Oceans, was also identified in this sample. The LO of the *N. kagaensis* group, which is observed at 0.7 Ma (Kucera and Kennett, 2000), is recorded in Sample 8H-CC (69.0 m CSF-A). The change in coiling direction of *N. pachyderma* (from dextral to sinistral) occurs between Samples 12H-CC (107.32 m CSF-A) and 13H-CC (117.7 m CSF-A), indicating the boundary between Zones PF8 and PF7 in the regional zonation for this marginal sea (Maiya, 1978). The FO of *G. praeinflata* in Sample 40H-CC (307.8 m CSF-A) indicates an age younger than 3.3 Ma (Lyle, Koizumi, Richter, et al., 1997). However, the position of this datum could be deeper because samples deeper than this level are devoid of planktonic foraminifers. Based on this datum, the boundary between Zones PF7 and PF6 is tentatively placed at 310.1 m CSF-A between Samples 40H-CC and 41H-CC.

Benthic foraminifers

Benthic foraminifers were examined in core catcher samples from Hole U1426A (57 samples). Samples with an average volume of ~30 cm^3 were processed from all core catchers to obtain quantitative estimates of benthic foraminiferal distribution patterns downhole. The mudline samples recovered in Holes U1426A and U1426B were also investigated. To assess assemblage composition and variability, all specimens from the >150 µm fraction were picked and transferred to slides for identification and counting. The presence and distribution of benthic foraminifers was additionally checked in the 63–150 µm fraction to ensure that assemblages in the >150 µm fraction were representative and that small species such as phytodetritus feeders or small infaunal taxa were not overlooked.

Benthic foraminifers vary substantially in abundance and preservation throughout the ~397 m thick Pliocene to Pleistocene succession recovered in Hole U1426A (Figs. **F21, F22;** Table **T9**). Benthic foraminifers are generally well preserved, abundant, and diverse within the Pleistocene interval shallower than Sample 346-U1426A-19H-CC (172.43 m CSF-A) (Fig. **F22**). Deeper in the succession, most samples are barren or consist of impoverished assemblages that are dominated by agglutinated species (Samples 19H-CC to 36H-CC [172.4–294 m CSF-A] and 43H-CC to 55H-CC [321.7–378.1 m CSF-A]). However, more diverse assemblages with poorly preserved calcareous foraminifers occur in Samples 22H-CC (201.3 m CSF-A), 24H-CC (218.6 m CSF-A), 37H-CC to 42H-CC (298–317 m CSF-A), 47H-CC (340.5 m CSF-A), and 56H-CC to 59H-CC (383–396.9 m CSF-A). The overall composition of assemblages at Site U1426 indicates middle bathyal paleodepths throughout the Pliocene to Pleistocene.

A total of 70 benthic foraminiferal taxa were identified. Table **T9** summarizes the downcore distribution of benthic foraminifers in core catcher samples from Hole U1426A. Figure **F23** illustrates characteristic taxa. Sample 346-U1426A-1H-CC contains 27 tests of *Elphidium*. This shallow-water dweller does not occur in the other core catcher samples, suggesting that tests may have been transported downslope. Species commonly recorded through the succession

include *Bolivina pacifica, Cassidulina japonica, Cassidulina norcrossi, Epistominella pulchella, Globobulimina pacifica, Trifarina angulosa* (= *Angulogerina kokozuraensis* of Kato, 1992), and *Uvigerina yabei*, which typically indicate enhanced organic flux and/or dysoxic conditions at the seafloor and within the uppermost few centimeters of the sediment (Gooday, 1993; Jorissen et al., 1995, 2007; Jorissen, 1999). Peak abundances in *Cassidulina* and *Uvigerina* alternate in the upper part of the succession, suggesting elevated but fluctuating food fluxes throughout the Middle to Late Pleistocene. In contrast, the agglutinated species *Martinotiella communis* and *Miliammina echigoensis* dominate in the late Pliocene to early Pleistocene (between ~173 and 294 m CSF-A). Similar distribution patterns are apparent at Sites U1422–U1425, which may be related to pervasive carbonate dissolution in the basin during this warmer climate period. However, two intervals containing calcareous taxa, including *E. pulchella, Cassidulina* spp., *G. pacifica, Melonis* spp., and *Uvigerina* spp. (298–317 and 383–397 m CSF-A), suggest transient periods of improved ventilation at the seafloor and reduced carbonate dissolution during the Pliocene. Comparable horizons recorded at Sites U1423 and U1425 cannot, however, be correlated because of the low resolution of shipboard samples. Overall, the highly variable composition of assemblages at Site U1426 suggests enhanced organic flux to the seafloor with marked variations in oxygenation and intense carbonate dissolution, in particular during the Pliocene. As noted previously, moderately to well-preserved diatoms and radiolarians are common to abundant in residues >150 and >63 µm throughout the succession, becoming dominant deeper than ~227 m CSF-A.

Ostracods

Core catcher samples were also examined for the presence of ostracods during shipboard preparation of benthic foraminifer samples. Ostracods are rare at Site U1426. They were observed only occasionally and always in very low numbers (1–2) throughout the sediment succession in Hole U1426A (Samples 346-U1426A-1H-CC, 4H-CC to 6H-CC, 8H-CC, 13H-CC, 15H-CC, 17H-CC, 40H-CC, and 58H-CC). Ostracod preservation ranges from poor (fragmented and showing signs of dissolution) to good (translucent single valves or carapace) (Fig. **F24**). The following taxa are present at Site U1426: *Krithe dolichodeira* Bold, *Acanthocythereis dunelmensis* Norman, *Legitimocythereis* sp., *Argilloecia lunata* Frydl, *Loxoconcha* sp. A, *Loxoconcha* sp. B, *Falsobuntonia* sp., and *Propontocypris* sp.

Mudline samples

The mudline sample from Hole U1426A was gently washed in order to preserve fragile, agglutinated foraminifer specimens with extremely low fossilization potential. The mudline sample contains organically cemented agglutinated species including *Haplophragmoides sphaeriloculum, Hyperammina elongata, M. echigoensis, Paratrochammina challengeri*, and *Reophax scorpiurus* (Fig. **F25**) as well as calcareous taxa including *B. pacifica, C. japonica, Cassidulina teretis, G. pacifica, Nummoloculina* sp., *Procerolagena gracillima, T. angulosa*, and *Uvigerina* sp. Most of the agglutinated and calcareous tests were stained with rose bengal. Several specimens of *H. elongata* bore a small test of *P. challengeri* or *Cribrostomoides subglobosus* attached in life position (Fig. **F26**). Diatoms are abundant, but no ostracods were recorded in the mudline sample from Hole U1426A. The mudline sample from Hole U1426B contains rare poorly preserved calcareous nannofossils. Very few specimens of *G. oceanica* and small *Gephyrocapsa* (<4 µm) were observed.

Geochemistry

Site U1426 is located on the Oki Ridge (see **"Background and objectives"**) at the position of Site 798 (Shipboard Scientific Party, 1990). It is also proximal to the positions of two relevant piston cores. Piston Core KH-77-3-L4 was taken ~16 km to the northeast, and an extensive array of interstitial water species was measured on this 4.95 m long core to define geochemical environments for deep-sea sediment of the marginal basin (Masuzawa and Kitano, 1983). Piston Core KH-79-3-PC3 was taken ~54 km to the east; several microfossil assemblage and stable isotope records were generated from this 9.93 m long core and used to reconstruct the basin's late Quaternary history (Oba et al., 1991).

Piston Core KH-77-3-L4 shows very steep gradients in certain pore water species. In particular, alkalinity and dissolved NH_4^+ increases from ~2.1 mM and ~0 µm at the seafloor to ~30 mM and ~1000 µm at 4.95 mbsf, respectively, whereas dissolved SO_4^{2-} decreases from ~28 mM at the seafloor to 8 mM at 4.95 mbsf. In addition, dissolved HS^- concentrations begin to increase at ~3 mbsf. These gradients have been ascribed to decomposition of organic carbon through organoclastic sulfate reduction, expressed as (Froelich et al., 1979; Masuzawa and Kitano, 1983)

$$(CH_2O)_{106}(NH_3)_{16}(H_3PO_4) + 53\ SO_4^{2-} \rightarrow$$
$$53\ HS^- + 106\ HCO_3^- + 16\ NH_4^+ + PO_4^{3-} + 40\ H^+$$
$$(\text{or } 53\ H_2S + 106\ HCO_3^- + 16\ NH_3 + H_3PO_4).$$

Interstitial water profiles generated at Site 798 (Shipboard Scientific Party, 1990) extend the piston core trends deeper. Alkalinity and dissolved NH_4^+ both continue to increase, exceeding 75 mM and ~8000 µm by 100 mbsf. Dissolved SO_4^{2-} continues to drop, reaching 0 mM somewhere between 5.75 and 9.85 mbsf. Similar to conclusions reached by Masuzawa and Kitano (1983), the ODP Leg 128 shipboard scientists attributed the changes in alkalinity, NH_4^+, and SO_4^{2-} to "bacterial degradation of organic matter primarily by sulfate reduction" (Shipboard Scientific Party, 1990).

At Site 798, however, headspace gas concentrations begin to increase deeper than 5.75 mbsf, and numerous gas cracks and gas voids begin to appear deeper than 18 mbsf (Shipboard Scientific Party, 1990). The composition of volatile hydrocarbons is >99.5% CH_4 (Shipboard Scientific Party, 1990), which strongly suggests a microbial origin for the gas (Hedberg, 1974). Available evidence suggests extreme CH_4 concentrations at Site 798, which leads to an alternative explanation for the geochemical profiles (Burdige, 2011). Rapid accumulation of sediment with a high organic carbon content leads to methanogenesis at depth (Ferry and Lessner, 2008):

$$CO_2 + 4H_2 \rightarrow CH_4 + 2H_2O.$$

CH_4 and other products generated at depth then return toward the seafloor through advection, diffusion, or both. However, across a sulfate–methane transition (SMT) within the upper few meters of sediment, CH_4 reacts with SO_4^{2-} via anaerobic oxidation of methane (AOM) (Reeburgh, 1976; Borowski et al., 1996):

$$CH_4 + SO_4^{2-} \rightarrow HCO_3^- + HS^- + H_2O.$$

In summary, the rise in alkalinity and NH_4^+ and the loss of SO_4^{2-} with depth may have little to do with bacterial degradation of organic matter by sulfate reduction. Instead, they reflect the combined effects of deep methanogenesis, shallow AOM, and mass transport of dissolved components (e.g., Burdige, 2011; Chatterjee et al., 2011).

The distinct potential pathways for carbon flow at Site 798 can be distinguished through flux-based calculations, numerical modeling, and detailed interstitial water profiles across the upper 20–30 m of sediment (Moore et al., 2004; Snyder et al., 2007; Chatterjee et al., 2011). As good low-resolution interstitial water profiles were generated over 517 m at Site 798 (Shipboard Scientific Party, 1990), we modified our basic Expedition 346 geochemistry sampling program (see **"Geochemistry"** in the "Methods" chapter [Tada et al., 2015b]) significantly for Site U1426. Our strategy was to collect a minimal number of samples from deep holes (Holes U1426A and U1426C) but gather a large number of samples from a short "geochemistry" hole (Hole U1426B). Our sampling and analytical effort could then be placed toward addressing six questions, which arise from considerations of AOM but cannot be answered with existing data at Site 798 (Fig. **F27**):

1. Does the alkalinity profile exhibit a concave downward inflection at the SMT? This would be consistent with production of HCO_3^-, HS^-, or both at the SMT.
2. Does the dissolved NH_4^+ profile show a constant gradient across the SMT? This would be consistent with no nitrogen release at the SMT.
3. Do headspace CH_4 concentrations rapidly rise below the SMT? This would be consistent with upward migrating CH_4 reacting with dissolved SO_4^{2-}.
4. Do dissolved SO_4^{2-} concentrations decrease nearly linearly over the upper 10 m or so? This would be consistent with AOM at a thin SMT dominating net consumption of SO_4^{2-}.
5. Do dissolved HS^- concentrations peak at the SMT? This would be consistent with production of HS^- by AOM.
6. Do dissolved HS^- and Fe profiles intersect above and below the SMT? This would be consistent with the notion that Fe-S solids remove much of the sulfide produced by AOM.

Sample summary

The geochemistry team collected and analyzed a range of samples, especially targeting the shallow sediment recovered in Hole U1426B. The samples included the following (Tables **T10, T11, T12, T13, T14, T15**):

- 2 mudline (ML) samples: 1 from Hole U1426A and 1 from Hole U1426B.
- 42 interstitial water samples from whole-round squeezing (IW-Sq): 19 from Hole U1426A and 23 from Hole U1426B. To conform to stated goals (above) and upon Co-Chief Scientist recommendation, IW-Sq samples from Hole U1426A were taken on prime-numbered cores. An additional IW-Sq sample was taken from Core 346-U1426A-51H.
- 120 interstitial water samples from Rhizons (IW-Rh) in Hole U1426B.
- 19 sediment samples from the interstitial water squeeze cakes of Hole U1426A, 23 sediment samples from the interstitial water squeeze cakes of

Hole U1426B, and an additional 18 sediment samples from the physical properties group.

- 76 headspace (HS) gas samples; 34 of these were paired with the above IW-Sq samples.
- 10 Vacutainer (VAC) samples recovered from Hole U1426A gas expansion voids with syringes.

Carbonate and organic carbon

The distance between samples for solid-phase analyses varies considerably with depth at Site U1426. Nevertheless, the carbonate, carbon, and nitrogen profiles (Tables **T10, T11;** Fig. **F28**) are consistent with those produced at Site 798 (Shipboard Scientific Party, 1990).

Sediment at Site U1426 contains relatively high amounts of $CaCO_3$ (up to 28.6 wt%) compared to material recovered at other sites cored in the northern portion of the marginal basin during Expedition 346 (e.g., Fig. **F25** in the "Site U1424" chapter [Tada et al., 2015d]). For lithologic Unit I (0–283.78 m CSF-A) (see **"Lithostratigraphy"**), carbonate contents are highest in Subunit IA and seem to decrease in Subunit IB. The upper 35 m CSF-A in Hole U1426B was examined at a much higher sample resolution. This suite of 23 samples averages 8 wt% carbonate with wide variance from 0.8 to 28.6 wt%. The carbonate content of Unit II (283.78–396.7 m CSF-A) (see **"Lithostratigraphy"**) is <3 wt% except for one value of 12 wt% at ~295 m CSF-A. The relatively high carbonate values at Site U1426 (i.e., typically >5 wt%) are consistent with micropaleontological observations (see **"Biostratigraphy"**), which indicate moderate abundance of calcareous microfossils such as foraminifers and nannofossils.

Total organic carbon (TOC) contents average 1.9 wt% at Site U1426, which is high for marine sediment (Müller and Suess, 1979; Emerson and Hedges, 1988). The variance in TOC contents is also relatively small, ranging between 0.7 and 2.5 wt%. However, the higher resolution sampling of Hole U1426B values alternate between intervals of high TOC contents (5–15 and 25–30 m CSF-A) and low TOC contents (3–5, 15–25, and 30–35 m CSF-A). From the top of Unit II to the base of the drilled site, TOC contents average ~1.5 wt% and decrease slightly with depth. We could not address the origin and preservation state of the sedimentary organic matter because the Source Rock Analyzer (Rock-Eval) remained inoperable.

The mean value of total nitrogen (TN) is relatively low at 0.28 wt%. The maximum content (0.38 wt%) is in the uppermost sample, whereas the minimum content (0.17 wt%) is at 32.3 m CSF-A. The downhole trend in TN follows that for TOC, except in the middle portion of the record (100–260 m CSF-A). The TN and TOC values of the high-resolution samples from Hole U1426B have a strong positive relationship (r^2 = 0.96).

We note an issue with TN measurements at Site U1426. Compared to results at Site 798 (Shipboard Scientific Party, 1990), samples from Site U1426 appear consistently richer in TN. However, the difference does not exceed the error for TN analysis within the present shipboard Chemistry Laboratory (±0.06 wt%, 1σ, at Site U1426, as determined by repeat analyses of an internal standard). Thus, any discrepancies could relate to different analytical procedures and equipment. For example, the furnace temperature in the laboratory differed between the two cruises (1000°C for Leg 128 and 950°C for Expedition 346).

The C:N values at Site U1426 are probably more reliable than for previous sites drilled during Expedition 346. This is because the higher organic matter contents reduce the influence of analytical error (calculated as ±0.17% for C). For sediment at Site U1426, the C:N (atom) ratio averages 7.3 and varies between 4.1 and 11.1.

Manganese and iron

The dissolved Mn and Fe profiles at Site U1426 (Table **T12;** Fig. **F29**) are somewhat similar to those generated at previously drilled sites during Expedition 346. This includes apparent offsets in Fe concentration between IW-Sq and IW-Rh samples. The distinguishing aspect of Site U1426 is that the Mn and Fe concentration maxima in shallowly buried sediment lie very near the seafloor.

Dissolved Mn concentration is 6 µM in the mudline sample. This is expectedly low, although higher than at previous sites. The uppermost interstitial water sample, from 0.05 m CSF-A below the apparent seafloor, has an Mn concentration of 90 µM. The maximum Mn concentration, 100 µM, occurs at 0.15 m CSF-A (Fig. **F29**). Deeper than 0.15 m CSF-A, Mn concentrations steadily decrease, falling below the detection limit (0.6 µM) at 6.8 m CSF-A. Dissolved Mn concentrations remain near zero for deeper samples, although we have not yet examined samples deeper than 34.7 m CSF-A. At Site 798, dissolved Mn concentration was 28 µM at 1.45 mbsf and 7 µM or less deeper than 4.5 mbsf (Shipboard Scientific Party, 1990).

Dissolved Fe is below the detection limit (1 µM) in the mudline sample, similar to that at previously drilled locations. The maximum dissolved Fe concentration of ~30 µM is found in the shallowest sample at 0.05 m CSF-A. Downhole from this depth, dis-

solved Fe decreases steeply to below detection limit at 0.4 m CSF-A. Dissolved Fe concentrations between 0.4 and 34.7 m CSF-A vary according to sampling method. For IW-Sq samples, Fe concentrations are generally low but erratic (0–27 µM), whereas for IW-Rh samples, Fe concentrations are consistently below the detection limit.

The shallowest Rhizon was inserted at 0.05 m CSF-A in Hole U1426B. Unfortunately, after correlation with other holes at this site, the depth of this sample appears to be at 0.32 m CCSF-A (as defined in the "Methods" chapter [Tada et al., 2015b]) (0.05 m CSF-A). Thus, the top of Hole U1426B may be missing or compressed. This may explain the absence of clearly defined metal peaks in uppermost sediment, including the double peaks in dissolved Fe found at Sites U1422, U1424, and U1425. Alternatively, the extremely high organic matter flux at this location leads to very rapid dissolution of metal oxides, and even the Rhizon sampling is not close enough to resolve distinct Mn and Fe peaks in interstitial water.

Dissolved Mn concentrations decrease below the detection limit at approximately the same depth as a major inflection in the alkalinity profile (below). In any case, alkalinity is very high at Site U1426, and formation of Mn-bearing carbonates, such as rhodochrosite, may be removing Mn from interstitial water. This is discussed in previous site chapter geochemistry sections.

The Fe maximum in the upper 1 m below the seafloor can be explained by microbially mediated reactions reducing Fe oxides during degradation of organic matter (e.g., Froelich et al., 1979). Interestingly however, and similar to other sites examined during Expedition 346, the Fe maximum occurs at a shallower depth than the Mn maximum. This is different than expected from the canonical model for oxidation of organic matter, which has Fe oxides being used as an electron acceptor after Mn oxides are no longer available (Froelich et al., 1979). The Fe story may be complicated because of the presence of several different Fe-bearing solids and because we have not identified the origin of different Fe concentrations in closely spaced IW-Sq and IW-Rh samples. We elaborate on this matter at the end of this section.

Alkalinity, ammonium, and phosphate

The profiles of alkalinity, dissolved NH_4^+, and PO_4^{3-} at Site U1426 are consistent with those at Site 798 (Shipboard Scientific Party, 1990). All three constituents increase from low values in the mudline sample to very high concentrations at depth (Table T12; Fig. F30). The maximum alkalinity, NH_4^+, and PO_4^{3-} concentrations are ~84 mM, 11,400 µM, and 297 µM, respectively. Clearly, at this location microbes consume large amounts of solid organic carbon, which releases HCO_3^-, NH_4^+, and PO_4^{3-} to interstitial water.

Over the upper 15 m, numerous IW-Sq and IW-Rh samples were examined for alkalinity and NH_4^+ (Fig. F31). In general, the two sampling techniques give similar values. Subtle differences in values between the two techniques are not considered meaningful because it is difficult to evaluate the cause without systematically reconstructing the time history of sampling and analyses. The same is true with the scatter in the IW-Rh samples. In particular, 23 Rhizons were inserted into Core 346-U1426B-2H at almost the same time. However, the collected water samples were analyzed individually and randomly over almost an entire day afterward.

The important aspects of the high-resolution interstitial water alkalinity and NH_4^+ profiles (Fig. F31) are twofold. The alkalinity profile has an obvious concave downward inflection at 8 m CSF-A. The NH_4^+ profile increases almost linearly. As outlined in the overview, both observations support focused consumption of CH_4 and SO_4^{2-} across a thin depth horizon.

Volatile hydrocarbons

As expected from descriptions of sediment recovered at Site 798 (Shipboard Scientific Party, 1990), significant gas expansion has impacted most sediment cores at Site U1426. Gas expansion cracks began at ~18 m CSF-A, and many gas voids appeared deeper than this depth. Methane was the dominant hydrocarbon gas (>99.9%) in all HS samples from Site U1426 (Table T13). The same is true for VAC gas samples (Table T14).

The headspace CH_4 profile at Site U1426 (Fig. F32) has several components. CH_4 concentrations are <30 ppmv over the upper 4.5 m CSF-A. Between this depth and 7.7 m CSF-A, CH_4 concentrations begin to rise rapidly. CH_4 concentration is 2,300 ppmv at 7.7 m CSF-A and climbs to a maximum of 36,000 ppmv at 13.7 m CSF-A. Deeper than 13.7 m CSF-A, CH_4 values rapidly decrease to 11,900 ppmv by ~21–30 m CSF-A and continue to decrease, albeit with high scatter, to the bottom of the drilled site.

Ethane concentrations in HS samples from Hole U1426A range between 0 and 40 ppmv and generally decrease with depth. However, the decrease in C_2H_6 concentration is less rapid than for CH_4. Consequently, the C_1/C_2 ratio generally decreases with depth (Fig. F32). The ratio is more than 1000 across the upper 30 m CSF-A but rapidly decreases to 400 at ~100 m CSF-A. Deeper than this depth, the C_1/C_2 ra-

tio gradually decreases, dipping to 124 at the base of the drilled site.

Gas concentrations were determined using the HS technique at Site 798. Between 12 and 35 mbsf, CH_4 concentration is much higher (50,000–90,000 ppmv) than that measured at Site U1426. Accordingly, the measured C_1/C_2 ratio of HS samples is much higher in shallowly buried sediment at Site 798. Here it is important to emphasize that, once the solubility of a gas has been surpassed during core recovery, gas concentration determined by the HS technique is no longer easily interpretable (e.g., Paull et al., 2000). Methane concentrations in cores from this location are probably greater than solubility at 1 atm pressure by 20 m CSF-A. Indeed, this is why gas cracks and gas voids begin to occur in sediment cores.

The most important aspects of the HS gas profiles are that the C_1/C_2 ratio is very high and that concentrations increase rapidly at approximately the same depth as the inflection in alkalinity. The first observation strongly suggests that CH_4 generated at depth has come through fermentation, as expected for microbial fermentation. The second observation strongly suggests that an upward flux of CH_4 drives AOM at ~8 m CSF-A.

Sulfate, sulfide, and barium

That AOM occurs across an SMT at ~8 m CSF-A can be demonstrated with profiles of dissolved SO_4^{2-} and HS^- (Table **T12;** Fig. **F33**). Dissolved SO_4^{2-} is 28.1 mM in the mudline samples, which is close to the 28.2 mM expected for Japan Sea Proper Water (JSPW) (Table **T10** in the "Methods" chapter [Tada et al., 2015b]). From the seafloor, SO_4^{2-} rapidly decreases to ~3.2 mM at ~8 m CSF-A and then to ~2.0 mM at 13 m CSF-A. The initial decrease is almost linear and terminates at the depth of the alkalinity peak. Deeper than 12 m CSF-A, SO_4^{2-} concentrations are below the detection limit.

By contrast, dissolved HS^- concentration is below the detection limit (~5 µM) at the seafloor, but forms a maximum in shallowly buried sediment. Starting at ~1.1 m CSF-A, HS^- concentrations rapidly increase, reaching a maximum value of 6032 µM at ~8 m CSF-A, or just deeper than the depth of the SMT. Deeper than ~8 m CSF-A, HS^- concentrations decrease to below the detection limit at ~35 m CSF-A.

The linear decrease and kink in the dissolved SO_4^{2-} profile strongly indicate major consumption of SO_4^{2-} at the SMT. The maximum in dissolved HS^- strongly indicates production of HS^- at the SMT. In theory, the loss of SO_4^{2-} at the SMT should equal the production of HS^-. However, some amount of sulfide escaped as H_2S gas during core recovery. Nevertheless, the coincident inflections of alkalinity, CH_4, and SO_4^{2-} and the peak in HS^-, all at ~8.0 CSF-A, are overwhelming evidence for AOM at this location.

A sharp SMT in shallowly buried sediment of deep-water depth should affect sedimentary barium cycling significantly (Dickens, 2001). The reasons have been provided in other site chapters and in several publications, as cited previously. The dissolved Ba profile (Fig. **F34**) suggests this to be the case at Site U1426. Ba concentrations of the mudline sample and Rhizon samples from the upper 6.5 m (CSF-A) of sediment are <13 µM. Deeper than 7 m CSF-A, dissolved Ba begins to increase, reaching 1200 µM at ~34 m CSF-A. Dissolved Ba concentrations were measured on samples from Site 798, although at low resolution (von Breymann et al., 1992). These authors show an increase in dissolved Ba starting somewhere shallower than 9.9 m CSF-A and 121 µM at ~37 m CSF-A.

Dissolved Fe concentrations in the Rhizon samples decrease to below the detection limit within 50 cm CSF-A shallower than the increase in HS^- concentrations. This was expected because the solubility of FeS minerals is extremely low (Schippers and Jørgensen, 2002).

The answers to the six questions outlined above are "yes" and were predicted before drilling commenced. This is because the chemistry of interstitial water at Site U1426 appears similar to that at other drill sites with substantial amounts of CH_4 at depth and a sharp SMT in the upper 10 or so meters below the seafloor. An interesting example is ODP Site 1230 on the Peru margin (Shipboard Scientific Party, 2003). At this site, a prominent SMT occurs at 8 mbsf, and the alkalinity, NH_4^+, CH_4, SO_4^{2-}, HS^-, and Ba profiles are all fairly comparable to those at Site U1426. Three other characteristics of interstitial water chemistry at Site 1230 are high Br^- concentrations, yellow interstitial water, and shallow carbonate precipitation. We discuss the similarities and their causes in the **"Site U1427"** chapter (Tada et al., 2015f) but document these characteristics below.

Bromide

The new ion chromatograph in the Geochemistry Laboratory allows determination of dissolved Br^- concentrations. However, the precision of Br^- on this instrument appears to be ~0.02 mM. Prior to Site U1426, the range in dissolved Br^- with respect to depth at sites drilled during Expedition 346 has been only minimally greater than this precision. As a result, downhole Br^- profiles have shown considerable scatter (e.g., **"Site U1422"** chapter [Tada et al.,

2015c]). By contrast, the Br^- profile is fairly clean at Site U1426 (Table T12; Fig. F35) because the concentrations are significantly higher than those at previous sites.

Br^- concentration of the mudline samples is 0.83 mM. This is comparable to the 0.84 mM inferred for JSPW (Table T10 in the "Methods" chapter [Tada et al., 2015b]). Below the seafloor, dissolved Br^- steadily increases, reaching 1.25 mM at 421 m CCSF-A. Such Br^- concentrations are much higher than at most drill sites and signify substantial degradation of organic matter over time (Gieskes and Mahn, 2007).

Absorbance/Yellowness

A total of 99 interstitial water samples collected at Site U1426 were analyzed for their "yellowness" by measuring absorbance at two wavelengths: 325 and 227 nm (Table T15). Three samples were also measured twice to assess reproducibility.

Absorbance of interstitial water samples, at least for the wavelengths examined, changes significantly with depth at Site U1426 (Fig. F36). Similar to previously drilled sites during Expedition 346, absorbance is very low in the mudline sample but rises rapidly beneath the seafloor. Absorbance reaches a maximum for both wavelengths by 30 m CSF-A, although the peak is shallower for measurements at 227 nm. For both wavelengths, the absorbance profile is smooth, except for several outliers. Similar to observations at Site U1425 (see "Geochemistry" in the "Site U1425" chapter [Tada et al., 2015e]), absorbance at 325 nm also decreases more rapidly with depth than at 227 nm.

The yellowness of marine water has been ascribed to dissolved organic carbon, as noted in other chapters. In general, absorbance of interstitial water at Site U1426 is greater than that of samples from Site U1425 but less than that of samples from Site U1427. This is similar to the relative concentrations of alkalinity, NH_4^+, and Br^- in interstitial water of these three sites.

Calcium, magnesium, and strontium

Interstitial water chemistry data from Site 798 depicts the overall deep hole trends of Ca and Mg. Thus, for Expedition 346 we focused on producing higher resolution data in the upper 40 m, with a few analyses performed at deeper depths (Fig. F37) to match Site U1426 data with Site 798 data (Table T12).

Ca concentrations decrease from ~10 mM near the seafloor to ~5 mM at 10 m CSF-A (Fig. F38). Ca concentration continues to decrease, reaching a minimum from ~35 to ~50 m CSF-A. Deeper than 50 m CSF-A, calcium concentrations begin to increase gradually, returning to ~10 mM at 393 m CSF-A, the deepest sample recovered (Fig. F37).

The Mg concentration profile has a similar shape to Ca in the upper 10 m but then shows an opposite trend deeper than 10 m CSF-A (Figs. F37, F38). Mg concentration is ~52 mM near the seafloor and decreases to ~45 mM at 8 m CSF-A. Unlike the continued decrease observed in Ca concentrations, Mg concentrations increase, reaching a relative maximum of ~52 mM between ~35 and ~90 m CSF-A. Mg concentrations then gradually decrease with depth to ~14 mM at 393 m CSF-A.

Data from Site 798 show that the increase in Ca and the decrease in Mg at depth continue until ~450 mbsf, where the concentrations are equal. The deeper trends are driven by uptake of Mg and release of Ca during reaction with basalt. The removal of Ca and Mg at shallower depths suggests the presence of dolomite formation.

Chlorinity and sodium

Although at very low resolution, the Cl^- profile at Site U1426 (Table T12; Fig. F39) exhibits aspects observed at all Expedition 346 sites drilled so far during this expedition. Cl^- concentration of the mudline sample is 542 mM, which compares well to 545 mM inferred for JSPW (Table T10 in the "Methods" chapter [Tada et al., 2015b]). Below the seafloor, Cl^- concentrations are generally lower than that of present-day bottom water, and the lowest value (526 mM) is found between 10 and 40 m CSF-A. The Cl^- profile appears to resemble that constructed at Site 798 (Shipboard Scientific Party, 1990), although neither are very detailed.

Sodium concentrations at this site show scatter, but overall trends are still apparent. At the mudline, concentration is between ~460 and 480 mM and decreases to 420–440 mM at 5 m CSF-A. Concentrations begin to increase gradually deeper than 5 m CSF-A to between 485 and 495 mM in the deepest samples (Fig. F39).

The cause and importance of low-salinity interstitial water have been discussed in previous chapters of this volume.

Potassium

Potassium concentration is ~10.5 mM at the seafloor (Table T12; Fig. F39). There is a slight increase in K concentrations between 1 and 4 m CSF-A to ~12 mM; however, the K maximum is not as prominent as at other sites drilled during Expedition 346. The continuing downcore trend shows K concentrations

increasing to 15 mM at 295 m CSF-A. The deepest samples analyzed show a decrease in K concentrations to 12.4 mM at 393 m CSF-A, and comparing these data with values from Site 798 shows that K concentrations continue to decrease to ~7 mM at ~500 mbsf.

The abrupt increase in K concentration just below the seafloor has been observed at other sites and has multiple possible origins. It could be from mineral dissolution or cation exchange reactions involving ammonium or other phases. It also could represent an effect of temperature (Sayles and Manheim, 1975). Variations in K concentrations throughout the sediment column suggest a change in clay mineralogy with transformation of smectite to illite or other diagenetic reactions incorporating potassium. The decline of potassium concentrations at depth is likely from the uptake of potassium during basalt alteration (Fig. **F39**).

Boron and lithium

The dissolved B profile in Hole U1426B (Table **T12;** Fig. **F40**) shows limited variation but considerable scatter over the upper 40 m. B concentrations range between 415 and 630 µM, but there are no real trends in the data.

The dissolved Li profile (Fig. **F40**) has an overall concave upward curvature. In general, Li concentrations increase from 26 µM at the mudline to 52 µM at 34.7 m CSF-A (37.5 m CCSF-A). This is similar to observations made at Site 798 (Shipboard Scientific Party, 1990). However, the high-resolution Li concentrations reach a minimum of ~22 mM near the SMT.

Silica

Dissolved H_4SiO_4 was not analyzed using the spectrophotometer because the basic profile is already known from work at Site 798 (Shipboard Scientific Party, 1990). However, dissolved Si was measured by inductively coupled plasma–atomic emission spectroscopy (ICP-AES), although only on samples from Hole U1426B to ~34 m CSF-A. The dissolved Si profile (Table **T12;** Fig. **F40**) gives an interesting perspective to the discussion.

The mudline sample has a dissolved Si concentration of 168 µM. By 0.05 m CSF-A (0.32 m CCSF-A), however, Si concentrations devilishly jump to 666 µM at 0.05 m CSF-A. Deeper than the uppermost 1 m, dissolved Si gradually rises, although with apparent oscillations between that range from ~567 to 807 µM. Data from Site 798 show Si values in this range for the upper 40 m (Shipboard Scientific Party, 1990). They also show Si concentrations increasing as high as 1700 µM until ~450 mbsf, where concentrations rapidly decline at the opal-A/opal-CT boundary.

Rhizon commentary

Two problems were encountered with Rhizon sampling of cores from Hole U1426B. First, water flow into Rhizons decreased significantly for many intervals in Cores 346-U1426B-3H and 4H. Water flow typically decreases with sedimentary depth, presumably because of sediment compaction, reduced porosity, and lower permeability. However, only 2 of 20 Rhizons inserted into Core 346-U1426B-4H extracted >9 mL of water after 4.5–5 h. We think that voids from gas expansion, drill holes into the core liner to relieve gas pressure, or both, may have slowed water flow considerably. It was also later recognized that using new syringes provided a better suction and reduced extraction time.

Second, and as also discussed for Site U1425 (see **"Geochemistry"** in the "Site U1425" chapter [Tada et al., 2015e]), the current Geochemistry Laboratory is not equipped at present to handle very large numbers of water samples arriving over a short time interval. Thus, 120 water samples arriving from Hole U1426B within <5 h proved to be challenging but not impossible.

A recurring issue during Expedition 346 is the concentration discrepancy for some species between IW-Sq and IW-Rh samples. Consistent offsets are found in the measured concentrations of certain dissolved metals from samples closely spaced in depth. One possibility is that the squeezers, the Rhizons, or both, modify the chemistry through contamination. To assess this possibility, a series of blanks were prepared and included with samples in ICP-AES runs. A squeezer blank was prepared by partially filling a squeezer with 18.2 MΩ water, letting the water sit for 1 h, and hand cranking the piston to press water through an interior filter, a wire mesh, a 0.45 µm filter, and into a syringe. Three Rhizons were soaked in an acid-cleaned beaker filled with 18.2 MΩ water for 1 h and then used to pass 10 mL of the water into a syringe. Three additional Rhizons were soaked in an acid-cleaned beaker filled with synthetic seawater ($NaCl + H_2O$) for 1 h and then used to pass 10 mL of this fluid into a syringe. Two of the three 18.2 MΩ water Rhizon blanks and two of the three synthetic seawater Rhizon blanks were acidified with nitric acid, exactly like samples are prepared. All these blanks, plus a pure 18.2 MΩ water blank and two pure synthetic seawater blanks were then stored in the cryogenic vials used for samples and eventually analyzed by ICP-AES along with interstitial water samples. The concentrations of all elements analyzed

were below detection for both blank squeezer and blank Rhizon samples.

Preliminary conclusions

Sediment at Site U1426 is characterized by relatively high contents of organic carbon (~2 wt%) and carbonate (up to 28.6 wt%) through the upper few hundred meters below the seafloor. Rapid increases in dissolved Mn and Fe over the uppermost few meters indicate reactions between the organic matter and metal oxides. Deeper in the sediment column, other reactions involving organic carbon, especially fermentation, lead to very high concentrations of alkalinity, ammonium, and phosphate. Microbial methanogenesis also produces very large amounts of CH_4. The low C_1/C_2 ratio and the occurrence of propane at depth suggest possible thermogenic gas near the bottom of the drilled site. However, the effects of degassing on measured gas concentration needs serious consideration.

High CH_4 concentrations at depth lead to an upward flux of CH_4, which reacts with dissolved SO_4^{2-}, diffusing downward from the seafloor through AOM. The consequence is a prominent SMT that occurs at ~8 m CSF-A. A major convex upward inflection in alkalinity, a constant concentration gradient in NH_4^+, and a peak in dissolved HS^- at this depth all indicate that the SMT indeed derives from AOM.

Intense microbial activity and shallow methane cycling impacts other interstitial water chemistry at Site U1426. Samples have high Br^- concentrations and yellow color at depth. Addition of alkalinity at the SMT drives authigenic carbonate precipitation. In many regards, Site U1426 resembles other drill sites with high CH_4 concentrations at depth.

The profiles of Cl^- and dissolved Si are similar to those at other sites in the marginal sea and likely reflect the influence of fresher bottom water in the past and silica diagenesis, respectively.

Paleomagnetism

Paleomagnetic samples and measurements

Paleomagnetic investigations at Site U1426 included the measurement of magnetic susceptibility of whole-round and archive-half split-core sections, and the natural remanent magnetization (NRM) of archive-half sections. NRM was measured before and after alternating field (AF) demagnetization with a 20 mT peak field for all archive-half sections from Hole U1426A at every 5 cm interval. Because of increased core flow and limited measurement time available at the paleomagnetism station, NRM of archive-half sections from Holes U1426B to U1426D was measured only after (not before) 20 mT AF demagnetization at 5 cm intervals. The FlexIT core orientation tool (see **"Paleomagnetism"** in the "Methods" chapter [Tada et al., 2015b]) was used to orient a total of 25 APC-collected cores in Hole U1426A, starting from Core 346-U1426A-2H (Table **T16**).

We collected one paleomagnetic discrete cube sample (see **"Paleomagnetism"** in the "Methods" chapter [Tada et al., 2015b]) from the first section of each of the 59 cores recovered in Hole U1426A (light blue triangles in Fig. **F41A, F41B**). Stepwise AF demagnetization on 16 discrete samples collected from Hole U1426A (orange triangles in figure) was performed at successive peak fields of 0, 5, 10, 15, 20, 25, 30, 40, 50, and 60 mT to verify the reliability of the split-core measurements and to determine the demagnetization behavior of the recovered sediment. Following each demagnetization step, NRM of the discrete samples was measured with the samples placed in the "top-toward" or "+*z*-axis toward magnetometer" orientation (see **"Paleomagnetism"** in the "Methods" chapter [Tada et al., 2015b]) on the discrete sample tray.

We processed data extracted from the shipboard Laboratory Information Management System (LIMS) database by removing all measurements collected from disturbed and void intervals, and all measurements that were made within 10 cm of the section ends, which are slightly biased by measurement edge effects. For declination data from cores in Hole U1426A where FlexIT tool data are available, we corrected the declination values for each core using the estimated orientation angles. A modified version of the UPmag software (Xuan and Channell, 2009) was used to analyze the NRM data of the split-core section samples. The disturbed and void intervals used in this process are reported in Table **T17.** The processed NRM inclination, declination, and intensity data after 20 mT AF demagnetization are reported in Table **T18** and shown in Figure **F41.**

Natural remanent magnetization and magnetic susceptibility

NRM intensity after 20 mT AF demagnetization in all four measured holes at Site U1426 is similar in magnitude for overlapping intervals, mostly ranging between ~10^{-4} and 10^{-2} A/m. For the uppermost ~90 m of the recovered sediment, NRM intensity of the measured core sections after 20 mT demagnetization is close to ~10^{-2} A/m, except the ~60–80 m CSF-A interval where NRM intensity is on the order of 10^{-4} to 10^{-3} A/m. Between ~90 and 256 m CSF-A, NRM intensity varies frequently between ~10^{-4} and ~10^{-3}

A/m. Deeper than ~256 m CSF-A until the bottom of the holes, NRM intensity appears to be more stable and is mostly close to ~10^{-3} A/m.

The AF demagnetization behavior of the 16 measured discrete samples is illustrated in Figure **F42.** Declination and inclination values acquired from the discrete sample measurement generally agree well with the split-core measurement after 20 mT AF demagnetization. All samples exhibit a steep normal overprint that was generally removed after AF demagnetization at peak fields of ~15–20 mT, demonstrating that the 20 mT AF demagnetization is, in general, sufficient to eliminate the drilling overprint. NRM measurement of discrete samples with weak intensity (e.g., Fig. **F42B, F42D, F42F, F42I, F42M, F42O, F42P**) often appears to have lower coercivity and acquire an anhysteretic remanent magnetization (ARM), possibly due to bias caused by ambient magnetic field during demagnetization.

Magnetic susceptibility measurements were taken on whole cores from all holes as part of the Whole-Round Multisensor Logger (WRMSL) analysis and on archive-half sections using the Section Half Multisensor Logger (SHMSL) (see **"Physical properties"**). The WRMSL-acquired susceptibility was stored in the database in raw meter units. These were multiplied by a factor of 0.68 × 10^{-5} to convert to the dimensionless volume SI unit (Blum, 1997). A factor of (67/80) × 10^{-5} was multiplied by the SHMSL-acquired susceptibility stored in the database. Magnetic susceptibility measurement is consistent between the two instruments and across the different holes for overlapping intervals and varies mostly between 2 × 10^{-5} and 20 × 10^{-5} SI (Fig. **F41,** fourth panel). Except for the 300–400 m CSF-A interval of recovered sediment in Hole U1426A, where the large-scale cyclic variation of magnetic susceptibility from ~1 × 10^{-5} to ~10 × 10^{-5} SI seems absent in NRM intensity, magnetic susceptibility of sediment in all holes, in general, mimics NRM intensity, suggesting that the magnetic minerals carrying NRM are the same or at least coexist with those that dominate magnetic susceptibility.

Magnetostratigraphy

Paleomagnetic inclination and declination data of the holes show patterns that allow for the determination of magnetic polarity for the top ~250 m of recovered sediment. Both magnetic declination and inclination after 20 mT AF demagnetization were used when possible for the magnetostratigraphic interpretation at Site U1426. The geomagnetic field at the latitude of Site U1426 (37.03°N) has an expected inclination of 56.47°, assuming a geocentric axial dipole field model, which is sufficiently steep to determine magnetic polarity in APC cores that lack horizontal orientation. We identified the Brunhes/Matuyama boundary (0.781 Ma) and the Jaramillo Subchron (0.988–1.072 Ma) in Holes U1426A, U1426C, and U1426D. The Olduvai Subchron (1.778–1.945 Ma) was recorded in Holes U1426A and U1426C. In Hole U1426A, we also identified the Matuyama/Gauss boundary (2.581 Ma) (Table **T19**).

Inclination of the four APC cores drilled in Hole U1426B after 20 mT AF demagnetization clearly varies around the expected normal polarity dipole value at the site location (Fig. **F41C**), and sediment recovered from Hole U1426B should have been deposited during the Brunhes Chron. The Brunhes/Matuyama boundary (0.781 Ma) is recorded at ~81.7 m CSF-A in Hole U1426A, ~76.4 m CSF-A in Hole U1426C, and ~80.9 m CSF-A in Hole U1426D. Above the Brunhes/Matuyama boundary, inclination values in Holes U1426A, U1426C, and U1426D after 20 mT AF demagnetization vary closely around the expected normal polarity dipole value at the site location (Fig. **F41A, F41D, F41E**). In Hole U1426A, the FlexIT-corrected declinations show a shift from values mostly around 0° to values around 180° at the interpreted Brunhes/Matuyama boundary (in Core 346-U1426A-10H). This interpretation is consistent with the stepwise demagnetization data of discrete samples. The discrete sample from 41.58 m CSF-A shows well-defined component directions with positive inclination (Fig. **F42A**), and the discrete sample from 80.42 m CSF-A appears to have transitional or negative inclination (Fig. **F42B**).

We interpret the positive inclination intervals from ~85.94 to 98.5 m CSF-A in Hole U1426A and from ~85 to 99.4 m CSF-A in Hole U1426C as the Jaramillo Subchron (0.988–1.072 Ma). Hole U1426D appears to have recorded the top of the Jaramillo Subchron (0.988) at ~86.1 m CSF-A. In Hole U1426A, the positive inclination interval is accompanied by FlexIT-corrected declinations varying around 0°. Declinations near the top and bottom of this interval in the two holes both show an apparent ~180° shift, supporting the two depth levels as polarity boundaries suggested by the inclination changes. In addition, the discrete sample from 90.56 m CSF-A has well-defined characteristic remanence with positive inclination (Fig. **F42C**), agreeing with the archive-half section measurement results.

The Olduvai Subchron (C2n, 1.778–1.945 Ma) is recorded from ~169.45 to 191.6 m CSF-A in Hole U1426A and from ~170.5 to 189.6 m CSF-A in Hole U1426C. During the interpreted Olduvai Subchron, inclinations in the two holes after 20 mT AF demagnetization are mostly positive and close to the ex-

pected normal polarity dipole value. Declinations near the top and bottom of this interval in the two holes both show an apparent ~180° shift, and FlexIT-corrected declinations in Hole U1426A are mostly close to 0° or 360° during this interval. The depth levels of the Olduvai Subchron in the holes are consistent with the discrete sample measurement results. The discrete sample from 182.71 m CSF-A recorded well-defined characteristic remanence with positive inclination (Fig. **F42G**), whereas the discrete samples from 163.31 m CSF-A (Fig. **F42F**) and from 201.36 m CSF-A (Fig. **F42H**) appear to have remanence with primarily negative inclinations. Our interpretation agrees well with the LO of radiolarian *A. acquilonium* (1.2–1.7 Ma) between ~172.43 and 182.25 m CSF-A and the LO of calcareous nannofossil *C. macintyrei* (~1.6 Ma) at ~173.67–175.04 m CSF-A in Hole U1426A (see **"Biostratigraphy"**).

The Matuyama/Gauss boundary (2.581 Ma) was recorded at ~254.6 m CSF-A (Core 346-U1426A-28H) in Hole U1426A. Inclination of Hole U1426A after 20 mT AF demagnetization apparently switches from dominantly negative values above this boundary to mostly positive values right below the boundary (Fig. **F41B**). The depth at which the Matuyama/Gauss boundary is found in Hole U1426A is consistent with a list of biostratigraphic events identified in the hole (see **"Biostratigraphy"**), including the FO of radiolarian *C. davisiana* (~2.7 Ma) at ~256.98–261.15 m CSF-A. Below the Matuyama/Gauss boundary, NRM inclination after 20 mT AF demagnetization shows mostly positive values that are apparently steeper than the expected normal polarity dipole inclination at the site location. Increased coring disturbance, strong drill string overprint, the lack of core orientation, and the large scatter in paleomagnetic declinations makes magnetostratigraphic interpretations difficult for the ~270 to ~396 m CSF-A interval of sediment recovered at Site U1426.

Physical properties

Site U1426 is a redrill of Site 798 (Ingle, Suyehiro, von Breymann, et al., 1990) on the Oki Ridge. Compared to the previously drilled Sites U1422–U1425, Site U1426 is much shallower and is protected from the input of coarse sediment because of its ridge location. As such, Site U1426 presents some unique physical properties that contrast with the pattern seen at the previous deeper sites, but it also has enough similarities to provide context for the overall regional interpretation. Better preservation of calcium carbonate together with increased organic carbon (see **"Geochemistry"**) and terrigenous clay input results in a more homogeneous sedimentary sequence in terms of physical properties compared to previously drilled sites. Dissolution of silica may affect physical properties in the lower part of the sequence (deeper than 300 m CSF-A). The same suite of whole- and split-core logging as well as discrete sample properties that was measured at previous sites was also measured at Site U1426; the results are presented in Figures **F43, F44, F45, F46, F47,** and **F48.** We adopt the lithostratigraphic unit definitions in the discussion because the physical properties are largely an expression of lithology.

Thermal conductivity

Thermal conductivity was measured once per core using the full-space probe, usually near the middle of Section 4. Overall, thermal conductivity values range from 0.6 to 1.7 W/(m·K) without a clear increasing trend with depth. However, thermal conductivity follows porosity and gamma ray attenuation (GRA) bulk density, and thus, in part, lithology, with broad peaks over ~1 W/(m·K) in the denser layers at the bottom of the site (i.e., the uppermost at 320 m CSF-A and the second at 400 m CSF-A).

Moisture and density

GRA bulk sediment density at Site U1426 is largely similar in pattern to the equivalent age sediment in Site 798 but differs significantly from Sites U1422–U1425. Unit I displays strong high-frequency variability (i.e., decimeter to multimeter scale in Subunit IA and largely multimeter scale in Subunit IB) within a general range between 1.2 and 1.6 g/cm^3 (Fig. **F43**). The upper limit of this range is significantly lower than at previous deeper sites despite an increase in carbonate in this unit at Site U1426. Variability in Unit I derives from alternating light colored clay-rich layers with dark colored organic carbon–rich layers (see **"Lithostratigraphy"**). Further downhole in Unit II, instead of being attenuated as at deeper water sites, variability continues and is expressed as multimeter-long cycles driven by alternating heavy clay-rich and lighter colored diatom-rich sediment. Successive increases in GRA bulk density with muted shorter scale variability possibly linked to lithification processes are also evident in Unit II and are separated by a broad local minimum in GRA bulk density at ~350 m CSF-A.

Discrete wet bulk density and derived parameters (i.e., porosity and water content) agree well with the primary trends in GRA bulk density (Figs. **F44, F45**), varying with lithology. Although porosity (and derived water content) decreases (increases) downhole, wet bulk and grain density display no clear trend. The relatively high carbonate content in the upper

part of Unit I and the largely decreased carbonate content deeper than 170 m CSF-A (see "Lithostratigraphy") also have no dramatic influence on the trend of discrete wet bulk and grain density. Comparing with XRD opal-A counts, discrete wet bulk and grain density show a contrary relationship with the opal-A counts trend (Fig. F45). Higher density values occur in low opal-A counts, whereas lower density values dominate in high opal-A counts. Therefore, although high carbonate occurs in Unit I, lithologic change alternating between clay-rich and biogenic component–rich (diatom, siliceous material, and nannofossil) sediment may be more responsible for these variations of density at Site U1426.

A comparison of high-resolution moisture and density (MAD) data in Hole U1426B collected for studies of pore water diffusion (see "Geochemistry") with low-resolution MAD data in Hole U1426A (Fig. F46) indicates that much of the fine structure in physical properties cannot be observed without higher frequency sampling. This underscores the need for shore-based studies to derive physical properties at high resolution by calibration of track to MAD data.

Magnetic susceptibility

Whole-core magnetic susceptibility as well as point magnetic susceptibility (SHMSL) show consistently low values downhole, typically $<10 \times 10^{-5}$ SI (Fig. F43). Although strong diagenetic processes at this site could affect magnetic minerals (see "Geochemistry"), a relatively good paleomagnetic signal is recorded (see "Paleomagnetism"). This suggests robust contributions of less diagenetically active terrigenous magnetic carriers.

Natural gamma radiation

NGR shows strong cyclicity (Figs. F43, F45) that parallels the GRA bulk density cyclicity downhole (see above), suggesting that their controls are closely related. NGR in Unit I is less driven by U associated with organic matter as at the deeper sites (see "Lithostratigraphy"). NGR counts are significantly lower than at previous deeper sites, ranging from 10 to 60 cps.

Compressional wave velocity

Compressional *P*-wave velocity was only measurable in the upper 12 m CSF-A at this site because of degassing (Fig. F43). Meter-scale cyclicity is evident, following cycles in GRA bulk density with a velocity range between 1475 and 1550 m/s.

Vane shear stress

Undrained shear strength shows a variable but steady increase from the seafloor to ~300 m CSF-A through all lithologic units. Values reach a maximum of ~120 kPa (Fig. F44), deeper than ~300 m CSF-A sediment becomes too stiff for shear strength measurements.

Diffuse reflectance spectroscopy

Color reflectance data measured on the split archive-half sections at Site U1426 are distinctly different from the previously drilled sites, especially in Unit I (Fig. F47). Although L*, a*, and b* show the highest variability in Unit I as at previous sites, this variability is not only caused by the alternating dark organic-rich and greenish organic-poor lithologic packages but also by a significant increase in calcium carbonate and possibly a different diagenetic state for the organic matter. This can be observed in the range of L* that extends primarily into the lighter domain relative to the average site value, compared to previous sites where L* in the time-equivalent Unit I extended primarily into the darker domain (Fig. F48). Parameters a* and b* combined indicate the variable presence of primarily yellowish compounds, particularly in dark organic-richer layers from the seafloor all the way to the boundary of Unit II, where they become cyclical at ~10–20 m scale. In contrast, the previous sites showed a larger dynamic range for a*, leading to a more diverse hue spectrum.

Summary

Physical properties at Site U1426 are significantly different from previous sites but preserve a similar time-correlative Unit I that records higher variability in lithologic composition and thus physical properties. In this unit, cyclical physical properties appear to be driven not only by the binary mixture of organic matter–hemipelagic sediment, but also by the addition of carbonate (see "Geochemistry") and possibly a decline in authigenic pyrite. This new type of mixture drives the density as well as color characteristics at the site. Compared to previous sites, clay present in a higher proportion appears to overtake organic matter in the main role in influencing NGR variability. Magnetic susceptibility is minimal, but magnetic carriers appear sturdy enough to preserve a good paleomagnetic signal (see "Paleomagnetism").

Downhole measurements

In situ temperature and heat flow

APCT-3 downhole temperature measurements were performed in Hole U1426A at five depths, including

the mudline. In situ temperatures range from 4.00°C at 31.0 m CSF-A to 13.88°C at 116.5 m CSF-A (Table T20), with a linear downhole increase indicating that the gradient is uniform with depth (Fig. F49). A linear fit of temperature versus depth gives a geothermal gradient of 115°C/km, slightly higher than was measured during ODP Leg 127 at Site 798 (111°C/km) (Ingle, Suyehiro, von Breymann, et al., 1990). The bottom water temperature at this site is estimated to be 0.51°C, based on the average of the mudline temperature and the four APCT-3 measurements. This is slightly higher than the mudline temperature measured at previous sites.

The thermal conductivity under in situ conditions was estimated from laboratory-determined thermal conductivity using the method of Hyndman et al. (1974) (see "Physical properties" in the "Methods" chapter [Tada et al., 2015b]). Thermal resistance was then calculated by cumulatively adding the inverse of the in situ thermal conductivity values over depth intervals downhole (Fig. F49). A heat flow of 94 mW/m² was obtained from the slope of the linear fit between in situ temperature and in situ thermal resistance (Pribnow et al., 2000). This value is in the range of the heat flows measured at Site 798 (91 mW/m² from Ingle, Suyehiro, von Breymann, et al. [1990] and 101 mW/m² from Langseth and Tamaki [1992]) and in the region (from 68 to 137 mW/m² from Ingle, Suyehiro, von Breymann, et al. [1990]).

Stratigraphic correlation and sedimentation rates

During drilling operations, real-time tracking of the relative positions of core gaps in Hole U1426C relative to those in Hole U1426A was accomplished using magnetic susceptibility and GRA density data from the WRMSL and Special Task Multisensor Logger (STMSL). Hole U1426B (four APC cores) was dedicated to geochemical measurements, whereas Hole U1426D (11 APC cores) was drilled rapidly without regard to gap locations in order to attain additional sediment for the anticipated volume of sampling requests. Data were collected at a resolution of 5 cm, sufficient to keep up with core recovery rates. At this site, the sea state was relatively calm but gas expansion was strong, resulting in extensive voids within the liners and extrusion of sediment out the top of the core barrel on the drill floor. Although these extruded sediments were recovered and curated as part of Section 1, they were very often strongly disturbed. Some of the voids were eliminated on the catwalk by drilling numerous holes along the liner and using a plunger to close the voids by sliding sediment up or down the liner. The remaining voids were left intact, whereas the whole-round sections were run through the WRMSL and STMSL. After splitting, the smaller voids within each section were further consolidated into large voids and filled with styrofoam for long-term curation. Because of these protocols, the data collected by the WRMSL and STMSL will plot differently than data collected by the remaining logging instruments. Detailed (centimeter scale) compositing and splicing (see "Stratigraphic correlation and sedimentation rates" in the "Methods" chapter [Tada et al., 2015b]) are based on the high-resolution RGB color data (blue) recovered from the Section Half Imaging Logger (SHIL) at 0.5 cm resolution. For detailed discussion of these data sets, see "Physical properties" in the "Methods" chapter (Tada et al., 2015b).

After all cores were composited (Table T21), a splice was constructed using intervals from three of the four holes (U1426A, U1426C, and U1426D), excluding the hole dedicated to geochemistry (Hole U1426B) (Table T22). The splice (Fig. F50) spans the upper 236.23 m CCSF-D (as defined in "Stratigraphic correlation and sedimentation rates" in the "Methods" chapter [Tada et al., 2015b]) of Site U1426 (210.49 m CSF-A). The only tie point in the splice that may require further evaluation is the tie between Sections 346-U1426C-15H-4, 146.7 cm, and 346-U1426A-15H-2, 66.9 cm (141.77 m CCSF-D). Structure in the vicinity of this tie is not sufficient for an exact (centimeter scale) correlation. Based on the difference between the CCSF-D and CSF-A depths at the bottom of the spliced interval, expansion at this site was ~12%.

A core composite depth below seafloor, Method C (CCSF-C) scale (as defined in "Stratigraphic correlation and sedimentation rates" in the "Methods" chapter [Tada et al., 2015b]) was created for cores that were not selected for use in the splice. This differs slightly from the approach at previous sites (e.g., Site U1423) where if part of a core was used in the splice, the remaining parts were assigned CCSF-C depths as well. The strong expansion (voids and Section 1 core disturbance) at this site preclude accurate assignment of CCSF-C depths to most intervals not used in the splice. Construction of the CCSF-C scale, where applicable, is based on centimeter-scale correlation of structure in the RGB (blue) data. These CCSF-C depth maps (CSF-A to CCSF-D) are provided in Table T23.

Age model and sedimentation rates

A preliminary age model (Fig. F51) was established on the basis of all available biostratigraphic and

paleomagnetic age control points. For details, see "Biostratigraphy" and "Paleomagnetism." At this site, line segments connecting all the paleomagnetic events, the FO of *H. parviakitaensis*, and the rapid increase of *S. arachnea* group yield a reasonable depth-age relationship (Fig. F51A) with three exceptional outliers including the LO of *N. koizumii*, the FO of *N. seminae*, and the LO of *T. temperei* (Table T4). Sedimentation rates in lithologic Subunit IA (~1.3–0 Ma, 125–0 m CSF-A) are ~110 m/m.y. with a high (~195 m/m.y.) interval in the lower part, whereas those in lithologic Subunit IB (~2.9–1.3 Ma, 283–125 m CSF-A) are less variable, from ~90 to ~140 m/m.y. Sedimentation rates in Unit II (~4.5–2.9 Ma, 396–283 m CSF-A) are ~90 m/m.y. in the upper part to the middle and decreased (at ~15 m/m.y.) in the lower part (Fig. F51B).

References

Blum, P., 1997. Physical properties handbook: a guide to the shipboard measurement of physical properties of deep-sea cores. *ODP Tech. Note,* 26. doi:10.2973/odp.tn.26.1997

Borowski, W.S., Paull, C.K., and Ussler, W., III, 1996. Marine pore-water sulfate profiles indicate in situ methane flux from underlying gas hydrate. *Geology,* 24(7):655–658. doi:10.1130/0091-7613(1996)024<0655:MPWSPI>2.3.CO;2

Burdige, D.J., 2011. Temperature dependence of organic matter remineralization in deeply-buried marine sediments. *Earth Planet. Sci. Lett.,* 311(3–4):396–410. doi:10.1016/j.epsl.2011.09.043

Chatterjee, S., Dickens, G.R., Bhatnagar, G., Chapman, W.G., Dugan, B., Snyder, G.T., and Hirasaki, G.J., 2011. Pore water sulfate, alkalinity, and carbon isotope profiles in shallow sediment above marine gas hydrate systems: a numerical modeling perspective. *J. Geophys. Res.: Solid Earth,* 116(B9):B09103. doi:10.1029/2011JB008290

deMenocal, P.B, Bristow, J.F., and Stein, R., 1992. Paleoclimatic applications of downhole logs: Pliocene–Pleistocene results from Hole 798B, Sea of Japan. *Proc. ODP Sci. Results,* 127/128 (Pt. 1): College Station, TX (Ocean Drilling Program), 337–353. doi:10.2973/odp.proc.sr.127128-1.143.1992

Dickens, G.R., 2001. Sulfate profiles and barium fronts in sediment on the Blake Ridge: present and past methane fluxes through a large gas hydrate reservoir. *Geochim. Cosmochim. Acta,* 65(4):529–543. doi:10.1016/S0016-7037(00)00556-1

Emerson, S., and Hedges, J.I., 1988. Processes controlling the organic carbon content of open ocean sediments. *Paleoceanography,* 3(5):621–634. doi:10.1029/PA003i005p00621

Ferry, J.G., and Lessner, D.J., 2008. Methanogenesis in marine sediments. *Ann. N. Y. Acad. Sci.,* 1125(1):147–157. doi:10.1196/annals.1419.007

Froelich, P.N., Klinkhammer, G.P., Bender, M.L., Luedtke, N.A., Heath, G.R., Cullen, D., Dauphin, P., Hammond, D., Hartman, B., and Maynard, V., 1979. Early oxidation of organic matter in pelagic sediments of the eastern equatorial Atlantic: suboxic diagenesis. *Geochim. Cosmochim. Acta,* 43(7):1075–1090. doi:10.1016/0016-7037(79)90095-4

Gieskes, J.M., and Mahn, C., 2007. Halide systematics in interstitial waters of ocean drilling sediment cores. *Appl. Geochem.,* 22(3):515–533. doi:10.1016/j.apgeochem.2006.12.003

Gooday, A.J., 1993. Deep-sea benthic foraminiferal species which exploit phytodetritus: characteristic features and controls on distribution. *Mar. Micropaleontol.,* 22(3):187–205. doi:10.1016/0377-8398(93)90043-W

Guo, Z., Biscaye, P., Wei, L., Chen, X., Peng, S., and Liu, T., 2000. Summer monsoon variations over the last 1.2 Ma from the weathering of loess-soil sequences in China. *Geophys. Res. Lett.,* 27(12):1751–1754. doi:10.1029/1999GL008419

Hase, H., Yoon, J.-H., and Koterayama, W., 1999. The current structure of the Tsushima Warm Current along the Japan coast. *J. Oceanogr.,* 55(2):217–235. doi:10.1023/A:1007894030095

Hedberg, H.D., 1974. Relation of methane generation to undercompacted shales, shale diapirs, and mud volcanoes. *AAPG Bull.,* 58(4):661–673. http://archives.datapages.com/data/bulletns/1974-76/images/pg/00580004/0650/06610.pdf

Hyndman, R.D., Erickson, A.J., and Von Herzen, R.P., 1974. Geothermal measurements on DSDP Leg 26. *In* Davies, T.A., Luyendyk, B.P., et al., *Init. Repts. DSDP,* 26: Washington, DC (U.S. Govt. Printing Office), 451–463. doi:10.2973/dsdp.proc.26.113.1974

Ingle, J.C., Jr., Suyehiro, K., von Breymann, M.T., et al., 1990. *Proc. ODP, Init. Repts.,* 128: College Station, TX (Ocean Drilling Program). doi:10.2973/odp.proc.ir.128.1990

Isoda, Y., 2011. Climate change and physical process associated with the Tsushima Warm Current. *Mem. Fac. Fish. Sci., Hokkaido Univ.,* 53(2):2–12. http://hdl.handle.net/2115/47547

Itaki, T., and Ikehara, K., 2003. Radiolarian biozonation for the upper Quaternary in the Japan Sea. *J. Geol. Soc. Jpn.,* 109(2):96–105. doi:10.5575/geosoc.109.96

Jorissen, F.J., 1999. Benthic foraminiferal microhabitats below the sediment-water interface. *In* Sen Gupta, B.K. (Ed.), *Modern Foraminifera:* Dordrecht (Kluwer), 161–179. doi:10.1007/0-306-48104-9_10

Jorissen, F.J., de Stigter, H.C., and Widmark, J.G.V., 1995. A conceptual model explaining benthic foraminiferal microhabitats. *Mar. Micropaleontol.,* 26(1–4):3–15. doi:10.1016/0377-8398(95)00047-X

Jorissen, F.J., Fontanier, C., and Thomas, E., 2007. Paleoceanographical proxies based on deep-sea benthic foraminiferal assemblage characteristics. *In* Hillaire-Marcel, C. and De Vernal, A. (Eds.), *Proxies in Late Cenozoic Paleoceanography.* Dev. Mar. Geol., 263–325. doi:10.1016/S1572-5480(07)01012-3

Kato, M., 1992. Benthic foraminifers from the Japan Sea: Leg 128. *In* Pisciotto, K.A., Ingle, J.C., Jr., von Breymann, M.T., Barron, J., et al., *Proc. ODP, Sci. Results,* 127/128 (Pt. 1): College Station, TX (Ocean Drilling Program), 365–392. **doi:10.2973/odp.proc.sr.127128-1.142.1992**

Kido, Y., Minami, I., Tada, R., Fujine, K., Irino, T., Ikehara, K., and Chun, J.-H., 2007. Orbital-scale stratigraphy and high-resolution analysis of biogenic components and deep-water oxygenation conditions in the Japan Sea during the last 640 kyr. *Palaeogeogr., Palaeoclimatol., Palaeoecol.,* 247(1–2):32–49. **doi:10.1016/j.palaeo.2006.11.020**

Kucera, M., and Kennett, J.P., 2000. Biochronology and evolutionary implications of late Neogene California margin planktonic foraminiferal events. *Mar. Micropaleontol.,* 40(1–2):67–81. **doi:10.1016/S0377-8398(00)00029-3**

Langseth, M.G., and Tamaki, K., 1992. Geothermal measurements: thermal evolution of the Japan Sea basins and sediments. *In* Tamaki, K., Suyehiro, K., Allan, J., McWilliams, M., et al., *Proc. ODP, Sci. Results,* 127/128 (Pt. 2): College Station, TX (Ocean Drilling Program), 1297–1309. **doi:10.2973/odp.proc.sr.127128-2.227.1992**

Lyle, M., Koizumi, I., Richter, C., et al., 1997. *Proc. ODP, Init. Repts.,* 167: College Station, TX (Ocean Drilling Program). **doi:10.2973/odp.proc.ir.167.1997**

Maiya, S., 1978. Late Cenozoic planktonic foraminiferal biostratigraphy of the oil-field region of Northeast Japan. *In* Fujita, K., Ichikawa, K., Ichihara, M., Chiji, M., Unabara, K., Fujita, T., and Takayanagi, Y. (Eds.), *Cenozoic Geology of Japan:* Osaka (Osaka City Univ.), 35–60.

Masuzawa, T., and Kitano, Y., 1983. Interstitial water chemistry in deep-sea sediments from the Japan Sea. *J. Oceanogr. Soc. Jpn.,* 39(4):171–184. **doi:10.1007/BF02070261**

Moore, T.S., Murray, R.W., Kurtz, A.C., and Schrag, D.P., 2004. Anaerobic methane oxidation and the formation of dolomite. *Earth Planet. Sci. Lett.,* 229(1–2):141–154. **doi:10.1016/j.epsl.2004.10.015**

Müller, P.J., and Suess, E., 1979. Productivity, sedimentation rate, and sedimentary organic matter in the oceans—I. Organic carbon preservation. *Deep-Sea Res., Part A,* 26(12):1347–1362. **doi:10.1016/0198-0149(79)90003-7**

Oba, T., Kato, M., Kitazato, H., Koizumi, I., Omura, A., Sakai, T., and Takayama, T., 1991. Paleoenvironmental changes in the Japan Sea during the last 85,000 years. *Paleoceanography,* 6(4):499–518. **doi:10.1029/91PA00560**

Paull, C.K., Lorenson, T.D., Dickens, G., Borowski, W.S., Ussler, W., III, and Kvenvolden, K., 2000. Comparisons of in situ and core gas measurements in ODP Leg 164 bore holes. *Ann. New York Acad. Sci.,* 912:23–31. **doi:10.1111/j.1749-6632.2000.tb06756.x**

Pribnow, D., Kinoshita, M., and Stein, C., 2000. *Thermal Data Collection and Heat Flow Recalculations for Ocean Drilling Program Legs 101–180:* Hanover, Germany (Inst. Joint Geosci. Res., Inst. Geowiss. Gemeinschaftsauf. [GGA]). **http://www-odp.tamu.edu/publications/heatflow/ODPReprt.pdf**

Reeburgh, W.S., 1976. Methane consumption in Cariaco Trench waters and sediments. *Earth Planet. Sci. Lett.,* 28(3):337–344. **doi:10.1016/0012-821X(76)90195-3**

Satoguchi, Y., and Nagahashi, Y., 2012. Tephrostratigraphy of the Pliocene to middle Pleistocene series in Honshu and Kyushu Islands, Japan. *Isl. Arc,* 21(3):149–169. **doi:10.1111/j.1440-1738.2012.00816.x**

Sayles, F.L., and Manheim, F., 1975. Interstitial solutions and diagenesis in deeply buried marine sediments: results from the Deep Sea Drilling Project. *Geochim. Cosmochim. Acta,* 39(2):103–127. **doi:10.1016/0016-7037(75)90165-9**

Schippers, A., and Jørgensen, B.B., 2002. Biogeochemistry of pyrite and iron sulfide oxidation in marine sediments. *Geochim. Cosmochim. Acta,* 66(1):85–92. **doi:10.1016/S0016-7037(01)00745-1**

Shipboard Scientific Party, 1990. Site 798. *In* Ingle, J.C., Jr., Suyehiro, K., von Breymann, M.T., et al., *Proc. ODP, Init. Repts.,* 128: College Station, TX (Ocean Drilling Program), 121–236. **doi:10.2973/odp.proc.ir.128.105.1990**

Shipboard Scientific Party, 2003. Site 1230. *In* D'Hondt, S.L., Jørgensen, B.B., Miller, D.J., et al., *Proc. ODP, Init. Repts.,* 201: College Station, TX (Ocean Drilling Program), 1–107. **doi:10.2973/odp.proc.ir.201.111.2003**

Snyder, G.T., Hiruta, A., Matsumoto, R., Dickens, G.R., Tomaru, H., Takeuchi, R., Komatsubara, J., Ishida, Y., and Yu, H., 2007. Pore water profiles and authigenic mineralization in shallow marine sediments above the methane-charged system on Umitaka Spur, Japan Sea. *Deep-Sea Res., Part II,* 54(11–13):1216–1239. **doi:10.1016/j.dsr2.2007.04.001**

Tada, R., 1994. Paleoceanographic evolution of the Japan Sea. *Palaeogeogr., Palaeoclimatol., Palaeoecol.,* 108(3–4):487–508. **doi:10.1016/0031-0182(94)90248-8**

Tada, R., 2004. Onset and evolution of millennial-scale variability in the Asian monsoon and its impact on paleoceanography of the Japan Sea. *In* Clift, P., Kuhnt, W., Wang, P., and Hayes, D. (Eds.), *Continent-Ocean Interactions within East Asian Marginal Seas*. Geophys. Monogr., 149:283–298. **doi:10.1029/149GM15**

Tada, R., Murray, R.W., Alvarez Zarikian, C.A., Anderson, W.T., Jr., Bassetti, M.-A., Brace, B.J., Clemens, S.C., da Costa Gurgel, M.H., Dickens, G.R., Dunlea, A.G., Gallagher, S.J., Giosan, L., Henderson, A.C.G., Holbourn, A.E., Ikehara, K., Irino, T., Itaki, T., Karasuda, A., Kinsley, C.W., Kubota, Y., Lee, G.S., Lee, K.E., Lofi, J., Lopes, C.I.C.D., Peterson, L.C., Saavedra-Pellitero, M., Sagawa, T., Singh, R.K., Sugisaki, S., Toucanne, S., Wan, S., Xuan, C., Zheng, H., and Ziegler, M., 2015a. Expedition 346 summary. *In* Tada, R., Murray, R.W., Alvarez Zarikian, C.A., and the Expedition 346 Scientists, *Proc. IODP,* 346: College Station, TX (Integrated Ocean Drilling Program). **doi:10.2204/iodp.proc.346.101.2015**

Tada, R., Murray, R.W., Alvarez Zarikian, C.A., Anderson, W.T., Jr, Bassetti, M.-A., Brace, B.J., Clemens, S.C., Dickens, G.R., Dunlea, A.G., Gallagher, S.J., Giosan, L., da Costa Gurgel, M.H., Henderson, A.C.G., Holbourn, A.E.,

Ikehara, K., Irino, T., Itaki, T., Karasuda, A., Kinsley, C.W., Kubota, Y., Lee, G.S., Lee, K.E., Lofi, J., Lopes, C.I.C.D., Peterson, L.C., Saavedra-Pellitero, M., Sagawa, T., Singh, R.K., Sugisaki, S., Toucanne, S., Wan, S., Xuan, C., Zheng, H., and Ziegler, M., 2015b. Methods. *In* Tada, R., Murray, R.W., Alvarez Zarikian, C.A., and the Expedition 346 Scientists, *Proc. IODP,* 346: College Station, TX (Integrated Ocean Drilling Program). **doi:10.2204/iodp.proc.346.102.2015**

Tada, R., Murray, R.W., Alvarez Zarikian, C.A., Anderson, W.T., Jr., Bassetti, M.-A., Brace, B.J., Clemens, S.C., da Costa Gurgel, M.H., Dickens, G.R., Dunlea, A.G., Gallagher, S.J., Giosan, L., Henderson, A.C.G., Holbourn, A.E., Ikehara, K., Irino, T., Itaki, T., Karasuda, A., Kinsley, C.W., Kubota, Y., Lee, G.S., Lee, K.E., Lofi, J., Lopes, C.I.C.D., Peterson, L.C., Saavedra-Pellitero, M., Sagawa, T., Singh, R.K., Sugisaki, S., Toucanne, S., Wan, S., Xuan, C., Zheng, H., and Ziegler, M., 2015c. Site U1422. *In* Tada, R., Murray, R.W., Alvarez Zarikian, C.A., and the Expedition 346 Scientists, *Proc. IODP,* 346: College Station, TX (Integrated Ocean Drilling Program). **doi:10.2204/iodp.proc.346.103.2015**

Tada, R., Murray, R.W., Alvarez Zarikian, C.A., Anderson, W.T., Jr., Bassetti, M.-A., Brace, B.J., Clemens, S.C., da Costa Gurgel, M.H., Dickens, G.R., Dunlea, A.G., Gallagher, S.J., Giosan, L., Henderson, A.C.G., Holbourn, A.E., Ikehara, K., Irino, T., Itaki, T., Karasuda, A., Kinsley, C.W., Kubota, Y., Lee, G.S., Lee, K.E., Lofi, J., Lopes, C.I.C.D., Peterson, L.C., Saavedra-Pellitero, M., Sagawa, T., Singh, R.K., Sugisaki, S., Toucanne, S., Wan, S., Xuan, C., Zheng, H., and Ziegler, M., 2015d. Site U1424. *In* Tada, R., Murray, R.W., Alvarez Zarikian, C.A., and the Expedition 346 Scientists, *Proc. IODP,* 346: College Station, TX (Integrated Ocean Drilling Program). **doi:10.2204/iodp.proc.346.105.2015**

Tada, R., Murray, R.W., Alvarez Zarikian, C.A., Anderson, W.T., Jr., Bassetti, M.-A., Brace, B.J., Clemens, S.C., da Costa Gurgel, M.H., Dickens, G.R., Dunlea, A.G., Gallagher, S.J., Giosan, L., Henderson, A.C.G., Holbourn, A.E., Ikehara, K., Irino, T., Itaki, T., Karasuda, A., Kinsley, C.W., Kubota, Y., Lee, G.S., Lee, K.E., Lofi, J., Lopes, C.I.C.D., Peterson, L.C., Saavedra-Pellitero, M., Sagawa, T., Singh, R.K., Sugisaki, S., Toucanne, S., Wan, S., Xuan, C., Zheng, H., and Ziegler, M., 2015e. Site U1425. *In* Tada, R., Murray, R.W., Alvarez Zarikian, C.A., and the Expedition 346 Scientists, *Proc. IODP,* 346: College Station, TX (Integrated Ocean Drilling Program). **doi:10.2204/iodp.proc.346.106.2015**

Tada, R., Murray, R.W., Alvarez Zarikian, C.A., Anderson, W.T., Jr., Bassetti, M.-A., Brace, B.J., Clemens, S.C., da Costa Gurgel, M.H., Dickens, G.R., Dunlea, A.G., Gallagher, S.J., Giosan, L., Henderson, A.C.G., Holbourn, A.E., Ikehara, K., Irino, T., Itaki, T., Karasuda, A., Kinsley, C.W., Kubota, Y., Lee, G.S., Lee, K.E., Lofi, J., Lopes, C.I.C.D., Peterson, L.C., Saavedra-Pellitero, M., Sagawa, T., Singh, R.K., Sugisaki, S., Toucanne, S., Wan, S., Xuan, C., Zheng, H., and Ziegler, M., 2015f. Site U1427. *In* Tada, R., Murray, R.W., Alvarez Zarikian, C.A., and the Expedition 346 Scientists, *Proc. IODP,* 346: College Station, TX (Integrated Ocean Drilling Program). **doi:10.2204/iodp.proc.346.108.2015**

Tamura, I., Yamazaki, H., and Mizuno, K., 2008. Characteristics for the recognition of Pliocene and early Pleistocene marker tephras in central Japan. *Quat. Int.,* 178(1):85–99. **doi:10.1016/j.quaint.2007.04.002**

von Breymann, M.T., Brumsack, H., and Emeis, K.C., 1992. Depositional and diagenetic behavior of barium in the Japan Sea. *In* Pisciotto, K.A., Ingle, J.C., Jr., von Breymann, M.T., Barron, J., et al., *Proc. ODP, Sci. Results,* 127/128 (Pt. 1): College Station, TX (Ocean Drilling Program), 651–665. **doi:10.2973/odp.proc.sr.127128-1.168.1992**

Xuan, C., and Channell, J.E.T., 2009. UPmag: MATLAB software for viewing and processing U channel or other pass-through paleomagnetic data. *Geochem., Geophys., Geosyst.,* 10(10):Q10Y07. **doi:10.1029/2009GC002584**

Yanagisawa, Y., and Akiba, F., 1998. Refined Neogene diatom biostratigraphy for the northwest Pacific around Japan, with an introduction of code numbers for selected diatom biohorizons. *Chishitsugaku Zasshi,* 104(6):395–414. **doi:10.5575/geosoc.104.395**

Publication: 28 March 2015
MS 346-107

Figure F1. Bathymetric map of Expedition 346 sites (red circles). Sites previously drilled by the Deep Sea Drilling Project (DSDP) and Ocean Drilling Program (ODP) (white circles) are also shown. Also illustrated are surface current systems.

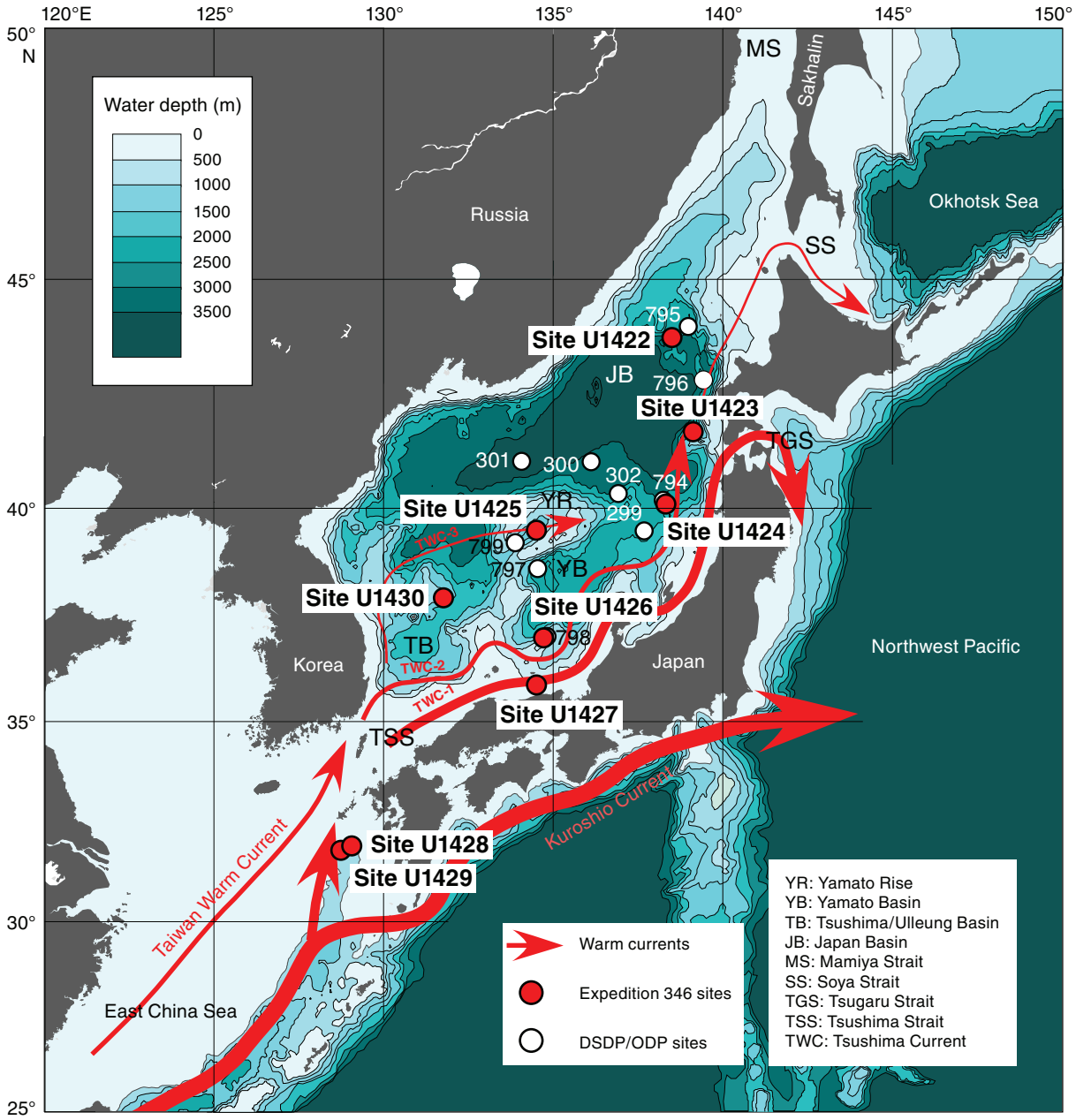

Figure F2. Lithologic summary, Hole U1426A. GRA = gamma ray attenuation.

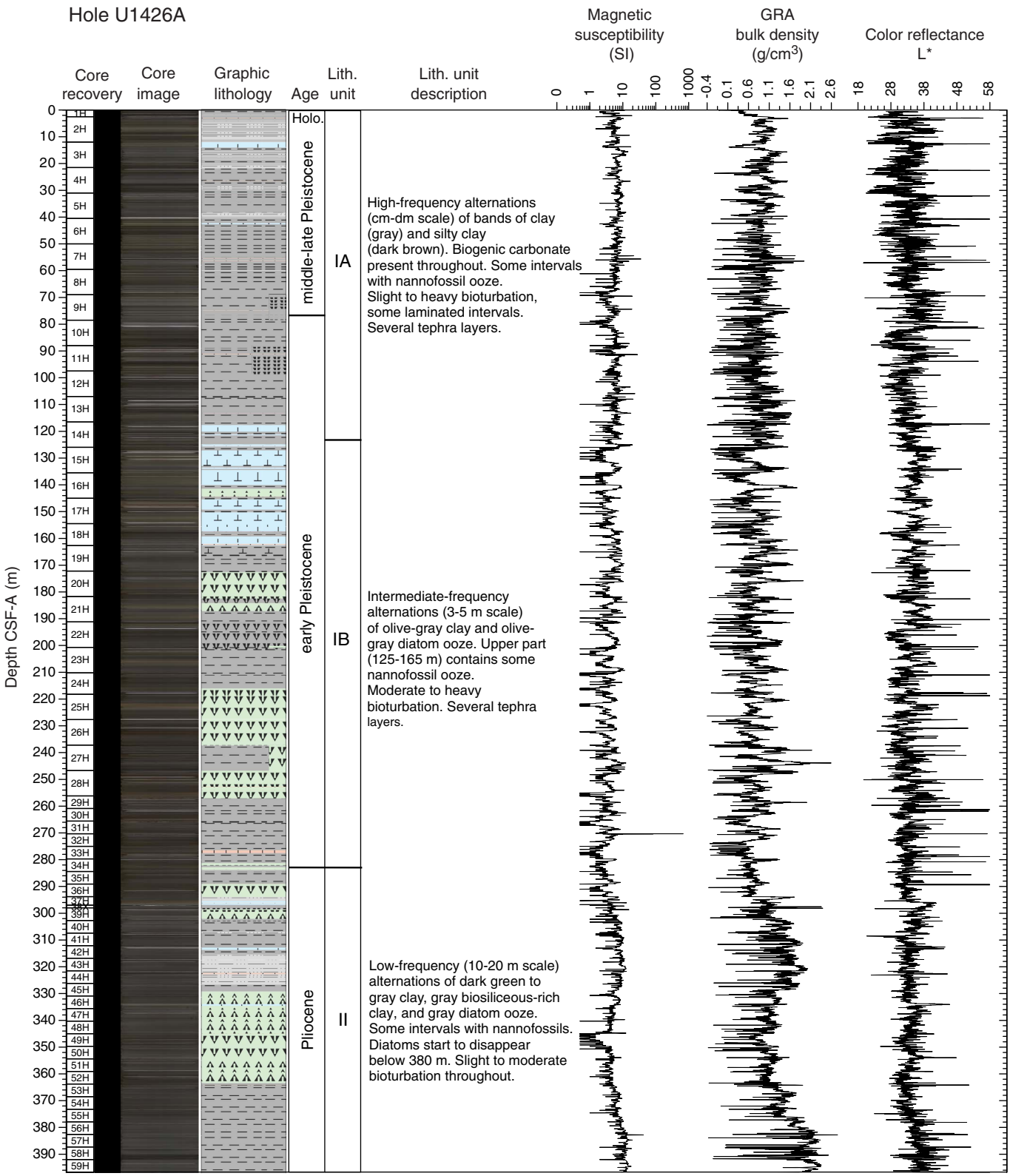

Figure F3. Lithologic summary, Hole U1426B. GRA = gamma ray attenuation.

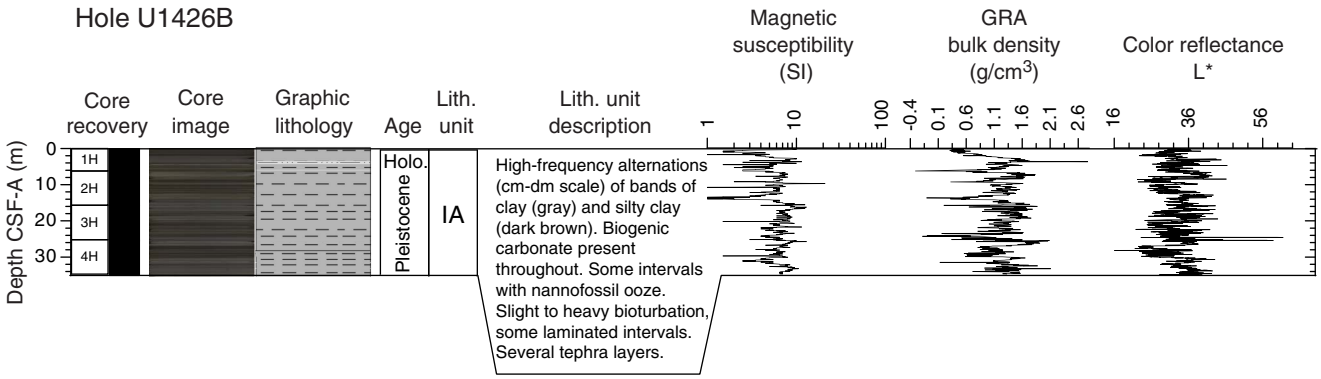

Figure F4. Lithologic summary, Hole U1426C. GRA = gamma ray attenuation.

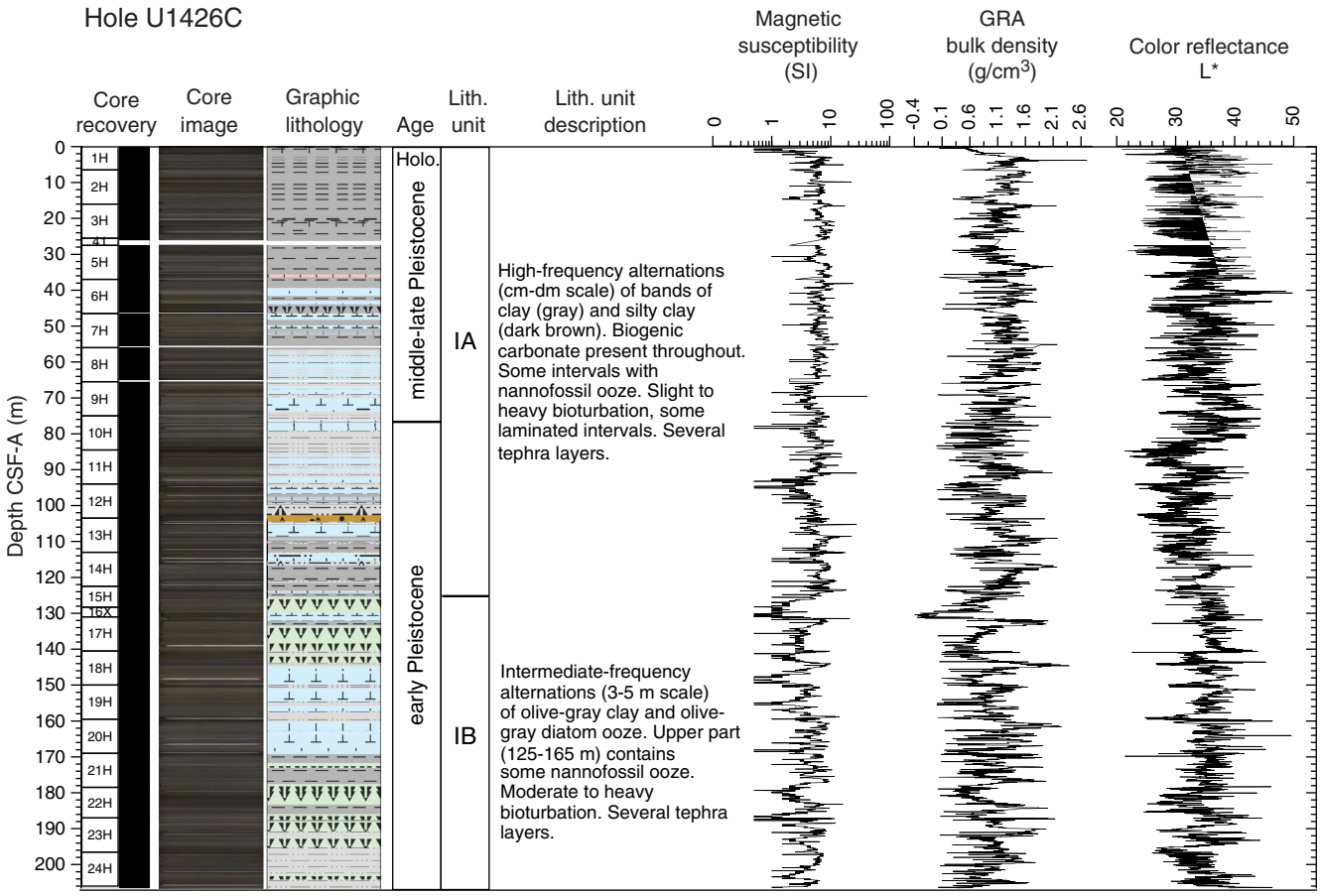

Figure F5. Lithologic summary, Hole U1426D. GRA = gamma ray attenuation.

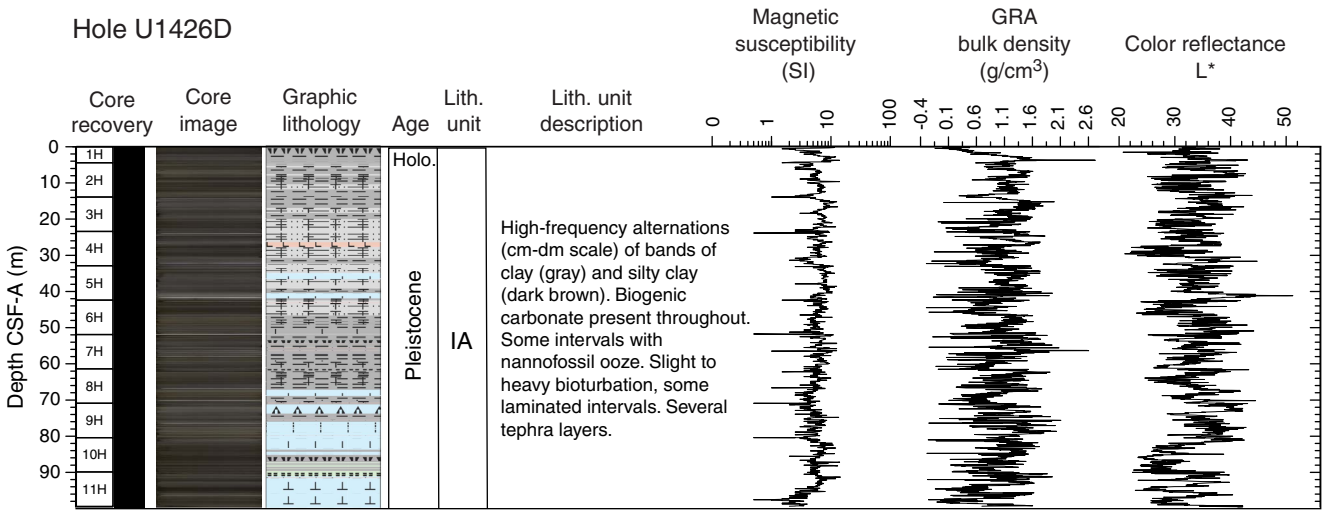

Figure F6. Hole-to-hole correlation based on the distribution of lithologic units, Site U1426.

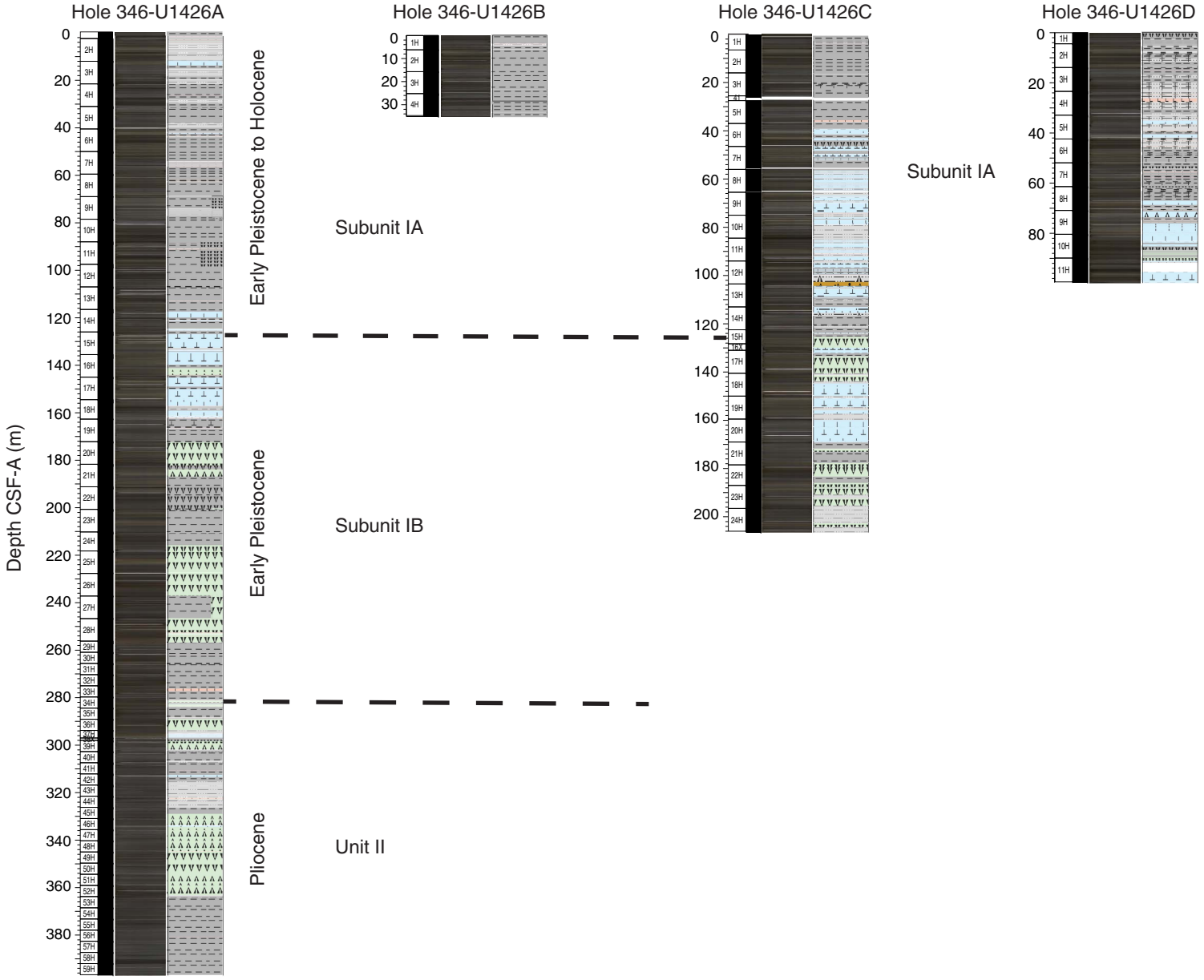

Figure F7. Example of vitric tephra layer (interval 346-U1426D-7H-4, 70–95 cm). Note enhanced color contrast to highlight sedimentary structures.

Figure F8. Detail of foraminifer-sand layer (interval 346-U1426A-7H-5, 101–108 cm). Note enhanced color contrast to highlight sedimentary structures.

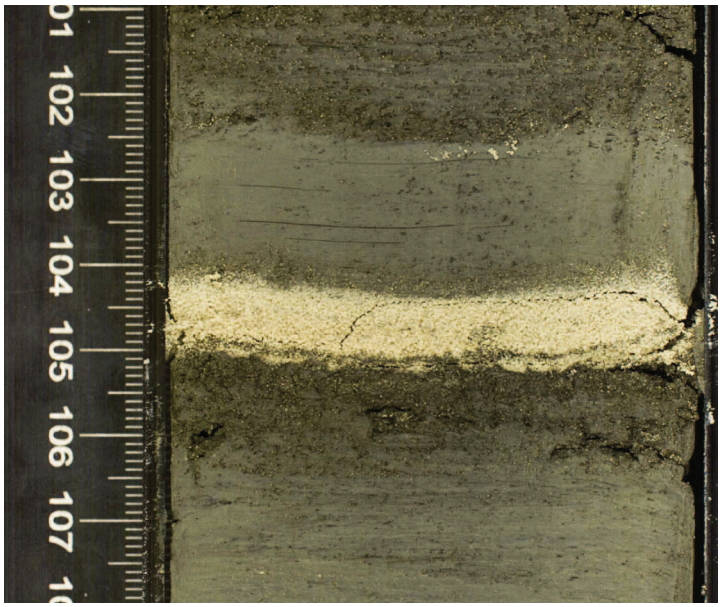

Figure F9. Turbidite layer showing normal grading (interval 346-U1426A-9H-5, 138–148 cm). Note enhanced color contrast to highlight sedimentary structures.

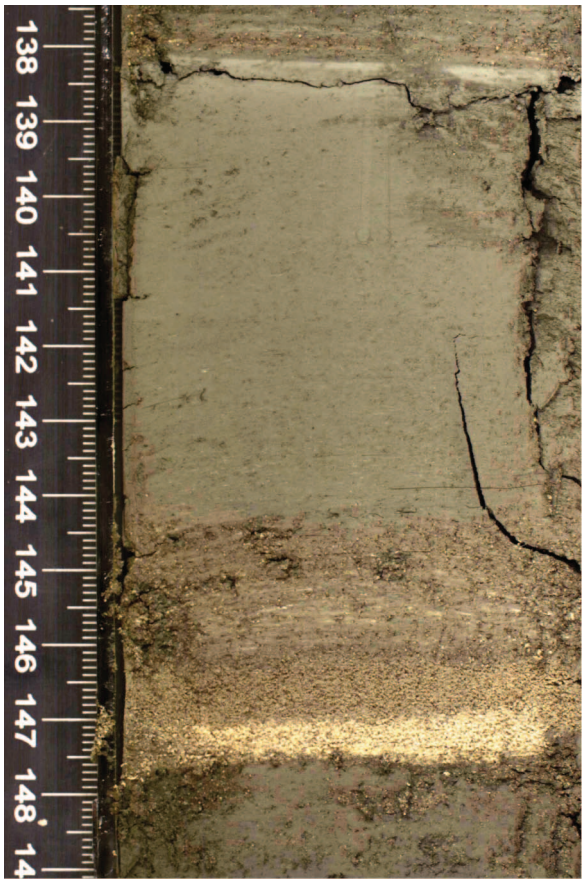

Figure F10. Distribution of tephra layers in Hole U1426A (number of tephra and total thickness in each core).

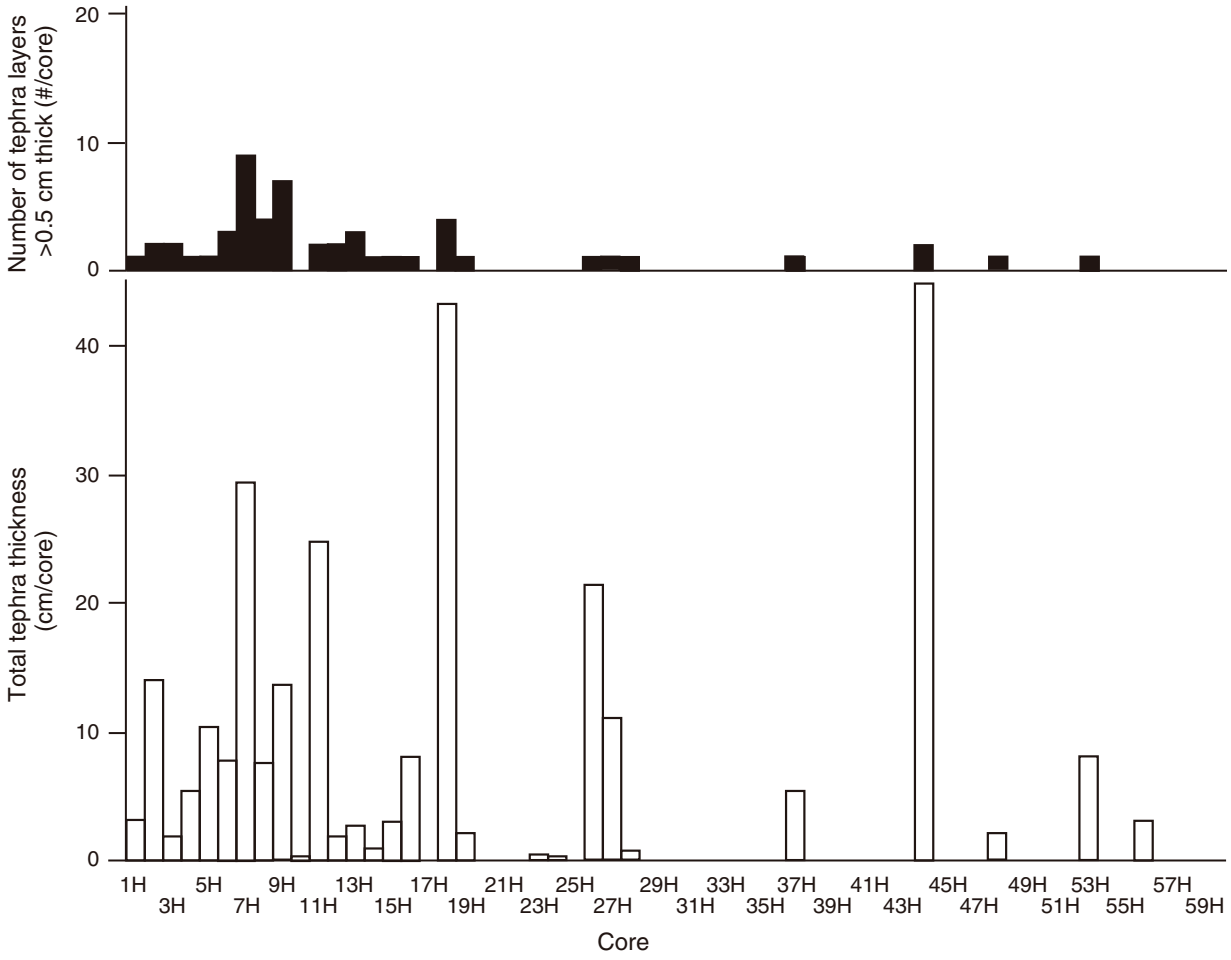

Figure F11. Photographs representative of Subunit IA, Hole U1426A. Note enhanced color contrast to highlight sedimentary structures.

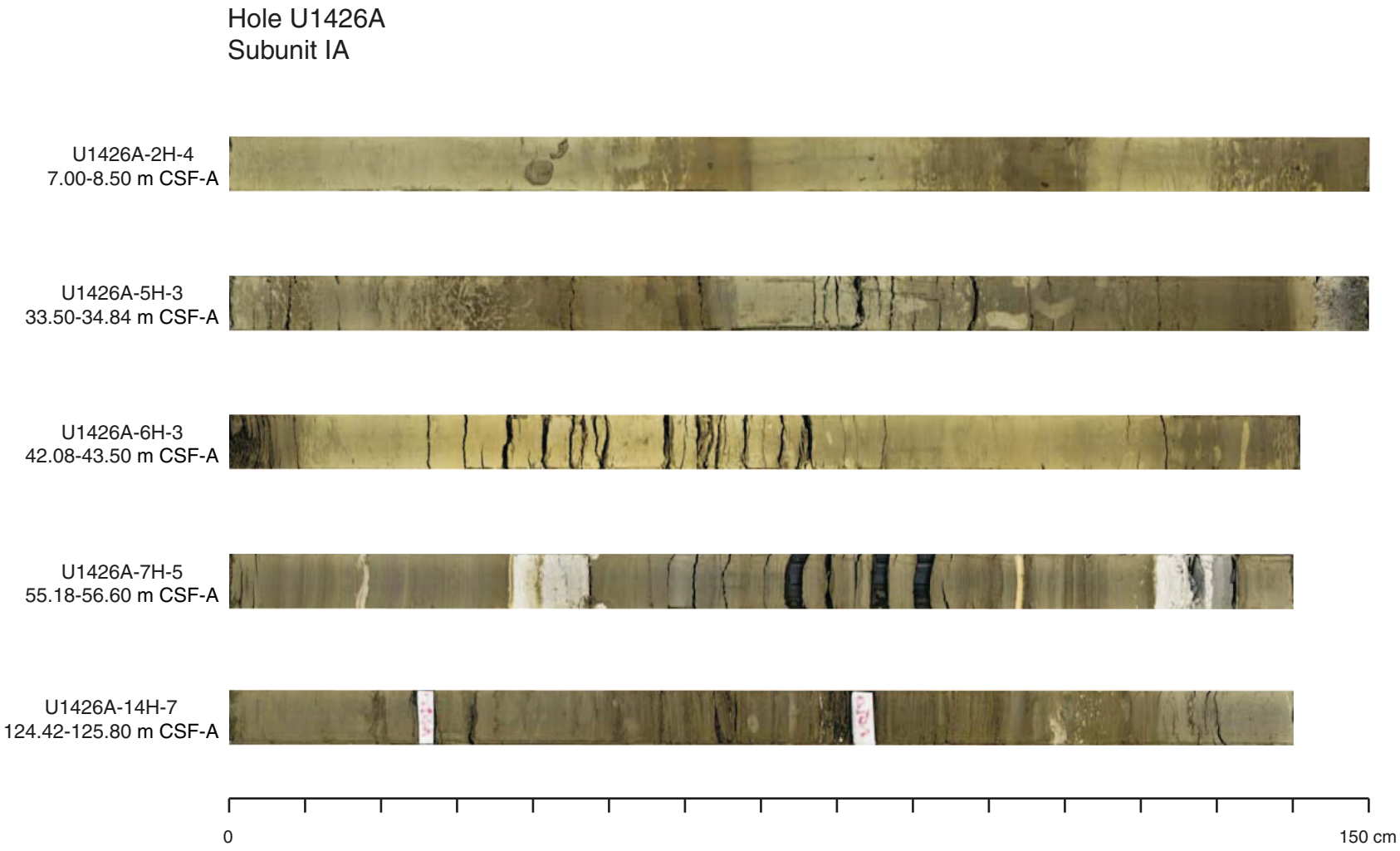

Figure F12. Detail of bioturbated dark–light color banding, Hole U1426A. Note enhanced color contrast to highlight sedimentary structures.

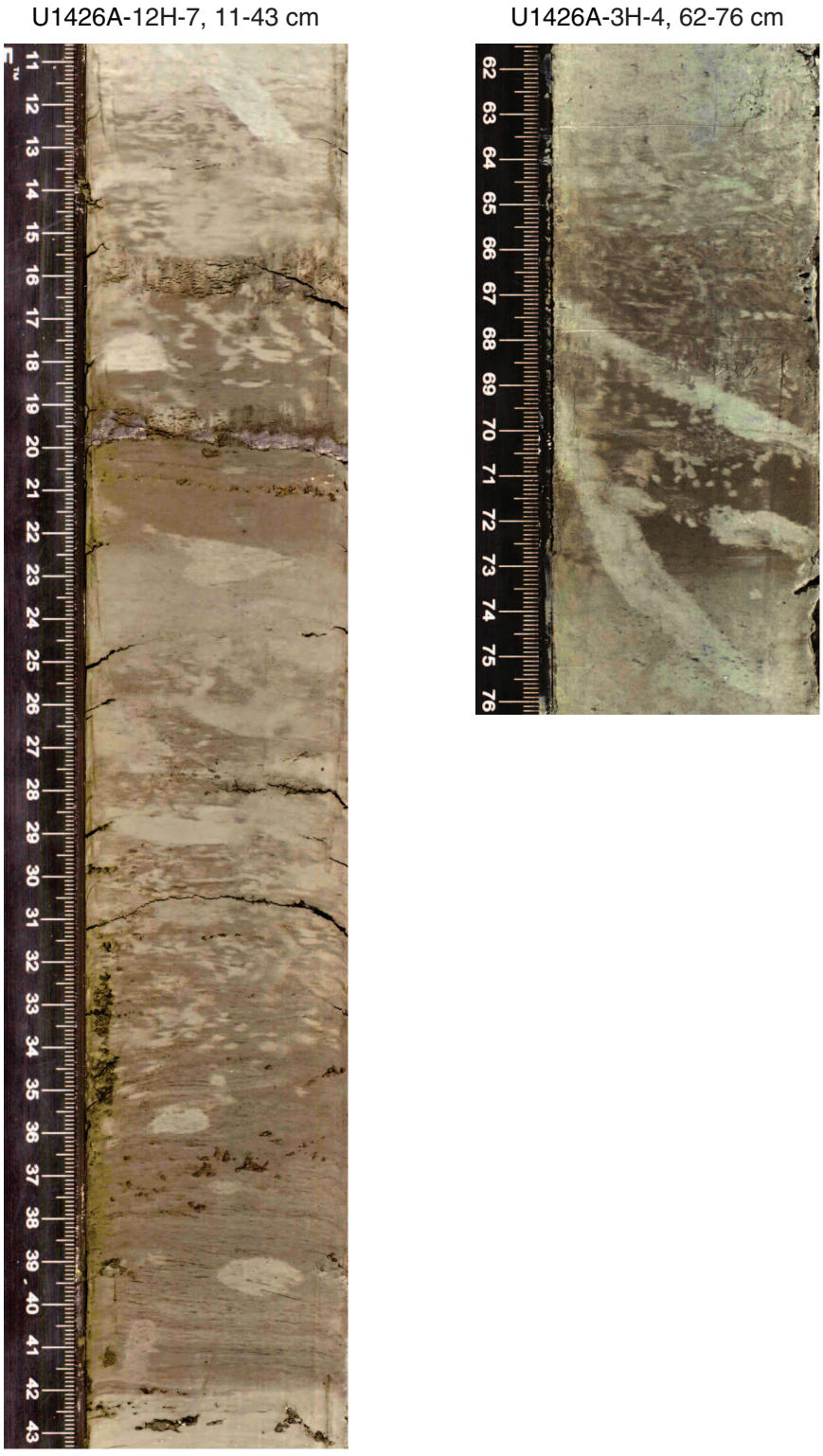

Figure F13. Detail of sediment with high nannofossil content (Section 346-U1426A-17H-2, 75 cm).

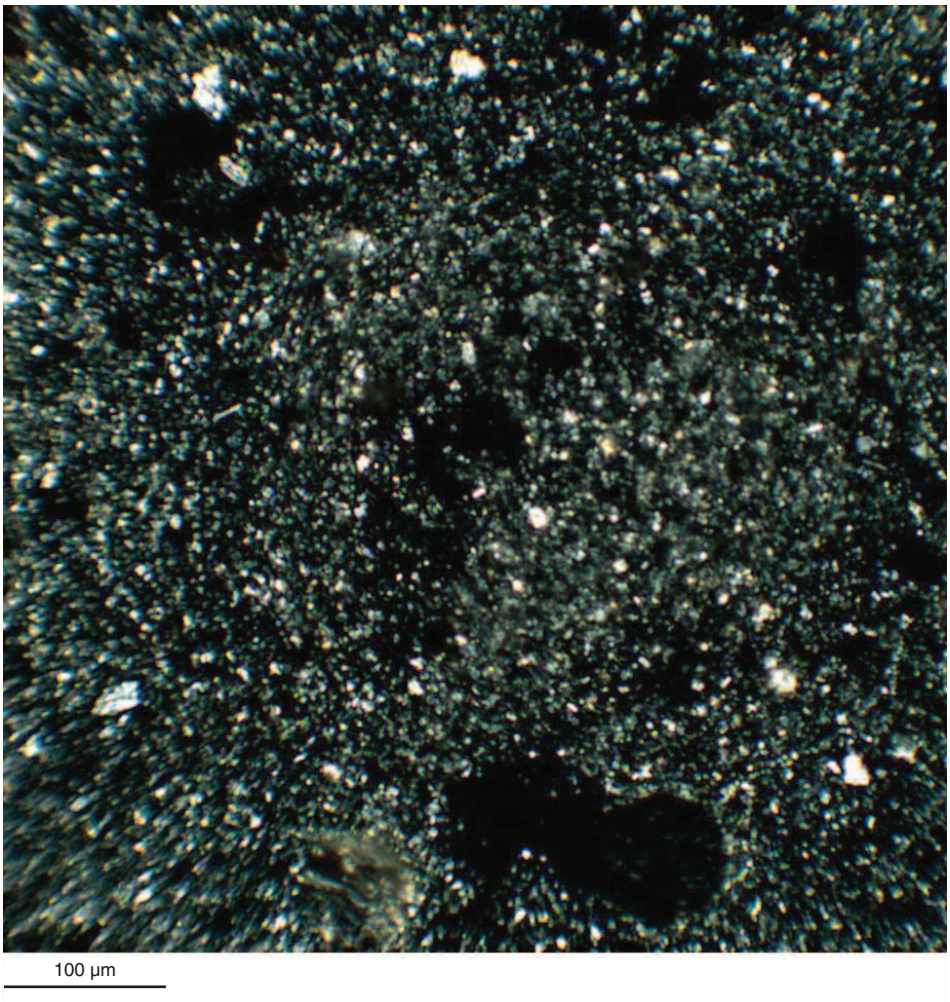

Figure F14. Detail of sediment with high dolomite content (Section 346-U1426A-3H-2, 75 cm).

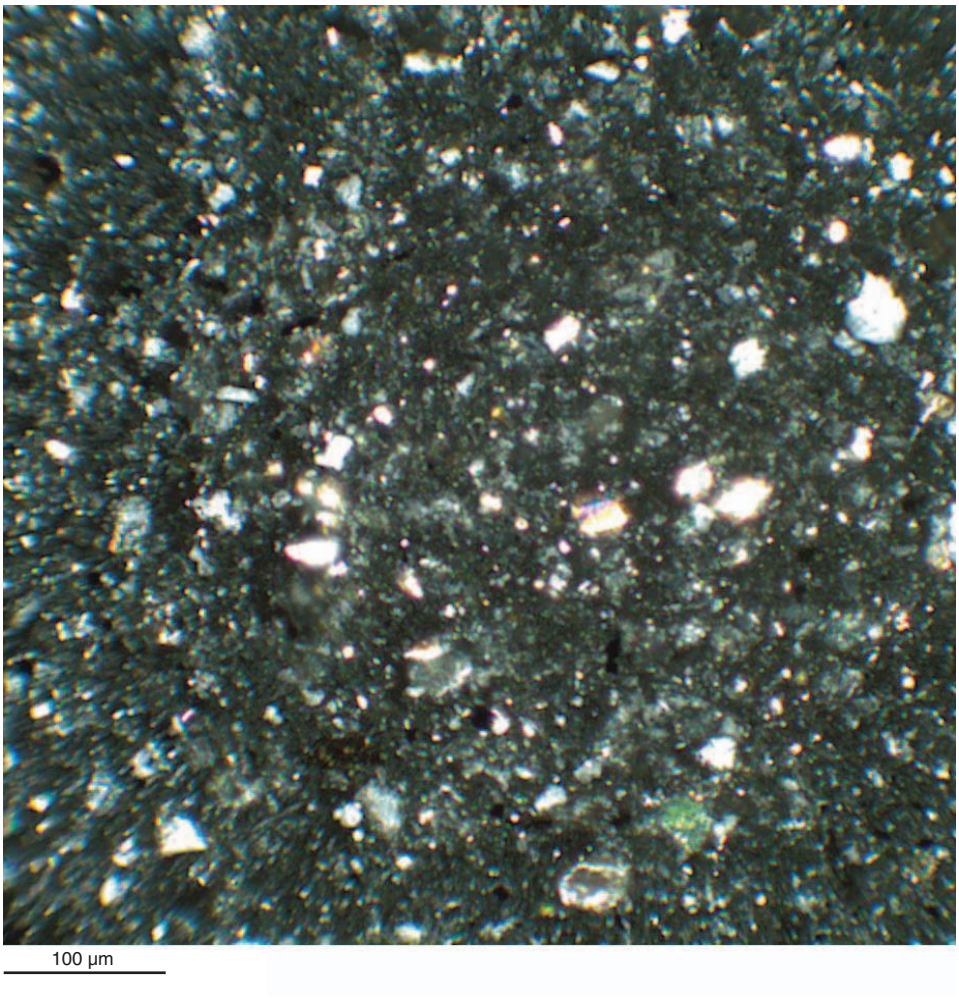

Figure F15. Photographs representative of Subunit IB, Hole U1426A. Note enhanced color contrast to highlight sedimentary structures.

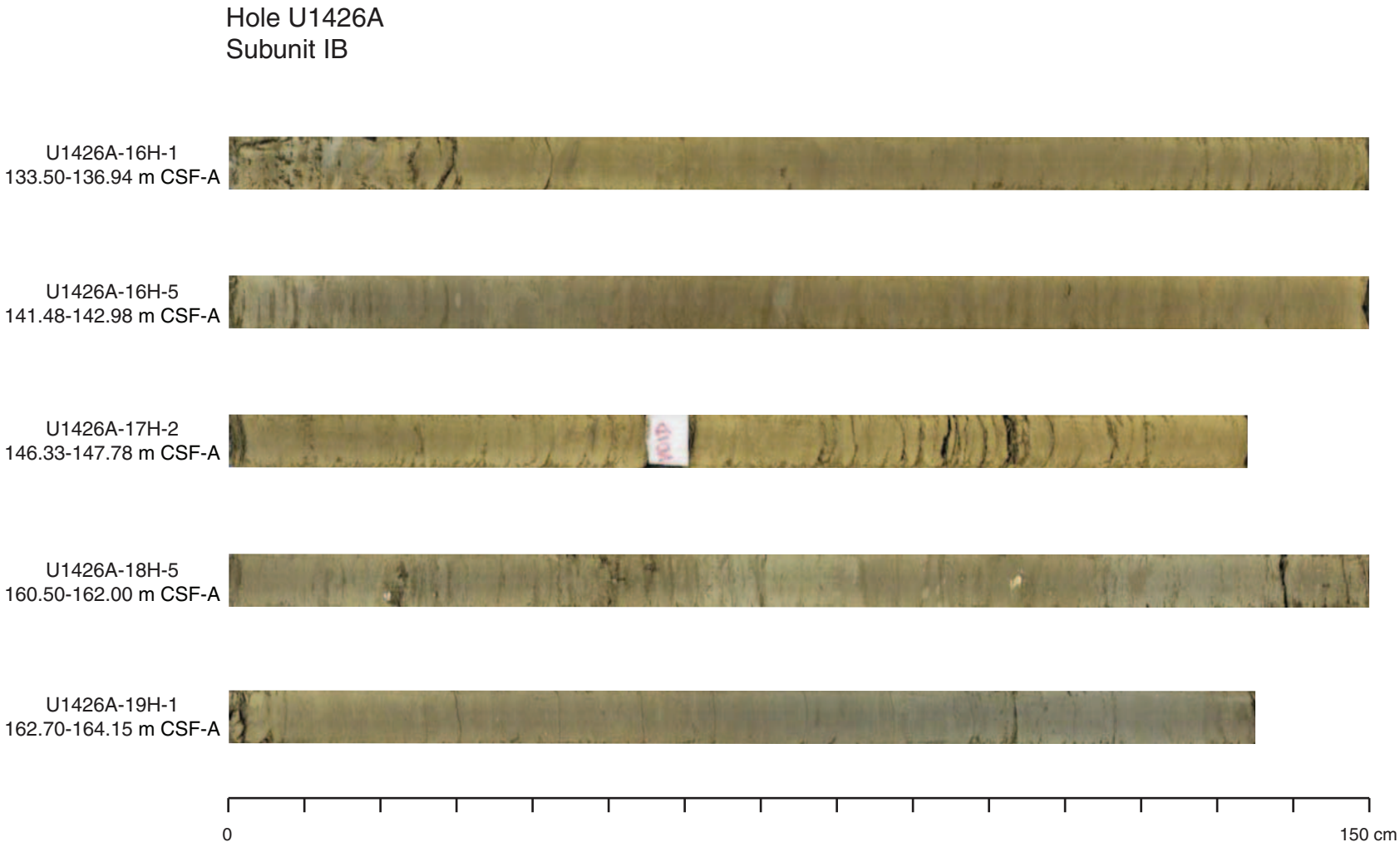

Figure F16. Photographs representative of Unit II, Hole U1426A. Note enhanced color contrast to highlight sedimentary structures.

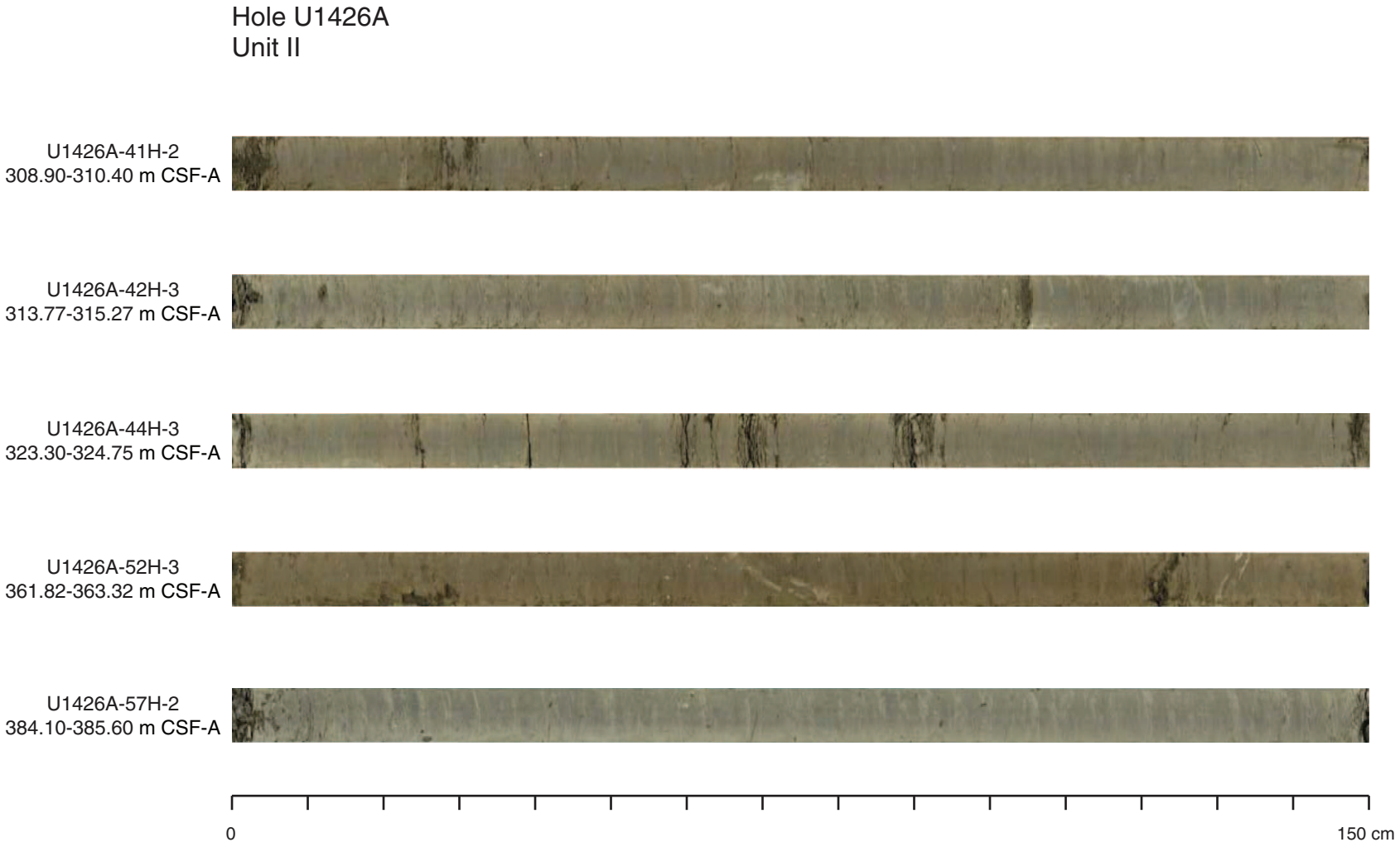

Figure F17. Detail of Unit II sediment showing low abundance of biosiliceous components (Section 346-U1426A-55H-4, 75 cm).

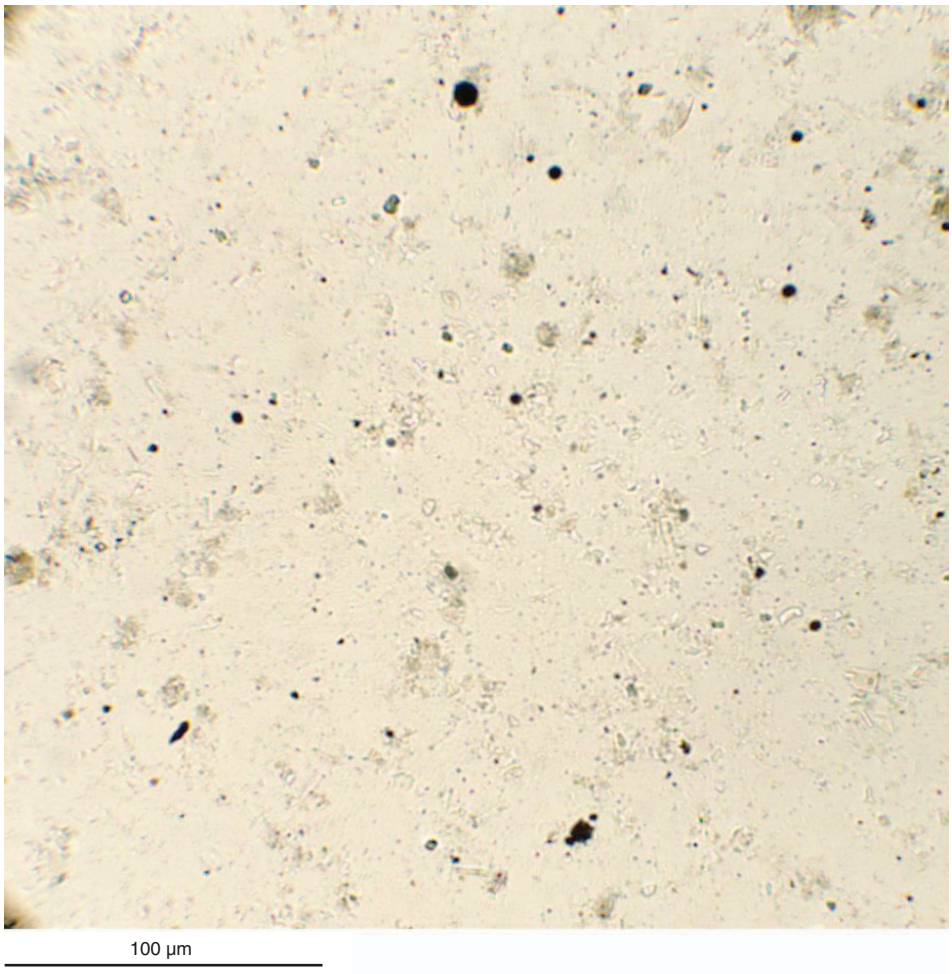

Figure F18. Variation of XRD peak intensity of identified minerals with depth, Hole U1426A.

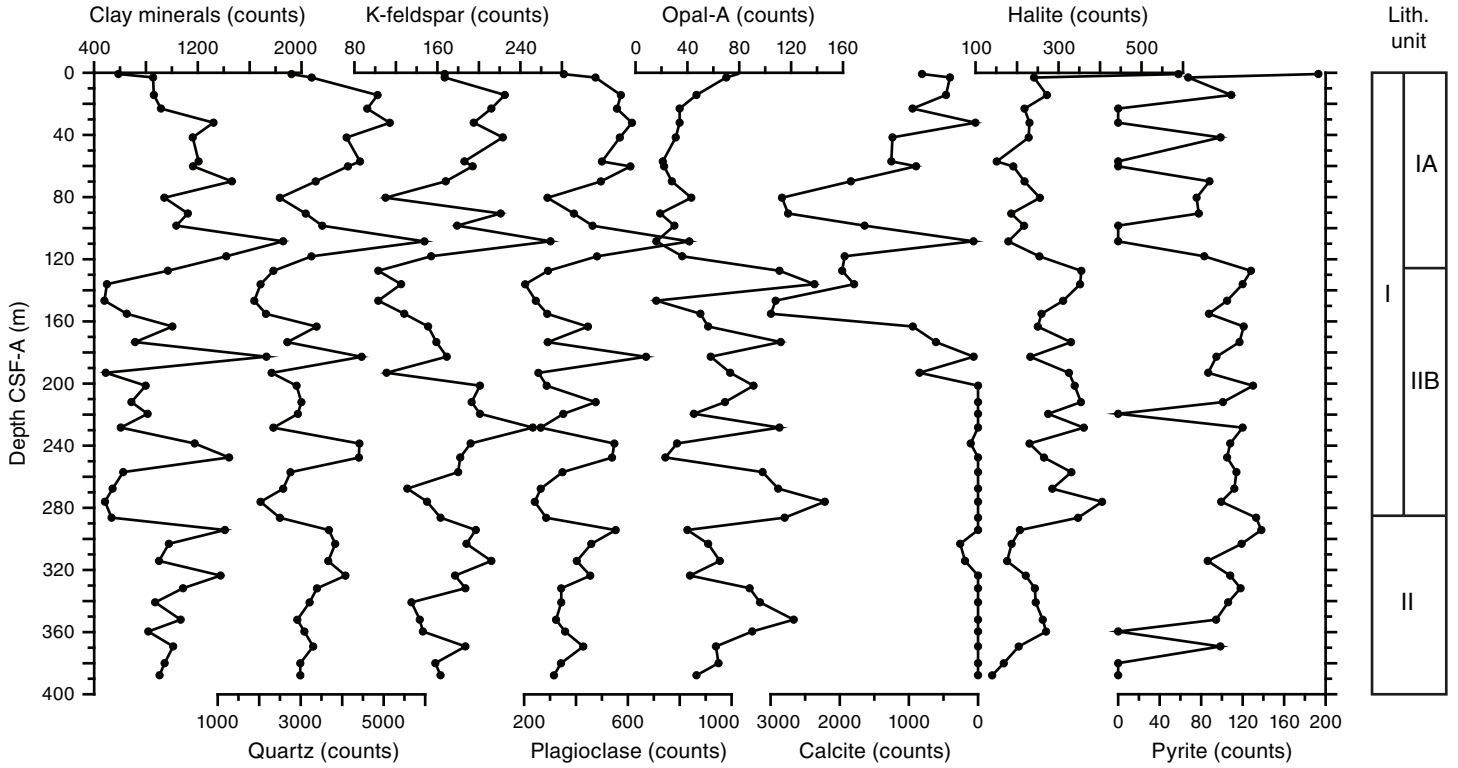

Figure F19. Integrated calcareous and siliceous microfossil biozonation, Site U1426.

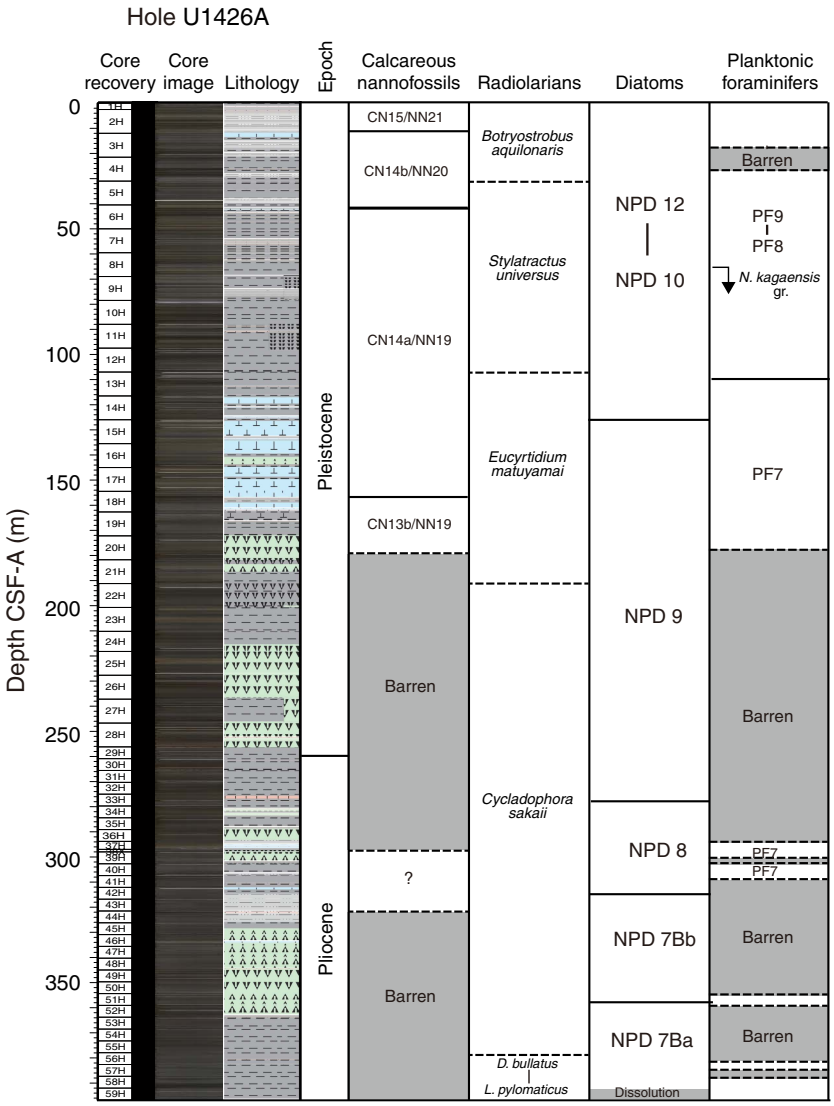

Figure F20. Age-depth profile, Site U1426. FO = first occurrence, LO = last occurrence, RI = rapid increase, D/S = dextral/sinistral crossover.

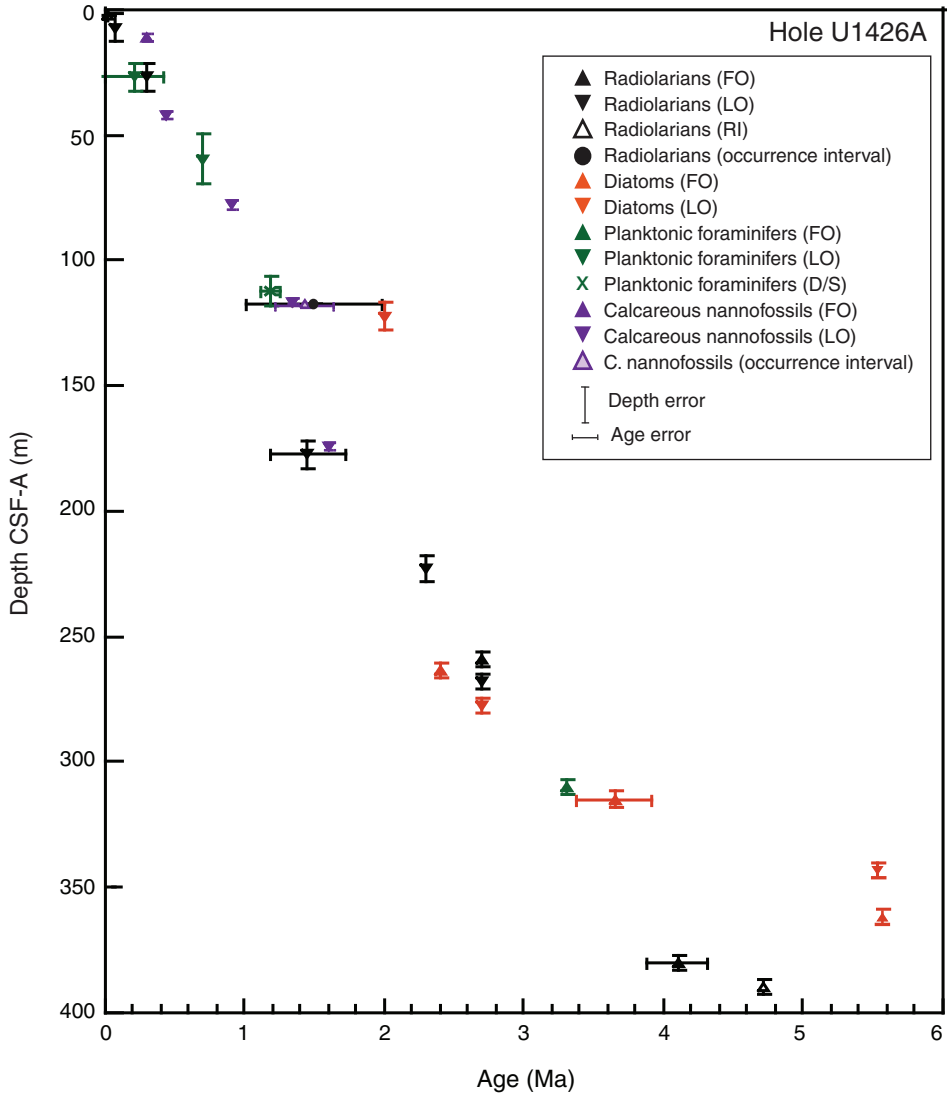

Figure F21. Distribution of siliceous and calcareous microfossils, Site U1426. B = barren, R = rare, F = few, C = common, A = abundant, D = dominant.

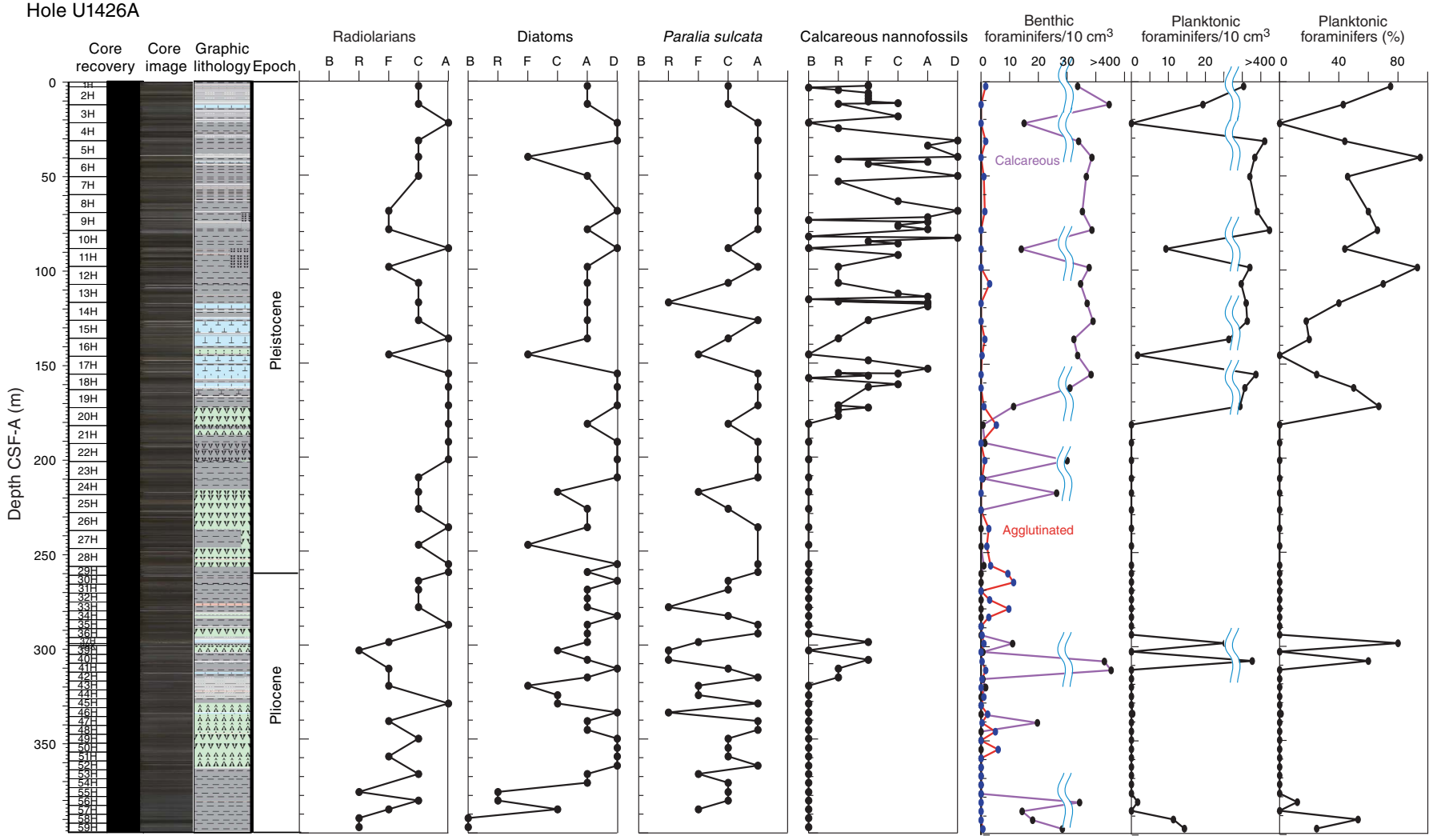

Figure F22. Distribution of benthic foraminifers in Hole U1426A showing percentage of various calcareous species as percentage of the total assemblage.

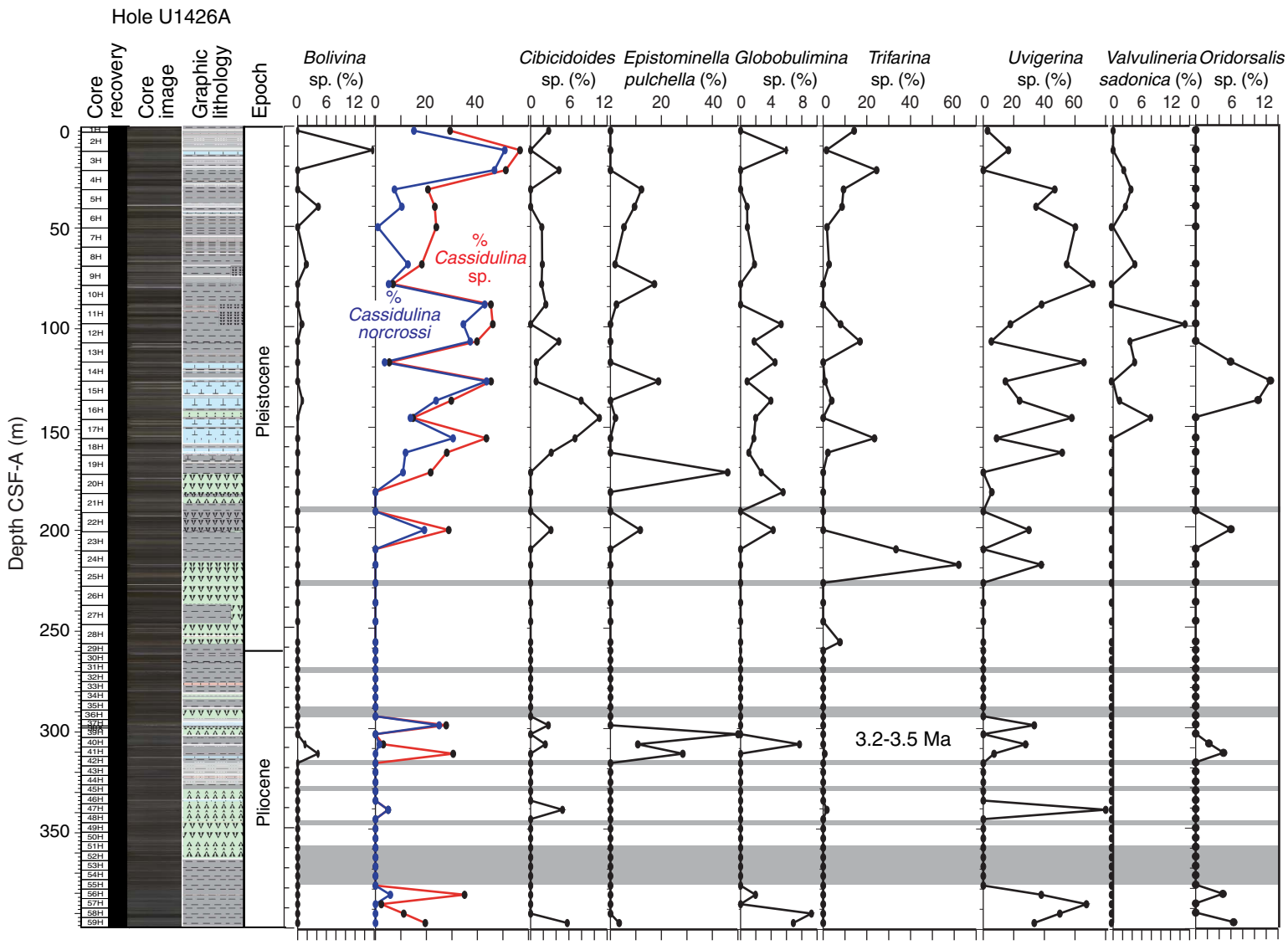

Figure F23. Benthic foraminifers. Scale bars = 100 µm. **1, 2.** *Cassidulina japonica;* (1) Sample 346-U1426A-6H-CC; (2) Sample 346-U1426A-2H-CC. **3, 4.** *Cassidulina teretis* (Sample 346-U1426A-2H-CC). **5.** *Uvigerina yabei* (Sample 346-U1426A-6H-CC). **6.** *Uvigerina peregina* (Sample 346-U1426A-4H-CC). **7, 8.** *Uvigerina hispida* (Sample 346-U1426A-4H-CC). **9.** *Eubulimina exilis* (Sample 346-U1426A-13H-CC). **10, 11.** *Trifarina angulosa;* (10) Sample 346-U1426A-2H-CC; (11) Sample 346-U1426A-4H-CC. **12.** *Karreriella baccata* (Sample 346-U1426A-6H-CC). **13.** *Planularia* sp. (Sample 346-U1426A-13H-CC). **14, 15.** *Valvulineria sadonica* (Sample 346-U1426A-4H-CC). **16.** *Globobulimina pacifica* (Sample 346-U1426A-2H-CC). **17.** *Bolivina pacifica* (Sample 346-U1426A-2H-CC).

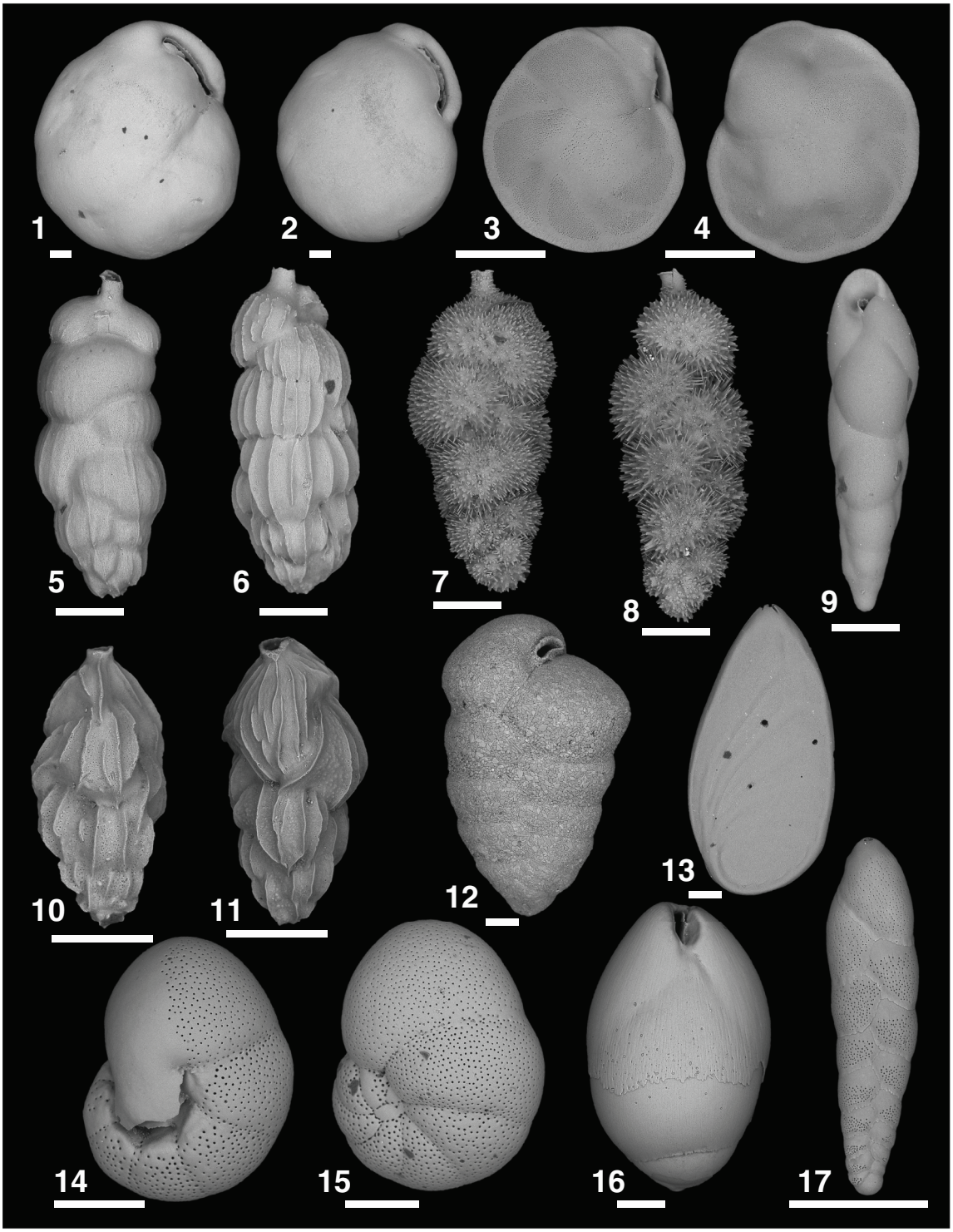

Figure F24. Ostracods. **1, 2.** *Loxoconcha*: (1) *Loxoconcha* sp. A (left valve), Sample 346-U1426A-13H-CC; (2) *Loxoconcha* sp. B. (left valve), Sample 346-U1426A-58H-CC. **3–5.** *Legitimocythere* sp. (juveniles, right valves, Samples 346-U1426A-1H-CC and 17H-CC). **6.** *Propontocypris* sp. (left valve, Sample 346-U1426A-13H-CC); **7–8, 10–12.** *Krithe* spp. (Samples 346-U1426A-1H-CC, 8H-CC, and 58H-CC). **9.** *Falsobuntonia* sp. (carapace, left valve side, Sample 346-U1426A-4H-CC). **13.** *Argilloecia lunata* (left valve, Sample 346-U1426A-4H-CC). **14, 15.** *Acanthocythereis dunelmensis* (14) left valve, Sample 346-U1426A-17H-CC; (15) left valve, Sample 346-U1426A-40H-CC).

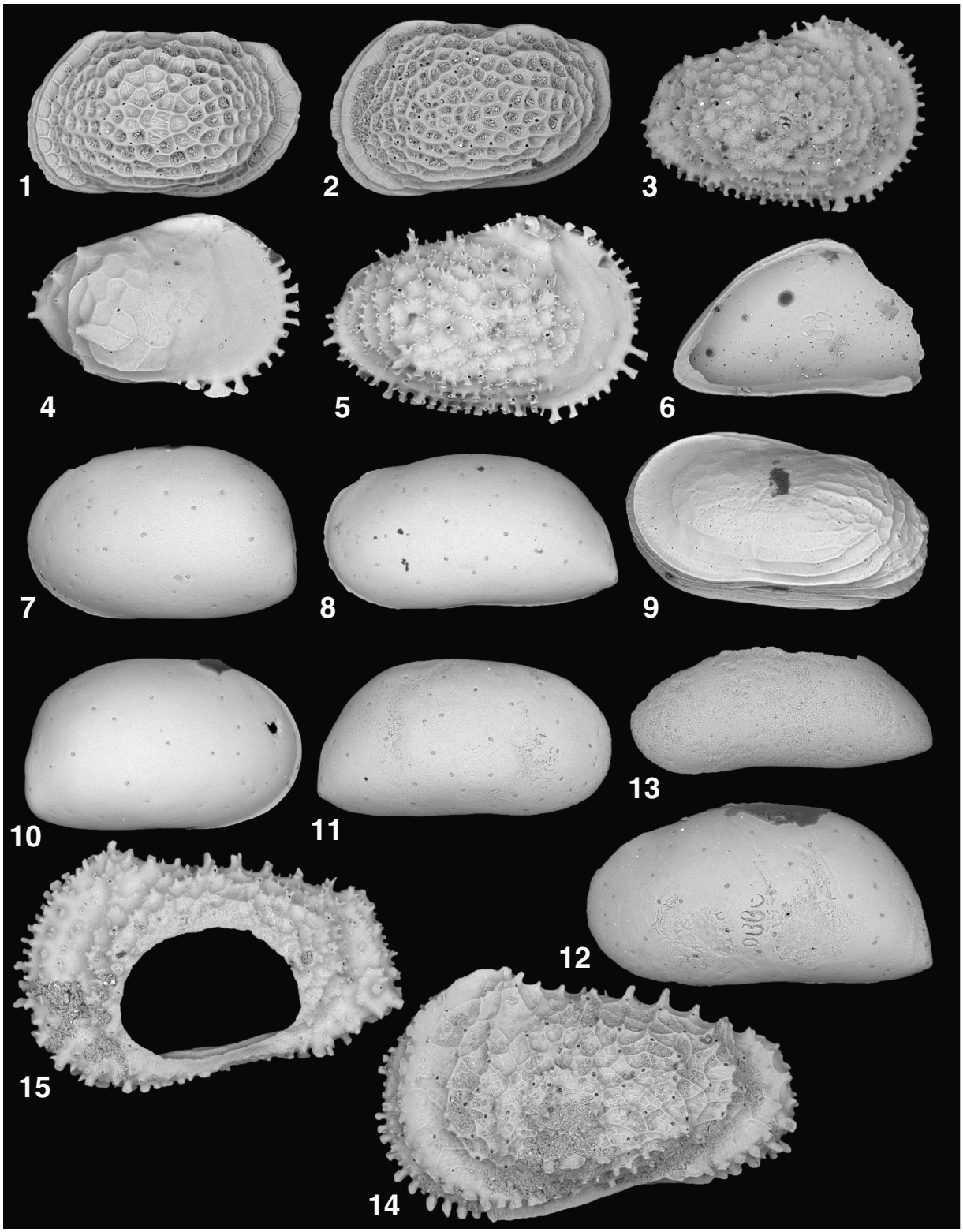

Figure F25. Calcareous and organically cemented, agglutinated foraminifers from Hole U1426A mudline sample. Scale bars = 100 µm. **1.** *Haplophragmoides sphaeriloculum*. **2, 3.** *Paratrochammina challengeri,* **4.** *Nummoloculina* sp. **5–7.** *Reophax scorpiurus* (stained specimens). **8–10.** *Hyperammina elongata* with attached test of *Paratrochammina challengeri* in life position (stained specimen). **11, 12.** *Hyperammina elongata* with attached test of *Cribrostomoides subglobosus* in life position (stained specimen). **13.** *Cassidulina japonica*. **14.** *Cassidulina teretis*. **15, 16.** *Trifarina angulosa*. **17, 18.** *Bolivina pacifica*. **19.** *Miliammina echigoensis*.

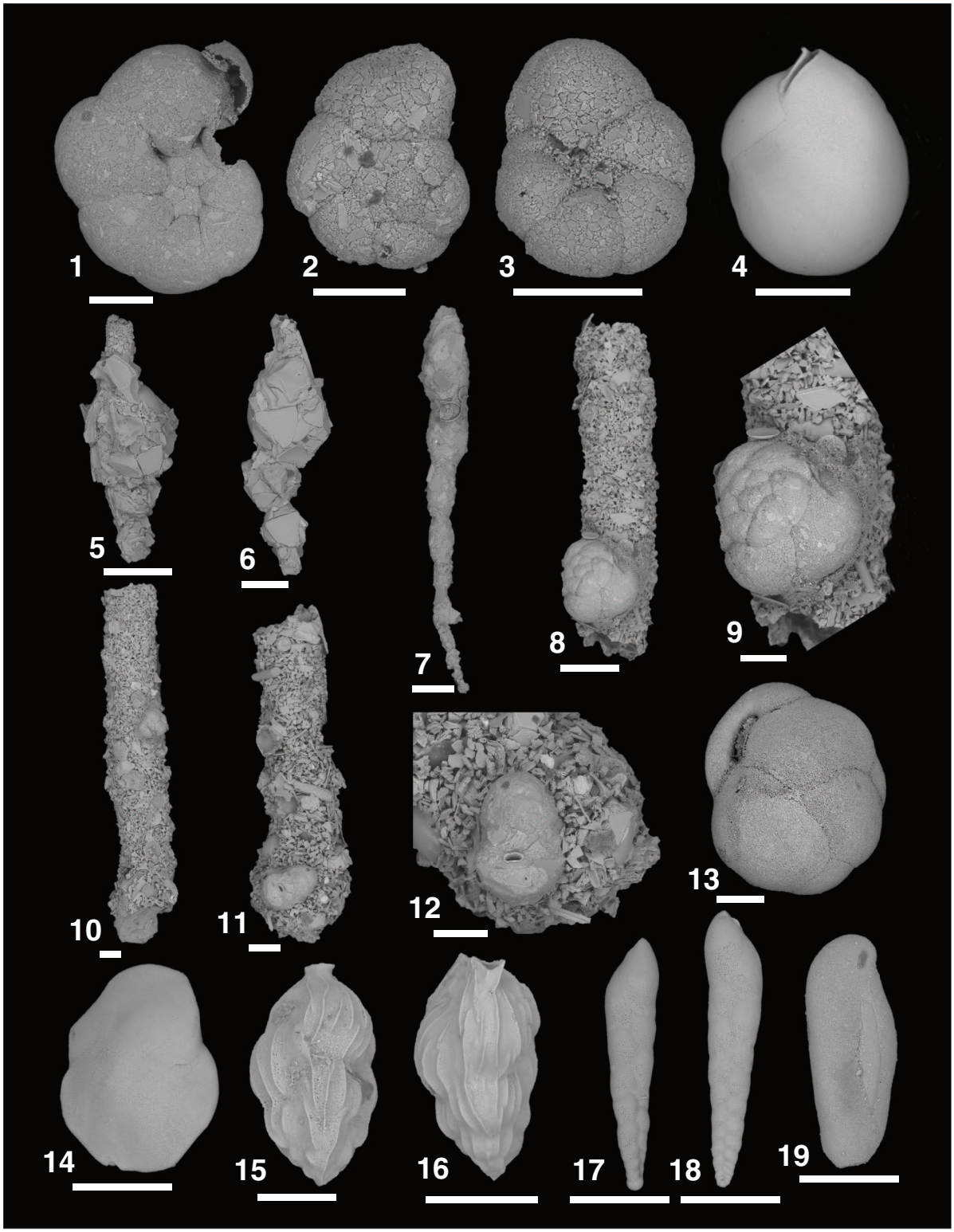

Figure F26. Overview of mudline benthic foraminiferal assemblage in slide. Scale bar = 50 µm. Note that live specimens are stained red with rose bengal.

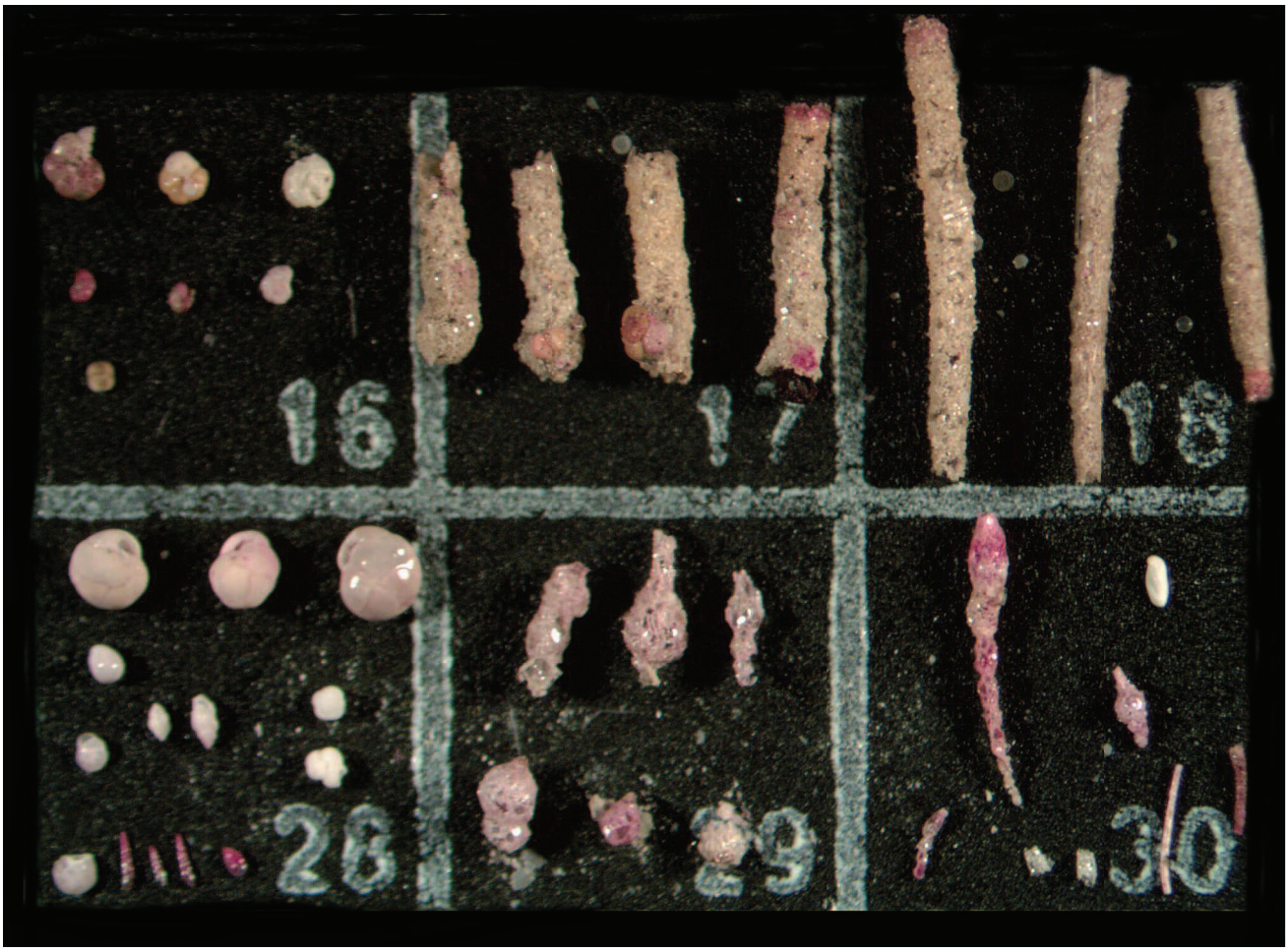

Figure F27. Conceptual diagram showing anaerobic oxidation of methane (AOM) in shallowly buried marine sediment and the impact on interstitial water chemistry (modified from Snyder et al., 2007). SMT = sulfate–methane transition.

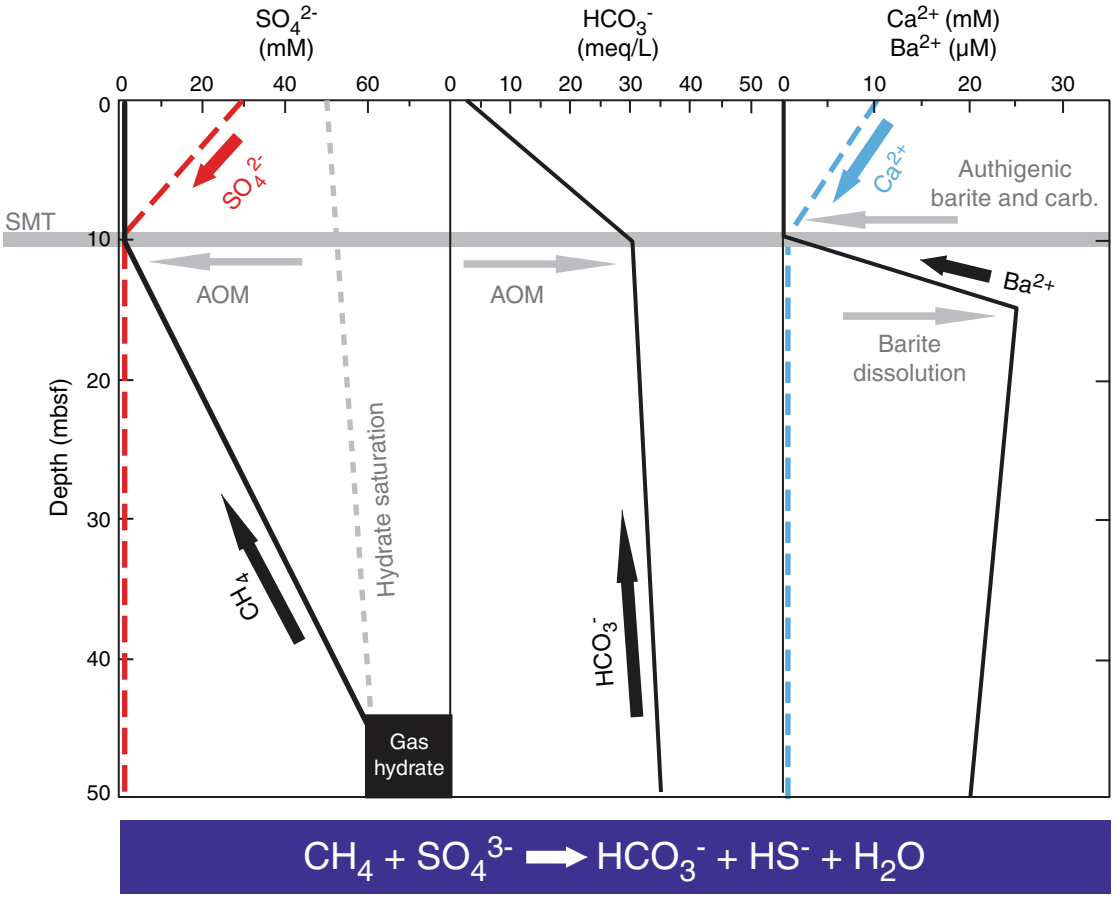

Figure F28. Solid-phase geochemistry of discrete sediment samples, Site U1426. TC = total carbon, TOC = total organic carbon, TN = total nitrogen.

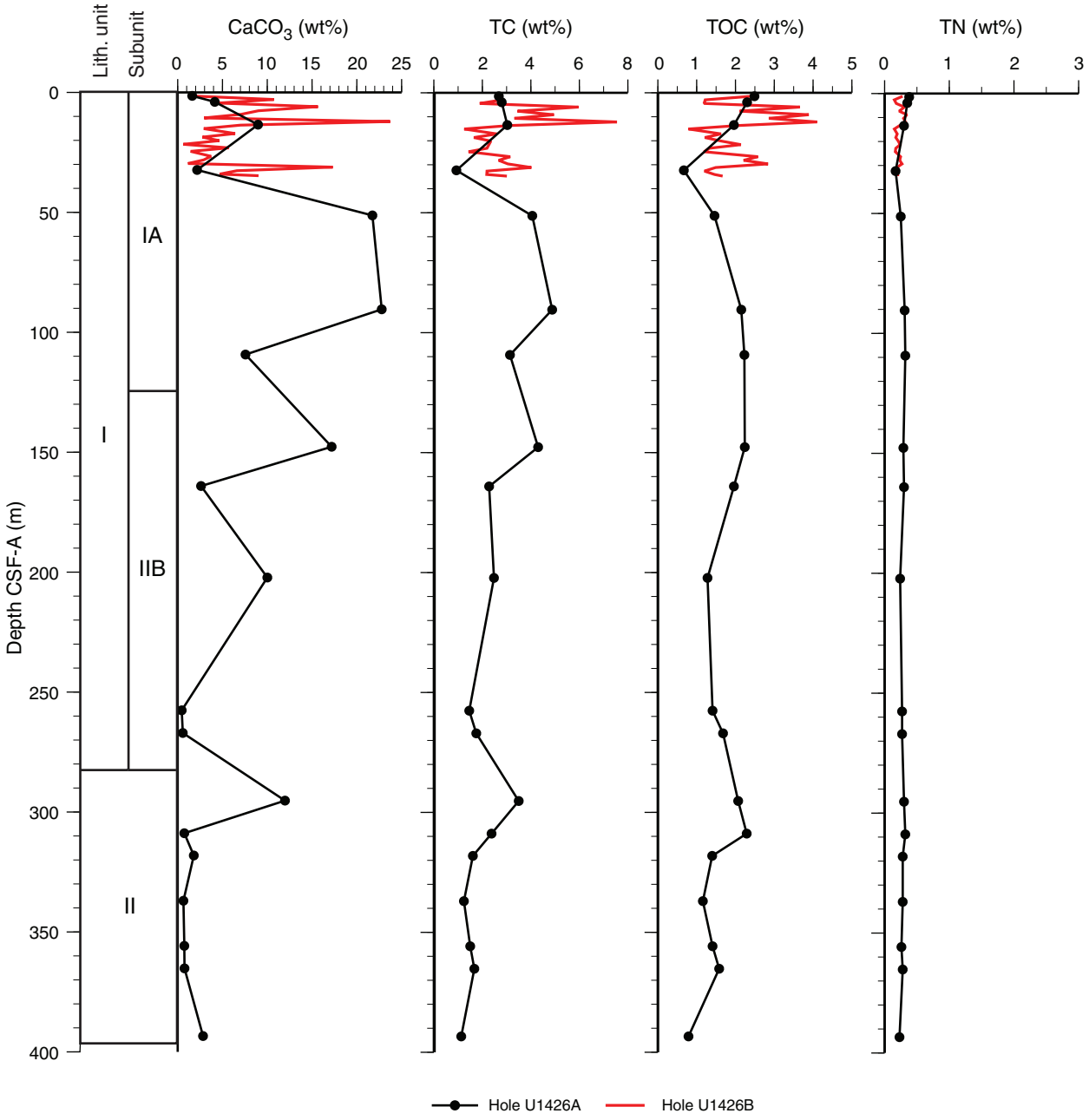

Figure F29. Dissolved Mn and Fe concentrations in squeezed interstitial water (IW-sq) and Rhizon samples, Hole U1426B. Magnetic susceptibility is plotted with Fe concentration for comparison.

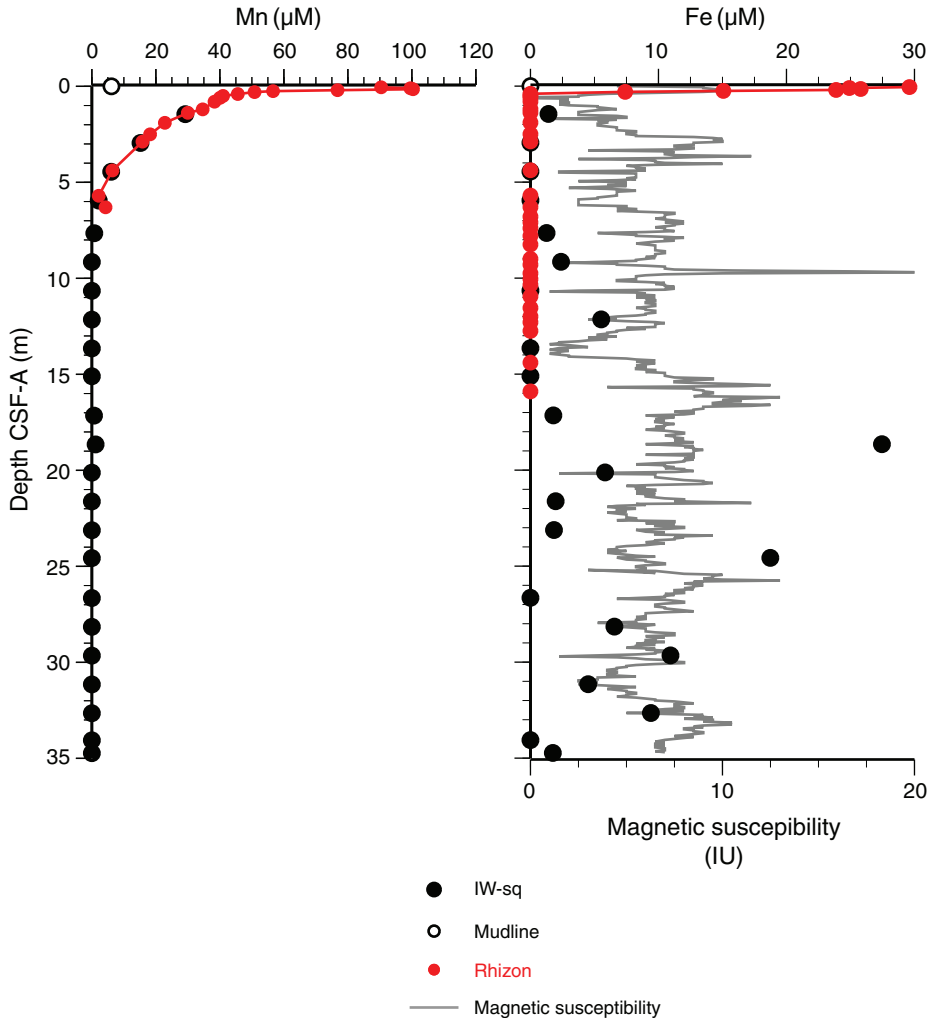

Figure F30. Dissolved alkalinity, ammonium, and phosphate concentrations with depth, Site U1426. IW-sq = squeezed interstitial water.

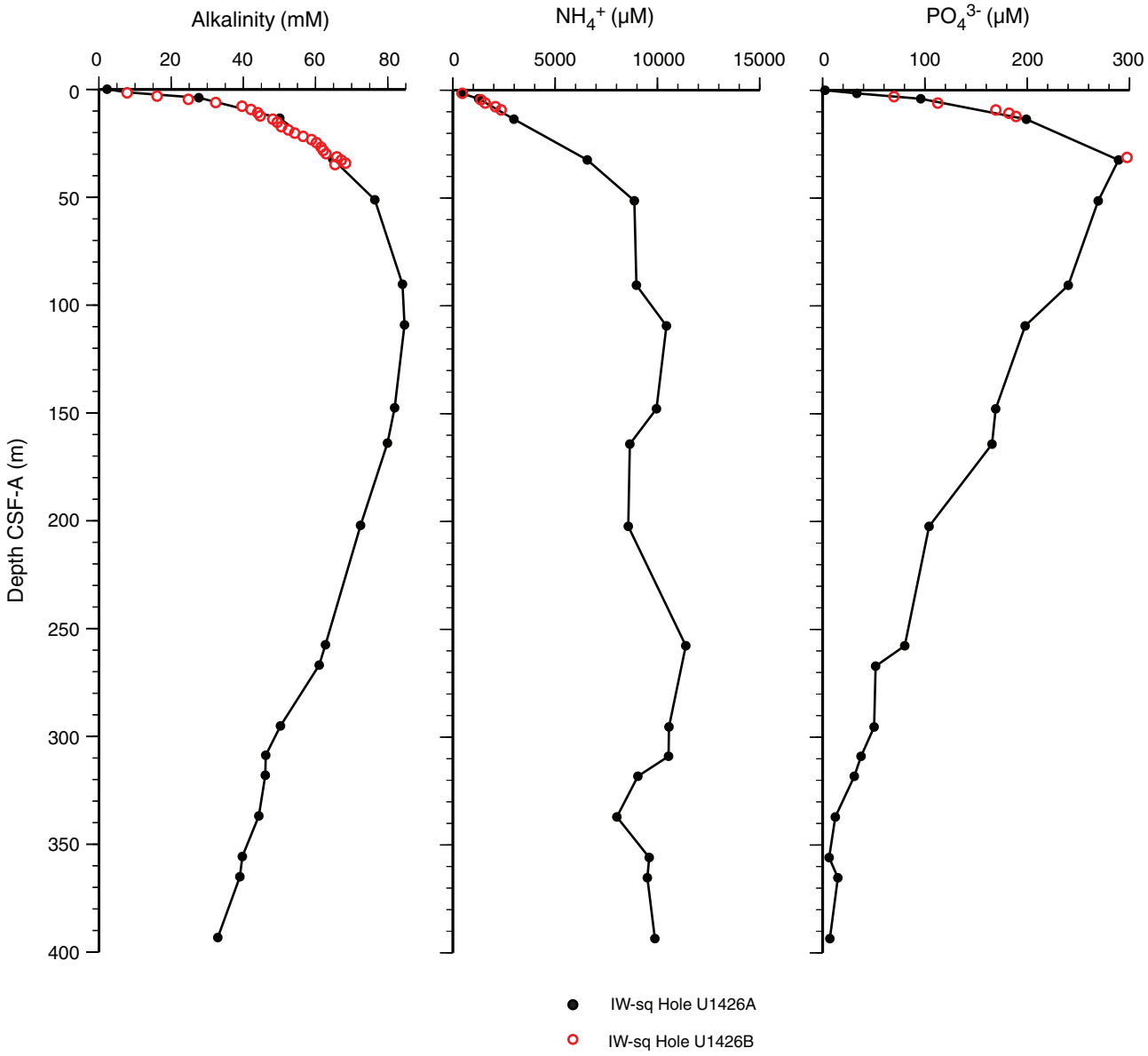

Figure F31. Dissolved alkalinity and ammonium concentrations in squeezed interstitial water (IW-sq) and Rhizon samples over the upper 15 m of sediment, Site U1426. Note the prominent inflection in alkalinity at ~7.9 m CSF-A (~8.5 m CCSF-A).

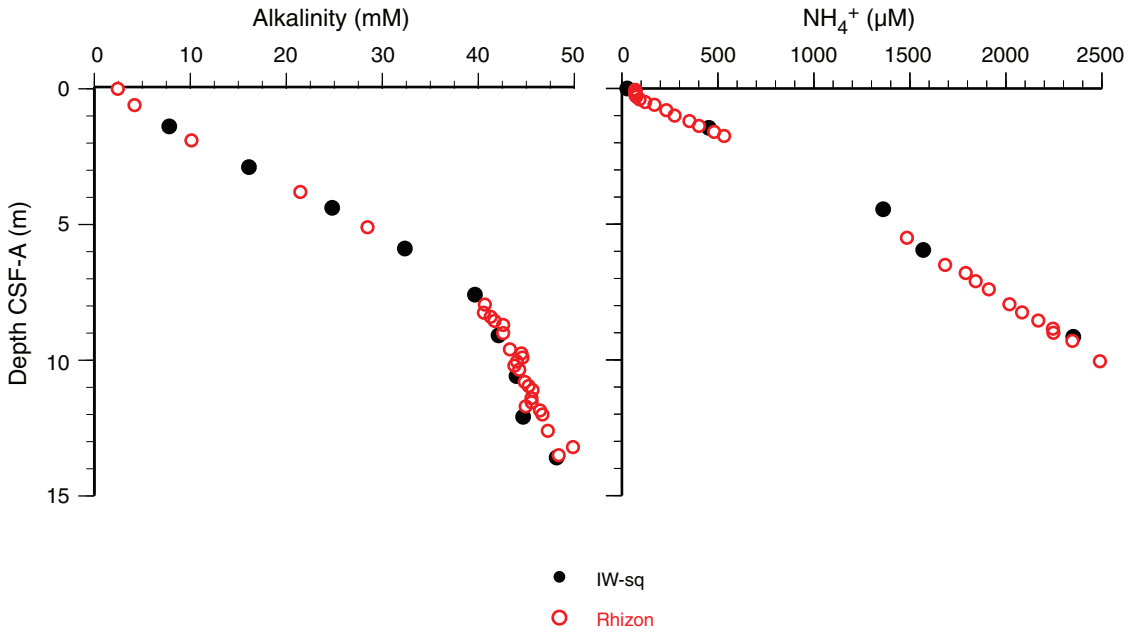

Figure F32. A. Headspace CH_4 concentrations at Site U1426 with Sites U1422–U1425 for comparison. Note that values are not meaningful in terms of in situ concentration at depths where CH_4 concentration surpasses saturation at 1 atm pressure. **B.** C_1/C_2 ratio from headspace samples at Site U1426.

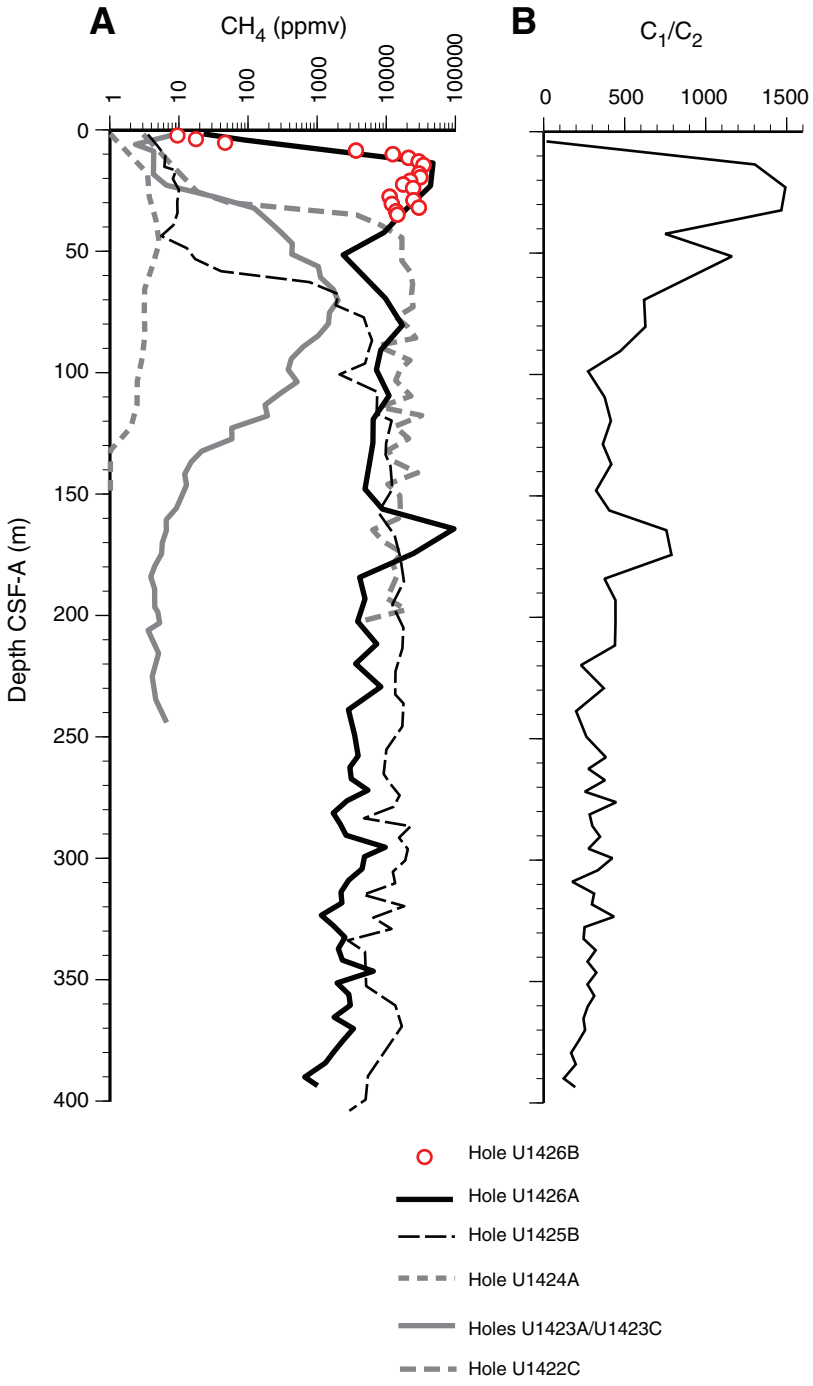

Figure F33. Sulfur chemistry of interstitial water samples across the upper 40 m, Site U1426. **A.** Sulfate concentrations from squeezed interstitial water (IW-sq) and Rhizon samples along with headspace CH_4 concentration. **B.** HS^- concentrations from squeeze and Rhizon samples along with headspace CH_4 concentrations. Note that CH_4 values are not meaningful at depths where CH_4 surpasses saturation at 1 atm pressure.

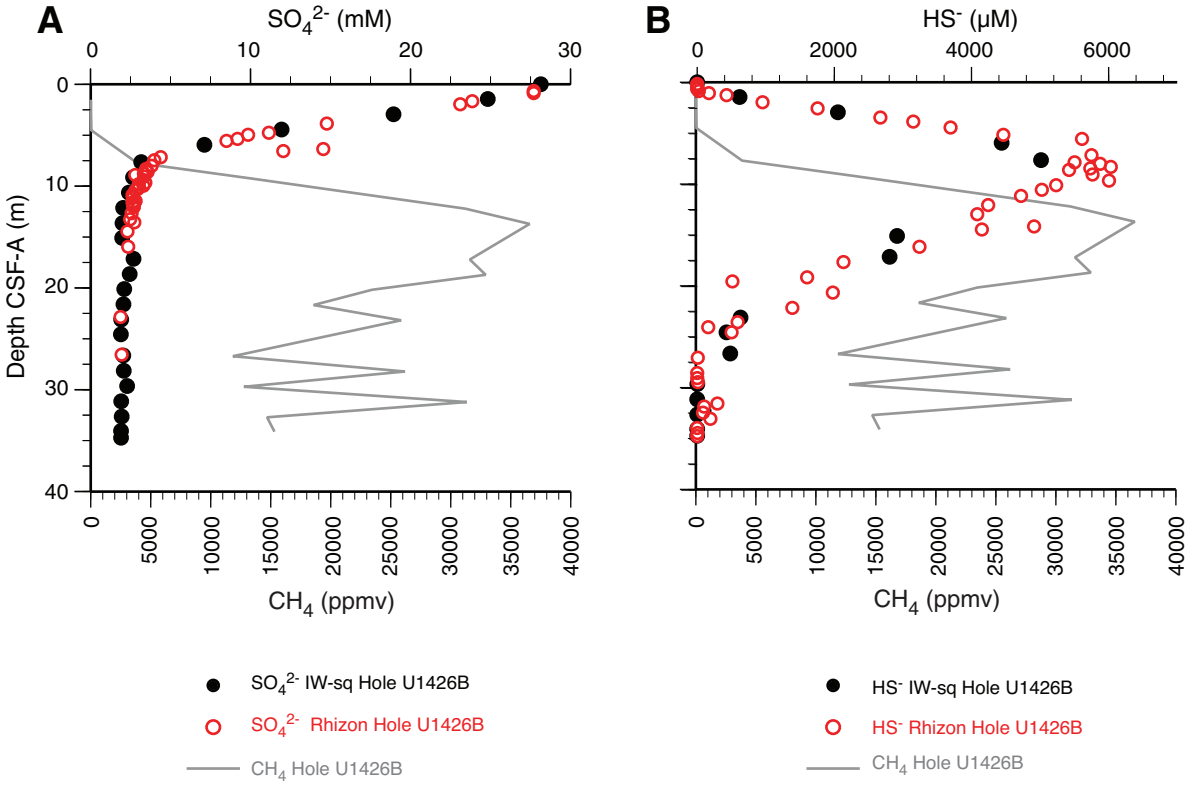

Figure F34. Dissolved Ba concentrations over the upper 40 m of sediment, Site U1426. IW-sq = squeezed interstitial water.

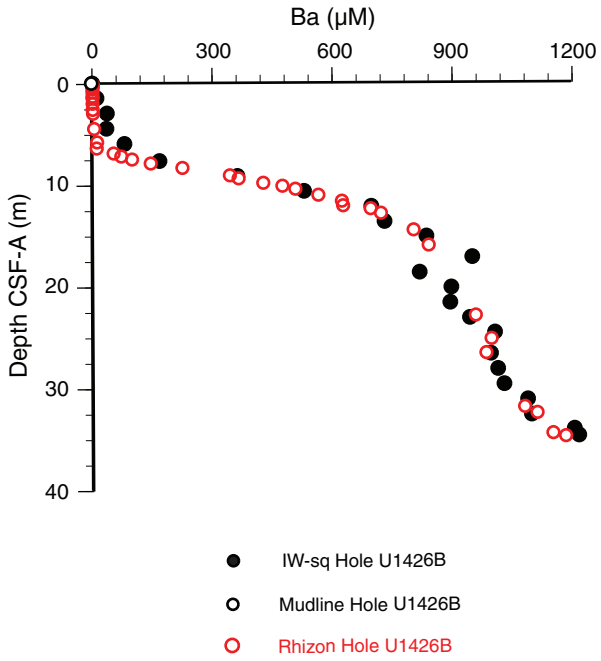

Figure F35. Dissolved Br^- concentrations over the entire sediment column, Site U1426. IW-sq = squeezed interstitial water.

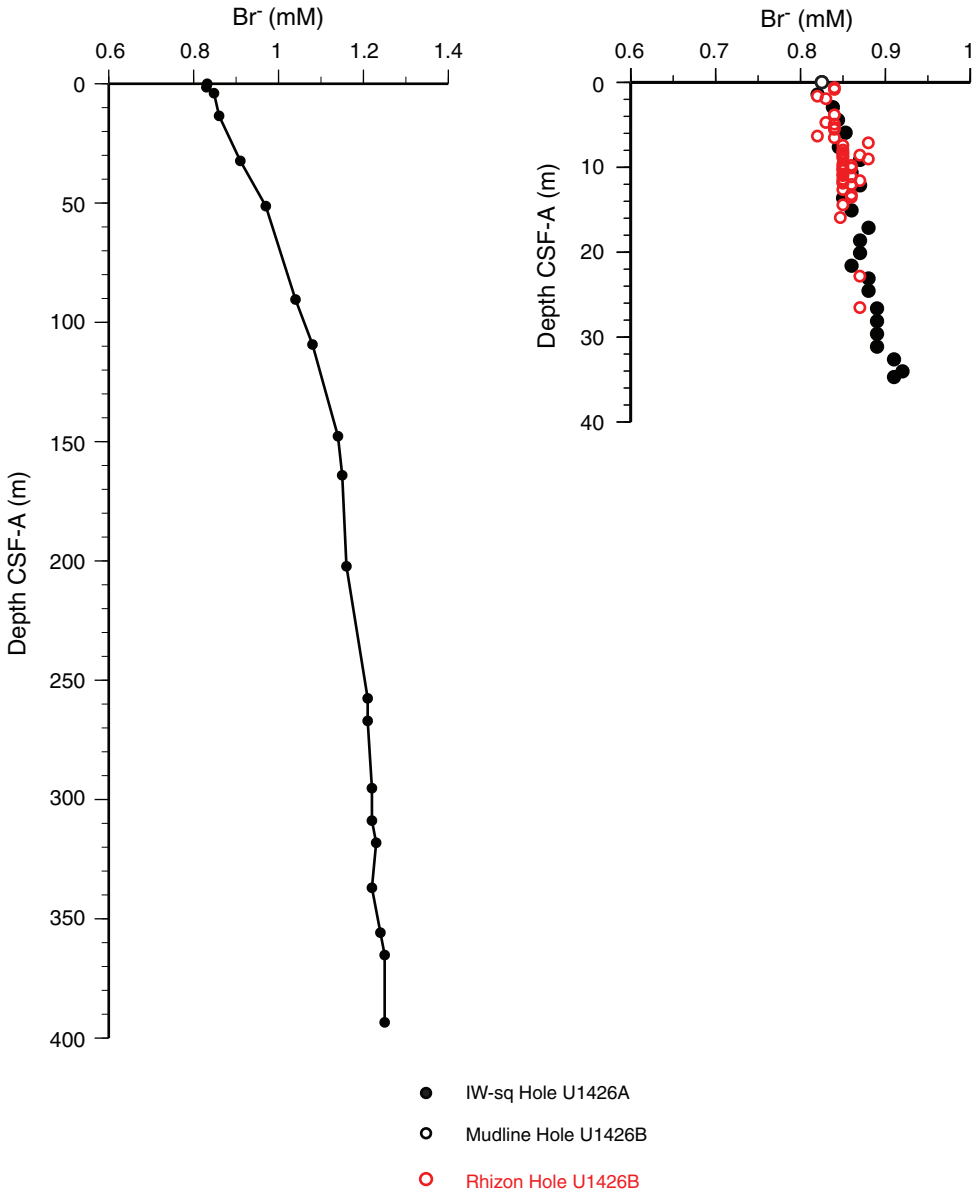

Figure F36. Absorbance of interstitial water at Site U1426 at two different wavelengths. IW-sq = squeezed interstitial water.

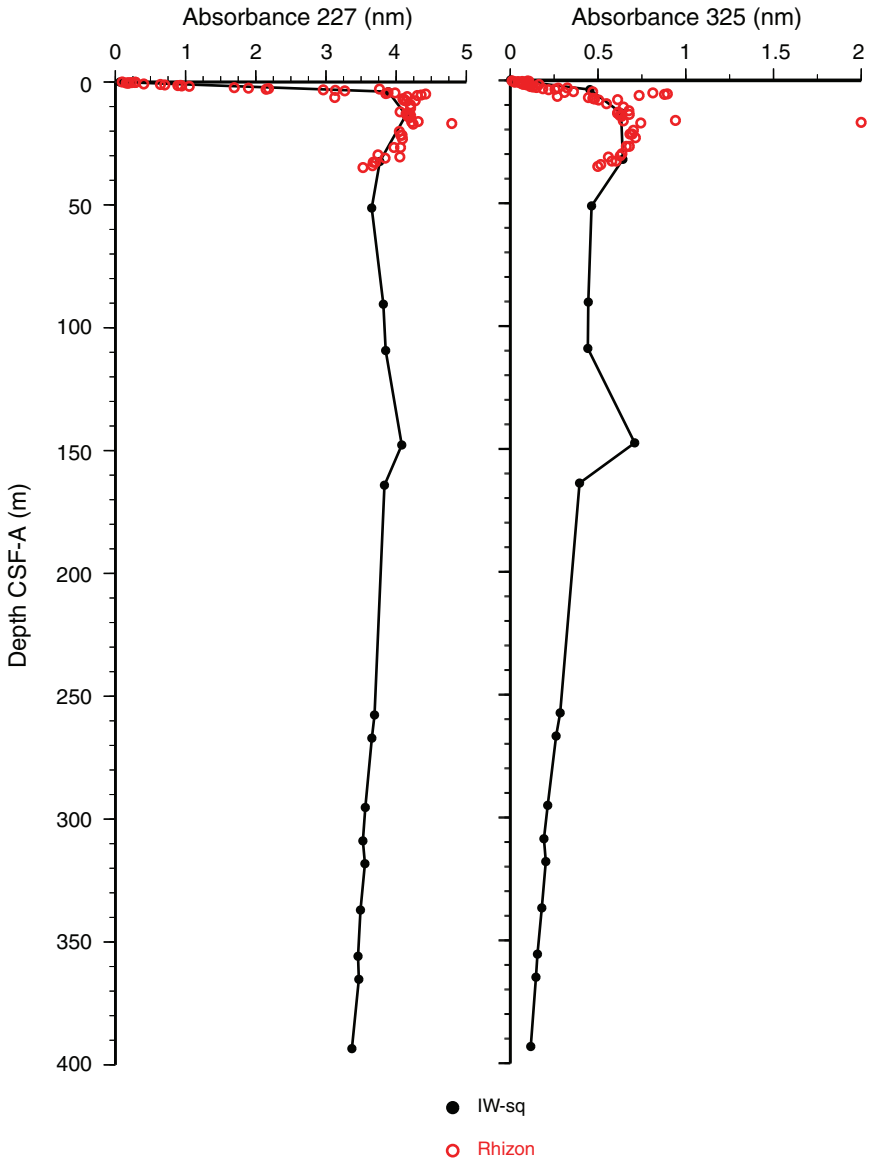

Figure F37. Dissolved calcium and magnesium profiles across the full depth, Site U1426.

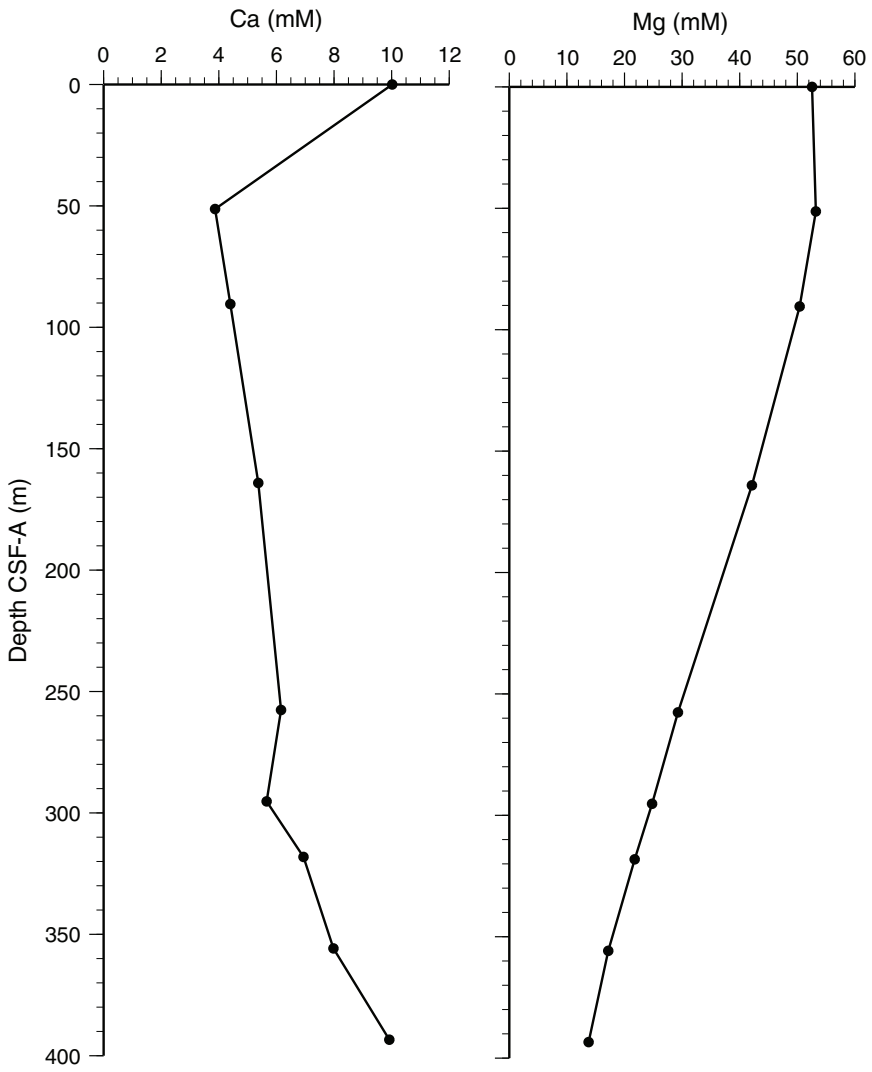

Figure F38. Dissolved calcium, magnesium, and strontium profiles over the upper 40 m depth, Site U1426. IW-sq = squeezed interstitial water.

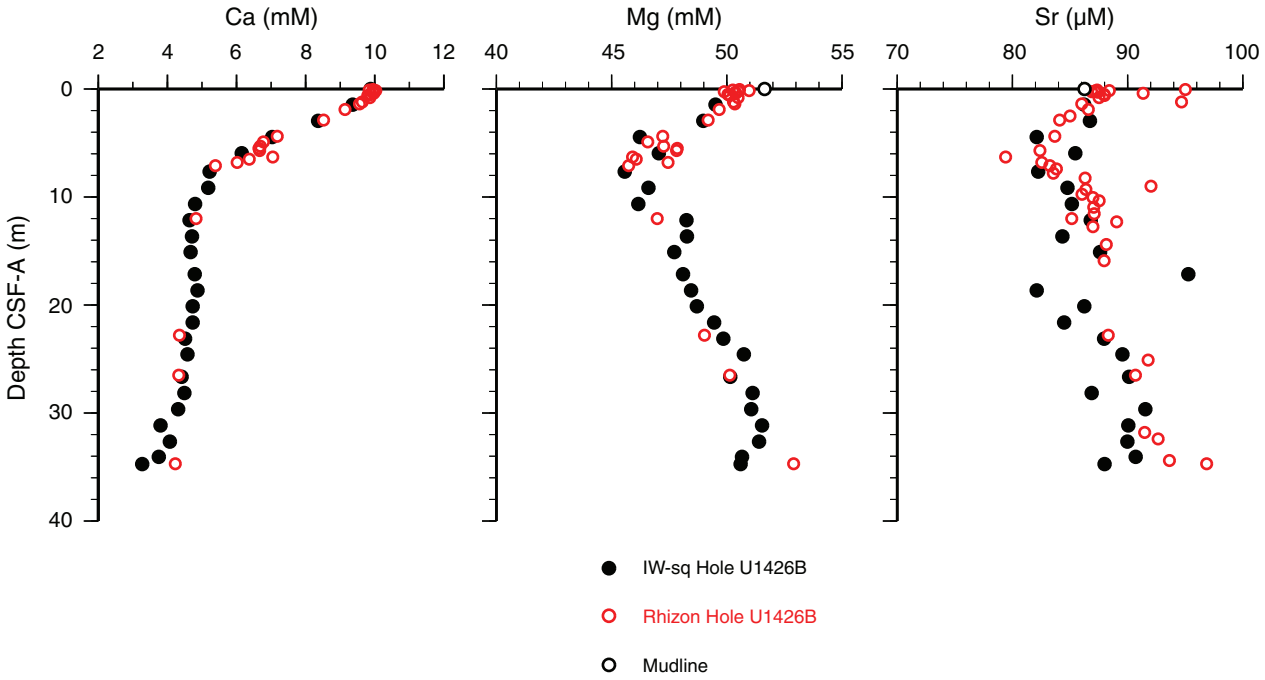

Figure F39. Dissolved chloride, sodium, and potassium concentrations across the full depth, Site U1426.

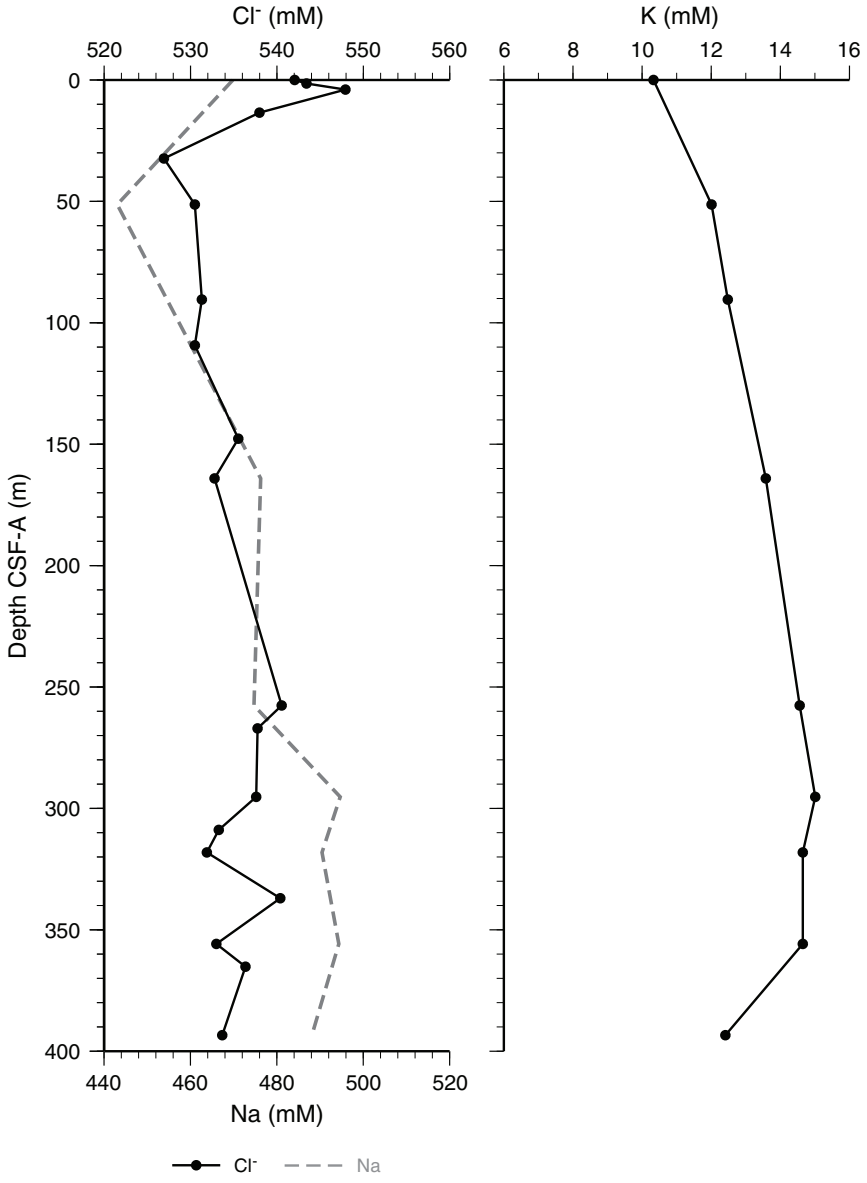

Figure F40. Dissolved boron, lithium, and silica profiles over upper 40 m depth, Site U1426. IW-sq = squeezed interstitial water.

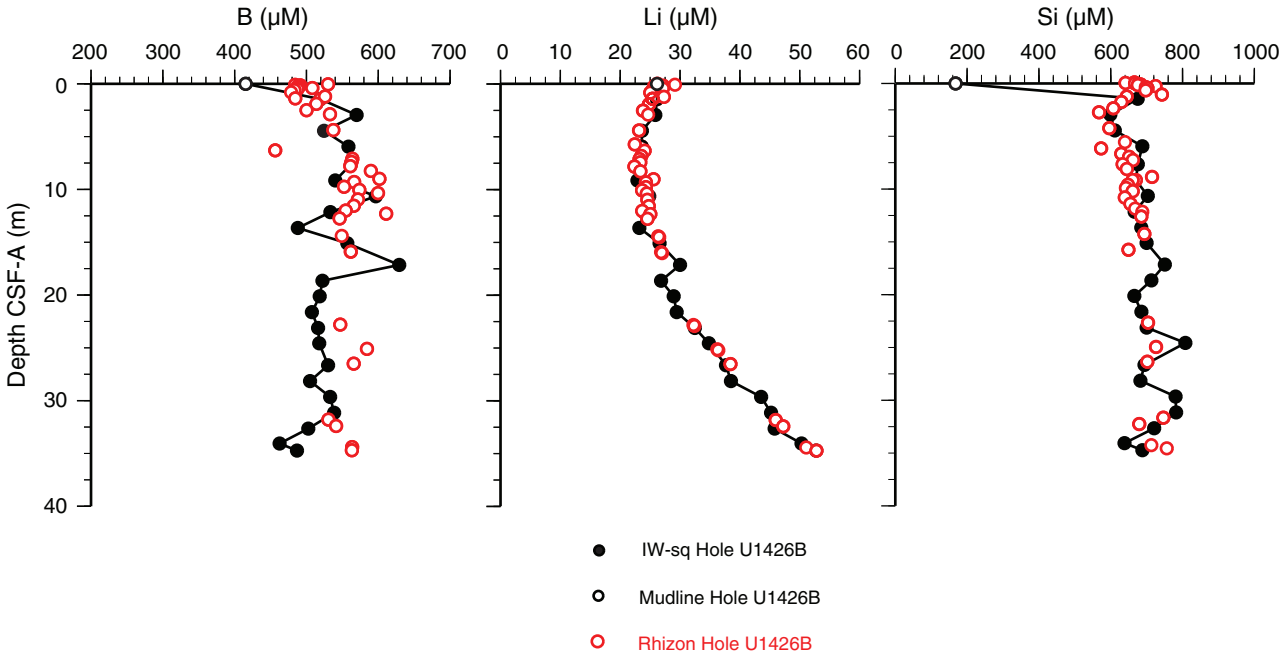

Figure F41. Paleomagnetism after 20 mT AF demagnetization, Site U1426. Chron column: black = normal polarity, white = reversed polarity, gray = zones or polarity boundaries without clear magnetostratigraphic interpretation. Inclination column: thin black dashed lines = expected geocentric axial dipole inclinations at the site latitude during reversed (left) and normal (right) polarities, triangles along the left side mark depths where discrete paleomagnetic cube samples were collected (orange = discrete samples measured during the expedition). Declination column: gray dots = measured declination values, green dots = declination values corrected using core orientation data collected by the FlexIT tool. Susceptibility column: magenta dots = SHMSL measured values, gray dots = WRMSL measured values. **A.** Hole U1426A shallower than 200 m CSF-A. (Continued on next four pages.)

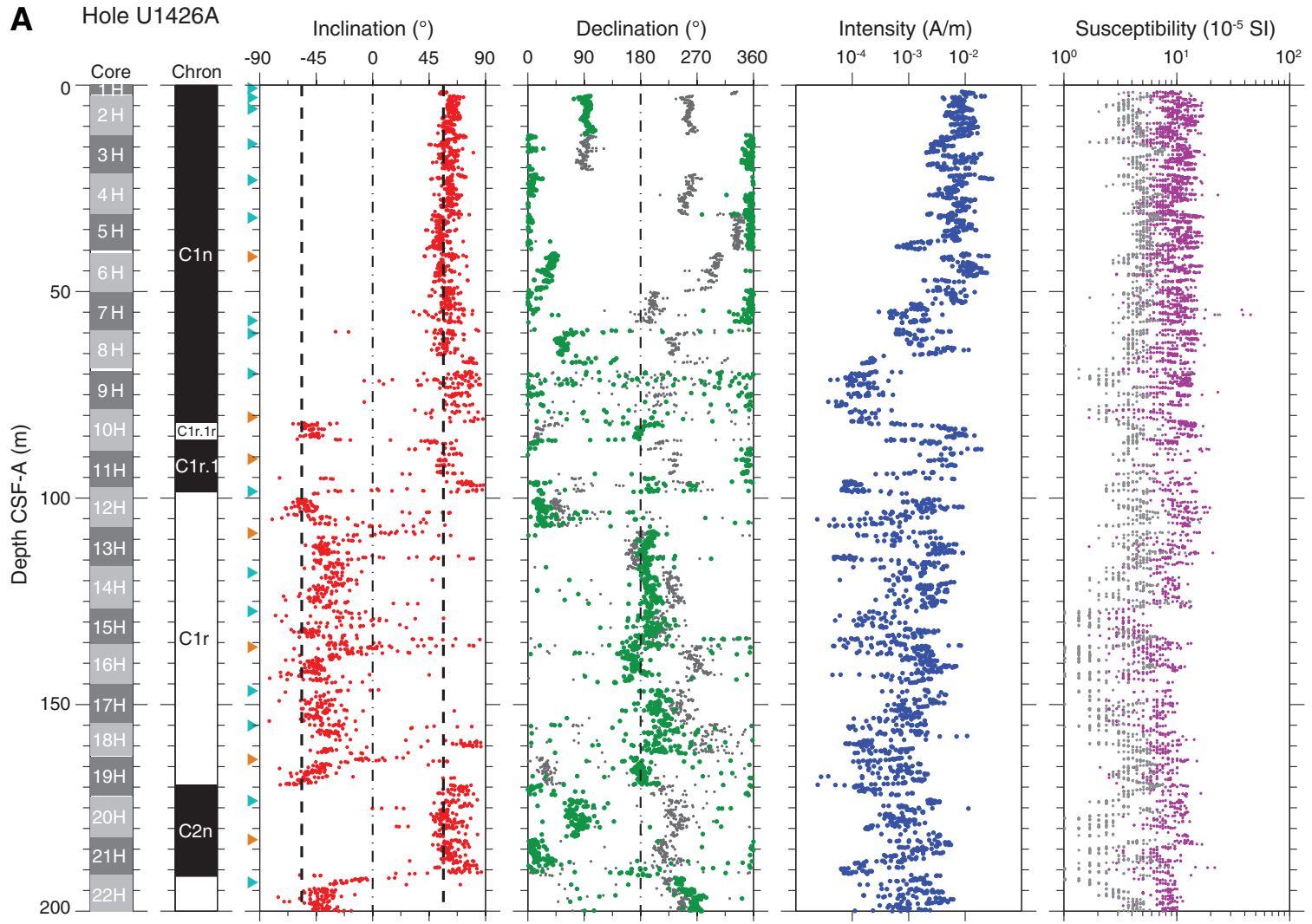

Figure F41 (continued). B. Hole U1426A deeper than 200 m CSF-A. (Continued on next page.)

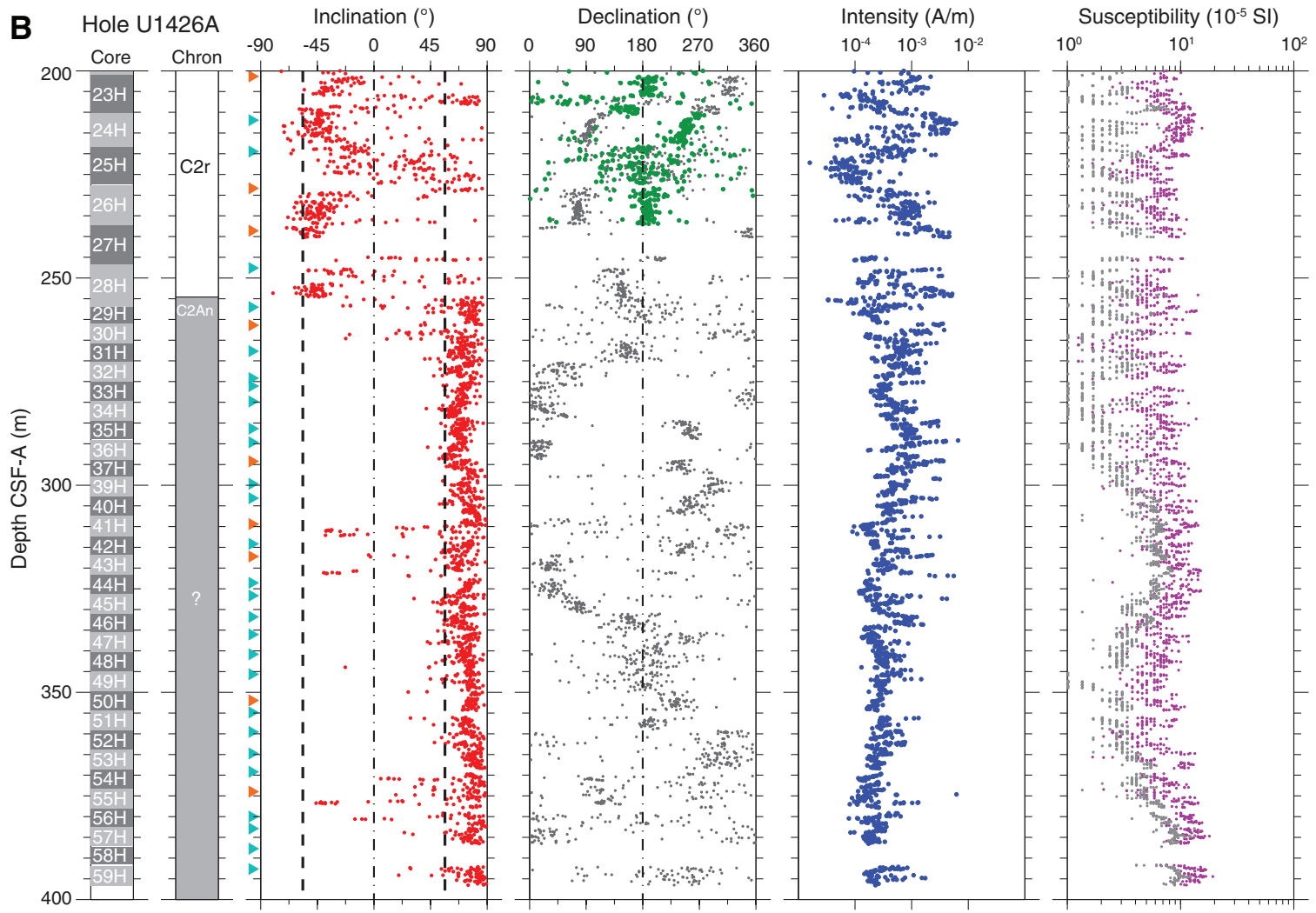

Figure F41 (continued). C. Hole U1426B. (Continued on next page.)

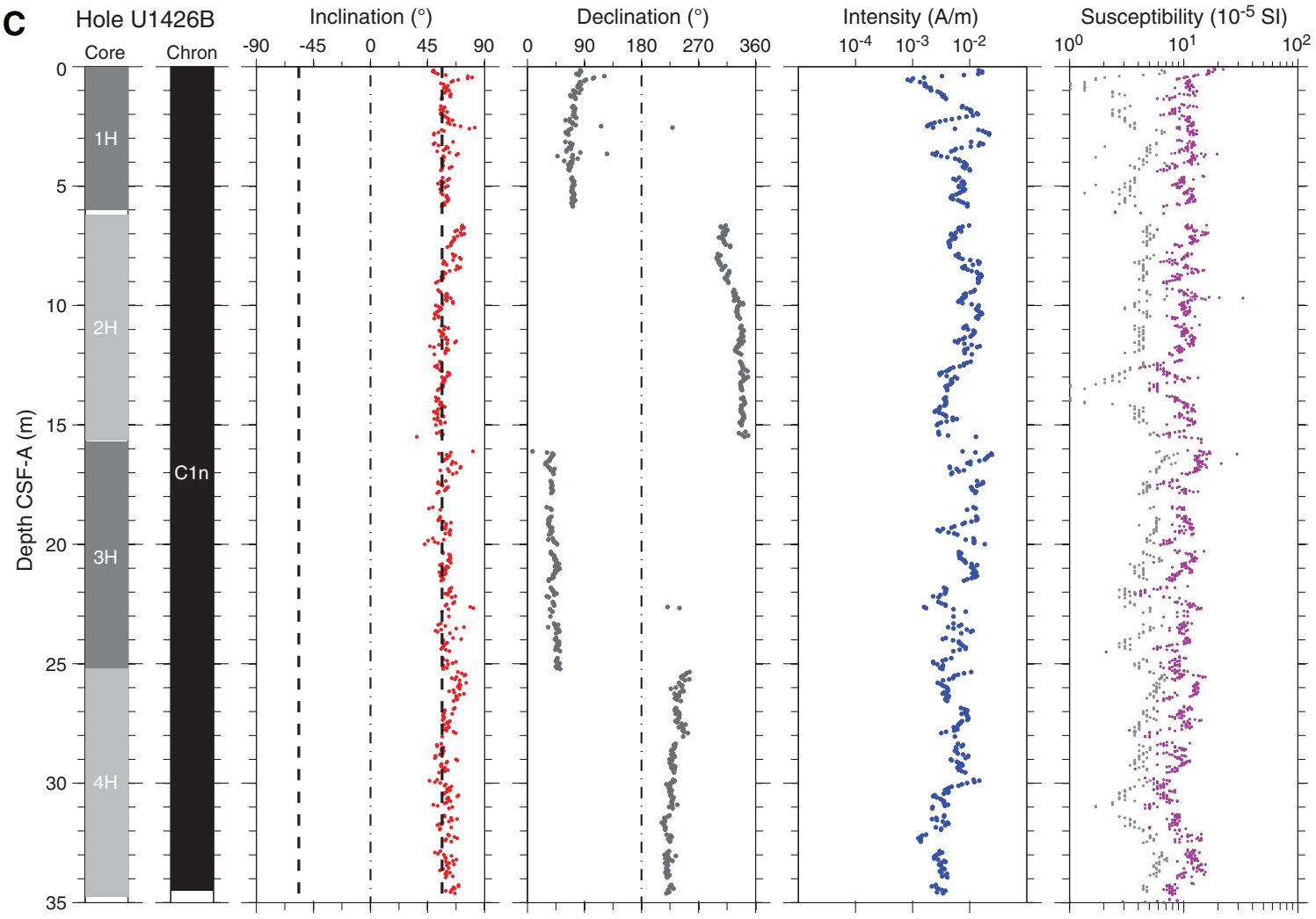

Figure F41 (continued). D. Hole U1426C. (Continued on next page.)

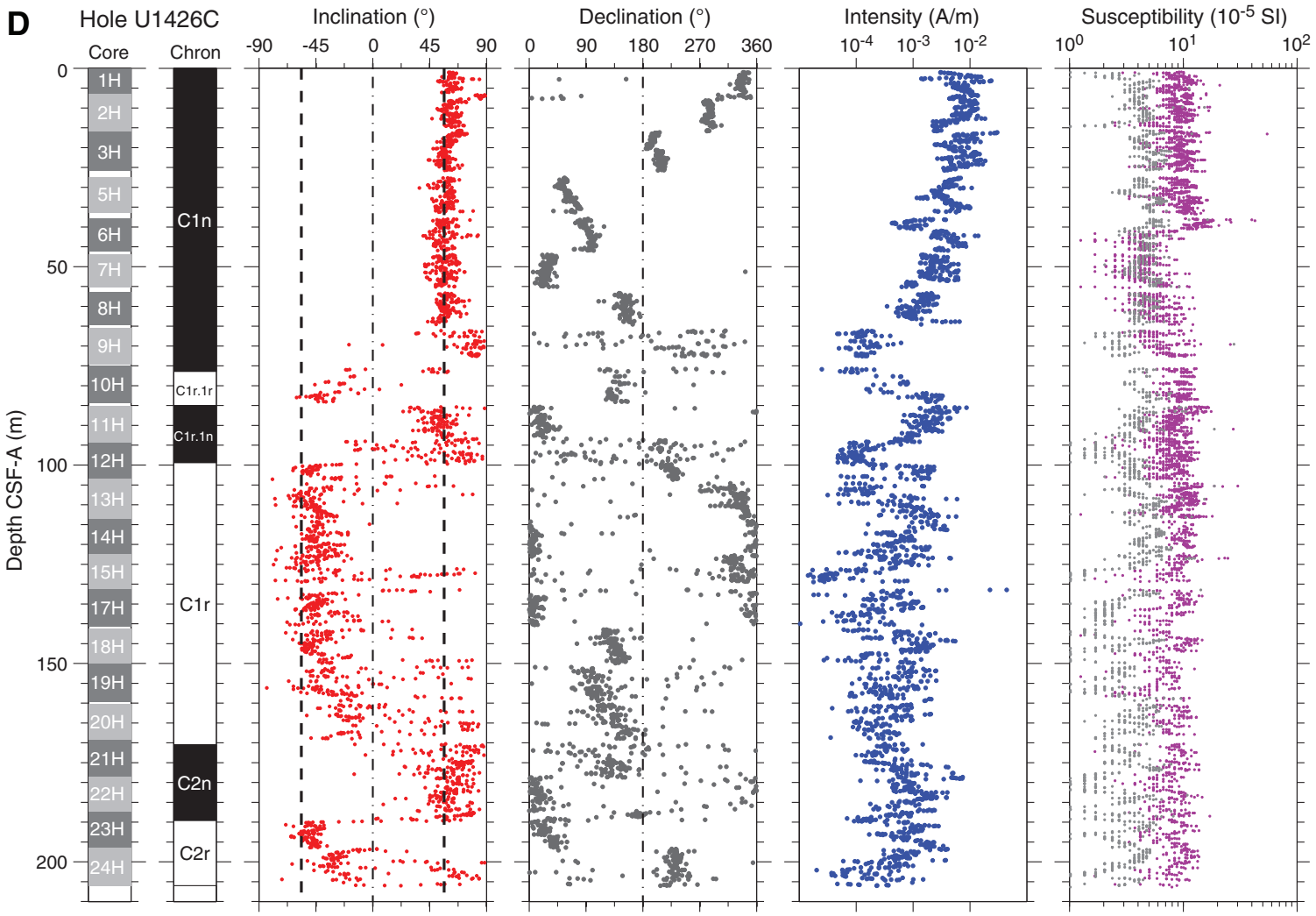

Figure F41 (continued). E. Hole U1426D.

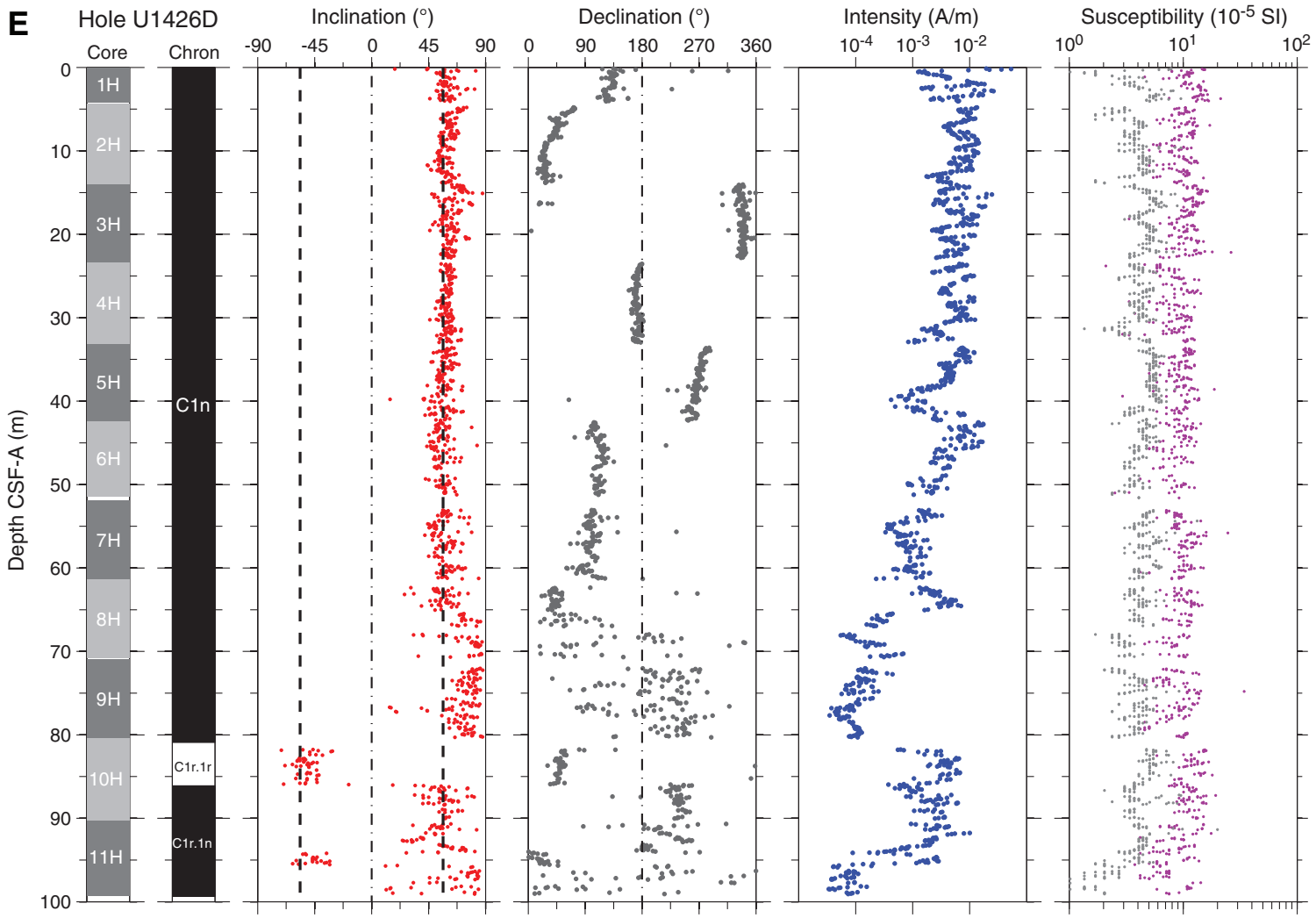

Figure F42. A–H. AF demagnetization results for discrete samples, Site U1426. For each sample, the left plot shows the intensity variation with progressive demagnetization. The middle and right plots show the NRM vector measured after each demagnetization treatment on an orthogonal projection (Zijderveld) and on an equal area projection respectively. In the orthogonal projection plot, squares = horizontal projections, circles = vertical projections. In the equal area projection plot, closed circles = projection data with positive inclinations, open circles = projection data with negative inclinations. Note that on the orthogonal projection (Zijderveld) plot, NRM data before demagnetization have been removed to better display the demagnetized data. (Continued on next page.)

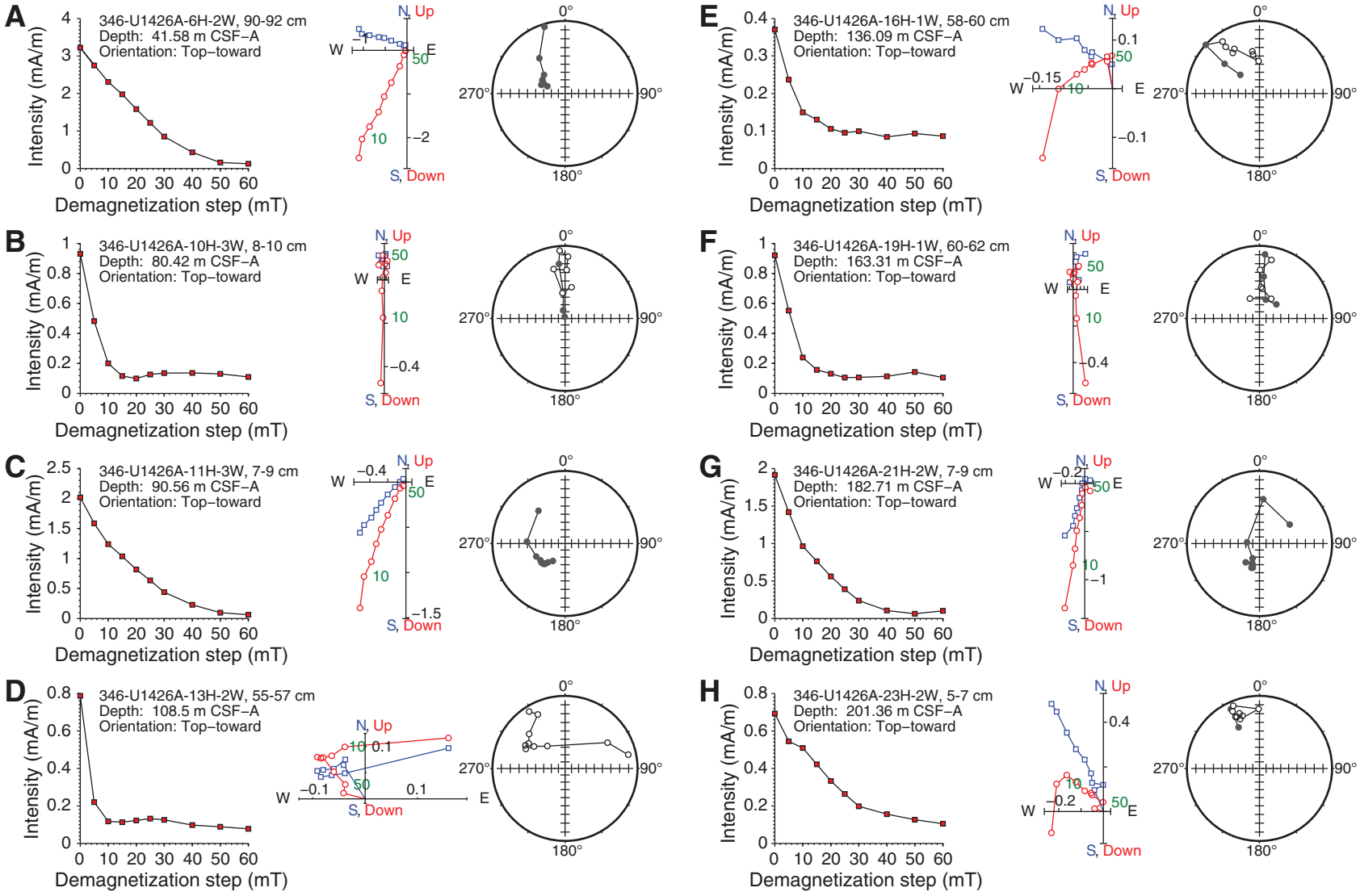

Figure F42 (continued). I–P.

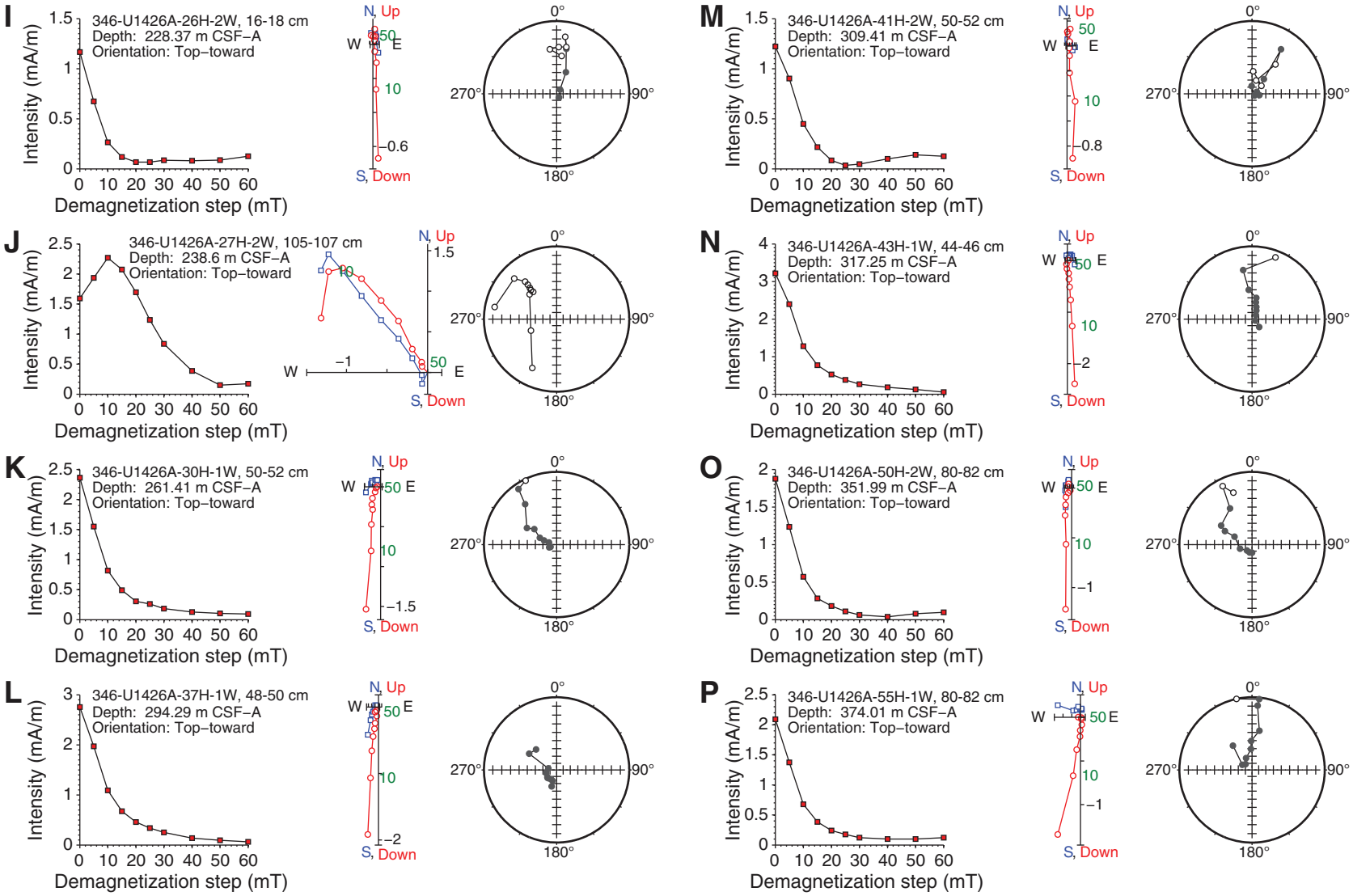

Figure F43. Suite of physical properties measured in Hole U1426A. The first magnetic susceptibility panel shows WRMSL data, whereas the second panel shows point SHMSL data. WRMSL data are shown in gamma ray attenuation (GRA) bulk density and *P*-wave velocity panels. Dashed horizontal line = lithologic subunit boundary, solid horizontal line = lithologic unit boundary. NGR = natural gamma radiation.

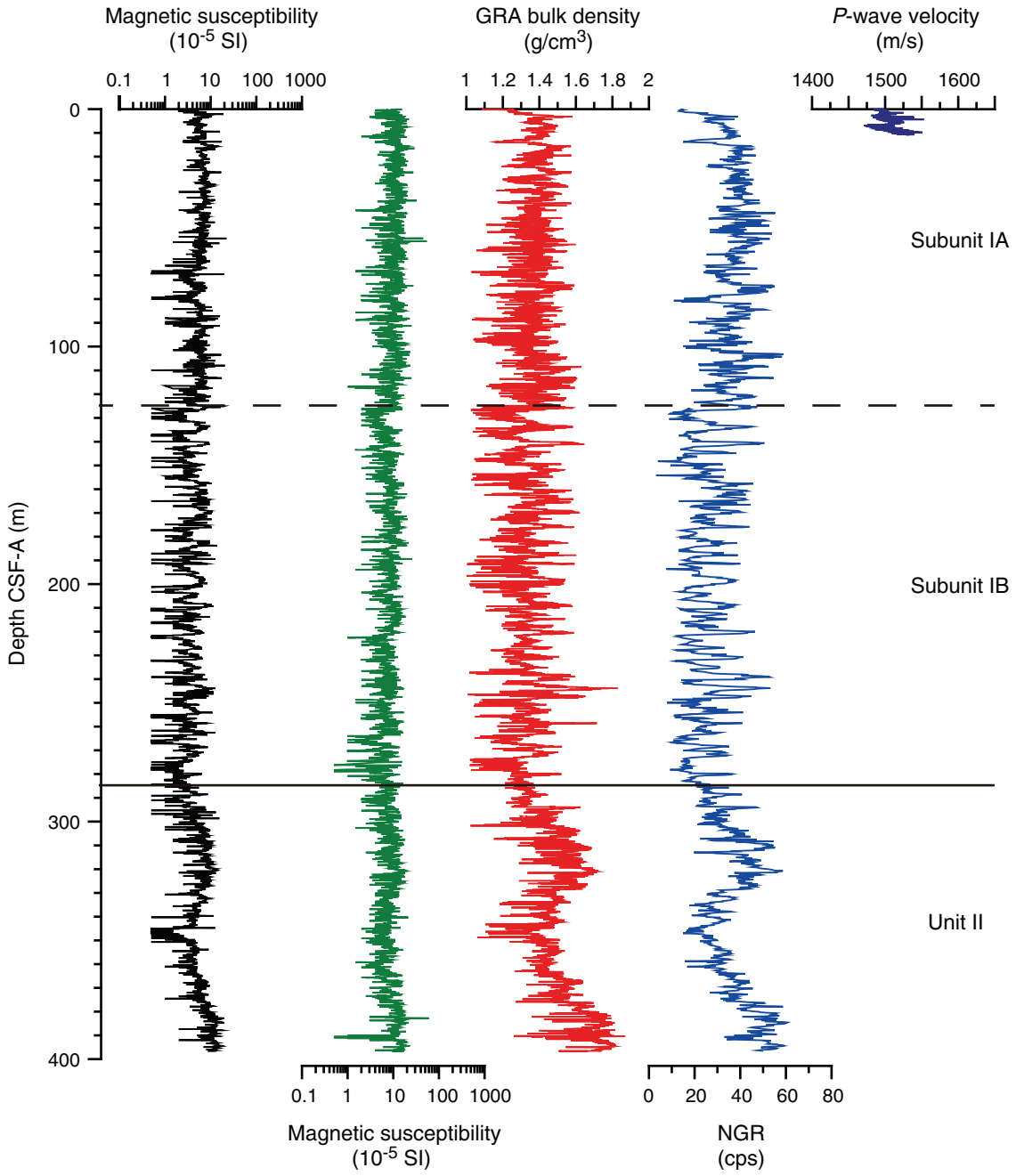

Figure F44. Discrete bulk density, grain density, porosity, water content, and shear strength, Site U1426. Dashed horizontal line = lithologic subunit boundary, solid horizontal line = lithologic unit boundary.

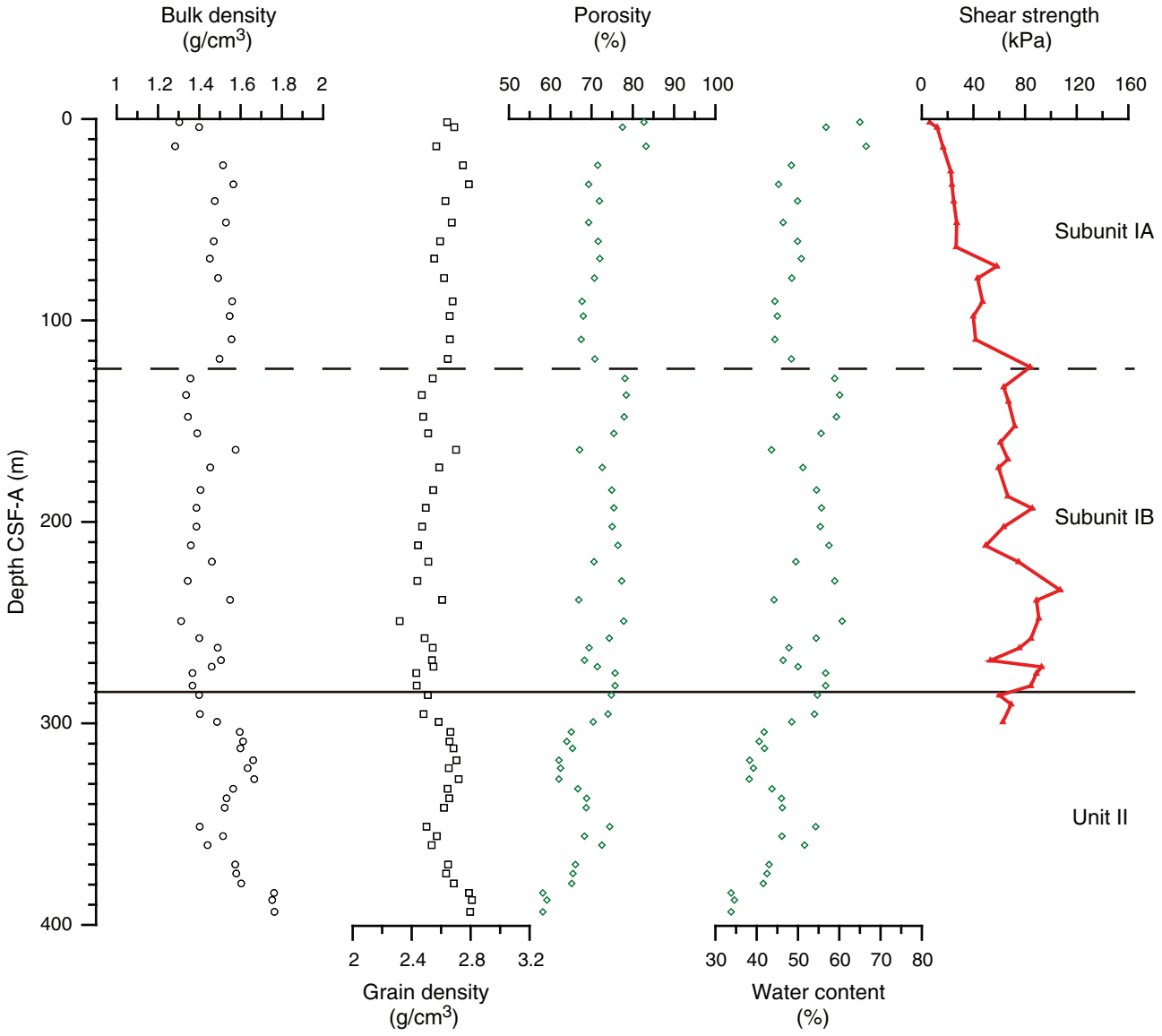

Figure F45. Relationship between GRA bulk density (red), discrete bulk density (black), grain density, natural gamma radiation (NGR), smear slide pyrite abundance (TR = trace, R = rare, C = common, A = abundant, D = dominant), X-ray diffraction (XRD) pyrite counts, and XRD opal-A counts. Shaded blue areas indicate clay-rich sediment interval and remains are biogenic component–rich sediment intervals.

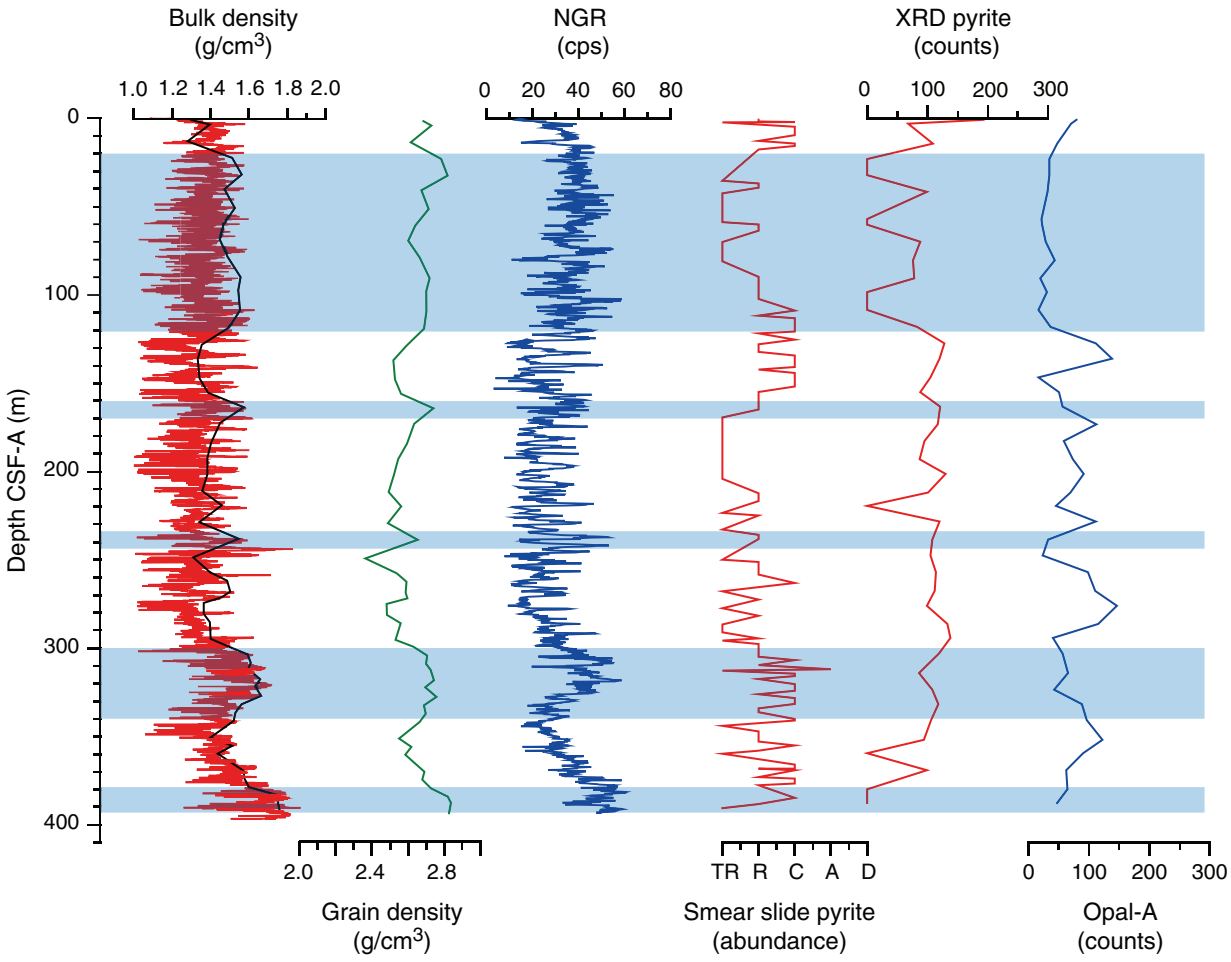

Figure F46. Comparison of low-resolution MAD data (squares) in Hole U1426A with high-resolution MAD data (lines) in Hole U1426B in the upper 35 m CSF-A.

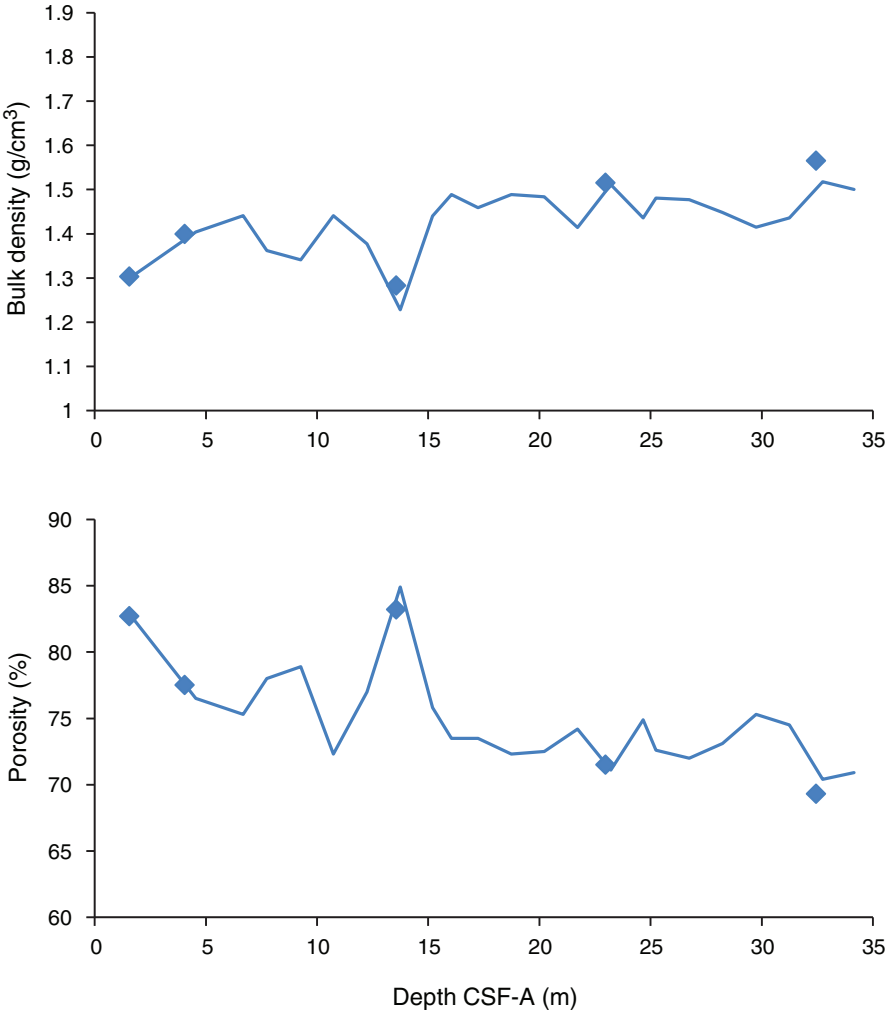

Figure F47. Color reflectance data, Hole U1426A. Dashed horizontal line = lithologic subunit boundary, solid horizontal line = lithologic unit boundary.

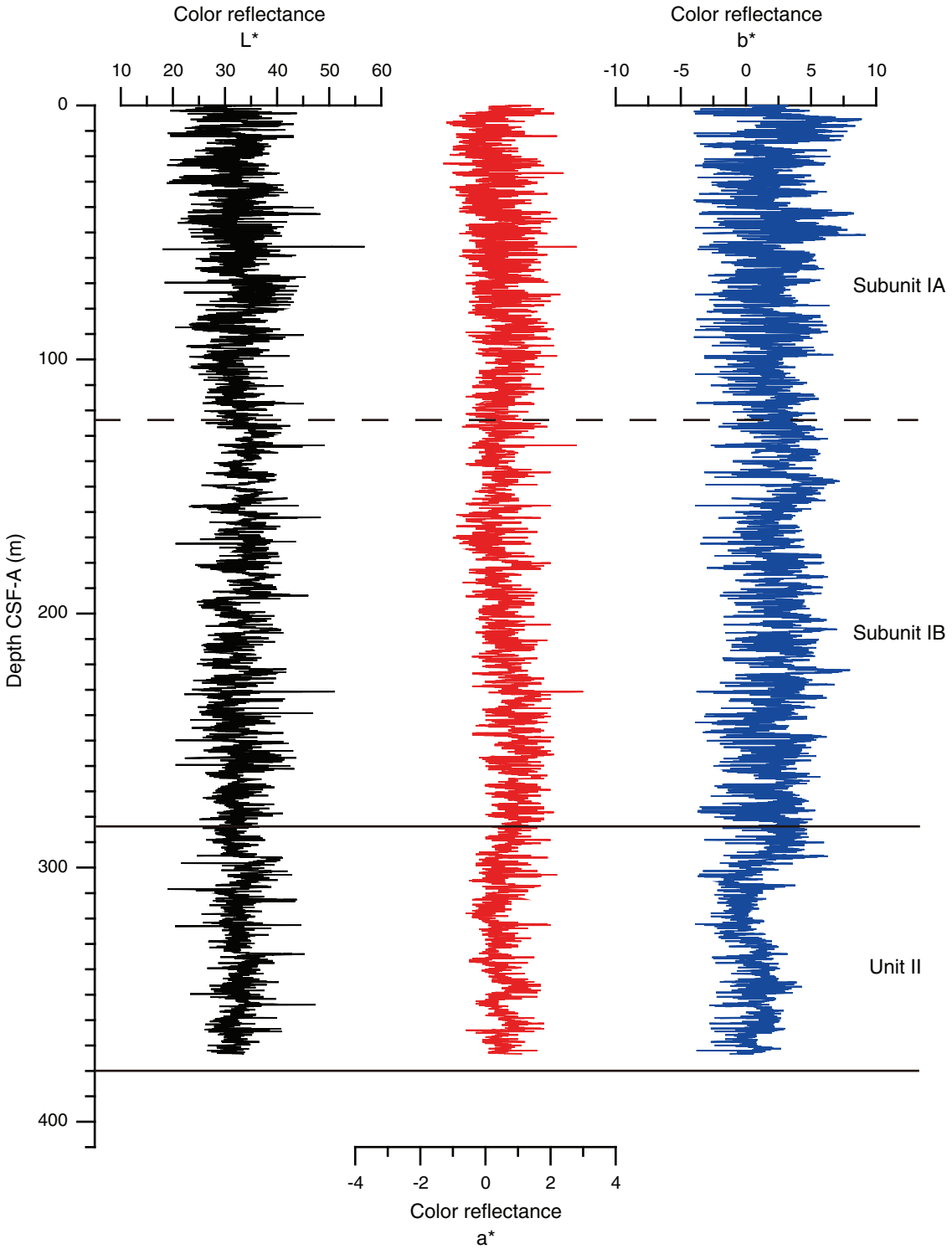

Figure F48. Color reflectance data comparison between Sites U1425 (deeper water depth) and U1426 in L*-a* and a*-b* color spaces. Average L* for each site is depicted by lines in upper panels.

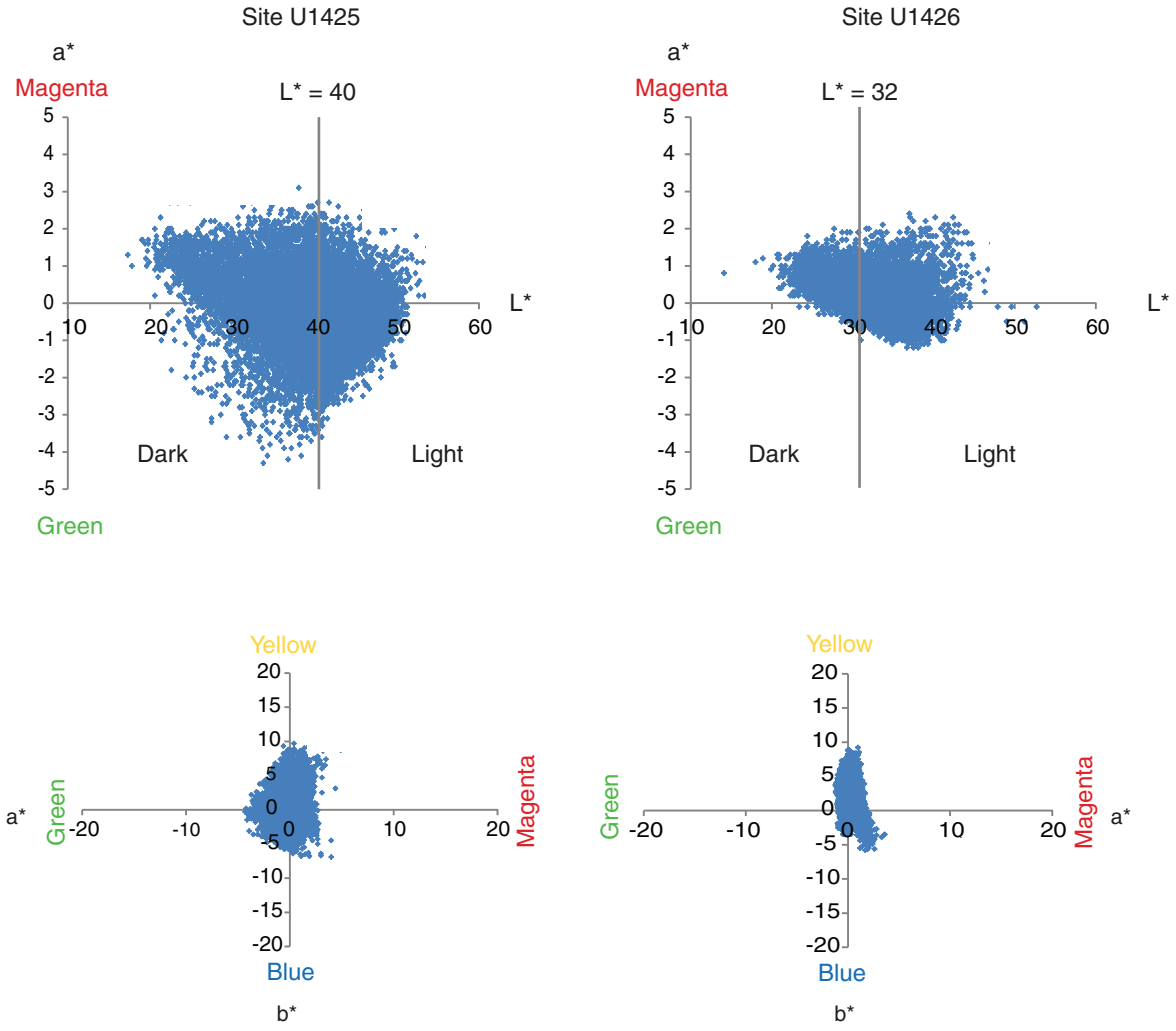

Figure F49. Plots of heat flow calculations, Hole U1426A. **A.** In situ sediment temperatures from advanced piston corer temperature tool (APCT-3) measurements with average values for Cores 346-U1426A-4H, 7H, 10H, and 13H (circles) and linear fit. **B.** In situ thermal conductivity data (squares) with calculated thermal resistance (solid line). **C.** Bullard plot of heat flow calculated from a linear fit of temperature vs. thermal resistance data.

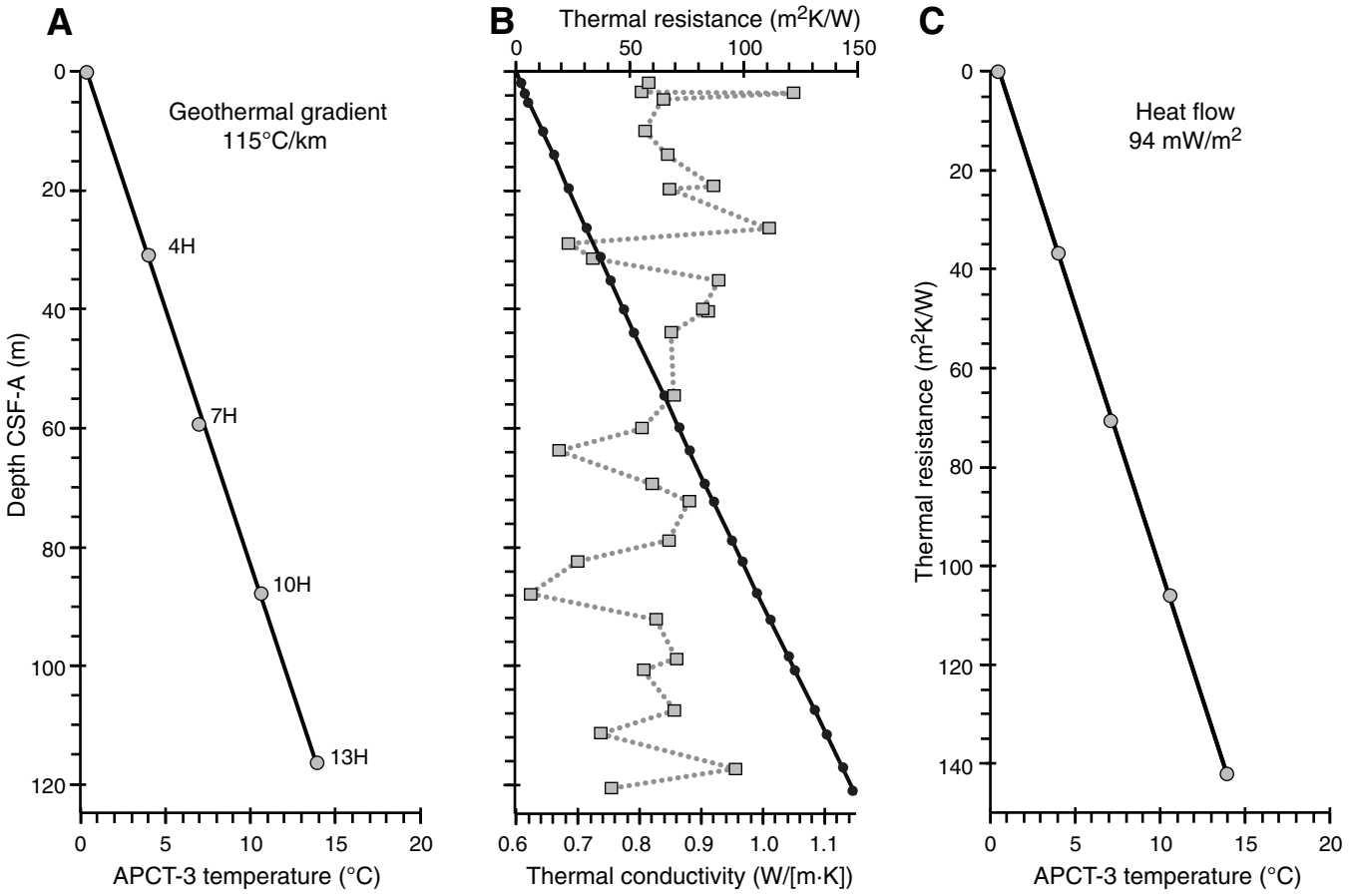

Figure F50. Composited cores and splice, Site U1426. Each core is depth adjusted by a constant amount to align it with adjacent cores at a chosen tie point (typically a distinctive feature in all of the data sets). Other features may or may not align among adjacent cores because of differential squeezing and stretching during the coring process or variable expansion characteristics. The splice is constructed from composited cores by selecting intervals from different holes such that coring gaps are avoided and drilling disturbances are minimized. Data included in the splice are plotted on the CCSF-D scale, whereas data not included in the splice are plotted on the CCSF-A scale. Vertical light blue lines indicate tie points where the splice changes from one hole to another. Only the splice is plotted on the correct *y*-axis scale; data from Holes U1426A, U1426B, and U1426C are offset by 40, 80, or 120 units, respectively, for illustrative purposes. One or two point spikes are artifacts generated when the track sensor measures beyond the end of the ~150 cm sections. **A.** 0–50 m CCSF-A. (Continued on next two pages.)

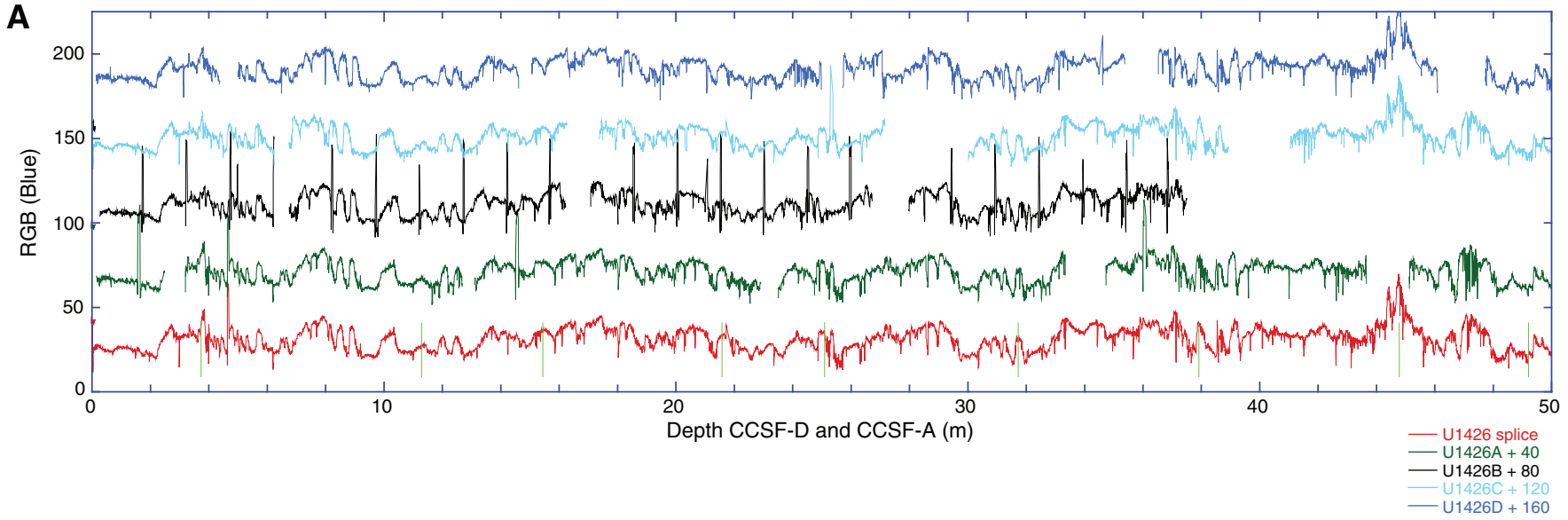

Figure F50 (continued). B. 50–150 m CCSF-A. (Continued on next page.)

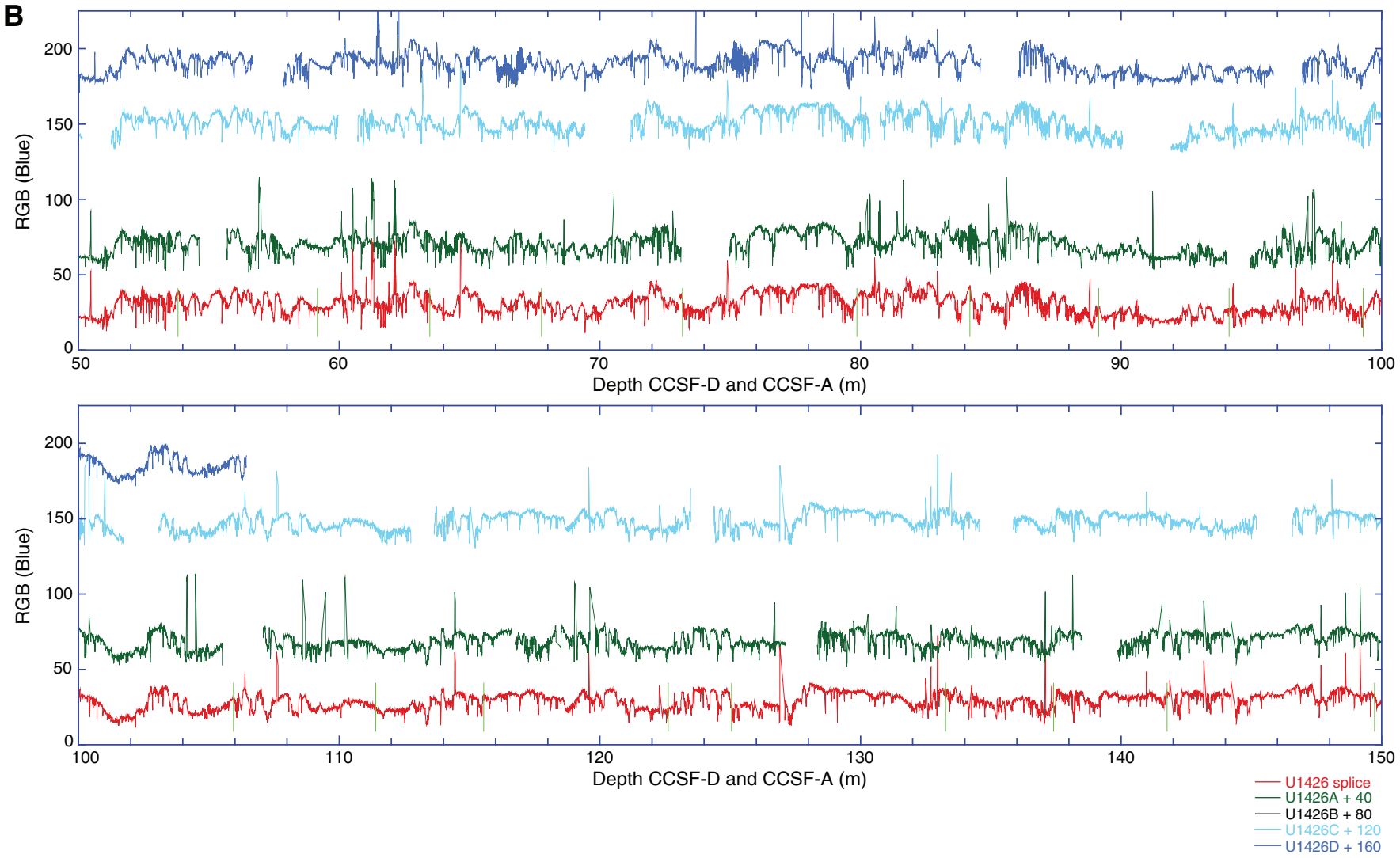

Figure F50 (continued). C. 150–240 m CCSF-A.

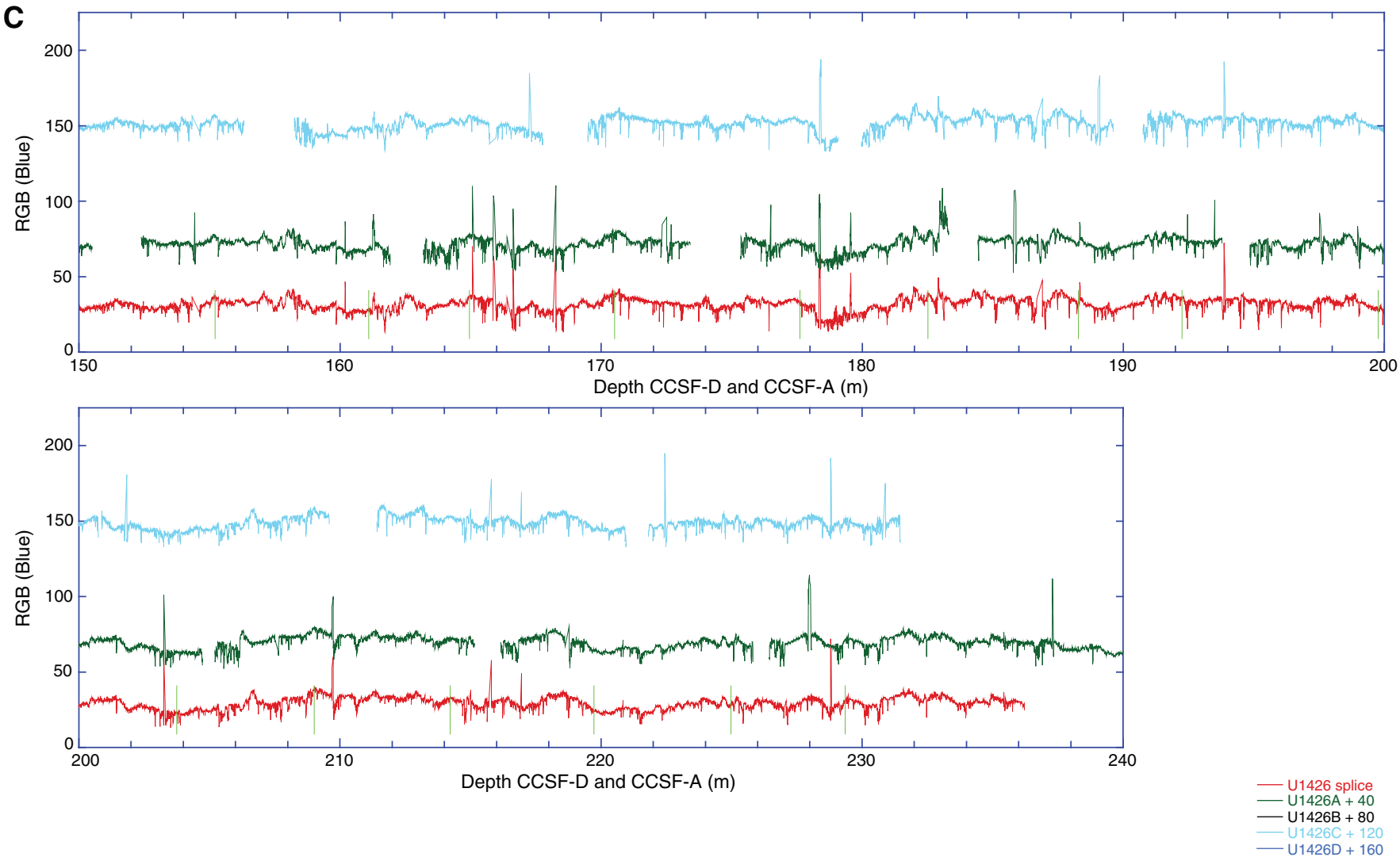

Figure F51. Age model and sedimentation rates, Site U1426. **A.** Synthesis of biostratigraphic, paleomagnetic, and tephra-based age control points fit with linear age-depth segments to establish a preliminary age model. **B.** Average sedimentation rates calculated for each lithologic unit.

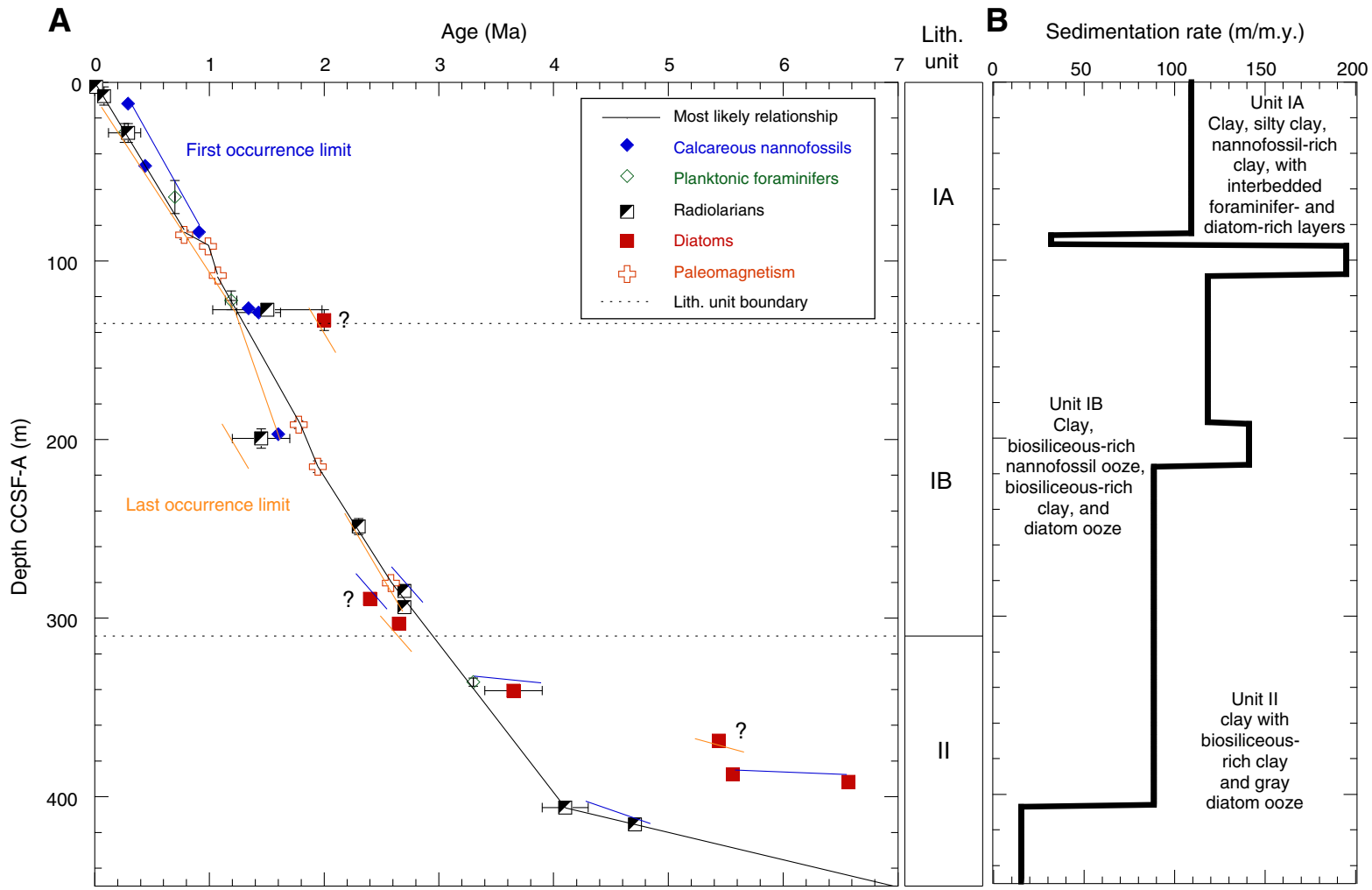

Table T1. Coring summary, Site U1426. (Continued on next two pages.)

Hole U1426A
Latitude: 37°1.9996′N
Longitude: 134°47.9999′E
Water depth (m): 902.98
Date started (UTC): 2136 h 2 September 2013
Date finished (UTC): 1430 h 4 September 2013
Time on hole (days): 1.70
Seafloor depth (drill pipe measurement below rig floor, m DRF): 914.4
Distance between rig floor and sea level (m): 11.42
Penetration DSF (m): 396.7
Cored interval (m): 396.7
Recovered length (m): 418.78
Recovery (%): 106
Drilled interval (m): NA
Drilled interval: 0
Total cores: 59
APC cores: 58
XCB cores: 1
RCB cores: 0
Other cores: 0

Hole U1426B
Latitude: 37°2.0088′N
Longitude: 134°48.0005′E
Water depth (m): 902.24
Date started (UTC): 1430 h 4 September 2013
Date finished (UTC): 1730 h 4 September 2013
Time on hole (days): 0.13
Seafloor depth (drill pipe measurement below rig floor, m DRF): 913.7
Distance between rig floor and sea level (m): 11.46
Penetration DSF (m): 34.7
Cored interval (m): 34.7
Recovered length (m): 35.82
Recovery (%): 103
Drilled interval (m): NA
Drilled interval: 0
Total cores: 4
APC cores: 4
XCB cores: 0
RCB cores: 0
Other cores: 0

Hole U1426C
Latitude: 37°1.9912′N
Longitude: 134°47.9997′E
Water depth (m): 902.94
Date started (UTC): 1730 h 4 September 2013
Date finished (UTC): 0525 h 5 September 2013
Time on hole (days): 0.50
Seafloor depth (drill pipe measurement below rig floor, m DRF): 914.4
Distance between rig floor and sea level (m): 11.46
Penetration DSF (m): 206
Cored interval (m): 204
Recovered length (m): 211.89
Recovery (%): 104
Drilled interval (m): 2
Drilled interval: 1
Total cores: 23
APC cores: 22
XCB cores: 1
RCB cores: 0
Other cores: 0

Hole U1426D
Latitude: 37°1.9996′N
Longitude: 134°47.9907′E
Water depth (m): 902.64
Date started (UTC): 0525 h 5 September 2013
Date finished (UTC): 1442 h 5 September 2013
Time on hole (days): 0.39
Seafloor depth (drill pipe measurement below rig floor, m DRF): 914.1
Distance between rig floor and sea level (m): 11.46
Penetration DSF (m): 99.4

Table T1 (continued). (Continued on next page.)

Cored interval (m): 99.4
Recovered length (m): 103.71
Recovery (%): 104
Drilled interval (m): NA
Drilled interval: 0
Total cores: 11
APC cores: 11
XCB cores: 0
RCB cores: 0
Other cores: 0

Site U1426 totals
Number of cores: 97
Penetration (m): 736.8
Cored (m): 734.8
Recovered (m): 770.2 (104.8%)

Core	Date (Sep 2013)	Time (h)	Top depth of cored interval DSF (m)	Bottom depth of cored interval DSF (m)	Interval advanced (m)	Top depth of recovered core CSF (m)	Bottom depth of recovered core CSF (m)	Length of core recovered (m)	Curated length (m)	Recovery (%)
346-U1426A-										
1H	3	0230	0.0	2.5	2.5	0.0	2.47	2.47	2.47	99
2H	3	0310	2.5	12.0	9.5	2.5	12.16	9.66	9.66	102
3H	3	0340	12.0	21.5	9.5	12.0	22.10	10.10	10.10	106
4H	3	0415	21.5	31.0	9.5	21.5	31.65	10.15	10.15	107
5H	3	0440	31.0	40.5	9.5	31.0	40.30	9.30	9.30	98
6H	3	0505	40.5	50.0	9.5	40.5	50.43	9.93	9.93	105
7H	3	0540	50.0	59.5	9.5	50.0	59.92	9.92	9.92	104
8H	3	0610	59.5	69.0	9.5	59.5	69.00	9.50	9.50	100
9H	3	0635	69.0	78.5	9.5	69.0	78.84	9.84	9.84	104
10H	3	0710	78.5	88.0	9.5	78.5	88.89	10.39	10.39	109
11H	3	0740	88.0	97.5	9.5	88.0	98.77	10.77	10.77	113
12H	3	0810	97.5	107.0	9.5	97.5	107.37	9.87	9.87	104
13H	3	0850	107.0	116.5	9.5	107.0	117.71	10.71	10.71	113
14H	3	0920	116.5	126.0	9.5	116.5	127.19	10.69	10.69	113
15H	3	1000	126.0	135.5	9.5	126.0	136.84	10.84	10.84	114
16H	3	1020	135.5	145.0	9.5	135.5	145.42	9.92	9.92	104
17H	3	1100	145.0	154.5	9.5	145.0	155.58	10.58	10.58	111
18H	3	1130	154.5	162.7	8.2	154.5	162.67	8.17	8.17	100
19H	3	1220	162.7	172.2	9.5	162.7	172.49	9.79	9.79	103
20H	3	1300	172.2	181.7	9.5	172.2	182.31	10.11	10.11	106
21H	3	1330	181.7	191.2	9.5	181.7	191.88	10.18	10.18	107
22H	3	1400	191.2	200.7	9.5	191.2	201.25	10.05	10.05	106
23H	3	1430	200.7	210.2	9.5	200.7	210.83	10.13	10.13	107
24H	3	1500	210.2	218.2	8.0	210.2	218.55	8.35	8.35	104
25H	3	1535	218.2	227.7	9.5	218.2	227.50	9.30	9.30	98
26H	3	1610	227.7	237.2	9.5	227.7	237.33	9.63	9.63	101
27H	3	1645	237.2	246.7	9.5	237.2	246.73	9.53	9.53	100
28H	3	1815	246.7	256.2	9.5	246.7	257.03	10.33	10.33	109
29H	3	1920	256.2	260.9	4.7	256.2	261.20	5.00	5.00	106
30H	3	2045	260.9	265.6	4.7	260.9	265.90	5.00	5.00	106
31H	3	2110	265.6	270.3	4.7	265.6	270.58	4.98	4.98	106
32H	3	2135	270.3	275.0	4.7	270.3	275.16	4.86	4.86	103
33H	3	2155	275.0	279.7	4.7	275.0	279.93	4.93	4.93	105
34H	3	2220	279.7	284.4	4.7	279.7	284.54	4.84	4.84	103
35H	3	2240	284.4	289.1	4.7	284.4	289.25	4.85	4.85	103
36H	3	2300	289.1	293.8	4.7	289.1	293.91	4.81	4.81	102
37H	3	2325	293.8	297.0	3.2	293.8	298.42	4.62	4.62	144
38X	4	0020	297.0	298.0	1.0	297.0	297.12	0.12	0.12	12
39H	4	0040	298.0	302.7	4.7	298.0	302.95	4.95	4.95	105
40H	4	0100	302.7	307.4	4.7	302.7	307.88	5.18	5.18	110
41H	4	0200	307.4	312.1	4.7	307.4	312.55	5.15	5.15	110
42H	4	0220	312.1	316.8	4.7	312.1	317.32	5.22	5.22	111
43H	4	0250	316.8	321.5	4.7	316.8	321.75	4.95	4.95	105
44H	4	0335	321.5	326.2	4.7	321.5	326.70	5.20	5.20	111
45H	4	0400	326.2	330.9	4.7	326.2	331.18	4.98	4.98	106
46H	4	0425	330.9	335.6	4.7	330.9	335.89	4.99	4.99	106
47H	4	0500	335.6	340.3	4.7	335.6	340.49	4.89	4.89	104
48H	4	0525	340.3	345.0	4.7	340.3	345.22	4.92	4.92	105
49H	4	0545	345.0	349.7	4.7	345.0	349.88	4.88	4.88	104
50H	4	0615	349.7	354.4	4.7	349.7	354.73	5.03	5.03	107

Table T1 (continued).

Core	Date (Sep 2013)	Time (h)	Top depth of cored interval DSF (m)	Bottom depth of cored interval DSF (m)	Interval advanced (m)	Top depth of recovered core CSF (m)	Bottom depth of recovered core CSF (m)	Length of core recovered (m)	Curated length (m)	Recovery (%)
51H	4	0640	354.4	359.1	4.7	354.4	359.32	4.92	4.92	105
52H	4	0700	359.1	363.8	4.7	359.1	364.15	5.05	5.05	107
53H	4	0725	363.8	368.5	4.7	363.8	368.74	4.94	4.94	105
54H	4	0750	368.5	373.2	4.7	368.5	373.41	4.91	4.91	104
55H	4	0825	373.2	377.9	4.7	373.2	378.19	4.99	4.99	106
56H	4	0850	377.9	382.6	4.7	377.9	382.77	4.87	4.87	104
57H	4	0945	382.6	387.3	4.7	382.6	387.45	4.85	4.85	103
58H	4	1015	387.3	392.0	4.7	387.3	392.12	4.82	4.82	103
59H	4	1100	392.0	396.7	4.7	392.0	396.87	4.87	4.87	104
				Total advanced (m):	396.7		Total recovered (m):	418.78		
346-U1426B-										
1H	4	1550	0.0	6.2	6.2	0.0	6.21	6.21	6.21	100
2H	4	1620	6.2	15.7	9.5	6.2	15.83	9.63	9.63	101
3H	4	1640	15.7	25.2	9.5	15.7	25.72	10.02	10.02	105
4H	4	1700	25.2	34.7	9.5	25.2	35.16	9.96	9.96	105
				Total advanced (m):	34.7		Total recovered (m):	35.82		
346-U1426C-										
1H	4	1800	0.0	6.5	6.5	0.0	6.48	6.48	6.48	100
2H	4	1825	6.5	16.0	9.5	6.5	16.31	9.81	9.81	103
3H	4	1845	16.0	25.5	9.5	16.0	26.12	10.12	10.12	107
41	4	1900				*****Drilled from 25.5 to 27.5 mbsf*****				
5H	4	1910	27.5	37.0	9.5	27.5	36.84	9.34	9.34	98
6H	4	1940	37.0	46.5	9.5	37.0	46.29	9.29	9.29	98
7H	4	2010	46.5	56.0	9.5	46.5	55.49	8.99	8.99	95
8H	4	2035	56.0	65.5	9.5	56.0	65.10	9.10	9.10	96
9H	4	2100	65.5	75.0	9.5	65.5	74.88	9.38	9.38	99
10H	4	2125	75.0	84.5	9.5	75.0	84.62	9.62	9.62	101
11H	4	2150	84.5	94.0	9.5	84.5	94.60	10.10	10.10	106
12H	4	2215	94.0	103.5	9.5	94.0	104.11	10.11	10.11	106
13H	4	2240	103.5	113.0	9.5	103.5	113.84	10.34	10.34	109
14H	4	2305	113.0	122.5	9.5	113.0	123.39	10.39	10.39	109
15H	4	2330	122.5	128.3	5.8	122.5	131.97	9.47	9.47	163
16X	5	0030	128.3	131.0	2.7	128.3	128.55	0.25	0.25	9
17H	5	0055	131.0	140.5	9.5	131.0	141.01	10.01	10.01	105
18H	5	0120	140.5	150.0	9.5	140.5	150.48	9.98	9.98	105
19H	5	0140	150.0	159.5	9.5	150.0	159.88	9.88	9.88	104
20H	5	0205	159.5	169.0	9.5	159.5	169.51	10.01	10.01	105
21H	5	0225	169.0	178.5	9.5	169.0	179.23	10.23	10.23	108
22H	5	0250	178.5	187.0	8.5	178.5	187.76	9.26	9.26	109
23H	5	0310	187.0	196.5	9.5	187.0	196.70	9.70	9.70	102
24H	5	0335	196.5	206.0	9.5	196.5	206.53	10.03	10.03	106
				Total advanced (m):	206.0		Total recovered (m):	211.89		
346-U1426D-										
1H	5	0605	0.0	4.4	4.4	0.0	4.40	4.40	4.40	100
2H	5	0630	4.4	13.9	9.5	4.4	14.29	9.89	9.89	104
3H	5	0650	13.9	23.4	9.5	13.9	24.11	10.21	10.21	107
4H	5	0710	23.4	32.9	9.5	23.4	33.43	10.01	10.03	105
5H	5	0730	32.9	42.4	9.5	32.9	42.94	10.04	10.04	106
6H	5	0750	42.4	51.9	9.5	42.4	51.77	10.02	9.37	105
7H	5	0805	51.9	61.4	9.5	51.9	61.77	9.87	9.87	104
8H	5	0830	61.4	70.9	9.5	61.4	71.15	9.75	9.75	103
9H	5	0855	70.9	80.4	9.5	70.9	80.73	9.83	9.83	103
10H	5	0925	80.4	89.9	9.5	80.4	90.39	9.99	9.99	105
11H	5	0950	89.9	99.4	9.5	89.9	99.60	9.70	9.70	102
				Total advanced (m):	99.4		Total recovered (m):	103.71		

DRF = drilling depth below rig floor, DSF = drilling depth below seafloor, CSF = core depth below seafloor. APC = advanced piston corer, XCB = extended core barrel, RCB = rotary core barrel. H = APC system, X = XCB system, numeric core type = drilled interval. NA = not applicable.

Table T2. XRD analysis of bulk samples, Site U1426.

Core section, interval (cm)	Top depth CSF-A (m)	Smectite (counts)	Illite (counts)	Kaolinite + chlorite (counts)	Opal-A (counts)	Opal-CT (counts)	Quartz (counts)	K-feldspar (counts)	Plagioclase (counts)	Calcite (counts)	Halite (counts)	Pyrite (counts)	Dolomite (counts)
346-U1426A-													
1H-1, 78.0–79.0	0.78	100	292	196	79	0	2779	167	353	810	589	193	0
2H-1, 52.0–53.0	3.02	152	425	278	70	0	3265	167	475	406	241	68	0
3H-2, 79.0–80.0	14.29	160	418	283	47	0	4852	225	573	463	272	109	0
4H-2, 11.0–12.0	23.02	192	418	306	34	0	4604	212	558	947	218	0	0
5H-1, 114.0–115.0	32.14	259	647	415	34	0	5148	195	616	38	230	0	0
6H-2, 93.0–94.0	41.6	223	571	367	31	0	4106	223	569	1237	228	99	0
7H-6, 44.0–45.0	57.04	225	576	405	21	0	4430	186	500	1254	151	0	0
8H-1, 70.0–71.0	60.2	215	552	396	22	0	4137	194	610	896	191	0	0
9H-2, 62.0–63.0	69.86	280	726	457	28	0	3361	168	496	1839	218	88	110
10H-3, 7.0–8.0	80.4	194	481	267	43	0	2498	110	290	2835	255	76	0
11H-3, 9.0–10.0	90.57	249	544	330	19	0	3120	221	392	2747	186	78	0
12H-2, 62.0–63.0	98.39	208	501	325	30	0	3520	179	464	1641	217	0	0
13H-2, 54.0–55.0	108.48	281	1013	564	16	0	5982	269	837	66	179	0	136
14H-2, 39.0–40.0	118.1	264	730	426	36	0	3259	154	481	1929	254	83	83
15H-2, 19.0–20.0	127.41	167	543	259	111	0	2343	103	292	1965	355	128	0
16H-1, 57.0–58.0	136.07	106	217	176	138	0	2032	125	204	1792	352	120	0
17H-2, 37.0–38.0	146.7	104	228	148	16	0	1882	103	245	2927	311	105	0
18H-1, 59.0–60.0	155.09	145	332	175	50	0	2162	128	289	2995	259	88	0
19H-1, 59.0–60.0	163.29	155	553	296	56	0	3384	151	446	943	250	121	0
20H-2, 39.0–40.0	173.31	82	433	201	112	0	2678	159	291	609	330	117	0
21H-2, 10.0–11.0	182.73	266	945	518	58	0	4469	169	670	64	232	95	0
22H-3, 9.0–10.0	193.07	103	246	141	73	0	2299	111	255	846	325	87	0
23H-2, 7.0–8.0	201.37	132	420	246	91	0	2901	201	287	0	339	130	0
24H-2, 34.0–35.0	211.93	97	413	178	69	0	3017	193	476	0	354	101	0
25H-1, 129.0–130.0	219.49	139	450	224	45	0	2931	201	351	0	275	0	66
26H-2, 14.0–15.0	228.34	104	340	162	111	0	2342	252	264	0	361	120	0
27H-2, 103.0–104.0	238.57	162	638	376	32	0	4415	192	548	106	230	108	98
28H-1, 90.0–91.0	247.6	221	789	431	23	0	4403	182	539	0	265	105	107
29H-1, 82.0–83.0	257.02	83	381	161	98	0	2754	180	348	0	331	114	0
31H-2, 54.0–55.0	267.64	90	310	143	110	0	2577	131	264	0	285	112	0
33H-1, 107.0–108.0	276.07	85	259	140	146	0	2032	150	241	0	405	99	0
35H-2, 45.0–46.0	286.35	74	306	155	115	0	2498	163	285	0	347	133	0
37H-1, 47.0–48.0	294.27	222	789	398	40	0	3680	197	553	0	207	138	0
40H-1, 43.0–44.0	303.13	199	476	302	56	0	3832	188	459	258	187	119	0
42H-3, 40.0–41.0	314.17	164	429	308	65	0	3664	212	403	188	176	86	0
44H-3, 29.0–30.0	323.59	258	718	400	42	0	4079	177	455	0	221	108	75
46H-1, 87.0–88.0	331.77	240	571	275	88	0	3393	187	343	0	243	118	0
48H-1, 51.0–52.0	340.81	166	470	235	96	0	3215	135	343	0	245	106	0
50H-2, 79.0–80.0	351.97	210	545	313	122	0	2918	143	323	0	262	94	0
52H-1, 47.0–48.0	359.57	144	417	257	90	0	3089	146	358	0	270	0	0
54H-1, 69.0–70.0	369.19	192	540	278	62	0	3301	187	428	0	204	99	0
56H-2, 59.0–60.0	379.99	255	453	236	64	0	2990	158	342	0	168	0	0
58H-2, 14.0–15.0	387.75	177	502	226	47	0	2991	163	315	0	140	0	0

Table T3. Visible tephra layers thicker than 0.5 cm, Hole U1426A.

Core, section, interval (cm)	Thickness (cm)	Color	Occurrence
346-U1426A-			
1H-2, 20–25	3.0	Olive-gray	Layered
2H-1, 60–72	12.0	Gray	Layered
2H-2, 29–32	2.0	White	Layered
3H-3, 52–53	0.5	Gray	Layered
3H-4, 42–43	1.0	Black	Layered
4H-3, 87–92	5.0	Gray	Layered
5H-3, 125–134	9.0	Gray	Layered
6H-6, 19.5–22.5	3.0	Gray	Patched
6H-8, 61–64	3.0	Olive-gray	Layered
6H-8, 64–69	0.5	Gray	Patched
7H-1, 110.5–111	0.5	Gray	Layered
7H-4, 62.5–65.5	3.0	Light gray	Layered
7H-4, 70.5–71	0.5	Black	Layered
7H-4, 78–78.5	0.5	Gray	Layered
7H-5, 17.2–18.6	1.4	White	Layered
7H-5, 37–48	9.0	White	Layered
7H-5, 122.2–133.2	11.0	White	Layered
7H-6, 29–30.5	1.5	Gray	Layered
7H-6, 134–137	0.5	Gray	Patched
8H-1, 6.7–7.8	1.1	Gray	Layered
8H-2, 107–111	4.0	Dark gray	Layered
8H-3, 83.5–85	1.5	Gray	Layered
8H-4, 3–3.5	0.5	Gray	Layered
9H-2, 26–28	2.0	Gray	Layered
9H-2, 30.3–31	0.7	Gray	Layered
9H-2, 93–97	4.0	Gray	Patched
9H-6, 4–4.5	0.5	White	Layered
9H-6, 8.5–10.7	2.2	Light gray	Layered
9H-6, 66.7–69	2.3	Gray	Layered
9H-7, 31.5–32	0.5	Light gray	Layered
11H-2, 0–1	1.0	Light gray	Layered
11H-3, 63–86.5	23.5	Light gray	Layered
12H-7, 19.5–20	0.5	Gray	Layered
12H-8, 15.2–15.8	0.6	Gray	Layered
13H-5, 76–77	1.0	Gray	Layered
13H-5, 91.5–92	0.5	Dark gray	Layered
13H-5, 95.5–96	0.5	Dark gray	Layered
14H-4, 95–97	0.7	Light gray	Patched
15H-6, 78–81	3.0	Light gray	Layered
16H-6, 139, to 16H-7, 6	8.0	Gray	Layered
18H-3, 1–7	6.0	White	Layered
18H-3, 32–32.5	0.5	White	Layered
18H-3, 120–128	2.0	White	Layered
18H-6, 13–48	35.0	Gray	Layered
19H-6, 93–96	2.0	Gray	Layered
26H-4, 1.5–23	21.5	Light gray	Layered
27H-3, 48–59	11.0	White	Layered
28H-6, 54–54.7	0.7	Light brownish gray	Layered
37H-2, 75–80	5.0	Gray	Layered
44H-2, 5–47	42.0	Dark gray	Layered
44H-2, 52–55	3.0	Light gray	Layered
48H-4, 45–49	2.0	Dark gray	Layered
53H-1, 38–46	8.0	Light gray	Layered
56H-2, 133–142	3.0	Black	Dispersed

Table T4. Microfossil bioevents, Site U1426.

Core, Section, interval (cm)		Event		Age	Depth CSF-A (m)				Depth CCSF-A (m)				Comments
Top	Bottom	type	Bioevents and epoch boundaries	(Ma)	Top	Bottom	Midpoint	±	Top	Bottom	Midpoint	±	
346-U1426A-	346-U1426A-												
1H-CC	1H-CC	R	*Stylochlamydium venustum* Zone	0.012–0.014	2.42	2.42	2.42	0.00	2.59	2.59	2.59	0.00	Itaki and Ikehara, 2003
1H-CC	2H-CC	R	LO *Amphimelissa setosa*	0.08	2.42	12.11	7.27	4.85	2.59	12.81	7.70	5.11	
2H-6W, 75	2H-7W, 25	CN	FO *Emiliania huxleyi*	0.29	10.75	11.75	11.25	0.50	11.45	12.45	11.95	0.50	
3H-CC	4H-CC	R	LO *Spongodiscus* sp.	0.29	22.05	31.60	26.83	4.78	23.17	33.61	28.39	5.22	
3H-CC	4H-CC	PF	FO and LO *Globigerinoides ruber* (pink)	0.12–0.4	22.05	31.60	26.83	4.78	23.17	33.61	28.39	5.22	
6H-2W, 90	6H-3W, 90	CN	LO *Pseudoemiliania lacunosa*	0.44	41.57	42.98	42.28	0.70	46.20	47.61	46.91	0.71	
6H-CC	8H-CC	PF	LO *Neogloboquadrina kagaensis* group	0.7	50.38	68.95	59.67	9.29	55.01	73.53	64.27	9.26	
9H-8W 3	9H-CC	CN	LO *Reticulofenestra asanoi*	0.91	77.01	78.79	77.90	0.89	82.99	84.77	83.88	0.89	
12H-CC	13H-CC	PF	X *Neogloboquadrina pachyderma* (D to S)	1.14–1.24	107.32	117.66	112.49	5.17	116.91	127.45	122.18	5.27	
13H-7W, 75	13H-CC	CN	LO *Helicosphaera sellii*	1.34	116.08	117.66	116.87	0.79	125.87	127.45	126.66	0.79	
13H-CC	13H-CC	R	*Eucyrtidium matuyamai*	1.03–1.98	117.66	117.66	117.66	0.00	127.45	127.45	127.45	0.00	Occurrence interval
13H-CC	14H-2W, 75	CN	*Gephyrocapsa* (>5.5 µm)	1.24–1.62	117.25	118.46	117.86	0.00	127.45	130.32	128.68	1.64	Occurrence interval
13H-CC	14H-CC	D	LO *Neodenticula koizumii*	2.0	117.66	127.14	122.40	4.74	127.45	139.00	133.22	5.77	
19H-CC	20H-CC	R	LO *Axoprunum acquilonium*	1.2–1.7	172.43	182.25	177.34	4.91	194.18	204.91	199.54	5.37	
20H-2W, 75	20H-3W, 75	CN	LO *Calcidiscus macintyrei*	1.60	173.67	175.04	174.36	0.69	196.33	197.70	197.01	0.69	
24H-CC	25H-CC	R	LO *Cycladophora sakaii*	2.3	218.50	227.45	222.98	4.47	244.24	253.19	248.72	4.47	
Pliocene/Pleistocene boundary				2.59									
28H-CC	29H-CC	R	FO *Cycladophora davisiana*	2.7	256.98	261.15	259.07	2.08	282.72	286.89	284.81	2.09	
29H-CC	30H-CC	D	FO *Nodenticula seminae*	2.4	261.15	265.84	263.50	2.34	286.89	291.58	289.24	2.34	
30H-CC	31H-CC	R	LO *Hexacontium parviakitaensis*	2.7	265.84	270.53	268.19	2.35	291.58	296.27	293.93	2.35	
32H-CC	33H-CC	D	LO *Neodenticula kamtschatica*	2.6–2.7	275.11	279.88	277.50	2.38	300.85	305.62	303.24	2.38	
40H-CC	41H-CC	PF	FO *Globorotalia praeinflata*	3.3	307.83	312.50	310.17	2.34	333.57	338.24	335.91	2.34	
41H-CC	42H-CC	D	FO *Neodenticula koizumii*	3.4–3.9	312.50	317.27	314.89	2.38	338.24	343.01	340.63	2.38	
47H-CC	48H-CC	D	LO *Thalassiosira temperei*	5.44	340.44	345.17	342.81	2.37	366.18	370.91	368.55	2.37	
51H-CC	52H-CC	D	FO *Thalassiosira oestrupii*	5.56	359.27	364.10	361.69	2.42	385.01	389.84	387.43	2.42	
55H-CC	56H-CC	R	FO *Hexacontium parviakitaensis*	3.9–4.3	378.14	382.72	380.43	2.29	403.88	408.46	406.17	2.29	
57H-CC	58H-CC	R	RI *Siphocampe arachnea* group	4.71	387.40	392.07	389.74	2.33	413.14	417.81	415.48	2.33	

R = radiolarian, F = foraminifer, CN = calcareous nannofossil, D = diatom. LO = last occurrence, F = first occurrence, RI = rapid increase.

Table T5. Preservation and estimated abundance of calcareous nannofossils, Site U1426. (Continued on next page.)

Core, section, interval (cm)	Top depth CSF-A (m)	Bottom depth CSF-A (m)	Preservation	Abundance	*Braarudosphaera bigelowii*	*Calcidiscus leptoporus*	*Calcidiscus macintyrei*	*Coccolithus pelagicus*	*Dictyococcites* spp.	*Emiliania huxleyi*	*Florisphaera profunda*	*Gephyrocapsa caribbeanica*	*Gephyrocapsa margerelii/muellerae*	*Gephyrocapsa oceanica s.s.*	*Gephyrocapsa* spp. (>4 µm)	*Gephyrocapsa* spp. large (>5.5 µm)	*Gephyrocapsa* spp. small (<4 µm)	*Helicosphaera carteri*	*Helicosphaera sellii*	*Pontosphaera japonica*	*Pontosphaera* spp.	*Pseudoemiliania lacunosa*	*Reticulofenestra asanoi*	*Reticulofenestra minuta*	*Reticulofenestra minutula*	*Reticulofenestra* spp.	*Umbilicosphaera sibogae*	Comments
346-U1426A-																												
1H-2, 63	2.13	2.13	M	F							F	F		C	C													
1H-CC	2.42	2.47	M	F				F		F		R		F			C				R							
2H-1, 85	3.35	3.35		B																								
2H-2, 75	4.75	4.75	M	R						F				C		R	A											
2H-3, 75	6.25	6.25	M	F	F					C		F		F			A											
2H-4, 75	7.75	7.75	P	F				C		F				F	C		A											
2H-5, 75	9.25	9.25	M	F	R			F		C				F	F		A											
2H-6, 75	10.75	10.75	M	F				R		R		R		R				R										
2H-7, 25	11.75	11.75	M	C										C			A											
2H-CC	12.11	12.16	M	R										R	F		R											
3H-5, 75	18.75	18.75	M	C	R			C						F			F											
3H-CC	22.05	22.10		B																								
4H-3, 75	25.05	25.05	P	R	R			F						R			R							R				
4H-CC	31.60	31.65	G	D	F	R		C				C	C	C			A	F			R							
5H-3, 75	34.25	34.25	G	A	R			R						R			D	R						C				
5H-CC	40.24	40.30	G	D	F							R	F				D											
6H-2, 90	41.57	41.57	P	R		R		F									C											
6H-3, 90	42.98	42.98	M	A				R				R		R	R		A					R		C				
6H-4, 45	43.95	43.95	M	F				R				R		R			C					R						
6H-CC	50.38	50.43	G	D		R		F				C		C			D	F				R						
7H-3, 75	53.31	53.31	M	R		R		R						R	R		R											
8H-4, 42	63.79	63.79	M	C				C				F		F			C							F				
8H-CC	68.95	69.00	G	D		R		F				F					D	R			R							
9H-4, 45	72.40	72.40	M	A		R		C				C		F			C					F		A				
9H-5, 90	73.86	73.86		B																								
9H-6, 63	74.93	74.93	P	A	F									R			A							A				
9H-7, 102	76.71	76.71	G	C	R			C				R		F			A			F	R			A				
9H-8, 3–4	77.01	77.02	G	C	R									F			A							A				
9H-CC	78.79	78.84	M	A	R			C				F		C			D				R	R	F					
10H-4, 100	82.68	82.68		B																								
10H-5, 51	83.33	83.33	G	D					C			R		F	F							C	A	C	C			
10H-6, 101	85.19	85.19	P	F	R			F				R		R			A						F	A				
10H-7, 81	86.40	86.40	M	C				F						R			A					R	R	C	C			
10H-CC	88.84	88.89		B																								
11H-4, 75	92.42	92.42	M	C		R		R									F						R	R	A			
11H-CC	98.72	98.77	M	R				F									C				F							
12H-CC	107.32	107.37	M	R		F		F							R		F											
13H-5, 75	113.06	113.06	P	C		R		F							R		C				R	R				F		
13H-6, 75	114.58	114.58	M	A		F		C				F			R		A	R					F	C			F	
13H-7, 75	116.08	116.08		B																								
13H-CC	117.66	117.71	G	A				C				F			C	R	F		R				R					
14H-1, 75	117.25	117.25	G	R				R						F		R	F					R	R			F		
14H-2, 75	118.46	118.46	G	A		F						C		C			C						F	C		F		
14H-3, 75	119.79	119.79	G	A		R		F				R		F			C						R	F	C			
14H-CC	127.14	127.19	G	F				C				R			F		C	R	F	R	R	R	R					
15H-CC	136.79	136.84	G	R				F				F			R		C	R			R		R					
16H-CC	145.37	145.42		B																								
17H-3, 75	148.53	148.53	M	F		R		F				F								R								
17H-6, 75	153.03	153.03	M	A		F		C				F		R			A						F	C	F			
17H-CC	155.53	155.58	G	C				C									C		F								R	
18H-1, 75	155.25	155.25	P	R				R									R		F									
18H-2, 75	156.75	156.75	P	F		F		F				R		R	R		F											Reworked specimens observed
18H-3, 36	157.86	157.86		B																								
18H-5, 75	161.25	161.25	G	C	R			A				R												F				
18H-CC	162.62	162.67	M	F	R	R		C							C				R					R	R			

Table T5 (continued).

Core, section, interval (cm)	Top depth CSF-A (m)	Bottom depth CSF-A (m)	Preservation	Abundance	*Braarudosphaera bigelowii*	*Calcidiscus leptoporus*	*Calcidiscus macintyrei*	*Coccolithus pelagicus*	*Dictyococcites* spp.	*Emiliania huxleyi*	*Florisphaera profunda*	*Gephyrocapsa caribbeanica*	*Gephyrocapsa margerelii/muellerae*	*Gephyrocapsa oceanica* s.s.	*Gephyrocapsa* spp. (>4 µm)	*Gephyrocapsa* spp. large (>5.5 µm)	*Gephyrocapsa* spp. small (<4 µm)	*Helicosphaera carteri*	*Helicosphaera sellii*	*Pontosphaera japonica*	*Pontosphaera* spp.	*Pseudoemiliania lacunosa*	*Reticulofenestra asanoi*	*Reticulofenestra minuta*	*Reticulofenestra minutula*	*Reticulofenestra* spp.	*Umbilicosphaera sibogae*	Comments
19H-CC	172.43	172.49	P	R				F									R				R							
20H-1, 40	172.60	172.60	P	R				R											R									
20H-2, 75	173.67	173.67	M	F		R	R						R						R			R		R	R			
20H-3, 75	175.04	175.04	P	R				R																				
20H-5, 75	178.04	178.04	P	R			R	F				R												R				
20H-CC	182.25	182.31		B																								
21H-CC	191.83	191.88		B																								
22H-CC	201.20	201.25		B																								
23H-CC	210.78	210.83		B																								
24H-CC	218.50	218.55		B																								
25H-CC	227.45	227.50		B																								
26H-CC	237.28	237.33		B																								
27H-CC	246.68	246.73		B																								
28H-CC	256.98	257.03		B																								
29H-CC	261.15	261.20		B																								
30H-CC	265.84	265.90		B																								
31H-CC	270.53	270.58		B																								
32H-CC	275.11	275.16		B																								
33H-CC	279.88	279.93		B																								
34H-CC	284.49	284.54		B																								
35H-CC	289.20	289.25		B																								
36H-CC	293.86	293.91		B																								
37H-CC	298.37	298.42	P	F													F									F		
39H-CC	302.87	302.91		B																								
40H-CC	307.83	307.88	M	F				F									C								C			
41H-CC	312.50	312.55	P	R				R									R											
42H-CC	317.27	317.32	P	R													R											
43H-CC	321.70	321.75		B																								
44H-CC	326.65	326.70		B																								
45H-CC	331.13	331.18		B																								
46H-CC	335.84	335.89		B																								
47H-CC	340.44	340.49		B																								
48H-CC	345.17	345.22		B																								
49H-CC	349.83	349.88		B																								
50H-CC	354.68	354.73		B																								
51H-CC	359.27	359.32		B																								
52H-CC	364.10	364.15		B																								
53H-CC	368.69	368.74		B																								
54H-CC	373.36	373.41		B																								
55H-CC	378.14	378.19		B																								
56H-CC	382.72	382.77		B																								
57H-CC	387.40	387.45		B																								
58H-CC	392.07	392.12		B																								
59H-CC	396.83	396.87		B																								
346-U1426B-																												
1H-CC	6.16	6.21	M	F				R		R			F	C			C											
2H-CC	15.78	15.83	M	R	F									R			R											
3H-CC	25.67	25.72	M	F	R			C				R		F			F											
4H-CC	35.11	35.16	G	A				R				F					A											

Preservation: G = good, M = moderate, P = poor. Abundance: D = dominant, A = abundant, C = common, F = few, R = rare, B = barren. Shaded intervals = barren.

Table T6. Preservation and estimated abundance of radiolarians, Hole U1426A. (Continued on next page.)

Core, section	Top depth CSF-A (m)	Bottom depth CSF-A (m)	Preservation	Abundance	*Actinomma boreale*	*Actinomma leptodermum*	*Amphimelissa setosa*	*Amphirhopalum ypsilon*	*Axoprunum acquilonium*	*Ceratospyris borealis*	*Cornutella profunda*	*Cycladophora cornutoides*	*Cycladophora davisiana*	*Cycladophora sakaii*	*Cyrtopera languncula*	*Dictyocoryne profunda*	*Dictyocoryne truncatum*	*Didymocyrtis tetrathalamus*	*Euchitonia furcata*	*Eucyrtidium matuyamai*	*Hexacontium parviakitaensis*	*Hymeniastrum euclidis*	*Lamprocyrtis heteroporos*	*Larcopyle polyacantha* group	*Larcopyle pylomaticus*	*Lychnocanoma sakaii*	*Octopyle/Tetrapyle* group	*Peripyramis circumtexta*	*Peripyramis woodringi*	*Phorticium pylonium* group	*Pseudodictyophimus gracilipes*	*Siphocampe arachnea* group	*Spongaster tetras tetras*	*Spongodiscus* sp.	*Spongopyle osculosa*	*Stichocorys* spp. group	*Stylochlamydium venustum*	*Stylochlamydium bensoni*	*Thecosphaera japonica*	*Thecosphaera pseudojaponica*
346-U1426A-																																							
1H-CC	2.42	2.47	G	C						F			C											R												A				
2H-CC	12.11	12.16	G	C			F			R														A		P	P			F			P			A				
3H-CC	22.05	22.10	G	A			R			P			R			F	F	R						R		A	P			P						A				
4H-CC	31.60	31.65	G	C				F					F			C	F	F	P					F			C							P		F				
5H-CC	40.24	40.30	G	C						A			A					P						F										C							
6H-CC	50.38	50.43	G	C				R		F			R			F	F	R	P					C			F				C			C							
8H-CC	68.95	69.00	G	F						A														R			C			C										
9H-CC	78.79	78.84	G	F												P	F							A			C			C										
10H-CC	88.84	88.89	G	A						C			F			P		P						A						F						A				
11H-CC	98.72	98.77	G	F						A														R												F				
12H-CC	107.32	107.37	G	C												C	F																				A			
13H-CC	117.66	117.71	M	C						A										F				P							P					F	A			
14H-CC	127.14	127.19	G	C				R								F	F							F						R							A			
15H-CC	136.79	136.84	G	A				P								F	F		P					P													A			
16H-CC	145.37	145.42	G	F						A			P											C				P			F					P	P			
17H-CC	155.53	155.58	G	A						R			R			F	R							C							F									
18H-CC	162.62	162.67	G	A				R		C			P			F	F		R					A			R									A		P		
19H-CC	172.43	172.49	G	A				F		C						C	F	F	C					C			C			C										
20H-CC	182.25	182.31	G	A					F	F		F	F			F			P					R	F															
21H-CC	191.83	191.88	G	A					C	P	P		F			F	P							C	P		P	P	F					P		P				
22H-CC	201.20	201.25	G	A		R					P		F			F							P	R	R		P	P			P					C	A			
23H-CC	210.78	210.83	G	C									A			P													F			R				P	A	P		
24H-CC	218.50	218.55	G	C					P	F			F			P																						R	C	
25H-CC	227.45	227.50	G	C		P			F	F		P	R	P											C										P				P		
26H-CC	237.28	237.33	G	A	R				C			R	P											F	F							P			F		F	F			
27H-CC	246.68	246.73	G	C						C		P		P										F				F	F							P	C	P		
28H-CC	256.98	257.03	G	A						F			R			P	P							P	F		P			P							C		P		
29H-CC	261.15	261.20	G	A									R	P		F								F	F												F	A	R		
30H-CC	265.84	265.90	G	C										R		F					R				F												C	R	P		
31H-CC	270.53	270.58	G	C										C							C			R	C						F									
33H-CC	279.88	279.93	G	C						P	P			F		P					C	R		R	F		F										C			
35H-CC	289.20	289.25	G	A										C			P				C	R		F	C		C		P								C	C	P		
37H-CC	298.37	298.42	G	F					P					F							C	R			F												C				
39H-CC	302.87	302.91	P	R										C																											
41H-CC	312.50	312.55	P	F					P		P			C		R					F			C	P					P											
43H-CC	321.70	321.75	P	F										F							C			C	P												C		P		
45H-CC	331.13	331.18	G	A					F					F		P	P				C				F				R			F					F	F	F		
47H-CC	340.44	340.49	G	F										C							P			P															F		
49H-CC	349.83	349.88	G	C										F	P	P					P				P			R				P			P		A				
51H-CC	359.27	359.32	G	F					F	P				C							R			F	P				P	R						F	R	P		
53H-CC	368.69	368.74	G	C					C					A							R				R				R	C		P		R		C				P
55H-CC	378.14	378.19	M	R					R					C							F											F						P		

Table T6 (continued).

Core, section	Top depth CSF-A (m)	Bottom depth CSF-A (m)	Preservation	Abundance	*Actinomma boreale*	*Actinomma leptodermum*	*Amphimelissa setosa*	*Amphirhopalum ypsilon*	*Axoprunum acquilonium*	*Ceratospyris borealis*	*Cornutella profunda*	*Cycladophora cornutoides*	*Cycladophora davisiana*	*Cycladophora sakaii*	*Cyrtopera languncula*	*Dictyocoryne profunda*	*Dictyocoryne truncatum*	*Didymocyrtis tetrathalamus*	*Euchitonia furcata*	*Eucyrtidium matuyamai*	*Hexacontium parviakitaensis*	*Hymeniastrum euclidis*	*Lamprocyrtis heteroporos*	*Larcopyle polyacantha* group	*Larcopyle pylomaticus*	*Lychnocanoma sakaii*	*Octopyle/Tetrapyle* group	*Peripyramis circumtexta*	*Peripyramis woodringi*	*Phorticium pylonium* group	*Pseudodictyophimus gracilipes*	*Siphocampe arachnea* group	*Spongaster tetras tetras*	*Spongodiscus* sp.	*Spongopyle osculosa*	*Stichocorys* spp. group	*Stylochlamydium venustum*	*Stylochlamydium bensoni*	*Thecosphaera japonica*	*Thecosphaera pseudojaponica*
56H-CC	382.72	382.77	G	C					F					F										F							A					C		P	
57H-CC	387.40	387.45	G	F										C										F							A			P		C		C	
58H-CC	392.07	392.12	P	R										A										P							P					P			
59H-CC	396.83	396.87	M	R					C					A																	F					F		P	

Preservation: G = good, M = moderate, P = poor. Abundance: A = abundant, C = common, F = few, R = rare, P = present.

Table T7. Preservation and estimated abundance of diatoms, Hole U1426A. (Continued on next page.)

Core, section	Top depth CSF-A (m)	Bottom depth CSF-A (m)	Datum	Preservation	Abundance	*Actinocyclus curvatulus*	*Actinocyclus oculatus*	*Actinoptychus senarius*	*Aulacoseira* spp.	*Azpeitia endoi*	*Azpeitia nodulifera*	*Chaetoceros* spp. and similar spores	*Coscinodiscus marginatus*	*Coscinodiscus oculus-iridis*	*Coscinodiscus radiatus*	*Diploneis bombus*	*Fragilariopsis doliolus*	*Neodenticula kamtschatica*	*Neodenticula koizumii*	*Neodenticula seminae*	*Paralia sulcata*	*Proboscia curvirostris*	*Rhizosolenia styliformis*	*Shionodiscus oestrupii*	*Stephanopyxis turris*	*Stephanopyxis* spp.	*Thalassionema nitzschioides*	*Thalassiosira antiqua*	*Thalassiosira eccentrica*	*Thalassiosira jouseae*	*Thalassiosira leptopus*	*Thalassiosira lineata*	*Thalassiosira manifesta*	*Thalassiosira nidulus*	*Thalassiosira pacifica*	*Thalassiosira temperei*	*Thalassiosira trifulta*	Comments
346-U1426A-																																					
1H-CC	2.42	2.47		G	A	R		R	R			A		R	R	R					C			F			C	F									
2H-CC	12.11	12.16		G	A	RR						A			R	R	R				C			F			A	F	R					R			
3H-CC	22.05	22.10		G	D	R		F				A	C		R	R					A			F			A		R								
4H-CC	31.60	31.65		G	D	F		C				A	C	F	F	R			R		A			A			A										
5H-CC	40.24	40.30		M	F	R						C				R											C										
6H-CC	50.38	50.43		G	A	R	R	C		R		A			R	F	R		R		A			F			A	R	F								
8H-CC	68.95	69.00		G	D	R						A				F	R		R	R	A			R			A		R								
9H-CC	78.79	78.84		G	A			C				A				R	R		R		A			F		R	A	A									
10H-CC	88.84	88.89		G	D			C	C	C		A				C	C		R	R	C				R		A										
11H-CC	98.72	98.77		G	A			R	F			C									A			R			C					F					
12H-CC	107.32	107.37		G	A	C		F				C	F			C	R		R		C	R		A		R	A										
13H-CC	117.66	117.71		G	A			R				A				F			R		R			C		R	A	R									
14H-CC	127.14	127.19	LO *Neodenticula koizumii*	G	A	F	R	A	F			C			R	R	R		C		A			C		R	C				F						
15H-CC	136.79	136.84		G	A	C		C	R			A	F				R		C		C	R	R	C		R	A	R		R							
16H-CC	145.37	145.42		G	F							A			R				R		F						C										
17H-CC	155.53	155.58		G	D	F		C	R			A	F	F	R		R		A	R	A		R	A		R	A						F				
18H-CC	162.62	162.67		G	D	F			F			A				R	R		A	F	A			F			A	R									
19H-CC	172.43	172.49		G	D	r		A	C			A			R	C			A	R	A			A		R	A	A	C				F				
20H-CC	182.25	182.31		G	A	c	R	C	R			A				R	F		A	F	C			F	F	F	A	R					F				
21H-CC	191.83	191.88		G	D	c	F	A		C		A		R		C	F		C		A			A	C	C	A	F					R				
22H-CC	201.20	201.25		G	D	C	A		A			A			F		R		A	F	A			F		F	A					R					
23H-CC	210.78	210.83		G	D	R				R		A	F		R				A	C	A			R		R	A	R									
24H-CC	218.50	218.55		G	C	R		R		F		C							F	R	F			C		R	C							R			
25H-CC	227.45	227.50		G	A	R				F		C	R		R		R		A		C				R	R	C										
26H-CC	237.28	237.33		G	A	F		R		R	R	C	R	R	R	R			A	C	A			A	F		A									R	
27H-CC	246.68	246.73		M	F							A							C	F							A										
28H-CC	256.98	257.03		G	D	C		R		R		A	R		R				A	A	A			C	A	R	A							R			
29H-CC	261.15	261.20	FO *Neodenticula seminae*	G	A	F		R				A							A	c	A			F			A										
30H-CC	265.84	265.90		G	D	R		C				A	A		A				A	R	C			C	A	C	A										
31H-CC	270.53	270.58		G	A	R		R				A							A		C			F	R	R	A		R								
32H-CC	275.11	275.16		G	A	R		C		R	F	A	A		A	C		R	A					C		F	A		R				F		F		
33H-CC	279.88	279.93	LO *Neodenticula kamtschatica*	G	A	R		R				A	R			R		A	A	R	R			F	F	F	A				R						
34H-CC	284.49	284.54		G	D	C						A	A		A	R		C	A		C			A	R	R	A										
35H-CC	289.20	289.25		G	A	R			R			A	A		C	A	R	R	C		A			C	R	R	A	R									
36H-CC	293.86	293.91		G	A	F					R	A	F			C		C	A		A			C	A	A	A	F									
37H-CC	298.37	298.42		G	A	C		R				C	C			C	R	A	C		F			C			A										
39H-CC	302.87	302.91		G	C			R				A	C					A	F		R						C		R								
40H-CC	307.83	307.88		G	A			R				A	A			A		A	C		R			C		F	A	F									
41H-CC	312.50	312.55	FO *Neodenticula koizumii*	G	D	F		R			R	A			R	A			C		C			C		R	A		C						R			

Table T7 (continued).

Core, section	Top depth CSF-A (m)	Bottom depth CSF-A (m)	Datum	Preservation	Abundance	*Actinocyclus curvatulus*	*Actinocyclus oculatus*	*Actinoptychus senarius*	*Aulacoseira* spp.	*Azpeitia endoi*	*Azpeitia nodulifera*	*Chaetoceros* spp. and similar spores	*Coscinodiscus marginatus*	*Coscinodiscus oculus-iridis*	*Coscinodiscus radiatus*	*Diploneis bombus*	*Fragilariopsis doliolus*	*Neodenticula kamtschatica*	*Neodenticula koizumii*	*Neodenticula seminae*	*Paralia sulcata*	*Proboscia curvirostris*	*Rhizosolenia styliformis*	*Shionodiscus oestrupii*	*Stephanopyxis turris*	*Stephanopyxis* spp.	*Thalassionema nitzschioides*	*Thalassiosira antiqua*	*Thalassiosira eccentrica*	*Thalassiosira jouseae*	*Thalassiosira leptopus*	*Thalassiosira lineata*	*Thalassiosira manifesta*	*Thalassiosira nidulus*	*Thalassiosira pacifica*	*Thalassiosira temperei*	*Thalassiosira trifulta*	Comments
42H-CC	317.27	317.32		G	A			R					C		R	C				A	A			F	R	R	A					R					
43H-CC	321.70	321.75		M	F			F								R					F						F										
44H-CC	326.65	326.70		G	C				R			A								C	F				R		R										
45H-CC	331.13	331.18		G	C			F	R			A				F				F	A			F	C		A										
46H-CC	335.84	335.89		G	D	R		A	A			A	A			A	A			A	R			F	F	R	A	C			F			R				
47H-CC	340.44	340.49		G	A			A			F	A	C		F	F				C	A			C	F	R	A	F									
48H-CC	345.17	345.22	LO *Thalassiosira temperei*	G	A	F		C				A	F			C				A	A			A	C	C	A	C	R							C		
49H-CC	349.83	349.88		G	D	F		C			R	A	C	F	R	C				A	C			F	C	C	A	C							C		
50H-CC	354.68	354.73		G	D	F		F	R			A	R		R	R				A	C				C	F	A	R	R						R		
51H-CC	359.27	359.32	FO *Shionodiscus oestrupii*	G	D			C				A	R		R					C	C			C	C	R	A		R						F		
52H-CC	364.10	364.15		G	D			F		F		A								A	A			F	C		A	F									
53H-CC	368.69	368.74		G	A	R		C		R		C			R					F	F			R	R		A										
54H-CC	373.36	373.41		G	A	R		C				C	R		R					R	C					R	A										
55H-CC	378.14	378.19		M	R	R						F									C						A										
56H-CC	382.72	382.77		M	R			F				R									C						C										
57H-CC	387.40	387.45		G	C							C									F						A										
58H-CC	392.07	392.12			B																																Dissolution
59H-CC	396.83	396.87			B																																Dissolution

Preservation: G = good, M = moderate. Abundance: D = dominant, A = abundant, C = common, F = few, R = rare, B = barren. LO = last occurrence, FO = first occurrence. Shaded intervals = barren.

Table T8. Preservation and estimated abundance of planktonic foraminifers, Hole U1426A. (Continued on next page.)

Core, section	Top depth CSF-A (m)	Bottom depth CSF-A (m)	Preservation	Abundance	% Planktonic foraminifers	*Globigerina bulloides*	*Globigerina umbilicata*	*Globigerina quinqueloba*	*Globigerina* sp.	*Globigerinita glutinata*	*Globigerinoides ruber* (pink)	*Globigerinoides ruber* (white)	*Globigerinoides sacculifer*	*Globigerinoides* sp.	*Globorotalia crassaformis*	*Globorotalia inflata*	*Globorotalia menardii*	*Globorotalia praeinflata*	*Globorotalia* sp.	*Globoturborotalita woodi*	*Neogloboquadrina dutertrei*	*Neogloboquadrina incompta*	*Neogloboquadrina kagaensis* and *N. inglei*	*Neogloboquadrina pachyderma*	*Neogloboquadrina pachyderma* (d)	*Neogloboquadrina pachyderma* (s)	*Neogloboquadrina* sp.	*Orbulina bilobata*	*Orbulina universa*	*Pulleniatina obliquiloculata*	Total number of planktonic foraminifers	Planktonic foraminifers/10 cm^3
346-U1426A-																																
1H-CC	2.42	2.47	G	D	75	61	3		12					1										3	1	10					91	30.3
2H-CC	12.11	12.16	G	A	43	26																				32					58	19.3
3H-CC	22.05	22.10		B	0																										0	0.0
4H-CC	31.60	31.65	G	A	44	59	11		1		10	2	5				3				8				4	4			1		108	36.0
5H-CC	40.24	40.30	G	D	95	74	3		2																	21					100	33.3
6H-CC	50.38	50.43	G	A	46	55			3												15	13			9	1					96	32.0
8H-CC	68.95	69.00	G	D	60	36		1	7												1		32			25					102	34.0
9H-CC	78.79	78.84	G	F	66	1															13		21			77					112	37.3
10H-CC	88.84	88.89	G	R	44	8	4																2		2	12					28	9.3
11H-CC	98.72	98.77	G	D	93	19			13												4		44		6	14					96	32.0
12H-CC	107.32	107.37	M	A	70	21		3			1										2		5		1	57				1	89	29.7
13H-CC	117.66	117.71	M	A	40	34	1		9							8							31		3	2	5				93	31.0
14H-CC	127.14	127.19	M	F	18	52		4	10														17		10	1					94	31.3
15H-CC	136.79	136.84	M	A	20	52	5	1		1									1		2		9		5	1	4				79	26.3
16H-CC	145.37	145.42	P	R	0	3		1																	1						5	1.7
17H-CC	155.53	155.58	M	R	25	51			1														35		12		2				101	33.7
18H-CC	162.62	162.67	M	A	50	44	6	4	1	6									3				18		12						92	30.7
19H-CC	172.43	172.49	M	A	67	47	1	13	3			1							1	16			6								88	29.3
20H-CC	182.25	182.31		B																											0	0.0
21H-CC	191.83	191.88		B																											0	0.0
22H-CC	201.20	201.25		B																											0	0.0
23H-CC	210.78	210.83		B																											0	0.0
24H-CC	218.50	218.55		B																											0	0.0
25H-CC	227.45	227.50		B																											0	0.0
26H-CC	237.28	237.33		B																											0	0.0
27H-CC	246.68	246.73		B																											0	0.0
28H-CC	256.98	257.03		B																											0	0.0
29H-CC	261.15	261.20		B																											0	0.0
30H-CC	265.84	265.90		B																											0	0.0
31H-CC	270.53	270.58		B																											0	0.0
32H-CC	275.11	275.16		B																											0	0.0
33H-CC	279.88	279.93		B																											0	0.0
34H-CC	284.49	284.54		B																											0	0.0
35H-CC	289.20	289.25		B																											0	0.0
36H-CC	293.86	293.91		B																											0	0.0
37H-CC	298.37	298.42	M	F	80	26	9											15		6			8		11		1				76	25.3
39H-CC	302.87	302.91		B																												0.0
40H-CC	307.83	307.88	M	A	60	18	5	3							4		19						24		24	1					98	32.7
41H-CC	312.50	312.55		B																											0	0.0
42H-CC	317.27	317.32		B																											0	0.0
43H-CC	321.70	321.75		B																											0	0.0
44H-CC	326.65	326.70		B																											0	0.0
45H-CC	331.13	331.18		B																											0	0.0
46H-CC	335.84	335.89	M	R		1																									1	0.3
47H-CC	340.44	340.49		B																											0	0.0
48H-CC	345.17	345.22		B																											0	0.0
49H-CC	349.83	349.88		B																											0	0.0
50H-CC	354.68	354.73		B																											0	0.0
51H-CC	359.27	359.32		B																											0	0.0
52H-CC	364.10	364.15		B																											0	0.0
53H-CC	368.69	368.74		B																											0	0.0
54H-CC	373.36	373.41		B																											0	0.0
55H-CC	378.14	378.19		B																											0	0.0
56H-CC	382.72	382.77	P	R	12	1	3	1																							5	1.7

Table T8 (continued).

Core, section	Top depth CSF-A (m)	Bottom depth CSF-A (m)	Preservation	Abundance	% Planktonic foraminifers	*Globigerina bulloides*	*Globigerina umbilicata*	*Globigerina quinqueloba*	*Globigerina* sp.	*Globigerinita glutinata*	*Globigerinoides ruber* (pink)	*Globigerinoides ruber* (white)	*Globigerinoides sacculifer*	*Globigerinoides* sp.	*Globorotalia crassaformis*	*Globorotalia inflata*	*Globorotalia menardii*	*Globorotalia praeinflata*	*Globorotalia* sp.	*Globoturborotalita woodi*	*Neogloboquadrina dutertrei*	*Neogloboquadrina incompta*	*Neogloboquadrina kagaensis* and *N. inglei*	*Neogloboquadrina pachyderma*	*Neogloboquadrina pachyderma* (d)	*Neogloboquadrina pachyderma* (s)	*Neogloboquadrina* sp.	*Orbulina bilobata*	*Orbulina universa*	*Pulleniatina obliquiloculata*	Total number of planktonic foraminifers	Planktonic foraminifers/10 cm^3
57H-CC	387.40	387.45		B																											0	0.0
58H-CC	392.07	392.12	P	R	53	10	9			2				3											1	1		3	5		34	11.3
59H-CC	396.83	396.87	P	F	25	30	6			2				1														1	3		43	14.3

Preservation: G = good, M = moderate, P = poor. Abundance: D = dominant, A = abundant, F = few, R = rare, B = barren. Shaded intervals = barren.

Table T9. Benthic foraminifers, Hole U1426A. This table is available in an **oversized format.**

Table T10. Calcium carbonate, total carbon (TC), total organic carbon (TOC), and total nitrogen (TN) contents of sediment samples from interstitial water squeeze cakes, Site U1426.

Core, section, interval (cm)	Top depth CSF-A (m)	Calcium carbonate (wt%)	TC (wt%)	TOC (wt%)	TN (wt%)
346-U1426A-					
1H-1, 145–150	1.45	1.62	2.68	2.49	0.38
2H-1, 145–150	3.95	4.14	2.80	2.30	0.35
3H-1, 145–150	13.45	8.97	3.03	1.96	0.30
5H-1, 133–138	32.33	2.17	0.93	0.67	0.17
7H-1, 129–134	51.29	21.74	4.06	1.46	0.25
11H-2, 142–147	90.43	22.78	4.88	2.15	0.31
13H-2, 135–140	109.29	7.57	3.14	2.23	0.32
17H-2, 140–145	147.73	17.19	4.30	2.24	0.29
19H-1, 140–145	164.10	2.61	2.28	1.96	0.30
23H-2, 95–100	202.25	10.01	2.48	1.28	0.24
29H-1, 141–146	257.61	0.45	1.46	1.41	0.27
31H-1, 145–150	267.05	0.57	1.75	1.68	0.27
37H-1, 145–150	295.25	11.98	3.50	2.07	0.30
41H-1, 145–150	308.85	0.74	2.38	2.29	0.32
43H-1, 133–138	318.13	1.80	1.61	1.40	0.28
47H-1, 140–145	337.00	0.64	1.24	1.16	0.28
51H-1, 141–146	355.81	0.74	1.50	1.41	0.26
53H-1, 139–144	365.19	0.76	1.67	1.58	0.28
59H-1, 140–145	393.40	2.83	1.13	0.79	0.23
346-U1426B-					
1H-1, 145–150	1.45	1.69	2.61	2.41	0.37
1H-2, 145–150	2.95	12.99	2.77	1.22	0.20
1H-3, 145–150	4.45	5.55	1.86	1.19	0.24
1H-4, 145–150	5.95	18.89	5.93	3.66	0.41
2H-1, 145–150	7.65	10.91	3.42	2.11	0.30
2H-2, 145–150	9.15	8.58	4.92	3.89	0.46
2H-3, 145–150	10.65	3.64	3.29	2.86	0.39
2H-4, 145–150	12.15	28.56	7.52	4.10	0.43
2H-5, 145–150	13.65	8.49	3.08	2.07	0.31
2H-6, 140–145	15.10	3.59	1.22	0.79	0.20
3H-1, 145–150	17.15	7.79	2.57	1.63	0.26
3H-2, 145–150	18.65	3.41	1.62	1.21	0.23
3H-3, 142–147	20.12	5.68	2.32	1.63	0.28
3H-4, 145–150	21.62	0.85	2.24	2.14	0.32
3H-5, 145–150	23.12	6.92	2.16	1.33	0.23
3H-6, 140–145	24.57	1.83	1.40	1.19	0.22
4H-1, 145–150	26.65	4.58	3.12	2.58	0.33
4H-2, 145–150	28.15	3.57	2.64	2.21	0.31
4H-3, 145–150	29.65	1.48	3.02	2.84	0.36
4H-4, 145–150	31.15	20.87	3.99	1.49	0.25
4H-5, 145–150	32.65	8.02	2.16	1.20	0.21
4H-6, 136–141	34.06	5.72	2.15	1.46	0.27
4H-7, 62–67	34.73	10.93	2.98	1.67	0.27

Table T11. Calcium carbonate, total carbon (TC), total organic carbon (TOC), and total nitrogen (TN) contents of sediment samples from light and dark intervals, Hole U1426A.

Core, section, interval (cm)	Top depth CSF-A (m)	Calcium carbonate (wt%)	TC (wt%)	TOC (wt%)	TN (wt%)
346-U1426A-					
1H-1, 52–54	0.52	3.1	2.61	2.24	0.40
1H-2, 60–62	2.10	9.3	5.26	4.14	0.52
1H-2, 74–76	2.24	7.1	2.55	1.70	0.29
2H-1, 3–5	2.53	12.0	2.98	1.54	0.24
2H-4, 64–66	7.64	14.9	4.81	3.03	0.41
2H-4, 108–110	8.08	12.1	5.38	3.93	0.49
2H-5, 43–45	8.93	6.5	4.84	4.06	0.49
2H-5, 99–101	9.49	14.7	3.17	1.41	0.27
2H-5, 132–134	9.82	22.1	6.10	3.44	0.45
3H-1, 50–52	12.50	17.9	3.70	1.55	0.29
3H-2, 29–31	13.79	4.9	2.81	2.23	0.35
3H-2, 98–100	14.48	3.6	1.54	1.10	0.28
3H-2, 128–130	14.78	4.5	1.93	1.40	0.28
3H-3, 58–60	15.58	10.0	2.48	1.28	0.23
6H-3, 99–101	43.07	37.2	6.71	2.24	0.27
6H-4, 22–24	43.72	3.7	4.16	3.71	0.42
6H-5, 20–22	44.77	15.5	3.83	1.97	0.29
6H-6, 60–62	46.23	15.2	6.05	4.23	0.44

Table T12. Interstitial water chemistry, Site U1426. This table is available in an **oversized format.**

Table T13. Headspace (HS) gas concentrations, Site U1426. This table is available in an **oversized format.**

Table T14. Vacutainer (VAC) gas concentrations, Site U1426.

Core, section, interval (cm)	Top depth CSF-A (m)	Sample type	CH_4 (ppmv) GC3 measured	Ethane (ppmv) GC3 measured	C_1/C_2 GC3	Propene (ppmv) GC3 measured	Propane (ppmv) GC3 measured
346-U1426A-							
5H-3, 87–88	34.37	VAC	891,570.42	451.40	1,975.12	0.52	0.00
10H-3, 128–128	81.61	VAC	900,338.20	495.03	1,818.75	0.00	12.28
11H-4, 22–23	91.89	VAC	904,331.25	604.38	1,496.30	0.00	19.35
12H-3, 129–129	100.00	VAC	908,072.52	666.60	1,362.25	0.00	22.03
14H-4, 23–24	120.42	VAC	894,982.03	909.72	983.80	0.00	37.90
15H-4, 21–22	130.22	VAC	851,009.11	813.30	1,046.37	0.00	32.41
16H-2, 59–60	137.53	VAC	861,231.03	828.49	1,039.52	1.40	35.14
17H-4, 5–6	149.33	VAC	886,763.00	878.24	1,009.70	0.00	40.48
18H-2, 135–136	157.35	VAC	911,632.35	1,003.97	908.03	0.00	63.51
19H-2, 130–131	165.45	VAC	894,845.80	910.52	982.79	0.00	53.47

GC3 = gas analyzer (C_1–C_3).

Table T15. Color measurements (absorbance) of interstitial water, Site U1426. (Continued on next page.)

Core, section, interval (cm)	Top depth CSF-A (m)	Top depth CCSF-A (m)	Alkalinity (mM)	Sample type	Absorbance 227 nm	Absorbance 325 nm
346-U1426A-						
1H-1, 0–5	0.00	0.17	2.26	ML	0.0655	0.0020
1H-1, 145–150	1.45	1.62	7.74	IW-Sq		
2H-1, 145–150	3.95	4.65	27.67	IW-Sq	3.8872	0.4540
3H-1, 145–150	13.45	14.57	50.10	IW-Sq	4.1400	0.6314
5H-1, 133–138	32.33	36.07	64.75	IW-Sq	3.7674	0.6419
7H-1, 129–134	51.29	56.98	76.43	IW-Sq	3.6516	0.4634
11H-2, 142–147	90.43	97.39	84.09	IW-Sq	3.8173	0.4447
13H-2, 135–140	109.29	119.08	84.65	IW-Sq	3.8506	0.4421
17H-2, 140–145	147.73	165.94	81.92	IW-Sq	4.0797	0.7091
19H-1, 140–145	164.10	185.85	79.93	IW-Sq	3.8332	0.3949
23H-2, 95–100	202.25	227.99	72.48	IW-Sq		
29H-1, 141–146	257.61	283.35	62.75	IW-Sq	3.6917	0.2845
31H-1, 145–150	267.05	292.79	61.02	IW-Sq	3.6536	0.2613
37H-1, 145–150	295.25	320.99	50.29	IW-Sq	3.5605	0.2135
41H-1, 145–150	308.85	334.59	46.21	IW-Sq	3.5259	0.1919
43H-1, 133–138	318.13	343.87	46.09	IW-Sq	3.5550	0.2026
47H-1, 140–145	337.00	362.74	44.30	IW-Sq	3.4917	0.1798
51H-1, 141–146	355.81	381.55	39.73	IW-Sq	3.4569	0.1551
53H-1, 139–144	365.19	390.93	39.05	IW-Sq	3.4682	0.1465
59H-1, 140–145	393.40	419.14	32.93	IW-Sq	3.3693	0.1169
346-U1426B-						
1H-1, 0–1	0.00	0.27	2.45	ML	0.0982	0.0105
1H-1, 10–11	0.10	0.37		IW-Rh	0.2842	0.0976
1H-1, 15–16	0.15	0.42		IW-Rh	0.2882	0.1064
1H-1, 20–21	0.20	0.47		IW-Rh	0.2780	0.0977
1H-1, 25–26	0.25	0.52		IW-Rh	0.2302	0.0683
1H-1, 30–31	0.30	0.57		IW-Rh	0.1911	0.0447
1H-1, 40–41	0.40	0.67		IW-Rh	0.1545	0.0219
1H-1, 50–51	0.50	0.77		IW-Rh	0.1816	0.0281
1H-1, 60–61	0.60	0.87	4.19	IW-Rh		
1H-1, 80–81	0.80	1.07		IW-Rh	0.4049	0.0551
1H-1, 100–101	1.00	1.27		IW-Rh	0.6424	0.0961
1H-1, 120–121	1.20	1.47		IW-Rh	0.7043	0.0690
1H-1, 138–139	1.38	1.65		IW-Rh	0.9282	0.0740
1H-1, 145–150	1.45	1.72	7.81	IW-Rh	0.8908	0.1636
1H-2, 10–11	1.60	1.87		IW-Rh	0.9442	0.0926
1H-2, 25–26	1.75	2.02		IW-Rh	1.0529	0.1163
1H-2, 40–41	1.90	2.17	10.12	IW-Rh		
1H-2, 80–81	2.30	2.57		IW-Rh	1.6935	0.1149
1H-2, 100–101	2.50	2.77		IW-Rh	1.8961	0.1291
1H-2, 120–121	2.70	2.97		IW-Rh	2.1820	0.1496
1H-2, 138–139	2.88	3.15		IW-Rh	3.7623	0.3251
1H-2, 145–150	2.95	3.22	16.11	IW-Rh	2.1480	0.2726
1H-3, 20–21	3.20	3.47		IW-Rh	2.9614	0.1857
1H-3, 40–41	3.40	3.67		IW-Rh	3.1334	0.2550
1H-3, 60–61	3.60	3.87		IW-Rh	3.2676	0.2187
1H-3, 138–139	4.38	4.65		IW-Rh	3.8845	0.3600
1H-3, 145–150	4.45	4.72	24.78	IW-Rh	3.9842	0.4696
1H-4, 20–21	4.70	4.97		IW-Rh	3.8527	0.3092
1H-4, 40–41	4.90	5.17		IW-Rh	4.4201	0.8125
1H-4, 80–81	5.30	5.57		IW-Rh	4.3560	0.8952
1H-4, 100–101	5.50	5.77		IW-Rh	4.3010	0.8791
1H-4, 145–150	5.95	6.22	32.35	IW-Rh	4.1569	0.7344
2H-1, 10–11	6.30	6.86		IW-Rh	3.1253	0.2683
2H-1, 60–61	6.80	7.36		IW-Rh	4.0953	0.4454
2H-1, 90–91	7.10	7.66		IW-Rh	4.1155	0.4705
2H-1, 120–121	7.40	7.96		IW-Rh	4.1072	0.4798
2H-1, 145–150	7.65	8.21	39.65	IW-Rh	4.2712	0.6119
2H-2, 10–11	7.80	8.36		IW-Rh	4.1450	0.5039
2H-2, 25–26	7.95	8.51	40.68	IW-Rh		
2H-2, 85–86	8.55	9.11	41.69	IW-Rh		
2H-2, 145–150	9.15	9.71	42.11	IW-Rh		
2H-3, 10–11	9.30	9.86		IW-Rh	4.2040	0.5484
2H-3, 40–41	9.60	10.16	43.29	IW-Rh		
2H-3, 55–56	9.75	10.31	44.49	IW-Rh		
2H-3, 70–71	9.90	10.46	44.60	IW-Rh		
2H-3, 85–86	10.05	10.61	44.02	IW-Rh		

Table T15 (continued).

Core, section, interval (cm)	Top depth CSF-A (m)	Top depth CCSF-A (m)	Alkalinity (mM)	Sample type	Absorbance 227 nm	Absorbance 325 nm
2H-3, 100–101	10.20	10.76	43.76	IW-Rh		
2H-3, 115–116	10.35	10.91	44.26	IW-Rh		
2H-3, 145–150	10.65	11.21	43.98	IW-Rh	4.2058	0.6452
2H-4, 40–41	11.10	11.66	45.65	IW-Rh		
2H-4, 85–86	11.55	12.11	45.55	IW-Rh		
2H-4, 115–116	11.85	12.41	46.43	IW-Rh		
2H-4, 130–131	12.00	12.56	46.68	IW-Rh		
2H-4, 145–150	12.15	12.71	44.67	IW-Rh	4.0560	0.6761
2H-5, 55–56	12.75	13.31		IW-Rh	4.1684	0.6149
2H-5, 70–71	12.90	13.46		IW-Rh	4.1412	0.6150
2H-5, 100–101	13.20	13.76	49.86	IW-Rh	4.1656	0.6113
2H-5, 145–150	13.65	14.21	48.16	IW-Rh	4.2060	0.6783
2H-6, 40–41	14.10	14.66		IW-Rh	4.1690	0.6251
2H-6, 70–71	14.40	14.96		IW-Rh	4.1990	0.6349
2H-6, 140–145	15.10	15.66	49.40	IW-Rh		
3H-1, 40–41	16.10	17.49		IW-Rh	4.3138	0.9414
3H-1, 60–61	16.30	17.69		IW-Rh	4.2210	0.6443
3H-1, 120–121	16.90	18.29		IW-Rh	4.7920	1.9994
3H-1, 145–150	17.15	18.54	50.54	IW-Rh	4.2426	0.7437
3H-2, 145–150	18.65	20.04	52.50	IW-Rh		
3H-3, 142–147	20.12	21.51	54.24	IW-Rh	4.0456	0.7019
3H-4, 145–150	21.65	23.04	56.56	IW-Rh	4.0839	0.6948
True replicate	21.65	23.04			4.0646	0.6821
3H-5, 145–150	23.15	24.54	58.89	IW-Rh	4.0894	0.7132
3H-6, 140–145	24.60	25.99	60.27	IW-Rh		
4H-1, 145–150	26.65	29.43	61.53	IW-Rh	4.0623	0.6785
True replicate	26.65	29.43			3.9687	0.6616
4H-2, 145–150	28.15	30.93	62.13	IW-Rh		
4H-3, 145–150	29.65	32.43	62.91	IW-Rh	3.7409	0.6364
4H-4, 80–81	30.50	33.28		IW-Rh	4.0525	0.6267
4H-4, 130–131	31.00	33.78		IW-Rh	3.8423	0.5593
4H-4, 145–150	31.15	33.93	65.90	IW-Rh		
4H-5, 145–150	32.65	35.43	67.14	IW-Rh	3.7041	0.6031
True replicate	32.65	35.43			3.6736	0.5792
4H-6, 136–141	34.06	36.84	68.33	IW-Rh	3.6622	0.5156
4H-7, 62–67	34.82	37.60	65.41	IW-Rh	3.5275	0.4988

ML = mudline, IW-Sq = interstitial water from whole-round squeezing, IW-Rh = interstitial water from Rhizons.

Table T16. FlexIT tool core orientation data, Hole U1426A.

Core	Orientation angle (°)	Orientation standard (°)
346-U1426A-		
2H	197.08	1.65
3H	263.69	0.95
4H	106.13	0.63
5H	22.59	0.72
6H	97.52	0.71
7H	157.55	0.44
8H	182.54	0.45
9H	147.30	0.80
10H	159.66	0.40
11H	116.18	0.25
12H	332.74	0.45
13H	17.87	0.57
14H	324.54	0.41
15H	343.69	0.23
16H	260.49	0.24
17H	324.81	0.22
18H	284.90	0.42
19H	150.43	0.20
20H	201.74	0.15
21H	155.34	0.35
22H	19.43	0.23
23H	230.94	0.33
24H	151.94	0.30
25H	350.81	0.25
26H	110.06	0.29

Table T17. Core disturbance intervals, Site U1426. (Continued on next five pages.)

Core, section, interval (cm)	Comments on disturbance	Drilling disturbance intensity
346-U1426A-		
1H-1, 0–140	Soupy	
1H-CC, 0–14		Slight
2H-1, 0–3		High
2H-1, 57–84	Disturbance	Destroyed
2H-2, 28–33	Ash and void	
2H-6, 95–98	Void	Destroyed
2H-CC, 0–16		Slight to moderate
3H-3, 48–75	Microfault and tilted	
3H-6, 105–153	Gas expansion	
3H-7, 0–74	Gas expansion	Slight
3H-CC, 0–29		Slight
4H-2, 31–35	Gas expansion	Slight
4H-2, 55–80	Gas expansion	Slight
4H-3, 0–5	Gas expansion	
4H-7, 10–48	Gas expansion	
5H-3, 41–88	Gas expansion	Slight
5H-7, 40–41	Void	
6H-1, 0–17	Gas expansion	
6H-3, 30–77	Gas expansion	
6H-6, 67–139	Gas expansion	Slight
6H-7, 74–120	Gas expansion	Slight
6H-8, 0–55	Gas expansion	Slight
6H-CC, 0–42	Gas expansion	Slight
7H-1, 84–95	Gas expansion	Slight
7H-2, 38–70	Gas expansion	Slight
7H-4, 73–88		Slight
7H-4, 103–110	Dropstone	
7H-5, 59–95	Gas expansion	Moderate
7H-5, 123–131	Ash and void	
7H-6, 0–17	Gas expansion	Moderate
7H-6, 96–127	Gas expansion	Moderate
7H-7, 0–106	Gas expansion	Moderate
8H-1, 0–35	Gas expansion	Slight
8H-2, 0–55	Gas expansion	
8H-2, 108–127	Ash and void	
8H-3, 10–30	Gas expansion	
8H-3, 52–60	Gas expansion	
8H-3, 85–102	Gas expansion	
8H-3, 120–142	Gas expansion	
8H-4, 58–70	Gas expansion	
8H-5, 0–25	Gas expansion	
8H-5, 90–110	Gas expansion	
8H-6, 13–35	Gas expansion	
8H-6, 52–89	Gas expansion	
8H-7, 60–107	Gas expansion	
8H-8, 0–66	Gas expansion	
9H-1, 0–22	Gas expansion, too short to measure	Slight
9H-2, 45–55	Gas expansion	
9H-3, 0–8	Gas expansion	
9H-5, 50–137	Gas expansion	
9H-6, 23–27	Gas expansion	
9H-6, 46–49	Gas expansion	
9H-6, 113–117	Gas expansion	
9H-7, 0–50	Tilted and microfault	
9H-7, 55–92	Gas expansion and voids	
9H-7, 106–127	Gas expansion and voids	
9H-8, 0–26	Gas expansion and voids	
9H-8, 80–150	Gas expansion and voids	
10H-2, 37–45	Void	Destroyed
10H-2, 63–140	Gas expansion	Severe
10H-3, 26–50	Void	Destroyed
10H-3, 63–95	Void	Destroyed
10H-5, 71–135	Gas expansion and mass transfer deposit?	
10H-6, 122–140	Gas expansion and voids	
10H-8, 0–79	Gas expansion and voids	
11H-1, 0–101	Gas expansion	Moderate
11H-2, 52–147	Gas expansion	
11H-3, 54–102	Gas expansion	
11H-4, 0–21	Gas expansion	
11H-4, 60–132	Gas expansion	
11H-5, 0–21	Microfault	
11H-5, 21–52	Gas expansion	
11H-5, 63–70	Gas expansion	
11H-6, 0–70	Gas expansion	
11H-6, 103–141	Gas expansion	
11H-7, 131–141	Gas expansion	
11H-8, 0–54	Gas expansion	
11H-8, 63–93	Gas expansion	
12H-1, 0–26	Too short to measure	
12H-2, 85–91	Gas expansion	
12H-3, 27–120	Gas expansion	Severe
12H-4, 53–67	Gas expansion	Severe
12H-6, 76–96	Gas expansion	Severe
12H-6, 81–101	Gas expansion	
12H-7, 52–55	Gas expansion	
12H-7, 105–140	Flow-in?	
13H-1, 0–94	Extruded on rig floor	
13H-2, 60–78	Void	
13H-3, 43–83	Void and gas expansion	
13H-3, 110–122	Void	
13H-4, 73–79	Void	
13H-5, 44–53	Gas expansion	Slight
13H-6, 25–35	Void and gas expansion	
13H-7, 40–41	Crack	
13H-8, 53–60	Void	
13H-CC, 0–35		Slight
14H-1, 0–121	Extruded on rig floor	
14H-2, 20–24	Gas expansion	Slight
14H-2, 60–74	Void	
14H-2, 74–104	Gas expansion	Slight
14H-3, 45–50	Void	
14H-3, 84–88	Gas expansion	Slight
14H-4, 28–45	Gas expansion	
14H-4, 68–74	Void	
14H-5, 68–74	Void	
14H-5, 94–102	Gas expansion	
14H-6, 38–45	Void	
14H-6, 45–80	Gas expansion	Slight
14H-7, 25–26	Void	
14H-7, 62–66	Gas expansion	Slight
14H-7, 76–83	Void	
14H-8, 49–51	Void	
15H-1, 0–122	Extruded on rig floor	
15H-1, 0–119	Gas expansion	Moderate
15H-1, 119–122	Void	
15H-2, 34–48	Void	
15H-2, 48–56	Gas expansion	Moderate
15H-2, 78–93	Void	
15H-2, 93–122	Gas expansion	Moderate
15H-3, 58–67	Void	
15H-3, 67–85	Gas expansion	Slight
15H-4, 35–65	Void and gas expansion	
15H-4, 97–107	Gas expansion	
15H-6, 72–81	Ash and void	
15H-7, 0–21	Gas expansion	
15H-7, 21–24	Void	
15H-7, 79–83	Void	
15H-8, 21–22	Crack	
16H-1, 0–12	Fall-in	Moderate
16H-2, 56–64	Gas expansion	Slight
16H-2, 59–61	Void	
16H-6, 32–34	Void	
16H-6, 34–63	Gas expansion	
16H-7, 40–65	Gas expansion	

Table T17 (continued). (Continued on next page.)

Core, section, interval (cm)	Comments on disturbance	Drilling disturbance intensity
17H -1, 0–133	Extruded on rig floor	
17H-2, 55–61	Void	
17H-2, 76–120	Gas expansion	
17H-3, 28–90	Void and gas expansion	
17H-4, 69–79	Void	
17H-4, 79–82	Gas expansion	Slight
17H-4, 102–110	Gas expansion	Slight
17H-7, 36–59	Void and gas expansion	
17H-7, 59–81	Gas expansion	Slight
17H-7, 67–71	Void	
17H-7, 76–81	Void and gas expansion	
18H-1, 0–20		Moderate
18H-1, 80–81	Crack	
18H-1, 100–107	Gas expansion	Slight
18H-1, 113–117	Void	
18H-1, 117–127	Gas expansion	
18H-3, 69–76	Gas expansion	Slight
18H-3, 30–97	Gas expansion	
18H-6, 12–48	Soupy	
18H-CC, 0–19		Slight
19H-2, 50–51	Crack	
19H-2, 82–93	Void	
19H-2, 93–97	Gas expansion	Moderate
19H-4, 29–31	Gas expansion	
19H-4, 74–76	Dropsotne	
19H-5, 142–150	Dropstone	
19H-6, 53–62	Void	
19H-6, 83–88	Gas expansion	
19H-7, 44–46	Void	
20H-1, 0–72	Extruded on rig floor	
20H-2, 110–128	Gas expansion	
20H-3, 58–72	Void	Destroyed
20H-3, 94–109	Void	Destroyed
20H-4, 47–67		
20H-7, 17–69	Void	Destroyed
21H-1, 0–93	Extruded on rig floor	
21H-4, 56–84	Gas expansion	Severe
21H-6, 47–73	Gas expansion	
21H-6, 145–149	Void	
22H-1, 0–65	Extruded on rig floor	
22H-2, 83–34	Crack	Severe
22H-2, 110–112	Void	
22H-3, 68–95	Void and gas expansion	Severe
22H-3, 85–140	Gas expansion	
22H-5, 63–77	Gas expansion	
22H-8, 24–35	Gas expansion	
23H -1, 0–60	Extruded on rig floor	Moderate to high
23H -3, 95–122	Gas expansion	
23H -4, 60–77	Gas expansion	
23H -4, 115–122	Gas expansion	
23H -7, 20–25	Gas expansion	
23H -7, 145–150	Void	
23H -8, 30–31	Crack	
24H-1, 65–85	Gas expansion	
24H-1, 95–105	Gas expansion	
24H-5, 135–138	Void	Severe
24H-6, 23–55	Gas expansion	Moderate to high
24H-6, 33–47	Void	Severe
25H-1, 141–150	Gas expansion and voids	
26H-1, 0–50	Extruded on rig floor, disturbed	
26H-2, 27–31	Gas expansion	
26H-3, 138–140	Void	
26H-4, 0–28	Thick ash layer	
26H-4, 65–87	Gas expansion	
26H-4, 145–150	Void	
27H-1, 0–34	Extruded on rig floor, disturbed	
27H-3, 43–60	Gas expansion and ash	
27H-3, 70–72	Gas expansion	
27H-3, 83–85	Gas expansion	
27H-3, 95–100	Gas expansion	
27H-5, 0–150	Shattered liner, disturbed	
27H-6, 0–130	Shattered liner, disturbed	
27H-7, 0–137	Shattered liner, disturbed	
27H-7, 125–127	Shattered liner, disturbed	
27H-8, 125–127	Crack	
27H-8, 0–35	Disturbed	
27H-9, 0–71	Shattered liner, disturbed	
28H-1, 0–101	Extruded on rig floor, disturbed	
28H-2, 88–110	Gas expansion	
28H-2, 131–150	Void	Severe
28H-3, 60–97	Void and gas expansion	Severe
28H-4, 25–30	Gas expansion	
28H-4, 43–46	Gas expansion	
28H-4, 76–86	Void and gas expansion	Severe
28H-7, 66–80	Gas expansion	
29H-1, 135–145	Void	
29H-2, 83–86	Void	Severe
29H-3, 40–50	Void and gas expansion	Severe
30H-1, 55–138	Gas expansion and void	
30H-3, 99–106	Gas expansion and void	
31H-1, 100–103	Void	
31H-2, 12–14	Void	Severe
31H-2, 71–73	Void	Severe
31H-4, 37–42	Void	Severe
32H-1, 70–73	Void	Severe
32H-3, 60–80	Gas expansion	Moderate to high
32H-4, 0–43	Gas expansion	
33H-1, 66–69	Gas expansion	Moderate to high
33H-1, 81–83	Gas expansion	Moderate to high
33H-2, 65–70	Void	Severe
33H-2, 115–131	Gas expansion	
33H-3, 40–70	Void and gas expansion	Severe
33H-3, 105–110	Void	Severe
34H-1, 99–103	Void	Severe
34H-1, 148–150	Void	
34H-3, 38–39	Void	
35H-1, 112–116	Gas expansion	
35H-3, 55–62	Crack	
36H-2, 116–123	Void	
36H-3, 15–60	Gas expansion	
37H-1, 0–15	Fall-in	Slight
37H-2, 60–62	Gas expansion	
37H-2, 75–80	Ash	
37H-3, 30–35	Void	
37H-4, 11–20	Nodule?	Moderate
39H-1, 0–30	Fall-in	Severe
39H-1, 55–93	Gas expansion	
39H-2, 110–113	Gas expansion	Moderate
39H-2, 110–130	Void	
39H-3, 45–56	Void	
39H-3, 67–72	Gas expansion	Moderate
39H-4, 20–31	Void	
39H-4, 27–31	Gas expansion	Moderate
40H-1, 60–70	Void	
40H-1, 80–90	Void	
40H-2, 112–116	Gas expansion	
40H-2, 135–137	Gas expansion	
40H-3, 33–37	Gas expansion	Slight
40H-4, 23–29	Void	
40H-4, 30–47	Gas expansion	Moderate
41H-1, 26–75	Gas expansion	Moderate
41H-1, 40–52	Void	
41H-1, 111–117	Void	
41H-1, 117–125	Gas expansion	Moderate
41H-2, 0–4	Gas expansion	Moderate
41H-3, 92–93	Gas expansion	
41H-CC, 0–24		Moderate
42H-1, 0–19	Extruded on rig floor, disturbed	

Table T17 (continued). (Continued on next page.)

Core, section, interval (cm)	Comments on disturbance	Drilling disturbance intensity
42H-1, 0–19	Fall-in	High
42H-2, 56–117	Gas expansion	Slight
42H-2, 60–73	Void	
42H-3, 113–115	Gas expansion	
42H-5, 6–11	Crack	
42H-5, 15–18	Crack	
42H-5, 28–36	Void	
43H-1, 65–100	Gas expansion	Slight
43H-2, 0–4	Gas expansion	Slight
43H-CC, 0–23	Gas expansion	Slight
44H-1, 10–20	Gas expansion	
44H-1, 28–31	Gas expansion	
44H-1, 46–48	Gas expansion	
44H-2, 0–57	Mixed and ash	
44H-2, 80–97	Gas expansion	
44H-3, 54–61	Gas expansion	Slight
44H-3, 75–88	Gas expansion	Slight
44H-3, 115–116	Crack	
44H-3, 119–120	Crack	
44H-4, 0–2	Gas expansion	Slight
44H-4, 12–13	Crack	
44H-4, 43–51	Gas expansion	Slight
44H-5, 18–22	Gas expansion	Slight
44H-5, 39–45	Gas expansion	Slight
44H-CC, 0–26	Gas expansion	Slight
45H-1, 77–81	Void	
45H-2, 0–3	Disturbed	Slight
45H-2, 17–21	Crack	
45H-2, 34–37	Deformed	
45H-4, 40–45	Void	
45H-4, 44–47	Gas expansion	Slight
46H-1, 56–59	Void	
46H-2, 0–3		Slight
46H-3, 67–74	Gas expansion	
46H-3, 97–104	Gas expansion	
46H-4, 21–36	Gas expansion	
46H-4, 36–40	Void	
47H-1, 0–10	Gas expansion	Slight
47H-2, 33–38	Void	
47H-2, 38–50	Gas expansion	Slight
47H-3, 41–57	Gas expansion	Slight
47H-3, 72–75	Gas expansion	
47H-3, 90–97	Void	
48H-3, 76–79	Void	
48H-3, 79–87	Gas expansion	Slight
48H-4, 16–18	Void	
48H-4, 18–23	Gas expansion	Slight
48H-CC, 0–40		Moderate
49H-1, 0–12		Slight
49H-1, 106–107	Void	
49H-1, 107–118	Gas expansion	Slight
49H-2, 0–44	Gas expansion	Slight to moderate
49H-2, 72–77	Void	
49H-2, 77–83	Gas expansion	Slight
49H-3, 60–65	Void	
49H-3, 65–72	Gas expansion	Slight
49H-3, 116–132	Gas expansion	
49H-CC, 0–22		Slight
50H-1, 35–40	Void	
50H-1, 49–51	Gas expansion	
50H-1, 60–76	Gas expansion	Slight
50H-1, 99–102	Void	
50H-1, 102–136	Gas expansion	Slight
50H-2, 0–25	Gas expansion	Slight
50H-CC, 0–22		Slight
51H-1, 0–140	Gas expansion	Slight
51H-4, 23–32	Void	
51H-4, 32–37	Gas expansion	Slight
51H-CC, 0–25		Slight
52H-1, 0–20	Extruded on rig floor, disturbed	
52H-2, 60–69	Void	
52H-2, 69–78	Gas expansion	Slight
52H-2, 100–104	Void	
52H-2, 104–146	Gas expansion	Slight
52H-3, 120–127	Crack	
52H-4, 16–18	Crack	
52H-CC, 0–21	Crack	Slight
53H-1, 0–48	Mixed with ash	
53H-1, 35–48	Ash	
53H-1, 64–67	Void	
53H-3, 76–83	Gas expansion	Slight
53H-CC, 0–21		Slight to moderate
54H-1, 0–117	Void and gas expansion	
54H-3, 53–59	Void	
54H-CC, 0–18		Slight
55H-1, 0–20	Gas expansion	Slight
55H-1, 58–60	Gas expansion	Slight
55H-2, 16–21		
55H-2, 41–47	Gas expansion	Slight
55H-2, 59–61	Gas expansion	
55H-2, 71–76	Gas expansion	Slight
55H-2, 114–118	Gas expansion	Slight
55H-4, 0–5		Slight to moderate
55H-4, 25–31	Gas expansion	
55H-CC, 0–22		Slight
56H-1, 0–120	Gas expansion	
56H-2, 132–143	Ash	
56H-4, 34–41	Void	
57H-1, 10–22	Gas expansion	
57H-1, 72–73	Void	Severe
57H-1, 113–115	Void	Severe
57H-3, 95–123	Flow-in	
57H-4, 0–28	Flow-in	
58H-1, 0–31	Shattered/split liner, extruded on rig floor	
58H-2, 0–150	Shattered/split liner, extruded on rig floor	
58H-3, 0–83	Shattered/split liner, extruded on rig floor	
58H-4, 0–150	Shattered/split liner, extruded on rig floor	
59H-1, 0–12	Gas expansion	
59H-4, 22–25	Gas expansion	High
59H-4, 35–40	Gas expansion	High
346-U1426B-		
2H-1, 0–40	Gas expansion	
3H-1, 0–35	Gas expansion	
3H-1, 99–102	Gas expansion	
3H-2, 70–120	Disturbance	
3H-3, 50–53	Crack	
3H-3, 93–101	Gas expansion	
3H-5, 60–71	Disturbed	
3H-5, 108–110	Crack	
3H-5, 120–130	Crack	
3H-6, 60–72	Crack	
4H-1, 52–56	Ash	
4H-2, 124–130	Void	
4H-3, 50–51	Crack	
4H-5, 60–61	Crack	
4H-5, 80–90	Crack	
4H-5, 130–140	Gas expansion	
4H-6, 80–81	Crack	
346-U1426C-		
1H-1, 0–95	Soupy	High
1H-3, 80–100	Ash and slight disturbance	
2H-1, 0–15	Soupy	High
2H-6, 90–150	Gas expansion	Slight
2H-6, 0–27	Gas expansion	
3H-1, 0–15	Disturbed	

Table T17 (continued). (Continued on next page.)

Core, section, interval (cm)	Comments on disturbance	Drilling disturbance intensity
3H-2, 34–36	Crack	
3H-2, 143–150	Void	High
3H-2, 45–47	Crack	
3H-2, 65–67	Crack	
3H-2, 145–150	Void	
3H-3, 135–150	Void	High
3H-4, 147–150	Void	High
3H-6, 41–50	Void	High
3H-6, 144–150	Void	High
3H-7, 78–85	Void	High
5H-2, 20–35	Gas expansion	Moderate
5H-3, 12–17	Gas expansion	
5H-3, 32–39	Gas expansion	
5H-7, 0–15	Gas expansion	
6H-1, 0–84	Extruded on rig floor, disturbed	
6H-3, 100–110	Crack	
6H-1, 0–84	Crack	High
6H-3, 122–145	Gas expansion	
6H-4, 53–65	Gas expansion	
6H-5, 88–101	Gas expansion	
6H-6, 0–17	Gas expansion	
6H-6, 42–46	Gas expansion	
6H-6, 55–61	Gas expansion	
6H-6, 81–91	Gas expansion	
6H-8, 0–20	Gas expansion	
7H-1, 0–38	Extruded on rig floor, disturbed	Severe
7H-6, 135–142	Disturbed	
8H-1, 0–57	Gas expansion	Slight to moderate
8H-3, 45–58	Gas expansion and void	
8H-4, 57–67	Gas expansion and void	
8H-6, 40–45	Gas expansion and void	
8H-6, 70–85	Gas expansion and void	
8H-6, 115–145	Gas expansion and void	
8H-7, 50–95	Gas expansion and void	
8H-7, 105–125	Gas expansion and void	
8H-CC, 0–35		Slight
9H-1, 0–52	Fall-in	Slight to moderate
9H-2, 52–57	Gas expansion	
9H-3, 61–63	Void	
9H-3, 63–140	Gas expansion	Slight
9H-4, 42–61	Gas expansion	Slight
9H-4, 69–74	Void	
9H-4, 74–82	Gas expansion	
9H-5, 62–68	Gas expansion	
9H-5, 90–140	Gas expansion	
9H-6, 0–30	Gas expansion	
9H-6, 45–58	Void and gas expansion	
9H-7, 0–131	Gas expansion	Slight
9H-8, 0–66	Gas expansion	Slight
10H-1, 0–57	Gas expansion	
10H-2, 50–75	Gas expansion	Slight to moderate
10H-3, 0–72	Gas expansion	Slight to moderate
10H-3, 52–60	Void	
10H-4, 0–62	Gas expansion	Slight
10H-4, 62–70	Void	
10H-4, 70–105	Gas expansion	Moderate to high
10H-5, 52–73	Gas expansion	Moderate
10H-5, 63–70	Void	
10H-5, 70–145	Gas expansion	Slight
10H-6, 30–80	Gas expansion	Moderate to high
10H-6, 103–116	Gas expansion	Slight
10H-7, 0–10	Gas expansion	
10H-7, 91–94	Void	
10H-7, 94–105	Gas expansion	Slight
10H-8, 0–24	Gas expansion	Slight
10H-8, 46–70	Gas expansion	Moderate
10H-CC, 0–29		High
11H-1, 0–69	Gas expansion	High
11H-3, 79–83	Void	
11H-3, 83–92	Gas expansion	Slight to moderate
11H-5, 85–86	Crack	
11H-6, 49–52	Void	
11H-6, 65–75	Ash	
11H-6, 138–145	Gas expansion	
11H-7, 11–18	Gas expansion	Moderate
11H-7, 37–58	Gas expansion	Moderate
11H-7, 90–111	Gas expansion	Moderate
11H-7, 111–128	Void	
11H-8, 34–40	Void	
11H-CC, 0–26		Moderate
12H-1, 57–68	Gas expansion	Moderate to high
12H-1, 68–77	Void	
12H-1, 112–122	Gas expansion	Slight
12H-3, 46–53	Gas expansion	
12H-3, 60–69	Void	
12H-4, 17–23	Gas expansion	
12H-4, 55–60	Void	
12H-6, 90–100	Gas expansion	
12H-6, 135–150	Gas expansion	
12H-7, 18–26	Gas expansion	Slight
12H-7, 117–136	Void	
12H-CC, 0–26		Slight
13H-1, 0–85	Gas expansion	Moderate
13H-1, 85–94	Void	
13H-2, 37–77	Gas expansion	High
13H-2, 44–59	Void	
13H-3, 65–69	Gas expansion	Slight
13H-4, 68–72	Void	
13H-5, 65–95	Gas expansion	
13H-5, 146–150	Void	
13H-6, 0–2		Slight
13H-7, 20–25	Gas expansion	
13H-7, 82–95	Gas expansion	
13H-7, 116–130	Void	
13H-8, 17–19	Gas expansion	
13H-8, 108–129	Void	
13H-CC, 0–28		Moderate
14H-1, 0–100	Gas expansion	High
14H-2, 50–57	Gas expansion	
14H-2, 57–73	Void	
14H-2, 73–89	Gas expansion	Moderate
14H-3, 31–50	Void	
14H-3, 63–85	Gas expansion	Moderate
14H-4, 72–73	Void	
14H-4, 119–121	Crack	
14H-7, 10.5–19	Void	
14H-7, 54.5–57.5	Void	
14H-7, 102–109	Void	
14H-8, 18–19	Crack	
15H-1, 0–25	Disturbed	
15H-2, 0–12	Disturbed	Slight
15H-2, 77–104	Gas expansion	Moderate
15H-3, 0–41	Gas expansion	Slight to moderate
15H-4, 67–69	Void	
15H-5, 100–103	Void	
15H-6, 0–96	Gas expansion	Slight
15H-7, 0–55	Gas expansion	Slight
15H-8, 0–63	Gas expansion	Slight
15H-CC, 0–14	Gas expansion	Slight
15H-CC, 8–19	Gas expansion	Moderate
17H-1, 0–15	mousselike	Severe
17H-1, 15–40	Gas expansion	Moderate to high
17H-2, 45–48	Void	
17H-2, 48–51	Gas expansion	Moderate
17H-7, 23–48	Gas expansion	
17H-7, 48–76	Void	
17H-8, 15–22	Crack	
17H-8, 55–99	Gas expansion	Slight
17H-CC, 0–24	Gas expansion	Slight
18H-1, 0–75	Gas expansion	Slight to moderate

Table T17 (continued). (Continued on next page.)

Core, section, interval (cm)	Comments on disturbance	Drilling disturbance intensity
18H-2, 53–55	Void	
18H-7, 70–100	Void	
18H-8, 69–78	Void	
18H-CC, 0–42		Slight
19H-1, 0–70	Disturbed came out of the top of core barrel	
19H-2, 52–55	Void	Destroyed
19H-3, 90–105	Crack	
19H-3, 114–115	Crack	
19H-4, 67–76	Gas expansion	
19H-4, 100–105	Gas expansion	
19H-5, 40–80	Gas expansion	
19H-8, 42–46	Gas expansion	
19H-8, 60–67	Gas expansion	
19H-8, 67–79	Void	Destroyed
19H-8, 79–86	Gas expansion	
20H-1, 0–71	Crack	High
20H-3, 78–86	Gas expansion	
20H-3, 86–112	Ash	
20H-5, 0–7	Gas expansion	
20H-5, 52–60	Gas expansion	
20H-5, 60–66	Gas expansion	
20H-6, 52–72	Gas expansion	High
20H-6, 72–93	Void	High
20H-6, 93–107	Gas expansion	High
20H-7, 45–47	Crack	
20H-8, 17–43	Gas expansion	Moderate
20H-8, 43–50	Void	High
21H-1, 0–112	Extruded on rig floor, disturbed	
21H-2, 51–60	Gas expansion	Moderate
21H-2, 113–115	Gas expansion	
21H-3, 60–66	Gas expansion	Moderate
21H-3, 66–70	Void	Moderate
21H-3, 122–131	Gas expansion	
21H-4, 50–118	Gas expansion	Moderate
21H-6, 51–53	Crack	
21H-6, 125–130	Gas expansion	
21H-8, 40–62	Gas expansion	
22H-1, 80–100	Void and gas expansion	High
22H-2, 55–90	Gas expansion	Moderate
22H-4, 30–37	Gas expansion	Moderate
22H-4, 55–62	Gas expansion	
22H-5, 68–91	Gas expansion	
22H-6, 43–45	Gas expansion	
22H-7, 0–20	Gas expansion	
23H-1, 0–10	Gas expansion	
23H-4, 15–23	Void	High
23H-4, 80–92	Gas expansion	
23H-4, 92–101	Void	High
23H-5, 61–67	Void	High
23H-6, 90–103	Gas expansion	
23H-6, 62–66	Disturbed	
24H-1, 0–23	Gas expansion	Moderate
24H-1, 62–70	Void and gas expansion	High
24H-2, 40–43	Gas expansion	
24H-2, 54–66	Gas expansion	
24H-2, 138–142	Gas expansion	
24H-3, 69–70	Gas expansion	
24H-4, 85–93	Void	High
24H-4, 93–101	Crack	Moderate to high
24H-5, 40–45	Gas expansion	
24H-5, 84–86	Gas expansion	
24H-5, 115–117	Void	High
24H-6, 85–100	Gas expansion	High
24H-7, 20–43	Gas expansion	
24H-7, 43–53	Void	
24H-7, 98–112	Gas expansion	
346-U1426D-		
2H-1, 0–5	Soupy	
2H-1, 0–38	Soupy	High
3H-3, 115–116	Crack	
3H-3, 140–141	Crack	
3H-7, 0–84	Gas expansion	Moderate
3H-5, 80–81	Crack	
3H-5, 104–105	Crack	
3H-5, 129–130	Crack	
3H-7, 0–8	Crack	
3H-7, 20–30	Crack	
3H-7, 50–55	Crack	
4H-2, 75–95	Crack	
4H-2, 90–95	Crack	
4H-2, 100–105	Crack	
4H-2, 117–118	Crack	
4H-3, 95–115	Tilted	
4H-3, 124–125	Crack	
4H-4, 114–115	Crack	
4H-6, 14–16	Crack	
5H-1, 0–56	Gas expansion	Moderate
5H-3, 10–15	Crack	
5H-6, 25–26	Crack	
5H-6, 34–35	Crack	
5H-6, 50–65	Gas expansion	
5H-6, 117–150	Gas expansion	
6H-1, 105–115	Gas expansion	
6H-2, 68–82	Crack	
6H-3, 80–81	Crack	
6H-3, 95–105	Crack	
6H-3, 115–120	Crack	
6H-4, 55–75	Tilted	
6H-5, 50–125	Tilted	
6H-6, 10–12	Crack	
6H-6, 24–26	Crack	
6H-6, 50–70	Crack	
6H-6, 147–150	Void	High
6H-7, 45–55	Tilted	
6H-7, 65–77	Gas expansion and void	High
7H-1, 0–100	Gas expansion	Moderate to high
7H-3, 8–13	Ash	
7H-3, 40–45	Nodule?	
7H-4, 0–10	Ash	
7H-4, 79–87	Ash	
7H-5, 69–72	Gas expansion	
7H-5, 129–140	Void	High
7H-6, 30–60	Gas expansion	Moderate
7H-6, 90–120	Gas expansion	
7H-7, 0–20	Gas expansion	
7H-7, 140–150	Gas expansion	
8H-1, 0–81	Gas expansion	High
8H-4, 25–60	Gas expansion	
8H-5, 65–85	Gas expansion and void	High
8H-6, 0–80	Tilted	
8H-7, 43–46	Void	High
8H-7, 90–151	Gas expansion and void	High
9H-1, 0–98	Gas expansion	Moderate to high
9H-2, 0–3	Gas expansion	Slight
9H-2, 80–82	Crack	
9H-3, 67–68	Void	
9H-3, 68–71	Gas expansion	Moderate
9H-3, 99–103	Void	
9H-3, 103–107	Gas expansion	Moderate
9H-4, 75–115	Gas expansion	Moderate
9H-5, 20–21	Crack	
9H-5, 48–54	Void	
9H-6, 80–100	Tilted	
9H-6, 136–144	Void	
9H-7, 62–76	Gas expansion and void	
9H-CC, 0–26	Gas expansion	Slight
10H-1, 0–120	Gas expansion	Slight

Table T17 (continued).

Core, section, interval (cm)	Comments on disturbance	Drilling disturbance intensity
10H-2, 50–71	Gas expansion	
10H-3, 82–85	Crack	
10H-4, 20–30	Gas expansion	Slight
10H-4, 26–41	Gas expansion	Moderate
10H-4, 69–71	Crack	
10H-4, 85–110	Gas expansion	Slight
10H-7, 15–35	Gas expansion	
10H-7, 80–81	Crack	
10H-8, 0–25	Gas expansion	
10H-CC, 0–18	Gas expansion	Moderate
11H-1, 0–63	Gas expansion	Moderate
11H-2, 86–106	Gas expansion	
11H-3, 38–60	Gas expansion	Slight
11H-3, 50–65	Gas expansion	
11H-5, 35–36	Crack	
11H-5, 44–46	Crack	
11H-5, 62–63	Crack	
11H-5, 109–110	Crack	
11H-5, 139–140	Crack	
11H-6, 70–80	Gas expansion	
11H-6, 10–25	Gas expansion	
11H-6, 25–27	Void	
11H-6, 142–150	Void	
11H-7, 26–63	Gas expansion	Slight
11H-8, 37–62	bowed	Moderate
11H-CC, 0–20	Gas expansion	Moderate

Table T18. NRM inclination, declination, and intensity data after 20 mT peak field AF demagnetization, Site U1426.

Core, section, interval (cm)	Depth CSF-A (m)	Inclination (°)	Declination (°)	FlexIT-corrected declination (°)	Intensity (A/m)
346-U1426A-					
1H-1	0				
1H-1, 5	0.05				
1H-1, 10	0.1				
1H-1, 15	0.15				
1H-1, 20	0.2				
1H-1, 25	0.25				
1H-1, 30	0.3				
1H-1, 35	0.35				
1H-1, 40	0.4				
1H-1, 45	0.45				
1H-1, 50	0.5				
1H-1, 55	0.55				
1H-1, 60	0.6				
1H-1, 65	0.65				
1H-1, 70	0.7				
1H-1, 75	0.75				
1H-1, 80	0.8				
1H-1, 85	0.85				
1H-1, 90	0.9				
1H-1, 95	0.95				
1H-1, 100	1				
1H-1, 105	1.05				
1H-1, 110	1.1				
1H-1, 115	1.15				
1H-1, 120	1.2				
1H-1, 125	1.25				
1H-1, 130	1.3				
1H-1, 135	1.35				
1H-1, 140	1.4				
1H-1, 145	1.45				
1H-1, 150	1.5				
1H-2	1.5				
1H-2, 5	1.55				
1H-2, 10	1.6				
1H-2, 15	1.65	54.7	333.8		0.008786
1H-2, 20	1.7	55.7	328.9		0.00962
1H-2, 25	1.75	58.8	329.6		0.009192
1H-2, 30	1.8	59.1	332.2		0.010253
1H-2, 35	1.85	58	331.3		0.011652
1H-2, 40	1.9	58.3	329.5		0.012388
1H-2, 45	1.95	56.7	329.9		0.013293
1H-2, 50	2	53.6	325.4		0.01402
1H-2, 55	2.05	53.7	327.6		0.012723
1H-2, 60	2.1	54.5	331.1		0.011506
1H-2, 65	2.15	54	324.9		0.009517
1H-2, 70	2.2				
1H-2, 75	2.25				
1H-2, 80	2.3				
2H-1	2.5				
2H-1, 5	2.55				
2H-1, 10	2.6				
2H-1, 15	2.65	65	262.8	99.88	0.01923
2H-1, 20	2.7	61.5	259.1	96.18	0.022321
2H-1, 25	2.75	64.2	257.4	94.48	0.01967
2H-1, 30	2.8	63.8	254.9	91.98	0.015391
2H-1, 35	2.85	68	261.1	98.18	0.010369
2H-1, 40	2.9	72.4	258	95.08	0.008034
2H-1, 45	2.95	69.7	253	90.08	0.006719
2H-1, 50	3	66.6	247	84.08	0.005908

Blank cells indicate depth levels where data were either not available (i.e., FlexIT-corrected declination data for nonoriented cores) or removed because of disturbance, voids, or measurement edge effects. Only a portion of this table appears here. The complete table is available in **ASCII.**

Table T19. Polarity boundary, Site U1426.

Core, section, interval (cm)		Polarity boundaries	Age (Ma)	Depth CSF-A (m)				Depth CCSF-D (m)			
Top	Bottom			Top	Bottom	Midpoint	±	Top	Bottom	Midpoint	±
346-U1426A-	346-U1426A-										
10H-3, ~87	10H-4, ~50	(B) C1n (Brunhes/Matuyama)	0.781	81.2	82.2	**81.7**	0.5	86.86	87.86	**87.36**	0.5
10H-6, ~115	10H-7, ~95	(T) C1r.1n (Jaramillo)	0.988	85.34	86.54	**85.94**	0.6	91.00	92.20	**91.60**	0.6
11H-8, ~50	12H-3, ~60	(B) C1r.1n (Jaramillo)	1.072	97.7	99.3	98.5	0.8	107.29	108.89	108.09	0.8
19H-5, ~70	19H-5, ~90	(T) C2n (Olduvai)	1.778	168.95	169.95	**169.45**	0.5	190.70	191.70	**191.20**	0.5
21H-7, ~45	22H-2, ~75	(B) C2n (Olduvai)	1.945	189.6	193.6	**191.6**	2	214.57	218.57	**216.57**	2
28H-6, ~10	28H-7, ~60	(T) C2An.1n (Matuyama/Gauss)	2.581	253.6	255.6	**254.6**	1	279.34	281.34	**280.34**	1
346-U1426C-	346-U1426C-										
9H-6, ~60	10H-2, ~85	(B) C1n (Brunhes/Matuyama)	0.781	71.9	80.9	76.4	4.5	77.66	86.66	82.16	4.5
10H-8, ~40	11H-2, ~80	(T) C1r.1n (Jaramillo)	0.988	84	86	**85**	1	91.42	93.42	**92.42**	1
12H-4, ~65	12H-5, ~75	(B) C1r.1n (Jaramillo)	1.072	98.6	100.2	**99.4**	0.8	107.70	109.30	**108.50**	0.8
21H-1, ~80	21H-2, ~110	(T) C2n (Olduvai)	1.778	168.8	172.2	170.5	1.7	190.57	193.97	192.27	1.7
23H-2, ~120	23H-4, ~25	(B) C2n (Olduvai)	1.945	188.6	190.6	**189.6**	1	213.03	215.03	**214.03**	1
346-U1426D-	346-U1426D-										
9H-8, ~40	10H-2, ~20	(B) C1n (Brunhes/Matuyama)	0.781	80	81.8	**80.9**	0.9	85.65	87.45	**86.55**	0.9
10H-5, ~25	10H-5, ~85	(T) C1r.1n (Jaramillo)	0.988	85.8	86.4	**86.1**	0.3	91.45	92.05	**91.75**	0.3

Bold = boundaries that are relatively well defined. B = bottom, T= top.

Table T20. Results from APCT-3 temperature profiles, Site U1426.

Core	Minimum temperature at mudline (°C)	Average temperature at mudline (°C)	Depth CSF-A (m)	In situ temperature (°C)	Thermal resistance (m^2K/W)
346-U1426A-					
4H	0.47	0.87	31.0	4.00	36.38
7H	0.45	0.85	59.5	7.01	70.72
10H	0.61	1.03	88.0	10.58	105.96
13H	0.50	0.85	116.5	13.88	142.16
Average:	0.51	0.90			

In situ temperatures were determined using TP-Fit software by Martin Heesemann. Thermal resistance was calculated from thermal conductivity data (see **"Physical properties"**) corrected for in situ conditions (see **"Downhole measurements"** in the "Methods" chapter [Tada et al., 2015b]).

Table T21. Vertical offsets required to correlate specific features among cores from adjacent holes, Site U1426.

Core	Vertical offset (m)	Y/N
346-U1426A-		
1H	0.166	Y
2H	0.700	Y
3H	1.120	Y
4H	2.011	Y
5H	3.736	Y
6H	4.632	Y
7H	5.686	Y
8H	4.584	Y
9H	5.983	Y
10H	5.655	Y
11H	6.963	Y
12H	9.588	Y
13H	9.794	Y
14H	11.855	Y
15H	13.879	Y
16H	16.899	Y
17H	18.205	Y
18H	20.843	Y
19H	21.747	Y
20H	22.657	Y
21H	23.515	Y
22H	24.973	Y
23H	25.744	Y
24H	25.744	N
25H	25.744	N
26H	25.744	N
27H	25.744	N
28H	25.744	N
29H	25.744	N
30H	25.744	N
31H	25.744	N
32H	25.744	N
33H	25.744	N
34H	25.744	N
35H	25.744	N
36H	25.744	N
37H	25.744	N
38X	25.744	N
39H	25.744	N
40H	25.744	N
41H	25.744	N
42H	25.744	N
43H	25.744	N
44H	25.744	N
45H	25.744	N
46H	25.744	N
47H	25.744	N
48H	25.744	N
49H	25.744	N
50H	25.744	N
51H	25.744	N
52H	25.744	N
53H	25.744	N
54H	25.744	N
55H	25.744	N
56H	25.744	N
57H	25.744	N
58H	25.744	N
59H	25.744	N
346-U1426B-		
1H	0.268	Y
2H	0.561	Y
3H	1.391	Y
4H	2.782	Y
346-U1426C-		
1H	0.000	N
2H	0.252	Y
3H	1.386	Y
4X	1.386	N
5H	2.534	Y
6H	4.062	Y
7H	4.761	Y
8H	4.719	Y
9H	5.666	Y
10H	5.758	Y
11H	7.424	Y
12H	9.095	Y
13H	10.143	Y
14H	11.372	Y
15H	13.371	Y
16X	13.371	N
17H	15.566	Y
18H	17.750	Y
19H	19.498	Y
20H	20.478	Y
21H	21.770	Y
22H	22.381	Y
23H	24.426	Y
24H	25.324	Y
346-U1426D-		
1H	0.152	Y
2H	0.603	Y
3H	1.164	Y
4H	2.336	Y
5H	3.629	Y
6H	5.337	Y
7H	5.947	Y
8H	4.617	Y
9H	4.175	Y
10H	5.649	Y
11H	7.064	Y

Table T22. Splice intervals, Site U1426.

Hole, core, section, interval (cm)	Depth in section (cm)	Depth CSF-A (m)	Depth CCSF-D (m)	Hole, core, section, interval (cm)	Depth in section (cm)	Depth CSF-A (m)	Depth CCSF-D (m)	Data used to tie
346-				346-				
U1426C-1H-1	0.00	0.00	0.00	U1426C-1H-3	73.78	3.74	3.74	Blue
U1426A-2H-1	53.78	3.04	3.74	U1426A-2H-6	59.96	10.60	11.30	Blue
U1426C-2H-4	4.76	11.05	11.30	U1426C-2H-6	119.37	15.19	15.45	Blue
U1426A-3H-2	82.54	14.33	15.45	U1426A-3H-6	93.77	20.47	21.59	Blue
U1426C-3H-3	120.21	20.20	21.59	U1426C-3H-6	21.14	23.71	25.10	Blue
U1426A-4H-2	17.62	23.09	25.10	U1426A-4H-6	136.29	29.72	31.73	Blue
U1426C-5H-2	22.97	29.20	31.73	U1426C-5H-6	77.69	35.39	37.92	Blue
U1426D-5H-2	83.24	34.29	37.92	U1426D-5H-7	67.14	41.16	44.79	Blue
U1426C-6H-3	138.82	40.73	44.79	U1426C-6H-8	7.14	45.15	49.21	Blue
U1426A-6H-5	1.18	44.58	49.21	U1426A-6H-8	81.61	49.20	53.83	Blue
U1426C-7H-3	84.63	49.07	53.83	U1426C-7H-7	69.71	54.41	59.17	Blue
U1426A-7H-3	92.30	53.48	59.17	U1426A-7H-6	119.38	57.79	63.48	Blue
U1426C-8H-3	80.05	58.76	63.48	U1426C-8H-6	93.27	63.05	67.77	Blue
U1426D-8H-2	94.43	63.15	67.77	U1426D-8H-6	144.26	68.56	73.18	Blue
U1426C-9H-3	37.42	67.51	73.18	U1426C-9H-8	14.96	74.20	79.87	Blue
U1426D-9H-4	129.01	75.69	79.87	U1426D-9H-8	41.97	80.02	84.19	Blue
U1426C-10H-4	54.71	78.44	84.19	U1426C-10H-7	126.47	83.38	89.14	Blue
U1426D-10H-3	85.34	83.49	89.14	U1426D-10H-6	145.09	88.50	94.15	Blue
U1426C-11H-3	65.55	86.73	94.15	U1426C-11H-7	16.16	91.87	99.30	Blue
U1426D-11H-3	63.20	92.23	99.30	U1426D-11H-8	16.74	98.89	105.95	Blue
U1426C-12H-3	39.60	96.86	105.95	U1426C-12H-6	133.29	102.31	111.41	Blue
U1426A-12H-5	32.07	101.82	111.41	U1426A-12H-8	21.93	105.96	115.55	Blue
U1426C-13H-2	96.38	105.40	115.55	U1426C-13H-8	22.37	112.49	122.64	Blue
U1426A-13H-5	53.25	112.84	122.64	U1426A-13H-6	144.32	115.27	125.07	Blue
U1426C-14H-1	69.58	113.70	125.07	U1426C-14H-7	86.81	121.90	133.27	Blue
U1426A-14H-4	122.48	121.41	133.27	U1426A-14H-7	114.09	125.56	137.42	Blue
U1426C-15H-2	4.49	124.04	137.42	U1426C-15H-4	146.70	128.40	141.77	Blue
U1426A-15H-2	66.88	127.89	141.77	U1426A-15H-7	134.51	135.86	149.73	Blue
U1426C-17H-3	99.84	134.17	149.73	U1426C-17H-7	134.78	139.65	155.21	Blue
U1426A-16H-2	137.48	138.31	155.21	U1426A-16H-6	122.99	144.21	161.11	Blue
U1426C-18H-4	18.81	143.36	161.11	U1426C-18H-6	141.83	147.21	164.96	Blue
U1426A-17H-2	42.37	146.75	164.96	U1426A-17H-6	3.55	152.32	170.52	Blue
U1426C-19H-2	32.26	151.02	170.52	U1426C-19H-7	116.63	158.12	177.61	Blue
U1426A-18H-2	77.13	156.77	177.61	U1426A-18H-5	117.40	161.67	182.52	Blue
U1426C-20H-3	51.87	162.04	182.52	U1426C-20H-7	80.02	167.81	188.29	Blue
U1426A-19H-3	89.13	166.54	188.29	U1426A-19H-6	35.39	170.50	192.25	Blue
U1426C-21H-2	36.11	170.48	192.25	U1426C-21H-7	73.17	178.00	199.77	Blue
U1426A-20H-4	132.45	177.11	199.77	U1426A-20H-7	80.96	181.10	203.76	Blue
U1426C-22H-2	137.60	181.38	203.76	U1426C-22H-7	29.45	186.63	209.01	Blue
U1426A-21H-3	137.02	185.50	209.01	U1426A-21H-7	58.75	190.72	214.23	Blue
U1426C-23H-3	91.60	189.81	214.23	U1426C-23H-7	44.16	195.31	219.74	Blue
U1426A-22H-4	38.44	194.76	219.74	U1426A-22H-7	113.16	200.01	224.99	Blue
U1426C-24H-3	23.06	199.66	224.99	U1426C-24H-6	18.14	204.03	229.36	Blue
U1426A-23H-3	131.22	203.61	229.36	U1426A-23H-8	74.50	210.49	236.23	Blue

Blue = RGB blue datum.

Table T23. CCSF-C depth scale, Holes U1426A, U1426B, U1426C, and U1426D.

Core, section, interval (cm)	Depth CCSF-C (m)	RGB (blue)	Depth CSF-A (m)	Core, section, interval (cm)	Depth CCSF-C (m)	RGB (blue)	Depth CSF-A (m)	Core, section, interval (cm)	Depth CCSF-C (m)	RGB (blue)	Depth CSF-A (m)	Core, section, interval (cm)	Depth CCSF-C (m)	RGB (blue)	Depth CSF-A (m)
346-U1426A-				346-U1426B-				346-U1426C-				346-U1426D-			
1H-2, 19.5	1.860807	22.9	1.70	1H-2, 43.51	2.20	21.6	1.94	6H-2, 26	42.20	37.5	38.10	1H-1, 5.5	0.21	26.3	0.01
1H-2, 20	1.865807	23.5	1.70	1H-2, 44.01	2.21	20.7	1.94	6H-2, 26.5	42.21	37.1	38.11	1H-1, 6	0.21	24.5	0.06
1H-2, 20.5	1.870807	23.5	1.71	1H-2, 44.51	2.21	20.6	1.95	6H-2, 27	42.21	36.8	38.11	1H-1, 6.5	0.22	25.7	0.07
1H-2, 21	1.875807	23.9	1.71	1H-2, 45.01	2.22	20.5	1.95	6H-2, 27.5	42.22	37.7	38.12	1H-1, 7	0.22	26.2	0.07
1H-2, 21.5	1.880807	24.4	1.72	1H-2, 45.51	2.22	20.8	1.96	6H-2, 28	42.22	37.3	38.12	1H-1, 7.5	0.23	26.8	0.08
1H-2, 22	1.885807	25.7	1.72	1H-2, 46.01	2.23	20.9	1.96	6H-2, 28.5	42.23	37.8	38.13	1H-1, 8.01	0.23	27.4	0.08
1H-2, 22.5	1.890807	23.9	1.73	1H-2, 46.51	2.23	20.8	1.97	6H-2, 29	42.23	37.1	38.13	1H-1, 8.51	0.24	26.2	0.09
1H-2, 23	1.895807	24	1.73	1H-2, 47.01	2.24	20.9	1.97	6H-2, 29.5	42.24	37.4	38.14	1H-1, 9.01	0.24	27.2	0.09
1H-2, 23.5	1.900807	24.4	1.74	1H-2, 47.51	2.24	20.9	1.98	6H-2, 30	42.24	36.8	38.14	1H-1, 9.51	0.25	28	0.10
1H-2, 24	1.905807	23.9	1.74	1H-2, 48.01	2.25	21	1.98	6H-2, 30.5	42.25	36.9	38.15	1H-1, 10.01	0.25	28.5	0.10
1H-2, 24.5	1.910807	24.6	1.75	1H-2, 48.51	2.25	21.4	1.99	6H-2, 31	42.25	37.1	38.15	1H-1, 10.51	0.26	27.5	0.11
1H-2, 25	1.915807	24.7	1.75	1H-2, 49.01	2.26	21.6	1.99	6H-2, 31.5	42.26	37.9	38.16	1H-1, 11.01	0.26	27.6	0.11
1H-2, 25.5	1.920807	24.6	1.76	1H-2, 49.51	2.26	21.4	2.00	6H-2, 32.01	42.26	38.1	38.16	1H-1, 11.51	0.27	27	0.12
1H-2, 26	1.925807	24.5	1.76	1H-2, 50.01	2.27	21.3	2.00	6H-2, 32.51	42.27	38.4	38.17	1H-1, 12.01	0.27	27	0.12
1H-2, 26.5	1.930807	23.8	1.77	1H-2, 50.51	2.27	20.7	2.01	6H-2, 33.01	42.27	38.6	38.17	1H-1, 12.51	0.28	27.1	0.13
1H-2, 27	1.935807	23.8	1.77	1H-2, 51.01	2.28	20.5	2.01	6H-2, 33.51	42.28	38.4	38.18	1H-1, 13.01	0.28	25.7	0.13
1H-2, 27.5	1.940807	23.7	1.78	1H-2, 51.51	2.28	21.6	2.02	6H-2, 34.01	42.28	38.6	38.18	1H-1, 13.51	0.29	25.3	0.14
1H-2, 28	1.945807	23.9	1.78	1H-2, 52.01	2.29	21.1	2.02	6H-2, 34.51	42.29	38.6	38.19	1H-1, 14.01	0.29	26.1	0.14
1H-2, 28.5	1.950807	25	1.79	1H-2, 52.51	2.29	21.2	2.03	6H-2, 35.01	42.29	37.5	38.19	1H-1, 14.51	0.30	26	0.15
1H-2, 29	1.955807	23.8	1.79	1H-2, 53.01	2.30	21.2	2.03	6H-2, 35.51	42.30	36.5	38.20	1H-1, 15.01	0.30	26.2	0.15
1H-2, 29.5	1.960807	21.8	1.80	1H-2, 53.51	2.30	22.2	2.04	6H-2, 36.01	42.30	36.6	38.20	1H-1, 15.51	0.31	26.2	0.16
1H-2, 30	1.965807	21.9	1.80	1H-2, 54.01	2.31	23.7	2.04	6H-2, 36.51	42.31	37.8	38.21	1H-1, 16	0.31	26.8	0.16
1H-2, 30.5	1.970807	21.6	1.81	1H-2, 54.51	2.31	22	2.05	6H-2, 37.01	42.31	37.9	38.21	1H-1, 16.5	0.32	26.6	0.17
1H-2, 31	1.975807	21.8	1.81	1H-2, 55.01	2.32	22	2.05	6H-2, 37.51	42.32	38	38.22	1H-1, 17	0.32	27.9	0.17
1H-2, 31.5	1.980807	22.3	1.82	1H-2, 55.51	2.32	21.9	2.06	6H-2, 38.01	42.32	37.6	38.22	1H-1, 17.5	0.33	28.3	0.18
1H-2, 32.01	1.985907	21.7	1.82	1H-2, 56.01	2.33	21.6	2.06	6H-2, 38.51	42.33	35.3	38.23	1H-1, 18	0.33	28.1	0.18
1H-2, 32.51	1.990907	21.5	1.83	1H-2, 56.51	2.33	21.1	2.07	6H-2, 39.01	42.33	33.9	38.23	1H-1, 18.5	0.34	27.1	0.19
1H-2, 33.01	1.995907	22	1.83	1H-2, 57.01	2.34	22.8	2.07	6H-2, 39.51	42.34	32.2	38.24	1H-1, 19	0.34	27.4	0.19
1H-2, 33.51	2.000907	22.3	1.84	1H-2, 57.51	2.34	24.6	2.08	6H-2, 40.01	42.34	32.5	38.24	1H-1, 19.5	0.35	27	0.20
1H-2, 34.01	2.005907	22.5	1.84	1H-2, 58.01	2.35	24.4	2.08	6H-2, 40.51	42.35	34.1	38.25	1H-1, 20	0.35	27.2	0.20
1H-2, 34.51	2.010907	22.3	1.85	1H-2, 58.51	2.35	24.9	2.09	6H-2, 41.01	42.35	34.3	38.25	1H-1, 20.5	0.36	27.3	0.21
1H-2, 35.01	2.015907	22.1	1.85	1H-2, 59.01	2.36	24.9	2.09	6H-2, 41.51	42.36	34	38.26	1H-1, 21	0.36	24.7	0.21
1H-2, 35.51	2.020907	22.5	1.86	1H-2, 59.51	2.36	25	2.10	6H-2, 42.01	42.36	35.3	38.26	1H-1, 21.5	0.37	26.2	0.22
1H-2, 36.01	2.025907	22	1.86	1H-2, 60.01	2.37	26.3	2.10	6H-2, 42.51	42.37	34.8	38.27	1H-1, 22	0.37	26.3	0.22
1H-2, 36.51	2.030907	21.4	1.87	1H-2, 60.51	2.37	26.2	2.11	6H-2, 43.01	42.37	34.7	38.27	1H-1, 22.5	0.38	26.9	0.23
1H-2, 37.01	2.035907	20.8	1.87	1H-2, 61.01	2.38	27.7	2.11	6H-2, 43.51	42.38	34.8	38.28	1H-1, 23	0.38	27.1	0.23
1H-2, 37.51	2.040907	21.2	1.88	1H-2, 61.51	2.38	27.9	2.12	6H-2, 44.01	42.38	34.7	38.28	1H-1, 23.5	0.39	27.3	0.24
1H-2, 38.01	2.045907	21.2	1.88	1H-2, 62.01	2.39	28.6	2.12	6H-2, 44.51	42.39	34.1	38.29	1H-1, 24	0.39	26.9	0.24
1H-2, 38.51	2.050907	21.2	1.89	1H-2, 62.51	2.39	28.5	2.13	6H-2, 45.01	42.39	32.1	38.29	1H-1, 24.5	0.40	27.2	0.25
1H-2, 39.01	2.055907	21	1.89	1H-2, 63.01	2.40	28.3	2.13	6H-2, 45.51	42.40	31.7	38.30	1H-1, 25	0.40	27.8	0.25
1H-2, 39.51	2.060907	20.8	1.90	1H-2, 63.51	2.40	28.9	2.14	6H-2, 46.01	42.40	31.5	38.30	1H-1, 25.5	0.42	26.9	0.26
1H-2, 40.01	2.065907	21.3	1.90	1H-2, 64	2.41	29.1	2.14	6H-2, 46.51	42.41	32.9	38.31	1H-1, 26	0.41	26.7	0.26
1H-2, 40.51	2.070907	21.6	1.91	1H-2, 64.5	2.41	30.6	2.15	6H-2, 47.01	42.41	33	38.31	1H-1, 26.5	0.42	26.8	0.27
1H-2, 41.01	2.075907	21.3	1.91	1H-2, 65	2.42	30.1	2.15	6H-2, 47.51	42.42	33.1	38.32	1H-1, 27	0.42	25.1	0.27
1H-2, 41.51	2.080907	21.2	1.92	1H-2, 65.5	2.42	30.6	2.16	6H-2, 48.01	42.42	33.6	38.32	1H-1, 27.5	0.43	26.5	0.28

Only a portion of this table appears here. The complete table is available in **ASCII.**